



Sergey V. Kochetov

Time- and frequency-domain modeling of passive interconnection structures in field and circuit analysis

The present-day electronic technologies require transmission of high-frequency signals via the different types of passive interconnection structures. Since the rise and fall times of signal waveforms may amount to tens of picoseconds, the parasitic effects of the passive interconnections may cause a number of phenomena, which are significant for both the development of electrical equipment and EMC analysis. Hence, the accurate electromagnetic modeling of passive interconnections is an important issue in the modern computational electromagnetics, which is thorough and pedagogically investigated in this monograph. The advanced approaches considered are consequently derived from the basic equations of the electromagnetic theory, which are briefly summarized at the begin of the monograph. The comparative study of the most wide-spread numerical techniques applied in the practice follows the theoretical fundamentals. The monograph gives a detailed survey of the transmission-line theory based methods, integral-equation techniques, differential methods, and reduction-order approaches, moreover, it develops a number of novel methods. In particular, one may select the following most important issues presented in this monograph:

- the generalized formulation of the Partial Element Equivalent Circuit (PEEC) method based on the mixed-potential integral equation (MPIE) with a dyadic Green's function for the vector magnetic and a scalar Green's function for the scalar electric potentials,
- the formulation of the PEEC method based on the MPIE with the dyadic Green's functions for the plane-stratified medium, which is applied to modeling multilayer PCB boards,
- the full-spectrum convolution macromodeling technique,
- the stable modification of the free-space PEEC method,

Sergey V. Kochetov: Modeling of passive interconnection structures

Time- and frequency-domain modeling of passive interconnection structures in field and circuit analysis

Habilitationsschrift

von Dr.-Ing. Sergey V. Kochetov

geb. am 17. April 1973

in Sankt Petersburg, Russland

zur Verleihung des akademischen Grades

Doktor-Ingenieur habitatus
(Dr.-Ing. habil.)

genehmigt von der Fakultät für Elektrotechnik und Informationstechnik der
Otto-von-Guericke Universität Magdeburg am 03. September 2008

Gutachter:

Prof. Dr.-Ing. Marco Leone
Prof. Dr.-Ing. Günter Wollenberg
Prof. Dr.-Ing. Hermann Singer

Res Electricae Magdeburgenses

Magdeburger Forum zur Elektrotechnik, Jg. 6, Band 28, 2008

IMPRESSUM

Herausgeber:

Prof. Dr. rer. nat. habil. Jürgen Nitsch

Institut für Grundlagen der Elektrotechnik und Elektromagnetische Verträglichkeit

Prof. Dr.-Ing. habil. Zbigniew Antoni Styczynski

Institut für Elektrische Energiesysteme

beide: Otto-von-Guericke-Universität Magdeburg, Postfach 4120, 39016 Magdeburg

V. i. S. d. P.:

Dr.-Ing. habil. Sergey V. Kochetov

Otto-von-Guericke-Universität Magdeburg, Postfach 4120, 39016 Magdeburg

1. Auflage, Magdeburg, Otto-von-Guericke-Universität, 2008

Redaktionsschluss: September 2008

ISSN: 1612-2526

ISBN: 978-3-940961-27-3

© Copyright 2008 Sergey V. Kochetov

Bezug über die Herausgeber

"A physicist is blind without mathematics..."

Mikhail V. Lomonosov (1711-1765)

Contents

List of symbols	viii
Zusammenfassung	1
Introduction and summary	4
1 Fundamentals of classical electrodynamics	9
1.1 Basic equations and definitions in electromagnetics	9
1.1.1 Maxwell's equations	9
1.1.2 Wave equations	11
1.1.3 Scalar electric and vector magnetic potentials	11
1.2 Some important theorems in electromagnetics	12
1.2.1 Uniqueness theorem	13
1.2.2 Sommerfeld radiation condition	13
1.2.3 Reciprocity theorem	14
1.2.4 Image theory for a perfectly conducting infinite plane	15
1.3 Green's function method	16
1.4 Integral-equation techniques	20
1.4.1 Electric-field integral equation	20
1.4.2 Mixed-potential integral equation (MPIE)	23
1.5 Transmission-line theory	25
1.5.1 Fundamental definitions	26
1.5.2 Green's functions for the transmission-line equations	27
1.5.3 Reciprocity of the transmission-line Green's functions	31
1.6 Causality	32
2 Computational methods for circuit analysis	35
2.1 Modified nodal analysis (MNA)	35
2.1.1 General formulation	35

2.1.2	MNA formulation by inspection	37
2.2	Time-domain simulation of linear circuits	39
2.2.1	Numerical integration of differential equations	39
2.2.2	Associated discrete circuits for the time-domain analysis	42
3	Computational methods in electrodynamics	44
3.1	Weighted residual method	45
3.2	Differential methods	49
3.3	Method of moments	52
3.4	Numerical modeling of transmission lines	53
3.5	PEEC method: motivation and state of development	55
3.6	Black-box modeling of passive interconnections	59
4	Partial Element Equivalent Circuit (PEEC) method	62
4.1	Generalized formulation of the PEEC method (DGF-PEEC)	62
4.1.1	Discretization and basis functions	63
4.1.2	Derivation of the generalized partial elements	65
4.1.3	Equivalent circuit for the DGF-PEEC method	68
4.2	PEEC models for free- and half-space problems	69
4.2.1	Derivation of the standard PEEC model in the frequency domain	69
4.2.2	Standard half-space PEEC model in the frequency domain	72
4.2.3	PEEC method in the time domain	74
4.2.4	Quasi-static formulation of the standard PEEC method	75
4.3	Inclusion of PEEC models in circuit simulators	77
4.3.1	PEEC models in Berkeley SPICE3f4	78
4.3.2	Standard full-wave PEEC model in the NEAN code	81
4.4	Skin effect in PEEC models	82
4.4.1	Calculation of the mean surface impedance	84
4.4.2	Time-domain modeling of skin effect using the stair-case circuits	86
4.4.3	Time-domain modeling of skin effect using the FSCM	89
4.5	Stability and accuracy	94
4.5.1	Static accuracy of the PEEC method	95
4.5.2	PEEC models with multipoint difference quotients	97
4.5.3	Stability of the PEEC method	102
4.5.4	Stability improvement for the full-wave PEEC method	111
4.5.5	Stable and effective PEEC models based on the FSCM	114

5	PEEC modeling of PCB boards	127
5.1	Half-space full-wave PEEC models for PCB boards	127
5.2	MPIE for layered media	129
5.2.1	Dyadic Green's functions for the electric and magnetic fields	131
5.2.2	Derivation of the MPIE for layered media	136
5.2.3	MPIE formulation for PCB boards with power planes	142
5.3	Green's functions for the stripline region	145
5.3.1	Green's functions in the spectrum domain	145
5.3.2	Green's functions in the spatial domain	147
5.3.3	Behavior and physical interpretation	152
5.4	PEEC based on the MPIE for layered media (DGFLM-PEEC method) . . .	159
5.4.1	Motivation	159
5.4.2	General formulation of the DGFLM-PEEC method	161
5.4.3	Frequency-domain DGFLM-PEEC model for the stripline region . . .	163
5.4.4	Quasi-static time-domain DGFLM-PEEC model	172
5.4.5	Quasi-dynamic time-domain DGFLM-PEEC model	174
5.5	Description of crosstalk using the DGFLM-PEEC method	183
5.5.1	Crosstalk between vias	184
5.5.2	Calculation of the wave impedance for striplines	185
5.5.3	Simulation example: crosstalk in a four-layer PCB board	187
A	Mathematical fundamentals	190
A.1	Vector identities	190
A.2	Dyadic identities	190
A.3	Integral theorems	191
A.4	Integral transformations	192
B	Calculation of the internal longitudinal impedance of wires	194

List of symbols

General conventions

Notation	Explanation
a	scalar value
$\underline{a}, \underline{a}^*$	complex, complex conjugate scalars
\mathbf{a}	complex or real vector
a_z	projection of the vector \mathbf{a} on the axis z
$\ \mathbf{a}\ $	Euclidean norm of the vector \mathbf{a}
$\hat{\mathbf{a}} = \mathbf{a} / \ \mathbf{a}\ $	normalized vector
$\{\hat{\mathbf{x}}, \hat{\mathbf{y}}, \hat{\mathbf{z}}\}$	Cartesian unit vectors
$\overline{\mathbf{A}}$	dyadic
\mathbf{xz}	dyad
\mathbb{A}	matrix
\mathbb{A}^T	transposed matrix
\mathbb{A}^{-1}	inverse matrix
\mathbb{I}	identity matrix
\mathbb{A}_{ij}	matrix element
$\mathbb{A}_{i.}, \mathbb{A}_{.j}$	row and column of a matrix
$u(t)$	instantaneous value
\hat{U}	amplitude of $u(t)$
$\Re\{\underline{Z}\}$	real part
$\Im\{\underline{Z}\}$	imaginary part
$\mathfrak{F}\{\}, \mathfrak{F}^{-1}\{\}$	direct and inverse Fourier transformations
$\mathfrak{F}_s\{\}, \mathfrak{F}_s^{-1}\{\}$	direct and inverse spatial Fourier transformations
$\tilde{a} = \mathfrak{F}_s\{a\}$	spectrum-domain functions
$\mathfrak{g}(z, z', \mathbf{k}_\rho) = \mathfrak{F}_s\{g(\mathbf{r}, \mathbf{r}')\}$	spectrum-domain Green's functions
$\mathfrak{D}\{\}$	Duhamel integral
$\mathfrak{L}\{\}$	linear operator

Symbols

A	magnetic vector potential
B	magnetic flux density
c	light velocity in vacuum
C	capacitance
\mathbb{C}	the set of complex numbers
D	electric flux density
dl	length element
$d\mathbf{l} = \hat{\mathbf{e}}_l dl$	vector length element
dS	surface element
$d\mathbf{S} = \hat{\mathbf{n}}_S dS$	vector surface element
dV	volume element
E	electric field strength
\mathbf{E}^s	scattered electric field
\mathbf{E}^i	incident electric field
$\hat{\mathbf{e}}_l$	direction vector
f	frequency
f_m	maximum frequency of interest
f_c	cutoff frequency
g	ohmic conductance
$g(\mathbf{r}, \mathbf{r})$	free-space scalar Green's function
$\overline{\overline{\mathbf{G}}}_J^E(\mathbf{r}, \mathbf{r}), \overline{\overline{\mathfrak{G}}}_J^E(z, z')$	spatial- and spectrum-domain electric-field dyadic Green's function for electric sources
$\overline{\overline{\mathbf{G}}}_M^E(\mathbf{r}, \mathbf{r}), \overline{\overline{\mathfrak{G}}}_M^E(z, z')$	spatial- and spectrum-domain electric-field dyadic Green's function for magnetic sources
$\overline{\overline{\mathbf{G}}}_J^H(\mathbf{r}, \mathbf{r}), \overline{\overline{\mathfrak{G}}}_J^H(z, z')$	spatial- and spectrum-domain magnetic-field dyadic Green's function for electric sources
$\overline{\overline{\mathbf{G}}}_M^H(\mathbf{r}, \mathbf{r}), \overline{\overline{\mathfrak{G}}}_M^H(z, z')$	spatial- and spectrum-domain magnetic-field dyadic Green's function for magnetic sources
$\overline{\overline{\mathbf{G}}}^A(\mathbf{r}, \mathbf{r}), \overline{\overline{\mathfrak{G}}}^A(z, z')$	spatial- and spectrum-domain dyadic Green's function for the vector magnetic potential
H	magnetic field strength
J	current density
\mathbf{J}_s	surface current density
I	current or current source
\mathbf{k}, k	wave vector and wave number
k_z	longitudinal (with respect to z) wave number
\mathbf{k}_ρ, k_ρ	transversal (with respect to z) wave vector and number
$K^\rho(\mathbf{r}, \mathbf{r}), \mathfrak{K}^\rho(z, z')$	spatial- and spectrum-domain Green's function for the electric scalar potential

l	length
L	inductance or partial inductance
M	mutual inductance
$\hat{\mathbf{n}}$	normal to a surface
p	potential coefficient
q	electric charge
\mathbb{R}	the set of real numbers
R	ohmic resistance
\mathbf{r}	observation point
\mathbf{r}'	source point
\mathbb{R}	the set of real numbers
S	surface
U	voltage
V	volume or voltage source
v_c	propagation velocity
x	reactive resistance
Y	complex admittance
y	reactive conductance
Z	complex impedance
Δl	cell length or grid step
δ	skin depth
$\epsilon = \epsilon_0 \epsilon_r$	permittivity
ϵ_0	electric constant
ϵ_r	relative permittivity
$\underline{\epsilon}$	complex permittivity
Φ	magnetic flux
φ	electric scalar potential
$\mu = \mu_0 \mu_r$	permeability
μ_0	magnetic constant
μ_r	relative permeability
∇^2	Laplace operator
λ_m	the wave number related to the maximum frequency of interest
ρ_v	volume charge density
ρ_s	surface charge density
σ	conductivity
σ_s	conductivity of a dielectric
τ	delay time
ω	radian frequency
ω_m	maximum frequency of interest
ω_c	cutoff frequency
Ψ	electric flux

Zusammenfassung

Die vorliegende Arbeit widmet sich den theoretischen Grundlagen und numerischen Verfahren zur Analyse passiver Verbindungsstrukturen auf der Basis der elektromagnetischen Feld- und Netzwerktheorie.

Die Simulation elektromagnetischer Phänomene gewinnt eine immer stärkere Bedeutung sowohl im Entwicklungsprozess elektronischer Komponenten und Systeme als auch bei der EMV-Analyse. Ständig steigende Operationsfrequenzen erfordern die Einbeziehung der passiven Verbindungsstrukturen in die Analyse sowohl im Frequenz- als auch im Zeitbereich. Dabei wächst insbesondere die Bedeutung von Zeitbereichsmethoden bei der Behandlung elektrodynamischer Probleme infolge zunehmender Schaltfrequenzen und immer steilerer Anstiegsflanken. Frequenzbereichsmethoden in Kombination mit der Fourierrücktransformation erfordern bei extrem breiten Frequenzspektren einen hohen Rechenaufwand, um Zeitbereichslösungen mit hinreichender Genauigkeit zu erhalten. Im Falle von Nichtlinearitäten sind Zeitbereichsmethoden sogar die einzige Möglichkeit.

Aus diesem Grunde wird in der vorliegenden Arbeit ein besonderer Schwerpunkt auf die Zeitbereichsmodellierung der Verbindungsstrukturen einschließlich der Schaltungsumgebung sowie die Behandlung mittels Netzwerksimulatoren gelegt.

Da eine adäquate Behandlung mit modernen Verfahren ohne die grundlegenden Kenntnisse der elektromagnetischen Feldtheorie nicht möglich ist, werden im **Kapitel 1** die Grundlagen der klassischen Elektrodynamik in komprimierter Form dargelegt. Dies betrifft die wichtigsten Differenzial- und Integralgleichungen sowie die Theoreme und Grundkonzepte der klassischen Elektrodynamik. Die im Kapitel 1 beschriebenen theoretischen Grundlagen dienen als Basis für die didaktisch konsistente Darstellung der in den nächsten Kapiteln dargelegten und entwickelten Mittel und Methoden.

Da die vorliegende Arbeit die simultane Modellierung von Verbindungsstrukturen in ihrer auch nichtlinearen Schaltungsumgebung untersucht und diese Modelle im Rahmen eines Netzwerksimulators programmiert werden, gibt **Kapitel 2** eine Übersicht über computerorientierte Methoden der Schaltungssimulation. Die wesentlichen Methoden für die Frequenz- und Zeitbereichsmodellierung beliebiger Schaltungen mittels SPICE-ähnlicher Programme sind mit Bezug auf nachfolgend verwendete, moderne Ansätze dargestellt und diskutiert.

Kapitel 3 ist den numerischen Methoden der elektromagnetischen Feldberechnung gewidmet, wobei im Besonderen ein Vergleich der verbreiteten numerischen Methoden bezüglich der Simulation von passiven Verbindungsstrukturen erfolgt. Das Kapitel beginnt mit der Methode des gewichteten Residuums, da diese als die Basis für viele numerische Metho-

den dient. Das Kapitel bietet eine Übersicht über die auf der Leitungstheorie beruhenden Methoden, über differenzielle Methoden, Integralgleichungsverfahren und Black-Box-Verfahren mit Bezug zur Modellierung von Verbindungsstrukturen. Aus der durchgeführten vergleichenden Analyse werden die Motivation und das Anwendungsgebiet der Methode der partiellen Elemente (PEEC-Methode) begründet. Wie jede der analysierten numerischen Methoden bezüglich der Anwendung auf unterschiedliche Aufgabentypen Vor- und Nachteile besitzt, gilt dies auch für die Methode der partiellen Elemente. Ein wesentlicher Vorteil ist, dass die Methode der partiellen Elemente die Modellierung von Verbindungsstrukturen im Zeitbereich auch bei Vorhandensein nichtlinearer Schaltelemente ermöglicht. Sie beruht auf der elektrischen Mixed-Potential-Feldintegralgleichung (MPIE) und der Anwendung des Galerkin-Verfahrens. Das Full-Wave-PEEC-Modell kann als ein lineares RLC-Netzwerk mit gesteuerten Quellen, deren Steuergrößen (Ströme, Spannungen) zeitlich retardiert sind, dargestellt werden. Dies ermöglicht in natürlicher Weise die Berücksichtigung der Schaltungsumgebung sowie die Behandlung mit Netzwerksolvern im Zeit- und Frequenzbereich. Das Kapitel endet mit der Einführung eines neuen Black-Box-Modellierungsverfahrens. Das Verfahren, genannt "Full Spectrum Convolution Macromodeling" (FSCM), wird zur Entwicklung effizienter Zeitbereichsmodelle von passiven Verbindungsstrukturen in nachfolgenden Kapiteln der Arbeit angewendet.

Im **Kapitel 4** wird zunächst eine verallgemeinerte Formulierung der PEEC-Methode, die vom Autor der Arbeit vorgeschlagen ist, eingeführt. Sie beruht auf der MPIE-Gleichung mit der dyadischen Greenschen Funktion für das magnetische Vektorpotenzial und der skalaren Greenschen Funktion für das elektrische Skalarpotenzial. Diese allgemeine Formulierung kann für alle Probleme, die durch die MPIE-Gleichung mit dyadischen Greenschen Funktionen beschrieben werden können, angewendet werden. Im Abschnitt 4.2 werden dann die üblichen Full-Wave- und quasi-statischen Modifikationen der PEEC-Methode aus der verallgemeinerten Formulierung für den Zeit- und den Frequenzbereich abgeleitet. Danach werden Fragen der Implementierung der PEEC-Modelle in Schaltungssimulatoren betrachtet. Schwerpunkte dabei sind die Nutzung von Berkeley-SPIICE sowie vom Autor entwickelte Simulationstools. Das Kapitel 4 schließt ab mit Untersuchungen zur Einbeziehung des Skin-effektes in die PEEC-Modellierung sowie ausführlichen Untersuchungen zur Stabilität und Genauigkeit der PEEC-Modelle.

Das **Kapitel 5** ist der Modellierung von Mehrlagenleiterplatten mittels der Methode der partiellen Elemente gewidmet. Zunächst wird der einfachste Ansatz, das Ersetzen des inhomogenen, geschichteten Mediums der Mehrlagenstruktur durch ein äquivalentes, homogenes Medium mit effektiven Parametern, diskutiert und als unbefriedigend bewertet. Der Autor entwickelt deshalb eine neue, originäre Formulierung der PEEC-Methode (genannt DGFLM-PEEC), die auf dem verallgemeinerten Konzept mit dyadischen Greenschen Funktionen basiert. Im Abschnitt 5.2 werden die dyadischen Greenschen Funktionen für allgemeine, planar geschichtete Medien hergeleitet. Im Abschnitt 5.3 werden die allgemeinen Formulierungen der dyadischen Greenschen Funktionen auf eine spezielle, häufig benutzte Leiterplattegeometrie, die so genannte Stripline-Anordnung, angewendet, untersucht und validiert. Danach werden im Abschnitt 5.4 die DGFLM-PEEC-Modelle für Zeit- und Frequenzbereich entwickelt. Die Anwendung dieser Modelle hat wesentliche Vorteile im Ver-

gleich zu anderen Methoden, die zur Analyse von Leiterplatten eingesetzt werden. Im Vergleich zu Leitungsmodellen können damit nicht nur homogene dünne Leiterbahnen, sondern beliebige Leiterzüge mit 2D-Wellenausbreitung und Durchkontaktierungen behandelt werden. Zusätzlich berücksichtigt das PEEC-Modell die Abstrahlung, die in einem konventionellen Leitungsmodell nicht enthalten ist. Im Vergleich zur Momentenmethode lassen sich mit dem DGFLM-PEEC-Modell Zeitbereichsanalysen in einer nichtlinearen Schaltungs-umgebung ohne weiteres durchführen. Im Zeitbereich wandelt das vorliegende DGFLM-PEEC-Modell eine beliebige Anordnung der Leiterbahnen und Durchkontaktierungen in eine SPICE-kompatible, diskrete Ersatzschaltung um. Diese Schaltung besteht aus Zeitbereichsmakromodellen für die Reaktionsintegrale im Frequenzbereich. Dieser Ansatz garantiert die Stabilität der Lösungen und ist außerdem numerisch effizient. Schließlich werden im Abschnitt 5.5 praktisch relevante Anwendungen des DGFLM-PEEC-Modells für die Beschreibung des Übersprechens bei Leiterplatten behandelt.

Introduction and summary

Throughout the first period of electrical-engineering history, *passive interconnections*, i.e., conductors serving as the connection of electronic devices or system components, were typically not considered in the system modeling, except for some special cases and "electrically long" structures, which were successfully described via the transmission-line theory. This changed dramatically after the wide-spread introduction of digital, radio-frequency, and microwave technologies, which required transmission via the passive interconnection structures of high-frequency (HF) signals. The parasitic effects introduced by passive interconnections at high frequencies have motivated modern digital-system designers to consider such interconnections more precisely.

The most important primary effect related to interconnections is the propagation time constrained by the propagation velocity, which may not exceed the light velocity in the vacuum and depends on the media, in which the interconnections are located. Both narrow-band oscillations and wide-band waveforms may be featured by the principal frequency range limited by the maximum frequency of interest. If the propagation time of the interconnection structure is at least 1/10 of the period related to the maximum frequency of interest, the time delay due to the interconnection changes the waveform significantly and has to be considered.

The frequency dependent attenuation of signals is the second significant effect. The waves propagating via interconnections can be attenuated due to several of the phenomena related to energy losses:

- conductor losses classified into DC losses and AC losses, which are caused by skin and proximity effects,
- in case of PCB boards, the frequency dependent dielectric losses due to imperfect dielectrics,
- losses due to radiation.

In general, frequency dependent attenuation leads to a decay of the waveform edge rates, i.e., makes waveforms strongly rounded as compared to intended pulses.

The two aforementioned principal effects of interconnections may distort the intended waveforms of signals and be an obstacle for the functionality of the electronic equipment. For PCB boards, these kind of problems are called *signal integrity* problems, and their consideration is a mandatory step in high-speed digital-system design.

Another problem characteristic of passive interconnections at high frequencies is *crosstalk*, which is the undesired coupling of energy between the parts of the product. In particular, for PCB boards, crosstalk appears between traces, vias, connectors, packages, cables, and connecting wires. It causes the signal-integrity problems as well as the violation of electromagnetic compatibility (EMC) regulatory requirements.

The high density of electronic equipment in the modern world has caused a complex electromagnetic environment produced by a large number of hazards. Since the electromagnetic fields scattered by different sources may influence the functionality of other devices, all products manufactured in developed countries must satisfy the EMC regulatory requirements, which guarantee the acceptable level of intra- and intersystem interferences. The EMC analysis implies an investigation of the product with respect to satisfaction of the EMC requirements. The fast growing of operational frequencies and pulse rates of the digital devices has progressively increased the importance of the EMC analysis.

The passive interconnection structures play one of dominant roles in the electromagnetic compatibility of electronic products, since they are one of the principle pathways for intra- and intersystem interferences. The electromagnetic devices may be stressed by inductive, capacitive, and radiation couplings between passive interconnections. Sometimes the passive interconnections may receive radiated emissions from other devices, lead these disturbances into shielded cases where they can be recoupled on internal interconnections and change the functionality of the product. In general, the EMC analysis of complex electronic systems needs precise models for passive interconnections including most of the high frequency phenomena, since interconnections can serve as unintended antenna-like structures.

Nowadays, the preferable requirements for an electromagnetic modeling tool for passive interconnection structures include the following main items:

- consideration of an arbitrary three-dimensional geometry of interconnections,
- full-wave modeling, in order to take into account the electromagnetic radiation,
- accounting for the most important high-frequency effects, e.g., skin and proximity effects, dielectric losses,
- the simultaneous modeling of passive interconnections with non-linear digital devices on the circuit-simulation level.

The last item above requires some further explanation. The simulation of an electronic product may be subdivided into the system, circuit, and electromagnetic modeling levels. The first level is the principle modeling of the product functionality. The circuit modeling level considers the circuit solutions for blocks on the system level. The electromagnetic-modeling level studies the non-ideal unintended phenomena, which disturb the product functionality. Of course, these phenomena are secondary with respect to the intended behavior of the product and should be considered against its background, i.e., the simultaneous modeling of passive interconnections and non-linear lumped circuits is needed. Since the simulation of non-linear circuits is possible only in the time domain, the importance of time-domain methods for both the development of electrical equipment and the EMC analysis is increasing.

This monograph is devoted to the numerical modeling of passive interconnection structures in the time-domain. In general, this may be achieved via three classes of methods. The first is based on transmission-line theory. These methods have very low computational costs as their most important advantage. However, the transmission-line models assume propagation of only TEM-waves and, thus, cannot take into account high frequency phenomena, although the generalization of the transmission-line theory may improve this drawback.

The second class of methods is based on the numerical solution of partial differential equations (PDE) of the electromagnetic field. A large number of numerical methods, the so-called *differential methods*, may be mentioned in this relation. These methods differ in their derivation and in details but have similarities. Namely, they require the discretization of the three-dimensional solution region into a large number of three-dimensional grid cells. The algebraization of PDEs in grid cells leads to a huge system of equations with a sparse system matrix. The differential methods take into account all significant physical effects but can have high computational costs, especially for open problems. They are especially appropriate for the simulation of interconnections in inhomogeneous media, e.g., PCBs with complex inhomogeneous or anisotropic substrates.

The third class of methods is based on approximate solutions of integral equations (IE) derived from Maxwell's equations. Such models provide full-wave numerical solutions for arbitrary interconnection systems. The integral-equation techniques require only the discretization of the conducting structures and not the total solution region. This is their most important advantage with respect to differential methods, since the number of unknowns in the resulted algebraic-equation formulation decreases strongly, although the system matrix is fully-filled.

Chapter 1 shortly summarizes the fundamentals of electromagnetic theory, which are necessary for understanding of the following chapters. The dynamic behavior of passive interconnections is governed by equations of classical electrodynamics, which are the basis for the derivation of the numerical models considered in Chapters 3 - 5. In addition, Chapter 1 introduces some important concepts and techniques of electrodynamics: uniqueness and causality of solutions, reciprocity theorem, image theory, Sommerfeld radiation boundary condition, the Green's function method, electric-field integral equations, etc. These well known theoretical fundamentals are systematically explained and summarized in order to make the monograph didactically understandable and to show the consistency between the numerical and analytical models in electrodynamics.

Chapter 2 gives a short survey of computational methods for the circuit analysis. As is above mentioned, the simultaneous modeling of passive interconnections and non-linear lumped circuits is of great importance. Since this monograph provides numerical methods, which are capable of full-wave modeling of passive interconnection structures using circuit-simulator codes, some fundamental techniques specific for the computer-aided circuit analysis have to be introduced. Chapter 2 serves as the didactic basis for understanding the advanced numerical methods derived in Chapters 4 and 5. This chapter is an alternative to referencing on a large number of literature sources.

Chapter 3 introduces a comparative study of the most wide-spread numerical techniques applied in practice for the simulation of passive interconnections. The detailed survey of transmission-line theory based methods, integral-equation techniques, differential methods, and reduction-order approaches is presented. Since a part of these methods is based on the weighted residual principle, it is introduced at the beginning of the chapter as a reference for several following derivations. Based on the presented comparative study, the motivation for the usage of the *partial element equivalent circuit* (PEEC) method is deduced. Of course, no numerical method may be accepted as the best universal tool for all kinds of electromagnetic problems, as well, the PEEC method has advantages and disadvantages as compared to other approaches. Its main merit is an equivalent circuit representation, which allows the full-wave PEEC model to be directly included in a circuit-simulation code. Thus, the simultaneous modeling of passive interconnection structures with the lumped active devices is achieved, which is very suitable for the EMC analysis as well as the design of electronic devices. This makes reasonable the development of the advanced PEEC models given in the two last chapters. In conclusion of the chapter, a novel approach for the time-domain macromodeling is presented. Systematically classified conjointly with other reduction-order approaches, this method, called *full-spectrum convolution macromodeling*, has a special importance in this monograph, since the four advanced PEEC models given in the next chapters apply it referencing to § 3.6.

Chapter 4 starts from the generalized formulation of the PEEC method (DGF-PEEC method) introduced by the author of this work. The DGF-PEEC method is based on the mixed-potential integral equation (MPIE) with a dyadic Green's function for the vector magnetic and a scalar Green's function for the scalar electric potentials. It is applicable for arbitrary interconnection structures, which may be described using the MPIE. § 4.2 shows the consistency of the DGF-PEEC formulation with the standard full-wave and quasi-static PEEC models that are derived from the generalized one. § 4.3 explains the inclusion of PEEC circuits in SPICE-like circuit-simulator codes. Several original approaches for the description of skin effect in the PEEC circuits are presented in § 4.4. The fundamental investigation of the stability and the accuracy of the PEEC method completes Chapter 4.

Chapter 5 considers the possibilities for modeling the PCB boards using the PEEC method. The first and simplest approach is studied in § 5.1. It applies the standard half-space PEEC model derived in § 4.2 using an effective permittivity value. Since this approach is quite inaccurate, the novel generalized concept of the DGF-PEEC method (see § 4.1) is applied. The DGF-PEEC formulation for layered media (called DGFLM-PEEC) is based on the MPIE with the dyadic Green's functions for the general plane-stratified medium, which are derived in § 5.2. The Green's functions for a particular plane-stratified medium (stripline region) are derived and investigated in § 5.3. The time- and frequency-domain DGFLM-PEEC formulations are developed and validated in § 5.4. The last section is devoted to the description of the crosstalk mechanism using the quasi-static DGFLM-PEEC method. This section provides a novel and compact description for crosstalk between vias and shows a validation of the computational model using the measurements with a network analyzer.

In short, Chapter 5 provides a novel family of full-wave numerical methods derived from the general DGF-PEEC model, whose equivalent circuit-representation may be computed with a common-purpose circuit-simulator code.

Chapter 1

Fundamentals of classical electrodynamics

1.1 Basic equations and definitions in electromagnetics

1.1.1 Maxwell's equations

The complete formulation of Maxwell's equations were established by James Clerk Maxwell in 1873 and serve as the basis for classical electrodynamics. These four partial differential equations relate four field vectors and four field sources at the space point \mathbf{r} and at the time t :

$$\begin{aligned}\nabla \times \mathbf{E}(\mathbf{r}, t) &= -\frac{\partial}{\partial t} \mathbf{B}(\mathbf{r}, t) - \mathbf{M}(\mathbf{r}, t), \\ \nabla \times \mathbf{H}(\mathbf{r}, t) &= \frac{\partial}{\partial t} \mathbf{D}(\mathbf{r}, t) + \mathbf{J}(\mathbf{r}, t), \\ \nabla \cdot \mathbf{B}(\mathbf{r}, t) &= \rho_v^m(\mathbf{r}, t), \\ \nabla \cdot \mathbf{D}(\mathbf{r}, t) &= \rho_v(\mathbf{r}, t),\end{aligned}\tag{1.1}$$

where $\mathbf{E}(\mathbf{r}, t)$ is the electric field intensity, $\mathbf{H}(\mathbf{r}, t)$ is the magnetic field intensity, $\mathbf{D}(\mathbf{r}, t)$ is the electric flux density, $\mathbf{B}(\mathbf{r}, t)$ is the magnetic flux density. $\mathbf{J}(\mathbf{r}, t)$ and $\mathbf{M}(\mathbf{r}, t)$ are the electric and magnetic current densities, respectively. $\rho_v(\mathbf{r}, t)$ and $\rho_v^m(\mathbf{r}, t)$ are the volume-distribution density of electric and magnetic charges. Since the magnetic currents and charges do not exist in reality, we set $\mathbf{M}(\mathbf{r}, t) = 0$ and $\rho_v^m(\mathbf{r}, t) = 0$. The inclusion of these additional formal sources in (1.1) makes the equation system symmetric and leads to derivation of some important electromagnetic principles, which are applied in this monograph.

Maxwell's equations are significantly simplified as compared to (1.1) in the frequency domain. They are derived by the application of the defined in (A.20) direct Fourier trans-

formation to (1.1):

$$\begin{aligned}\nabla \times \mathbf{E}(\mathbf{r}) &= -j\omega \mathbf{B}(\mathbf{r}) - \mathbf{M}(\mathbf{r}), \\ \nabla \times \mathbf{H}(\mathbf{r}) &= j\omega \mathbf{D}(\mathbf{r}) + \mathbf{J}(\mathbf{r}), \\ \nabla \cdot \mathbf{B}(\mathbf{r}) &= \rho_v^m(\mathbf{r}), \\ \nabla \cdot \mathbf{D}(\mathbf{r}) &= \rho_v(\mathbf{r}),\end{aligned}\tag{1.2}$$

where $\mathbf{E}(\mathbf{r})$, $\mathbf{H}(\mathbf{r})$, $\mathbf{B}(\mathbf{r})$, $\mathbf{D}(\mathbf{r})$, $\mathbf{M}(\mathbf{r})$, $\mathbf{J}(\mathbf{r})$, $\rho_v^m(\mathbf{r})$, and $\rho_v(\mathbf{r})$ are complex vector or scalar functions called *phasors*, which are the frequency-domain counterparts for the corresponding functions calculated as follows:

$$\mathbf{A}(\mathbf{r}) = \mathfrak{F}\{\mathbf{A}(\mathbf{r}, t)\},\tag{1.3}$$

where $\mathfrak{F}\{\}$ denotes the Fourier transformation, $\mathbf{A}(\mathbf{r}, t)$ is a time-domain function, and $\mathbf{A}(\mathbf{r})$ is its frequency-domain counterpart.

The continuity equations for electric and magnetic sources are developed through the application of the divergence operator to the first and second equations in (1.2) in view of the vector identity (A.5):

$$\nabla \cdot \mathbf{J}(\mathbf{r}) + j\omega \rho_v(\mathbf{r}) = 0, \quad \nabla \cdot \mathbf{M}(\mathbf{r}) + j\omega \rho_v^m(\mathbf{r}) = 0.\tag{1.4}$$

The material equations relate the electric and magnetic flux densities to the electric and magnetic field intensities, respectively:

$$\mathbf{D}(\mathbf{r}) = \bar{\epsilon} \cdot \mathbf{E}(\mathbf{r}), \quad \mathbf{B}(\mathbf{r}) = \bar{\mu} \cdot \mathbf{H}(\mathbf{r}),\tag{1.5}$$

where $\bar{\epsilon} = \bar{\epsilon}(\mathbf{r}, j\omega)$ is the *permittivity*, and $\bar{\mu} = \bar{\mu}(\mathbf{r}, j\omega)$ is the *permeability*. In general, they are dyadic (see [146]) functions of space coordinates and frequency that corresponds to a linear anisotropic non-uniform media. However, (1.5) may be simplified to the usually implied formulation in the case of an isotropic linear media:

$$\mathbf{D}(\mathbf{r}) = \epsilon \mathbf{E}(\mathbf{r}), \quad \epsilon = \epsilon_r \epsilon_0,\tag{1.6}$$

and

$$\mathbf{B}(\mathbf{r}) = \mu \mathbf{H}(\mathbf{r}), \quad \mu = \mu_r \mu_0,\tag{1.7}$$

where ϵ_r and μ_r are the relative permittivity and permeability, $\epsilon_0 = 8.854 \cdot 10^{-12}$ F/m is the *dielectric constant*, and $\mu_0 = 4\pi \cdot 10^{-7}$ H/m is the *magnetic constant*.

The substitution of the material equations (1.5) into Maxwell's equations (1.2) results in two independent curl equations relating the vectors $\mathbf{E}(\mathbf{r})$ and $\mathbf{H}(\mathbf{r})$:

$$\begin{aligned}\nabla \times \mathbf{E}(\mathbf{r}) &= -j\omega \bar{\mu} \cdot \mathbf{H}(\mathbf{r}) - \mathbf{M}(\mathbf{r}), \\ \nabla \times \mathbf{H}(\mathbf{r}) &= j\omega \bar{\epsilon} \cdot \mathbf{E}(\mathbf{r}) + \mathbf{J}(\mathbf{r}),\end{aligned}\tag{1.8}$$

for anisotropic medium or

$$\begin{aligned}\nabla \times \mathbf{E}(\mathbf{r}) &= -j\omega \mu \mathbf{H}(\mathbf{r}) - \mathbf{M}(\mathbf{r}), \\ \nabla \times \mathbf{H}(\mathbf{r}) &= j\omega \epsilon \mathbf{E}(\mathbf{r}) + \mathbf{J}(\mathbf{r}),\end{aligned}\tag{1.9}$$

for isotropic one.

1.1.2 Wave equations

The system of the first order partial differential equations (1.8) can be decoupled into two second order partial differential equations called *vector wave equations*:

$$\begin{aligned}\nabla \times \bar{\bar{\mu}}^{-1} \cdot \nabla \times \mathbf{E}(\mathbf{r}) - \omega^2 \bar{\bar{\epsilon}} \cdot \mathbf{E}(\mathbf{r}) &= -j\omega \mathbf{J}(\mathbf{r}) - \nabla \times \bar{\bar{\mu}}^{-1} \cdot \mathbf{M}(\mathbf{r}), \\ \nabla \times \bar{\bar{\epsilon}}^{-1} \cdot \nabla \times \mathbf{H}(\mathbf{r}) - \omega^2 \bar{\bar{\mu}} \cdot \mathbf{H}(\mathbf{r}) &= -j\omega \mathbf{M}(\mathbf{r}) + \nabla \times \bar{\bar{\epsilon}}^{-1} \cdot \mathbf{J}(\mathbf{r}).\end{aligned}\quad (1.10)$$

The solution of either wave equation in (1.10) provides the complete description of the electromagnetic field in the solution region because other field vectors may be calculated using the Maxwell's equations (1.8) and the material equations (1.5).

The formulation (1.10) for the vector wave equations is simplified for an isotropic and homogeneous medium as

$$\begin{aligned}\nabla \times \nabla \times \mathbf{E}(\mathbf{r}) - k^2 \mathbf{E}(\mathbf{r}) &= -j\omega\mu \mathbf{J}(\mathbf{r}) - \nabla \times \mathbf{M}(\mathbf{r}), \\ \nabla \times \nabla \times \mathbf{H}(\mathbf{r}) - k^2 \mathbf{H}(\mathbf{r}) &= -j\omega\epsilon \mathbf{M}(\mathbf{r}) + \nabla \times \mathbf{J}(\mathbf{r}),\end{aligned}\quad (1.11)$$

where $k = \omega\sqrt{\mu\epsilon}$ is the *wavenumber*. The *scalar wave equations* also named *Helmholtz equations* are derived from (1.11) in view of the vector identity (A.7) and the dyadic identity (A.9) as

$$\begin{aligned}\nabla^2 \mathbf{E}(\mathbf{r}) + k^2 \mathbf{E}(\mathbf{r}) &= j\omega\mu \left(\bar{\bar{\mathbf{I}}} + \frac{\nabla\nabla}{k^2} \right) \cdot \mathbf{J}(\mathbf{r}) + \nabla \times \mathbf{M}(\mathbf{r}), \\ \nabla^2 \mathbf{H}(\mathbf{r}) + k^2 \mathbf{H}(\mathbf{r}) &= j\omega\epsilon \left(\bar{\bar{\mathbf{I}}} + \frac{\nabla\nabla}{k^2} \right) \cdot \mathbf{M}(\mathbf{r}) - \nabla \times \mathbf{J}(\mathbf{r}),\end{aligned}\quad (1.12)$$

where $\bar{\bar{\mathbf{I}}}$ is the identity dyadic defined in (A.13), and the notation $\nabla\nabla$ means dyad (see [146]). Below the Helmholtz equations for the electric and magnetic fields (1.12) are given for the source-free medium in the homogeneous form:

$$\begin{aligned}\nabla^2 \mathbf{E}(\mathbf{r}) + k^2 \mathbf{E}(\mathbf{r}) &= 0, \\ \nabla^2 \mathbf{H}(\mathbf{r}) + k^2 \mathbf{H}(\mathbf{r}) &= 0.\end{aligned}\quad (1.13)$$

1.1.3 Scalar electric and vector magnetic potentials

The Helmholtz equations in the homogeneous space may be solved using several approaches. One of them is the introduction of auxiliary potential functions, in which the unknown field vectors are expressed. The most wide-spread potentials are the *Hertz potentials* (see, e.g., [44]), the vector potential for electric and magnetic fields (see, e.g., [122]), and the most commonly used in electrical engineering scalar electric $\varphi(\mathbf{r})$ and vector magnetic $\mathbf{A}(\mathbf{r})$ potentials (see, e.g., [34]) leading to the mixed-potential integral equation. Since this monograph deals with the mixed-potential integral equation, these last potentials will be considered below.

The derivation of potentials $\varphi(\mathbf{r})$ and $\mathbf{A}(\mathbf{r})$ is accomplished in absence of magnetic field sources, i.e., we set $\mathbf{M}(\mathbf{r}) = 0$ and $\rho_v^m(\mathbf{r}) = 0$, which does not introduce any assumption, as the magnetic sources do not exist physically. Since $\rho_v^m(\mathbf{r}) = 0$, the magnetic field is solenoidal and may be computed as

$$\mathbf{B}(\mathbf{r}) = \nabla \times \mathbf{A}(\mathbf{r}), \quad (1.14)$$

where $\mathbf{A}(\mathbf{r})$ is an auxiliary vector function called vector magnetic potential. The substitution of (1.14) in the first equation in (1.2) results in the expression for the solenoidal part of the electric field intensity $-j\omega\mathbf{A}(\mathbf{r})$. According to the Helmholtz-decomposition theorem [86], a vector may be uniquely represented as the sum its solenoidal and laminar parts, where the laminar part is the gradient of a scalar function. Thus, the electric field intensity is calculated as

$$\mathbf{E}(\mathbf{r}) = -j\omega\mathbf{A}(\mathbf{r}) - \nabla\varphi(\mathbf{r}), \quad (1.15)$$

where $\varphi(\mathbf{r})$ is an unknown scalar function named scalar electric potential.

The derivation of the differential equations for the introduced potentials requires a unique definition for $\mathbf{A}(\mathbf{r})$. Up to here, only the curl of $\mathbf{A}(\mathbf{r})$ is defined by (1.14), while its divergence is not defined. The form of equations for the potentials depends on this definition, which is called *gauge*. The *Lonrentz gauge* is

$$\nabla \cdot \mathbf{A}(\mathbf{r}) = -j\omega\mu\epsilon \nabla\varphi(\mathbf{r}), \quad (1.16)$$

it leads to the scalar wave equations for the both potentials:

$$\begin{aligned} \nabla^2 \mathbf{A}(\mathbf{r}) + k^2 \mathbf{A}(\mathbf{r}) &= -\mu\mathbf{J}(\mathbf{r}), \\ \nabla^2 \varphi(\mathbf{r}) + k^2 \varphi(\mathbf{r}) &= -\frac{\rho_v}{\epsilon}. \end{aligned} \quad (1.17)$$

The second wide-spread alternative is the *Coulomb gauge*

$$\nabla \cdot \mathbf{A}(\mathbf{r}) = 0, \quad (1.18)$$

which results in

$$\begin{aligned} \nabla^2 \mathbf{A}'(\mathbf{r}) + k^2 \mathbf{A}'(\mathbf{r}) &= -\mu\mathbf{J}(\mathbf{r}) + j\omega\mu\epsilon \nabla\varphi'(\mathbf{r}), \\ \nabla^2 \varphi'(\mathbf{r}) &= -\frac{\rho_v}{\epsilon}, \end{aligned} \quad (1.19)$$

where the second equation in (1.19) is *Poisson equation*, which is simpler than Helmholtz equations (1.17). However, (1.19) are not decoupled, in contrast to (1.17), which can be considered as a disadvantage of the potentials $\mathbf{A}'(\mathbf{r})$ and $\varphi'(\mathbf{r})$. The conventional formulation of the mixed-potential integral equation is derived in § 1.4.2 on the basis of the Lorenz-gauge potentials $\mathbf{A}(\mathbf{r})$ and $\varphi(\mathbf{r})$.

1.2 Some important theorems in electromagnetics

The present section introduces a short summary of some general concepts in the classical electrodynamics, which are applied in the next chapters of this monograph.

1.2.1 Uniqueness theorem

The uniqueness theorem specifies the necessary conditions needed for a unique solution of an electromagnetic problem. We consider a problem described by the wave equations (1.11) in the solution region V constrained with a closed surface $S = \partial V$. Assuming the existence of two different solutions $\mathbf{E}_1(\mathbf{r})$ and $\mathbf{E}_2(\mathbf{r})$ for the same excitation, we may write

$$\begin{aligned}\nabla \times \nabla \times \mathbf{E}_1(\mathbf{r}) - k^2 \mathbf{E}_1(\mathbf{r}) &= -j\omega\mu \mathbf{J}(\mathbf{r}) - \nabla \times \mathbf{M}(\mathbf{r}), \\ \nabla \times \nabla \times \mathbf{E}_2(\mathbf{r}) - k^2 \mathbf{E}_2(\mathbf{r}) &= -j\omega\mu \mathbf{J}(\mathbf{r}) - \nabla \times \mathbf{M}(\mathbf{r}).\end{aligned}\quad (1.20)$$

The subtraction of the first equation (1.20) from the second one yields

$$\nabla \times \nabla \times \mathbf{E}_\delta(\mathbf{r}) - k^2 \mathbf{E}_\delta(\mathbf{r}) = 0 \quad \text{with} \quad \mathbf{E}_\delta(\mathbf{r}) = \mathbf{E}_2(\mathbf{r}) - \mathbf{E}_1(\mathbf{r}). \quad (1.21)$$

The condition $\mathbf{E}_\delta(\mathbf{r}) = 0$, $\mathbf{r} \in V$ guarantees that both solutions are equal and, consequently, unique. In order to prove this condition, we write the volume integral over V of the scalar product $\mathbf{E}_\delta^*(\mathbf{r}) \cdot (1.21)$:

$$\iiint_V \mathbf{E}_\delta^*(\mathbf{r}) \cdot (\nabla \times \nabla \times \mathbf{E}_\delta(\mathbf{r})) \, dV = k^2 \iiint_V \mathbf{E}_\delta^*(\mathbf{r}) \cdot \mathbf{E}_\delta(\mathbf{r}) \, dV. \quad (1.22)$$

The kernel of the right-hand side integral in (1.22) may be more or equal to zero. Since it is zero if and only if $\mathbf{E}_\delta(\mathbf{r}) = 0$. Thus, the right-hand side integral is equal to zero if and only if the solution is unique. Hence, the solution is unique if the left-hand side integral in (1.22) is zero. The left-hand side integral can be rewritten as:

$$\begin{aligned}\iiint_V \mathbf{E}_\delta^*(\mathbf{r}) \cdot (\nabla \times \nabla \times \mathbf{E}_\delta(\mathbf{r})) \, dV &= \\ -j\omega\mu \oint_S \mathbf{E}_\delta^*(\mathbf{r}) \cdot (\hat{\mathbf{n}} \times \mathbf{H}_\delta(\mathbf{r})) \, dS &= j\omega\mu \oint_S \mathbf{H}_\delta(\mathbf{r}) \cdot (\hat{\mathbf{n}} \times \mathbf{E}_\delta^*(\mathbf{r})) \, dS.\end{aligned}\quad (1.23)$$

One may observe (1.23) and formulate the theorem, which is proved above for a homogeneous medium, but may be applied in all cases. The boundary-value problem formulated as

1. a wave equation with
2. non contradicting boundary conditions for the tangential component of either electric or magnetic field intensity

has a unique solution.

1.2.2 Sommerfeld radiation condition

The *Sommerfeld radiation condition* introduced by A. Sommerfeld [142] is used for the correct formulation of open or partially open boundary-value problems. According to the

uniqueness theorem, solutions of these problems are not unique if the boundary condition is not defined. The Sommerfeld radiation condition defines the electric and magnetic field intensities at infinitely large distances from the scatterer equal to zero, which allows one to obtain a unique solution. The apparent voluntarism of this definition has a rigorous physical explanation. The solution in the proximity of the scatterer consists of only outgoing waves, while incoming waves cannot appear there because of the infinite propagation time from the boundary. The outgoing waves get the finite energy from the scatterer. As any medium has a dissipation, the energy of the outgoing wave decreases towards increasing the distance from the scatterer and yields zero at infinite distance. The Sommerfeld radiation condition is applicable for not dissipative media also, since the artificial introduction of a tiny dissipation does not change the solution in the scatterer proximity, but results in zero fields at the infinite distance.

1.2.3 Reciprocity theorem

The Lorentz reciprocity theorem is one of the most useful tools in the electromagnetic theory. In the following, the reciprocity theorem is derived for an anisotropic linear medium with a symmetric dyadic permittivity and permeability ($\bar{\epsilon} \cdot \mathbf{E} = \mathbf{E} \cdot \bar{\epsilon}$ and $\bar{\mu} \cdot \mathbf{H} = \mathbf{H} \cdot \bar{\mu}$). We suppose that the electromagnetic field in the volume V is excited by two various systems of sources, we denote by \mathbf{E}_1 and \mathbf{H}_1 the field intensities caused by the electric and magnetic currents \mathbf{J}_1 and \mathbf{M}_1 , while \mathbf{E}_2 and \mathbf{H}_2 are resulted by \mathbf{J}_2 and \mathbf{M}_2 . Maxwell's equations (1.8) for both excitations are

$$\begin{aligned}\nabla \times \mathbf{E}_1(\mathbf{r}) &= -j\omega\bar{\mu} \cdot \mathbf{H}_1(\mathbf{r}) - \mathbf{M}_1(\mathbf{r}), \\ \nabla \times \mathbf{H}_1(\mathbf{r}) &= j\omega\bar{\epsilon} \cdot \mathbf{E}_1(\mathbf{r}) + \mathbf{J}_1(\mathbf{r})\end{aligned}\quad (1.24)$$

and

$$\begin{aligned}\nabla \times \mathbf{E}_2(\mathbf{r}) &= -j\omega\bar{\mu} \cdot \mathbf{H}_2(\mathbf{r}) - \mathbf{M}_2(\mathbf{r}), \\ \nabla \times \mathbf{H}_2(\mathbf{r}) &= j\omega\bar{\epsilon} \cdot \mathbf{E}_2(\mathbf{r}) + \mathbf{J}_2(\mathbf{r}).\end{aligned}\quad (1.25)$$

The substitution of (1.24) and (1.25) into the expression $\nabla \cdot (\mathbf{E}_1 \times \mathbf{H}_2 - \mathbf{E}_2 \times \mathbf{H}_1)$ leads to the equation

$$\nabla \cdot (\mathbf{E}_1 \times \mathbf{H}_2 - \mathbf{E}_2 \times \mathbf{H}_1) = \mathbf{H}_1 \cdot \mathbf{M}_2 + \mathbf{E}_2 \cdot \mathbf{J}_1 - \mathbf{H}_2 \cdot \mathbf{M}_1 - \mathbf{E}_1 \cdot \mathbf{J}_2, \quad (1.26)$$

which may be integrated over the volume V . The application of the Gauss theorem (A.15) to this integral gives the final formulation for the reciprocity theorem:

$$\begin{aligned}\oint_{S=\partial V} (\mathbf{E}_1 \times \mathbf{H}_2 - \mathbf{E}_2 \times \mathbf{H}_1) \cdot d\mathbf{S} &= \\ &= \iiint_V (\mathbf{H}_1 \cdot \mathbf{M}_2 + \mathbf{E}_2 \cdot \mathbf{J}_1 - \mathbf{H}_2 \cdot \mathbf{M}_1 - \mathbf{E}_1 \cdot \mathbf{J}_2) dV,\end{aligned}\quad (1.27)$$

where $S = \partial V$ is the closed boundary of the volume V , and the direction of $d\mathbf{S}$ is the outward normal to the boundary.

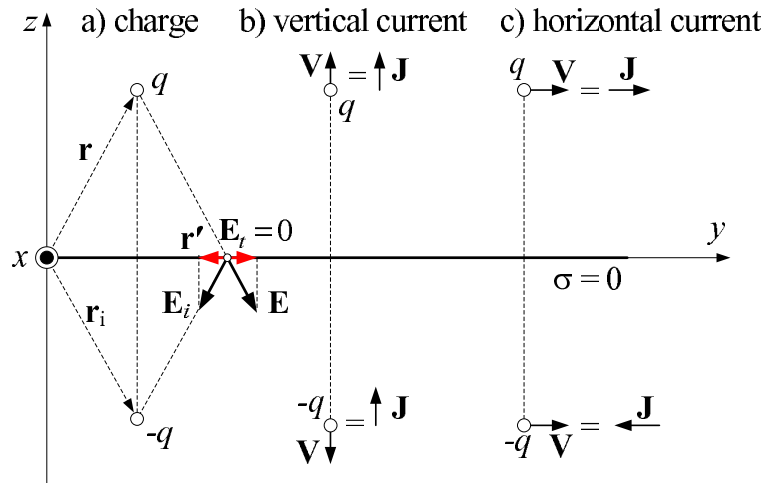


Figure 1.1: Imaged sources for charges (a), and for vertical (b) and horizontal (c) currents.

1.2.4 Image theory for a perfectly conducting infinite plane

The electromagnetic field produced by a scatterer may be changed by obstacles in its proximity. One of the most wide-spread obstacles, which appear in problems related to passive interconnection structures, is the well conducting ground plane. A large number of objects may be considered as ground planes, e.g., the conducting earth surface, conducting device cases, metalized layers in printed circuit boards, etc. In all these cases, the surfaces are finite conductive but may be considered as perfectly conducting ones. This may be explained using the *Leontovich surface impedance boundary condition* (1.57), which states that the effective conductance of a conducting surface decreases towards the frequency increasing. Hence, each conductive surface may be considered as perfectly conducting at high frequencies. Since the influence of scattering increases at high frequencies, conducting surfaces may be assumed to be perfect conducting in a large number of problems related to scattering.

A scatterer located in the proximity of a perfectly conducting plane may be simply described using the *image theory*, which is given in this section for the point charge and current sources above an infinite ground plane. In general, the image theory may be applied not only in this case. However, this monograph considers only this most important application of the image theory, which is used in the following chapters.

The boundary-value problem shown in Fig. 1.1a is considered. The electric field intensity caused by a point charge has to be computed in the higher half space, whose lower boundary is the perfectly conducting ground plane located in the (x, y) plane at $z = 0$. The point charge q is located at the point $\mathbf{r} = (x, y, z)$. We consider a free-space problem, where the ground plane is replaced by an *image charge* $q_i = -q$ located at the point $\mathbf{r}_i = (x, y, -z)$. We consider the tangential component of the electric field intensity produced by q and q_i at the point $\mathbf{r}' = (x', y', 0)$ of the boundary surface. As shown in Fig. 1.1a, $\mathbf{E}_t(\mathbf{r}) = 0$ at all points of the boundary. Thus, the solution of the free-space problem satisfies the boundary condition for the tangential component of the electric field intensity and, certainly, to the wave equation. Because of the uniqueness theorem (see § 1.2.1), the solution of this

equivalent free-space problem is the unique solution for the initial boundary-value problem.

The second boundary-value problem is shown in Fig. 1.1b. The charge q moves in the vertical direction that may be considered as a point current source $\mathbf{J}(\mathbf{r})$. According to Fig. 1.1a, the equivalent free-space problem is obtained replacing the ground plane by the image charge $q_i = -q$ moving in the negative vertical direction, which means a current in the same direction as $\mathbf{J}(\mathbf{r})$.

The third boundary-value problem is shown in Fig. 1.1c. The charge q moves in the horizontal direction that may be considered as a point current source $\mathbf{J}(\mathbf{r})$. According to Fig. 1.1a, the equivalent free-space problem is obtained replacing the ground plane by the image charge $q_i = -q$ moving in the same direction, which means a current in the opposite direction (see Fig. 1.1c).

These three auxiliary boundary-value problems allow one to deduce the image principle. The field produced by a system of currents and charges in the proximity of a ground plane may be computed using an equivalent free-space problem, which replaces the ground plane by the mirror images of the current and charge sources. The charges and the horizontal components of currents are reflected with a negative sign, while the vertical components of currents are reflected with a positive sign.

1.3 Green's function method

This analytic technique was developed for the solution of a particular problem, namely, Poisson equation by George Green in 1828. Nowadays, the Green's function method is the most wide-spread analytic approach for solution of **linear** boundary-value problems (BVP). The Green's function method is limited only by linear BV problems because it is based on the superposition principle. In the following, a linear boundary-value problem is written in the operator form:

$$\mathfrak{L}\{f(\mathbf{r})\} = e(\mathbf{r}), \quad \mathbf{r} \in V \subset \mathbb{R}^3, \quad f(\mathbf{r}), e(\mathbf{r}) \in \mathbb{C}, \quad (1.28)$$

where V is the three-dimensional *solution region* with the closed boundary $S = \partial V$, $f(\mathbf{r})$ is the unknown function, $e(\mathbf{r})$ is the known excitation function, and $\mathfrak{L}\{\}$ is the linear differential operator. Since the solution of (1.28) is not unique, we complete it with Dirichlet, Neumann or mixed boundary conditions:

$$\begin{aligned} \text{Dirichlet boundary condition} \quad & f(\mathbf{r}) = \alpha(\mathbf{r}), \\ \text{Neumann boundary condition} \quad & \frac{\partial}{\partial n} f(\mathbf{r}) = \beta(\mathbf{r}), \quad \mathbf{r} \in S, \\ \text{mixed boundary condition} \quad & f(\mathbf{r}) + \alpha(\mathbf{r}) \frac{\partial}{\partial n} f(\mathbf{r}) = \beta(\mathbf{r}). \end{aligned} \quad (1.29)$$

The Green's function method gives the solution of the BVP (1.28) in the form of a space-convolution integral over the solution region V :

$$f(\mathbf{r}) = - \iiint_V g(\mathbf{r}, \mathbf{r}') e(\mathbf{r}') dV', \quad (1.30)$$

where dV' means the integration over \mathbf{r}' . $g(\mathbf{r}, \mathbf{r}')$ is named the Green's function for the BVP, \mathbf{r} and \mathbf{r}' are the *observation* and the *source* points, respectively.

The excitation $e(\mathbf{r})$ may be represented using the three-dimensional Dirac delta function $\delta(\mathbf{r} - \mathbf{r}')$:

$$e(\mathbf{r}) = \iiint_V \delta(\mathbf{r} - \mathbf{r}') e(\mathbf{r}') dV'. \quad (1.31)$$

The definition for the Green's function is derived by the substitution of (1.30) and (1.31) in (1.28). In view that $\mathfrak{L}\{\}$ is a linear operator with respect to \mathbf{r} , we write:

$$- \iiint_V \mathfrak{L}\{g(\mathbf{r}, \mathbf{r}')\} e(\mathbf{r}') dV' = \iiint_V \delta(\mathbf{r} - \mathbf{r}') e(\mathbf{r}') dV'. \quad (1.32)$$

The comparison of the right- and left-hand sides of (1.32) results in

$$\mathfrak{L}\{g(\mathbf{r}, \mathbf{r}')\} = -\delta(\mathbf{r} - \mathbf{r}'). \quad (1.33)$$

Thus, the Green's function is the solution of the BVP at the observation point excited by the minus Dirac delta function at the source point.

Green's functions for wave equations in free space

The most wide-spread application of the Green's function method in electrodynamics is the solution of the scalar wave equation for the free space. The free space is defined as the homogeneous isotropic unlimited space with $\epsilon = \epsilon_0$ and $\mu = \mu_0$. The Green's function may be derived as the solution of the wave equation for the scalar electric potential (1.17) excited by $-\delta(\mathbf{r} - \mathbf{r}')$:

$$\nabla^2 g(\mathbf{r}, \mathbf{r}') + k^2 g(\mathbf{r}, \mathbf{r}') = -\delta(\mathbf{r} - \mathbf{r}'). \quad (1.34)$$

Assuming the source point at the coordinate origin and in view of the spherical symmetry, (1.34) may be rewritten in the spherical coordinates $\{\hat{\mathbf{r}}, \hat{\boldsymbol{\theta}}, \hat{\boldsymbol{\phi}}\}$ as follows:

$$\frac{1}{r^2} \frac{\partial}{\partial r} \left(r^2 \frac{\partial}{\partial r} g(r) \right) + k^2 g(r) = -\delta(r). \quad (1.35)$$

(1.35) is a linear ordinary differential equation (ODE) of the second order, whose solution may be expanded in two independent functions [86]. The functions $\frac{e^{\pm jkr}}{r}$ with $k = \omega\sqrt{\mu_0\epsilon_0}$ satisfy the homogeneous equation (1.35) and, thus, compose the basis for the solution subspace of (1.35) in the functional space. Hence, the solution of (1.35) may be expressed via these two functions:

$$g(r) = A \frac{e^{-jkr}}{r} + B \frac{e^{jkr}}{r}. \quad (1.36)$$

Since the second term in (1.36) does not satisfy the Sommerfeld radiation boundary condition (see § 1.2.2), the coefficient B has to be zero. The coefficient A may be defined via application

to the inhomogeneous differential equation (1.34) the following operator:

$$\lim_{r \rightarrow 0} \iiint_V \nabla \cdot \nabla g(\mathbf{r}) dV + k^2 \lim_{r \rightarrow 0} \iiint_V g(\mathbf{r}) dV = - \lim_{r \rightarrow 0} \iiint_V \delta(\mathbf{r}) dV, \quad (1.37)$$

where the volume V is a sphere with a radius r about the coordinate origin. The first term on the left-hand side is

$$\lim_{r \rightarrow 0} \iiint_V \nabla \cdot \nabla g(\mathbf{r}) dV = \lim_{r \rightarrow 0} \oint_{A=\partial V} \nabla g(\mathbf{r}) dA = -4\pi A. \quad (1.38)$$

The second term is

$$k^2 \lim_{r \rightarrow 0} \iiint_V g(\mathbf{r}) dV = k^2 \lim_{r \rightarrow 0} \int_0^r 4\pi r^2 A \frac{e^{-jkr}}{r} dr = 0. \quad (1.39)$$

Since the right-hand side of (1.37) gives -1 , the unknown constant A is equal to $\frac{1}{4\pi}$, and the solution for (1.35) is

$$g(r) = \frac{1}{4\pi} \frac{e^{-jkr}}{r}. \quad (1.40)$$

Using (1.40), the *free-space scalar Green's function* for an arbitrary source point is derived as follows:

$$g(\mathbf{r}, \mathbf{r}') = \frac{1}{4\pi} \frac{e^{-jk|\mathbf{r}-\mathbf{r}'|}}{|\mathbf{r}-\mathbf{r}'|}. \quad (1.41)$$

The free-space scalar Green's function (1.41) is the fundamental solution for the scalar wave equation (1.34), which is identical to the equations for the scalar electric and vector magnetic potentials (1.17). Thus, the potentials may be calculated using the Green's function method (1.30). Applying $e(\mathbf{r}') = -\rho_v(\mathbf{r}')/\epsilon_0$, we may compute the scalar potential as follows:

$$\varphi(\mathbf{r}) = \frac{1}{\epsilon_0} \iiint_V g(\mathbf{r}, \mathbf{r}') \rho_v(\mathbf{r}') dV. \quad (1.42)$$

In case of the vector magnetic potential, the excitation is $e(\mathbf{r}') = -\mu_0 \mathbf{J}(\mathbf{r}')$. Thus, we obtain the solution in the following form:

$$\mathbf{A}(\mathbf{r}) = \mu_0 \iiint_V g(\mathbf{r}, \mathbf{r}') \mathbf{J}(\mathbf{r}') dV. \quad (1.43)$$

The solution of the scalar wave equations for the electric and magnetic field intensity (1.12) may be expressed using the scalar Green's function (1.41). At the beginning, the wave equation for the electric field caused by the electric current sources is considered. The right-hand side of the wave equation is formulated in (1.12):

$$e(\mathbf{r}') = j\omega\mu_0 \left(\bar{\mathbf{I}} + \frac{\nabla' \nabla'}{k^2} \right) \cdot \mathbf{J}(\mathbf{r}'), \quad (1.44)$$

where ∇' is the differential operator with respect to \mathbf{r}' . In view of (1.44), the solution of (1.12) is computed according to (1.30) as follows:

$$\mathbf{E}(\mathbf{r}) = -j\omega\mu_0 \iiint_V g(\mathbf{r}, \mathbf{r}') \left(\bar{\bar{\mathbf{I}}} + \frac{\nabla'\nabla'}{k^2} \right) \cdot \mathbf{J}(\mathbf{r}') dV'. \quad (1.45)$$

Applying the vector identity (A.4) and the volume gradient theorem (A.16), the expression (1.45) may be rewritten in an alternative form:

$$\mathbf{E}(\mathbf{r}) = j\omega\mu_0 \iiint_V \left[\left(\bar{\bar{\mathbf{I}}} + \frac{\nabla'\nabla'}{k^2} \right) g(\mathbf{r}, \mathbf{r}') \right] \cdot \mathbf{J}(\mathbf{r}') dV'. \quad (1.46)$$

It can be proved that $\nabla'\nabla' g(\mathbf{r}, \mathbf{r}') = \nabla\nabla g(\mathbf{r}, \mathbf{r}')$ for the free-space Green's function. Thus, (1.46) can be finally rewritten in the conventional form:

$$\begin{aligned} \mathbf{E}(\mathbf{r}) &= - \iiint_V \bar{\bar{\mathbf{G}}}_J^E(\mathbf{r}, \mathbf{r}') \cdot \mathbf{J}(\mathbf{r}') dV' \\ &\text{with } \bar{\bar{\mathbf{G}}}_J^E(\mathbf{r}, \mathbf{r}') = -j\omega\mu_0 \left(\bar{\bar{\mathbf{I}}} + \frac{\nabla\nabla}{k^2} \right) g(\mathbf{r}, \mathbf{r}'). \end{aligned} \quad (1.47)$$

The dyadic function $\bar{\bar{\mathbf{G}}}_J^E(\mathbf{r}, \mathbf{r}')$ is named the *electric-field dyadic Green's function (DGF) for electric sources*. The electric-field dyadic Green's function for magnetic sources, and *magnetic-field dyadic Green's functions* for electric and magnetic sources are obtained using the similar way of derivation:

$$\begin{aligned} \bar{\bar{\mathbf{G}}}_M^E(\mathbf{r}, \mathbf{r}') &= -\nabla \times \bar{\bar{\mathbf{I}}} g(\mathbf{r}, \mathbf{r}'), \\ \bar{\bar{\mathbf{G}}}_J^H(\mathbf{r}, \mathbf{r}') &= \nabla \times \bar{\bar{\mathbf{I}}} g(\mathbf{r}, \mathbf{r}'), \\ \bar{\bar{\mathbf{G}}}_M^H(\mathbf{r}, \mathbf{r}') &= -j\omega\epsilon \left(\bar{\bar{\mathbf{I}}} + \frac{\nabla\nabla}{k^2} \right) g(\mathbf{r}, \mathbf{r}'). \end{aligned} \quad (1.48)$$

The general solutions for the electric and magnetic fields governed by (1.12) are expressed in terms of the free-space dyadic Green's functions (1.47) and (1.48) as follows:

$$\begin{aligned} \mathbf{E}(\mathbf{r}) &= - \iiint_V \bar{\bar{\mathbf{G}}}_J^E(\mathbf{r}, \mathbf{r}') \cdot \mathbf{J}(\mathbf{r}') dV' - \iiint_V \bar{\bar{\mathbf{G}}}_M^E(\mathbf{r}, \mathbf{r}') \cdot \mathbf{M}(\mathbf{r}') dV', \\ \mathbf{H}(\mathbf{r}) &= - \iiint_V \bar{\bar{\mathbf{G}}}_J^H(\mathbf{r}, \mathbf{r}') \cdot \mathbf{J}(\mathbf{r}') dV' - \iiint_V \bar{\bar{\mathbf{G}}}_M^H(\mathbf{r}, \mathbf{r}') \cdot \mathbf{M}(\mathbf{r}') dV'. \end{aligned} \quad (1.49)$$

The electric- and magnetic-field dyadic Green's functions can be developed not only for the free-space problem. The classical literature in the electromagnetic theory proposes ones for several particular geometries of the solution region, e.g., half-space problems, rectangular

and cylindrical waveguides and cavities, stratified media, etc. Of course, the Green's function derivation for these specific problems involves other boundary conditions in contrast to the free-space geometry. The closed-form Green's functions are derived using some sophisticated analytical techniques, e.g., for the plane-stratified media, through the two-dimensional spatial Fourier transformation (see details in § 5.2). Thus, the general solution for electric and magnetic fields based on the dyadic Green's functions (1.49) is applicable for a number of canonical solution regions, in particular, for the interconnection structures in layered media.

1.4 Integral-equation techniques

The integral-equation (IE) techniques are one of the most important approaches for the computation of the unknown current density distribution on the surface of conducting objects. The IE methods formulate the problem in terms of an integral equation, which is written with respect to the unknown current distribution. This can be realized only if the problem geometry allows the field intensity to be calculated via the Green's functions according to (1.49), which is possible only in the solution region with a linear medium. There is a large number of the integral-equation formulations based on the surface and volume equivalence principles (see, e.g., [122]). In the following, the most wide-spread IE formulation named the *electric-field integral equation* (EFIE) is considered (see § 1.4.1). This formulation is the most appropriate for modeling the passive interconnection structures, which are the main subject of this work. The most important disadvantage of the EFIE is the hypersingular behavior of the space-convolution integral kernels [27]. The calculation of the integrals of these singular functions is a hard problem, which may be avoided via the application of the so-called *mixed-potential integral equation* (MPIE). This is also an electric-field integral-equation formulation developed in § 1.4.2 using the scalar electric and vector magnetic potentials introduced in § 1.1.3. The MPIE has integral kernels with weaker singularities than those in the EFIE and, consequently, is more suitable for application.

1.4.1 Electric-field integral equation

A passive interconnection structure located in the free-space solution region V (see Fig. 1.2) is considered. The conductivity of interconnections σ is assumed high, consequently, the electric field in the conductor is computed via the Ohm's law in differential form:

$$\mathbf{E}(\mathbf{r}) = \frac{\mathbf{J}(\mathbf{r})}{\sigma}. \quad (1.50)$$

Since the interconnection system is located in a linear medium, the electric field intensity may be computed using the superposition principle:

$$\mathbf{E}(\mathbf{r}) = \mathbf{E}^i(\mathbf{r}) + \mathbf{E}^s(\mathbf{r}), \quad (1.51)$$

where $\mathbf{E}^i(\mathbf{r})$ is the electric field generated by the sources located out of the solution region, which is denoted by *incident field*, and $\mathbf{E}^s(\mathbf{r})$ is the electric field scattered by the sources

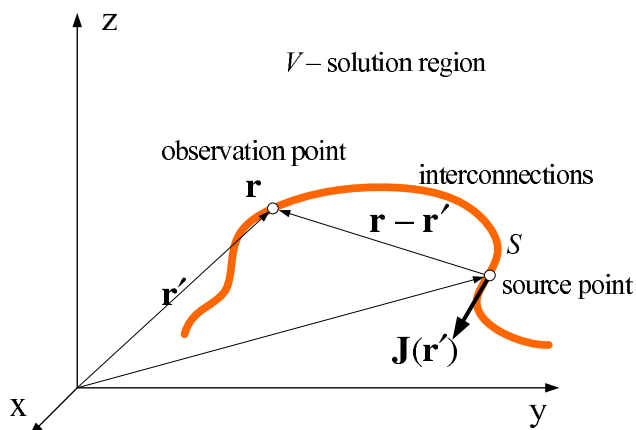


Figure 1.2: Interconnection structure.

located inside the solution region, which is called the *scattered field*. Generally, the incident field induces currents in interconnections. These currents produce the scattered field, which influences the current and change distribution. Thus, the incident field is the initial source for the field, which cannot be explicitly calculated. As shown in § 1.3, the electric field scattered by a space distribution of currents may be expressed using the Green's function method. The general expression (1.49) for the electric field in presence only of electric currents yields:

$$\mathbf{E}^s(\mathbf{r}) = - \iiint_V \overline{\mathbf{G}}_J^E(\mathbf{r}, \mathbf{r}') \cdot \mathbf{J}(\mathbf{r}') dV'. \quad (1.52)$$

Of course, the space-convolution integration over the total solution region in (1.52) does not need to be computed. The electric currents flow in interconnections that allows one to reduce the integration area to the volume of conductors.

In the following, the current distribution in conductors is considered. It is inhomogeneous at high frequencies. Usually, the currents flow near to the surface (or skin) of conductors. This phenomenon is called *skin effect*. The amount of the current penetration in the conductor is called the *skin depth* calculated as

$$\delta = \sqrt{\frac{2}{\omega\sigma\mu}}. \quad (1.53)$$

Obviously, the skin depth decreases at high frequencies and for well conducting metals. The skin depth of the perfect electric conductor is zero at all frequencies, thus, the volume current distribution $\mathbf{J}(\mathbf{r}')$ in (1.52) may be replaced with a surface current distribution $\mathbf{J}_s(\mathbf{r}')$. (1.52) becomes

$$\mathbf{E}^s(\mathbf{r}) = - \iint_S \overline{\mathbf{G}}_J^E(\mathbf{r}, \mathbf{r}') \cdot \mathbf{J}_s(\mathbf{r}') dS', \quad (1.54)$$

where S is the total surface of conductors. The metals applied in interconnection structures have high but finite values of the conductance. Assuming the skin effect strong, the expression (1.54) may be approximately applied to structures with a finite conductivity. The

assumption of the strong skin effect is exact only at high frequencies but may be applied at a wide-band frequency range, since the electromagnetic interferences caused by the scattering decrease towards low frequencies and a minor inaccuracy in the assumption does not influence results.

The tangential component of the electric field intensity on the conductor surface may be computed by (1.50) and, alternatively, by (1.51), where the scattered field is expressed via (1.54). The substitution of (1.51) in (1.50) yields the boundary condition:

$$\mathbf{E}_t^i(\mathbf{r}) + \mathbf{E}_t^s(\mathbf{r}) = \frac{\mathbf{J}_t(\mathbf{r})}{\sigma}, \quad (1.55)$$

where $\mathbf{E}_t^i(\mathbf{r})$ and $\mathbf{E}_t^s(\mathbf{r})$ are the tangential components of $\mathbf{E}^i(\mathbf{r})$ and $\mathbf{E}^s(\mathbf{r})$. They are defined using the projection operator $-\hat{\mathbf{n}} \times \hat{\mathbf{n}} \times$ as follows: $\mathbf{E}_t^i(\mathbf{r}) = -\hat{\mathbf{n}} \times \hat{\mathbf{n}} \times \mathbf{E}^i(\mathbf{r})$ and $\mathbf{E}_t^s(\mathbf{r}) = -\hat{\mathbf{n}} \times \hat{\mathbf{n}} \times \mathbf{E}^s(\mathbf{r})$, where $\hat{\mathbf{n}}$ is the positive normal to the conductor surface. The substitution of (1.54) in (1.55) results in the EFIE formulation

$$-\hat{\mathbf{n}} \times \hat{\mathbf{n}} \times \mathbf{E}^i(\mathbf{r}) = -\hat{\mathbf{n}} \times \hat{\mathbf{n}} \times \left(\frac{\mathbf{J}(\mathbf{r})}{\sigma} + \iint_{S'} \overline{\overline{\mathbf{G}}}_J^E(\mathbf{r}, \mathbf{r}') \cdot \mathbf{J}_s(\mathbf{r}') dS' \right). \quad (1.56)$$

An alternative formulation for the EFIE may be derived using the Leontovich surface-impedance boundary condition (see [103], [44]), which is formulated analogous to (1.55) with respect to the surface current density \mathbf{J}_s :

$$\mathbf{E}_t^i(\mathbf{r}) + \mathbf{E}_t^s(\mathbf{r}) = Z_s(j\omega) \mathbf{J}_s, \quad (1.57)$$

where $Z_s(j\omega)$ is the surface impedance defined as follows:

$$Z_s(j\omega) = (1 + j) \sqrt{\frac{\mu\omega}{2\sigma}}. \quad (1.58)$$

The EFIE based on (1.57) differs from (1.56) in only the formulation for losses:

$$-\hat{\mathbf{n}} \times \hat{\mathbf{n}} \times \mathbf{E}^i(\mathbf{r}) = -\hat{\mathbf{n}} \times \hat{\mathbf{n}} \times \left(Z_s(j\omega) \mathbf{J}_s(\mathbf{r}) + \iint_{S'} \overline{\overline{\mathbf{G}}}_J^E(\mathbf{r}, \mathbf{r}') \cdot \mathbf{J}_s(\mathbf{r}') dS' \right). \quad (1.59)$$

Both expressions given by (1.56) and (1.59) are integrodifferential equations with respect to the unknown surface current distribution, whose solutions define the electric fields in the total solution region:

$$\mathbf{E}(\mathbf{r}) = \mathbf{E}^i(\mathbf{r}) - \iiint_V \overline{\overline{\mathbf{G}}}_J^E(\mathbf{r}, \mathbf{r}') \cdot \mathbf{J}(\mathbf{r}') dV', \quad (1.60)$$

while the magnetic field may be computed from Maxwell's equations (1.2) based on the known electric field intensity. Usually, the EFIE is solved numerically using the method of

moments (see § 3.3). The numerical method requires the discretization of the space, where the unknown variable is distributed, i.e., the surface of conductors. Normally, the surface of conductors is a minor part of the solution volume, which has to be completely discretized for the numerical solution via a differential method (see § 3.2). Thus, the number of variables required for the numerical solution of the EFIE is much less than that for a numerical solution of Maxwell's equations. The summary about numerical methods used for the EFIE is presented in Chapter 3.

The EFIE involves the electric field Green's function that is hypersingular [27]. E.g., Pocklington equation, which is derived from the EFIE in the free space for a straight thin wire (see [122]), has fifth order singularity in the integral kernel at point $\mathbf{r} = \mathbf{r}'$. The calculation of such singular functions may be avoided via the introduction of a MPIE formulation, which is less singular.

1.4.2 Mixed-potential integral equation

The considered EFIE is based on the boundary condition (1.55). Since the scattered electric field in free space may be expressed in terms of the scalar electric and vector magnetic potentials (1.15), it is possible to derive an alternative integral equation formulation via the substitution of (1.15) in (1.55):

$$-\hat{\mathbf{n}} \times \hat{\mathbf{n}} \times (\mathbf{E}^i(\mathbf{r}) - j\omega\mathbf{A}(\mathbf{r}) - \nabla\varphi(\mathbf{r})) = -\hat{\mathbf{n}} \times \hat{\mathbf{n}} \times \frac{\mathbf{J}(\mathbf{r})}{\sigma}. \quad (1.61)$$

The scalar and vector potentials in (1.61) are given by (1.42) and (1.43). The volume integration in the general formula (1.42) can be replaced by the surface one, since the charges are distributed on the conductor surfaces. As well, the vector magnetic potential (1.43) may be computed via a surface integral assuming a surface current distribution caused by strong skin effect as in § 1.4.1. Thus, the potentials yield

$$\begin{aligned} \varphi(\mathbf{r}) &= \frac{1}{\epsilon_0} \iint_S g(\mathbf{r}, \mathbf{r}') \rho_s(\mathbf{r}') dS', \\ \mathbf{A}(\mathbf{r}) &= \mu_0 \iiint_S g(\mathbf{r}, \mathbf{r}') \mathbf{J}_s(\mathbf{r}') dS', \end{aligned} \quad (1.62)$$

where $\rho_s(\mathbf{r})$ is the surface charge density. The substitution of (1.62) in (1.61) results in the conventional formulation of the mixed-potential integral equation for the free space:

$$\begin{aligned} &-\hat{\mathbf{n}} \times \hat{\mathbf{n}} \times \mathbf{E}^i(\mathbf{r}) = \\ &-\hat{\mathbf{n}} \times \hat{\mathbf{n}} \times \left(\frac{\mathbf{J}(\mathbf{r})}{\sigma} + j\omega\mu_0 \iint_{S'} g(\mathbf{r}, \mathbf{r}') \mathbf{J}_s(\mathbf{r}') dS' + \frac{\nabla}{\epsilon_0} \iint_{S'} g(\mathbf{r}, \mathbf{r}') \rho_s(\mathbf{r}') dS' \right). \end{aligned} \quad (1.63)$$

(1.63) is an integrodifferential equation with respect to the unknown current and charge distributions. Usually, the MPIE in this form is numerically solved by the method of moments

and the partial element equivalent circuit method, which are explained in Chapter 4. The comparison of the integral kernels in (1.63) and (1.56) shows that the kernels in the MPIE are less singular. E.g., in the free space, the Pocklington equation has the fifth order of singularity, while the MPIE provides only the first order of singularity caused by the scalar Green's function.

Since the current and charge distributions are coupled functions, another MPIE formulation written with respect only to the current distribution may be developed. One substitutes the continuity equation for electric sources (1.4) in (1.63), which yields

$$\begin{aligned} -\hat{\mathbf{n}} \times \hat{\mathbf{n}} \times \mathbf{E}^i(\mathbf{r}) &= -\hat{\mathbf{n}} \times \hat{\mathbf{n}} \times \frac{\mathbf{J}(\mathbf{r})}{\sigma} \\ &- \hat{\mathbf{n}} \times \hat{\mathbf{n}} \times \left(+j\omega\mu_0 \iint_{S'} g(\mathbf{r}, \mathbf{r}') \mathbf{J}_s(\mathbf{r}') dS' - \frac{\nabla}{j\omega\epsilon_0} \iint_{S'} g(\mathbf{r}, \mathbf{r}') \nabla' \cdot \mathbf{J}_s(\mathbf{r}') dS' \right). \end{aligned} \quad (1.64)$$

The numerical solution of this MPIE needs fewer unknowns as compared to (1.63) because only currents have to be calculated, while it remains less singular than the corresponding EFIE formulation.

The free-space MPIE (1.63) can be rewritten using a more general formalism

$$\begin{aligned} -\hat{\mathbf{n}} \times \hat{\mathbf{n}} \times \mathbf{E}^i(\mathbf{r}) &= -\hat{\mathbf{n}} \times \hat{\mathbf{n}} \times \frac{\mathbf{J}(\mathbf{r})}{\sigma} \\ &- \hat{\mathbf{n}} \times \hat{\mathbf{n}} \times \left(j\omega\mu \iint_{S'} \overline{\overline{\mathbf{G}}}^A(\mathbf{r}, \mathbf{r}') \cdot \mathbf{J}_s(\mathbf{r}') dS' + \frac{\nabla}{\epsilon} \iint_{S'} K^\varphi(\mathbf{r}, \mathbf{r}') \rho_s(\mathbf{r}') dS' \right), \end{aligned} \quad (1.65)$$

where $\overline{\overline{\mathbf{G}}}^A(\mathbf{r}, \mathbf{r}')$ is the dyadic Green's function for the vector magnetic potential, $K^\varphi(\mathbf{r}, \mathbf{r}')$ is the scalar Green's function for the vector magnetic potential. As the dyadic Green's functions for electric and magnetic fields (1.49), the Green's functions $\overline{\overline{\mathbf{G}}}^A(\mathbf{r}, \mathbf{r}')$ and $K^\varphi(\mathbf{r}, \mathbf{r}')$ can be derived for several canonical geometries of the solution region. E.g., in the free space, these functions are trivially expressed in terms of the scalar Green's function:

$$\overline{\overline{\mathbf{G}}}^A(\mathbf{r}, \mathbf{r}') = g(\mathbf{r}, \mathbf{r}') \overline{\overline{\mathbf{I}}}, \quad (1.66)$$

$$K^\varphi(\mathbf{r}, \mathbf{r}') = g(\mathbf{r}, \mathbf{r}') \quad (1.67)$$

with $\epsilon = \epsilon_0$ and $\mu = \mu_0$. The Green's functions $\overline{\overline{\mathbf{G}}}^A(\mathbf{r}, \mathbf{r}')$ and $K^\varphi(\mathbf{r}, \mathbf{r}')$ can be also developed for more complex solution regions, e.g., see § 5.2, which is devoted to the MPIE for stratified media. The layered medium can be described using the EFIE and MPIE formulations. The advantage of the MPIE is a less singular behavior of the Green's functions.

In general, the Green's functions $\overline{\overline{\mathbf{G}}}^A(\mathbf{r}, \mathbf{r}')$ and $K^\varphi(\mathbf{r}, \mathbf{r}')$ may be defined as functions satisfying

$$\varphi(\mathbf{r}) = \frac{1}{\epsilon} \iiint_V K^\varphi(\mathbf{r}, \mathbf{r}') \rho_v(\mathbf{r}') dV \quad (1.68)$$

and

$$\mathbf{A}(\mathbf{r}) = \mu \iiint_V \overline{\mathbf{G}}^A(\mathbf{r}, \mathbf{r}') \cdot \mathbf{J}(\mathbf{r}') dV, \quad (1.69)$$

while $\mathbf{E}^s(\mathbf{r}) = -j\omega\mathbf{A}(\mathbf{r}) - \nabla\varphi(\mathbf{r})$, and μ and ϵ are related to the medium in the observation-point area. Of course, the choice of potentials is not unique, and they satisfy the Lorenz or Coulomb gauges not in all solution-region geometries (see, e.g., in [108]).

1.5 Transmission-line theory

A large number of electromagnetic problems can be analyzed in terms of *transverse electromagnetic* (TEM) waves (or modes). Some of these problems are directly related to the TEM waves as the propagation of plane waves in free space, waveguides, transmission lines, and cables, while other problems can be solved using the decompositions into TEM modes (see, e.g., the approach used for the derivation of the dyadic Green's functions for layered media in § 5.2).

A TEM mode can be defined as an electromagnetic field configuration, whose electric and magnetic field intensity at every point is tangent to a so-called equiphase surface, which may be non-planar. The electric and magnetic field intensities compose a right-handed system with the positive normal to the equiphase surface that is the wave-propagation direction. As an example, one may consider the two-dimensional spatial Fourier transformation given in (A.22), where the function $g(\mathbf{r}, \mathbf{r}')$ is decomposed into TEM modes $e^{j\mathbf{k}_\rho \cdot \boldsymbol{\rho}}$, whereby the equiphase surfaces are cylindrical, and the propagation directions are $\hat{\boldsymbol{\rho}}$.

The TEM wave, whose equiphase surface is a plane, is named *plane wave*. The plane wave, whose amplitude does not change on the equiphase plane, is called a *uniform plane wave*, while the equiphase plane is also the equiamplitude plane. The propagation of the uniform plane wave is described using the one-dimensional scalar wave equation, which is solved in closed form. The electromagnetic fields in uniform transmission lines propagate as uniform plane waves, thus, the conventional transmission-line theory may be applied in order to obtain the solutions for uniform plane wave modes.

The time-domain models for multilayer PCB boards developed in § 5.4 involve the dyadic Green's functions for the vector magnetic and scalar electric potentials, whose scalar components are derived in § 5.2 and § 5.3 in terms of the transmission-line Green's functions. In order to simplify the understanding of these sections, the required fundamental definitions of the transmission-line theory for two-wire lines are summarized in § 1.5.1, while the transmission-line Green's functions are derived in § 1.5.2. This section does not cover all questions related to transmission lines, and introduces instead only a minimal necessary set of definitions.

The state-of-the-art in the direct modeling of passive interconnection structures using the conventional and generalized transmission-line models is summarized in § 3.4 as compared to other computational methods.

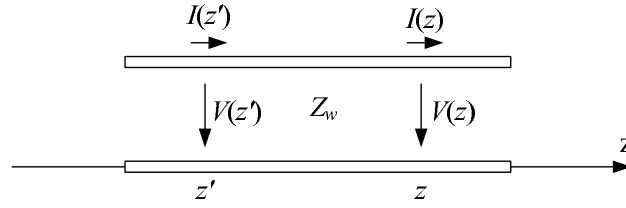


Figure 1.3: Two-wire transmission line.

1.5.1 Fundamental definitions

A uniform two-wire transmission line directed along the axis z is shown in Fig. 1.3. It is governed by the *telegrapher's equations* also known as *transmission-line equations*, which are derived from Maxwell's equations:

$$\begin{aligned} -\frac{\partial}{\partial z}u(z,t) &= \frac{1}{v}Z_w\frac{\partial}{\partial t}i(z,t) + V_s(z,t), \\ -\frac{\partial}{\partial z}i(z,t) &= \frac{1}{v}\frac{1}{Z_w}\frac{\partial}{\partial t}u(z,t) + J_s(z,t), \end{aligned} \quad (1.70)$$

where v is the propagation velocity, Z_w is the wave impedance, $u(z,t)$ and $i(z,t)$ are the transversal voltage and longitudinal current of the line, which are excited by the distributed current and voltage sources $V_s(z,t)$ and $J_s(z,t)$. In the frequency domain, the transmission-line equations (1.70) yield:

$$\begin{aligned} -\frac{\partial V(z)}{\partial z} &= jkZ_w I(z) + V_s(z), \\ -\frac{\partial I(z)}{\partial z} &= \frac{jk}{Z_w}V(z) + J_s(z), \end{aligned} \quad (1.71)$$

where $k = \omega/v$ is the wave number. The substitution one of the equations (1.71) in another leads to one-dimensional wave equations, which have the following general solutions for the current and voltage:

$$V(z) = V^+(z) + V^-(z), \quad Z_w I(z) = V^+(z) - V^-(z) \quad (1.72)$$

with

$$V^+(z) = V^+(z') e^{-jk(z-z')}, \quad V^-(z) = V^-(z') e^{jk(z-z')}, \quad (1.73)$$

where z and z' are two points of the z axis (see Fig. 1.3). The wave $V^+(z)$ propagating in the positive z direction is denoted by the *forward traveling or incident wave*, while the propagating in the negative z direction wave $V^-(z)$ is called the *backward traveling or reflected wave*.

The ratio between the complex amplitudes of the reflected and incident waves is called the *reflection coefficient*:

$$\Gamma(z) = \frac{V^-(z)}{V^+(z)}. \quad (1.74)$$

The traveling-wave representation of the complex amplitudes (1.73) can be substituted in (1.74) that results in the relation for the reflection coefficients in two different points:

$$\Gamma(z) = \Gamma(z') e^{jk 2(z-z')}. \quad (1.75)$$

The solutions for the voltage and current (1.72) may be rewritten in terms of the reflection coefficient:

$$V(z) = V^+(z)(1 + \Gamma(z)), \quad Z_w I(z) = V^+(z)(1 - \Gamma(z)). \quad (1.76)$$

The input impedance of the transmission line at the point z is defined as the ratio between the voltage and current at this point, which can be expressed using (1.76) as follows:

$$Z(z) = \frac{V(z)}{I(z)} = Z_w \frac{1 + \Gamma(z)}{1 - \Gamma(z)}, \quad (1.77)$$

The relation between the current and voltage complex amplitudes at two different points of the transmission line may be derived by the combination of (1.73), (1.75), and (1.76), which results in

$$\begin{aligned} V(z) &= V(z') \cosh jk(z - z') - Z_w I(z') \sinh jk(z - z'), \\ I(z) &= -V(z') \frac{\sinh jk(z - z')}{Z_w} + I(z') \cosh jk(z - z'). \end{aligned} \quad (1.78)$$

1.5.2 Green's functions for the transmission-line equations

This section studies an approach to the derivation of the Green's functions for the piecewise uniform transmission lines in the source region, which are used for development of the dyadic Green's functions of layered media in § 5.2. We consider a transmission line with n uniform regions as shown in Fig. 1.4a, where $Z_{w,m}$, k_m , and h_m are the wave impedance, wave number, and length of the m -th region, respectively. The region m is located between points z_{m-1} and z_m , thus, $h_m = z_m - z_{m-1}$. The ends of the line are loaded with impedances \overline{Z}_0 and \overline{Z}_n . We assume that the source and observation points are located in the same region m as shown in Fig. 1.4a. The transmission-line equations (1.71) may be applied to all regions.

Since the transmission-line equations are linear, and the equations (1.71) have two kinds of excitations, the solutions for $V(z)$ and $I(z)$ may be calculated through the integration over the solution region using four scalar Green's functions:

$$\begin{aligned} V(z) &= - \int V_u(z, z') V_s(z') dz' - \int V_i(z, z') J_s(z') dz', \\ I(z) &= - \int I_u(z, z') V_s(z') dz' - \int I_i(z, z') J_s(z') dz', \end{aligned} \quad (1.79)$$

where the Green's functions $V_u(z, z')$ and $I_u(z, z')$ are the voltage and current responses on the excitation $V_s(z') = -\delta(z - z')$, while $V_i(z, z')$ and $I_i(z, z')$ are the voltage and current responses on the excitation $J_s(z') = -\delta(z - z')$.

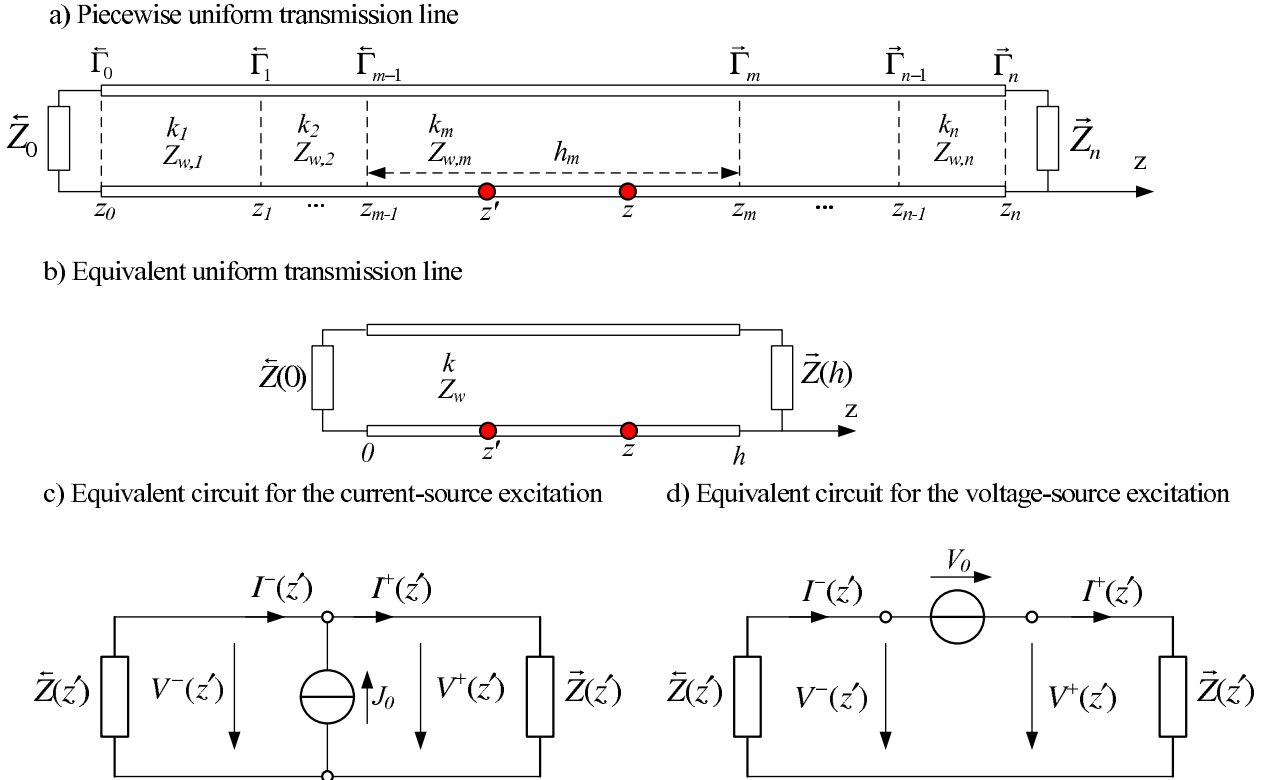


Figure 1.4: Derivation of the Green's function for cascaded transmission lines.

Equivalent uniform transmission line

The derivation of the Green's function for the piecewise uniform line for the observation point in the source region may be essentially simplified using its equivalent uniform-line representation shown in Fig. 1.4b. The parameters of this line correspond to the source region of the piecewise uniform line: $Z_w = Z_{w,m}$, $k = k_m$, and $h = h_m$.

The left termination of the equivalent line $\bar{Z}(0)$ is calculated by the following consecutive formula:

$$\begin{aligned} \bar{\Gamma}_{q-1} &= \frac{\bar{Z}_{q-1} - Z_{w,q}}{\bar{Z}_{q-1} + Z_{w,q}}, & \bar{Z}_q &= Z_{w,q} \frac{1 + \bar{\Gamma}_{q-1} e^{-jk 2h_q}}{1 - \bar{\Gamma}_{q-1} e^{-jk 2h_q}}, & q &= \overline{1, m-1}, \\ \bar{Z}(0) &= \bar{Z}_{m-1}, \end{aligned} \quad (1.80)$$

where \bar{Z}_q and $\bar{\Gamma}_q$ are the input impedance and the reflection coefficient for the backward-traveling wave at the point z_q calculated using (1.77) and (1.75). The right termination of the equivalent line $\bar{Z}(h)$ is calculated as follows:

$$\begin{aligned} \bar{\Gamma}_q &= \frac{\bar{Z}_q - Z_{w,q}}{\bar{Z}_q + Z_{w,q}}, & \bar{Z}_{q-1} &= Z_{w,q} \frac{1 + \bar{\Gamma}_q e^{-jk 2h_q}}{1 - \bar{\Gamma}_q e^{-jk 2h_q}}, & q &= \overline{n, m+1}, \\ \bar{Z}(h) &= \bar{Z}_m, \end{aligned} \quad (1.81)$$

where \overrightarrow{Z}_q and $\overrightarrow{\Gamma}_q$ are the input impedance and the reflection coefficient for the forward-traveling wave at the point z_q .

Green's functions for the uniform loaded lines

According to their definition, the Green's functions $V_u(z, z')$ and $I_u(z, z')$ may be derived through the substitution in the equations for the uniform transmission line (1.71) of the excitation $V'_s(z') = -\delta(z - z')$ and $J'_s(z') = 0$:

$$\begin{aligned} -\frac{\partial}{\partial z} V_u(z, z') &= jkZ_w I_u(z, z') - \delta(z - z'), \\ -\frac{\partial}{\partial z} I_u(z, z') &= \frac{jk}{Z_w} V_u(z, z'), \end{aligned} \quad (1.82)$$

while the Green's functions $V_i(z, z')$ and $I_i(z, z')$ are derived with $V'_s(z') = 0$ and $J'_s(z') = -\delta(z - z')$:

$$\begin{aligned} -\frac{\partial}{\partial z} V_i(z, z') &= jkZ_w I_i(z, z'), \\ -\frac{\partial}{\partial z} I_i(z, z') &= \frac{jk}{Z_w} V_i(z, z') - \delta(z - z'). \end{aligned} \quad (1.83)$$

The first equation in (1.82) and the second one in (1.83) may be integrated over z on the interval $z' - \varsigma \leq z \leq z' + \varsigma$ with $\varsigma \rightarrow 0$. These integrals lead to the jump condition for the Green's functions at the source point:

$$\begin{aligned} V_u(z' + \varsigma, z') - V_u(z' - \varsigma, z') &= 1, \\ I_i(z' + \varsigma, z') - I_i(z' - \varsigma, z') &= 1, \end{aligned} \quad \text{with } \varsigma \rightarrow 0. \quad (1.84)$$

The condition $I_i(z' + \varsigma, z') - I_i(z' - \varsigma, z') = 1$ may be interpreted as a lumped current source $J_0 = 1$ A included transversally at the point z' , in which case, the equivalent circuit shown in Fig. 1.4c may be applied to derivation of the voltage and current at the source point [44]. This equivalent circuit introduces following notations: $V_i^-(z')$ and $V_i^+(z')$ are the voltages before and after the source point, $I_i^-(z')$ and $I_i^+(z')$ are the currents before and after the source point. Since the left and right parts of the loaded line may be considered as two one-port circuits connected to the current source from the left and right sides, they are denoted by the input impedances $\overleftarrow{Z}(z')$ and $\overrightarrow{Z}(z')$ (see Fig. 1.4c). These input impedances are calculated on the basis of the known line terminations $\overleftarrow{Z}(0)$ and $\overrightarrow{Z}(h)$ using (1.77) and (1.75) as follows:

$$\begin{aligned} \overleftarrow{Z}(z') &= Z_w \frac{1 + \overleftarrow{\Gamma}(0) e^{-jk 2z'}}{1 - \overleftarrow{\Gamma}(0) e^{-jk 2z'}}, & \text{with } \overleftarrow{\Gamma}(0) &= \frac{\overleftarrow{Z}(0) - Z_w}{\overleftarrow{Z}(0) + Z_w}, \\ \overrightarrow{Z}(z') &= Z_w \frac{1 + \overleftarrow{\Gamma}(h) e^{-jk 2(h-z')}}{1 - \overleftarrow{\Gamma}(h) e^{-jk 2(h-z')}}, & \text{with } \overleftarrow{\Gamma}(h) &= \frac{\overleftarrow{Z}(h) - Z_w}{\overleftarrow{Z}(h) + Z_w}. \end{aligned} \quad (1.85)$$

Due to simplification, we introduce the following impedances and admittances derived from $\overleftarrow{Z}(z')$ and $\overrightarrow{Z}(z')$:

$$\begin{aligned}\overleftarrow{Z}(z') &= \overleftarrow{Z}(z') + \overrightarrow{Z}(z'), \\ \overleftarrow{Y}(z') &= \overleftarrow{Y}(z') + \overrightarrow{Y}(z'), \quad \overrightarrow{Y}(z') = 1/\overrightarrow{Z}(z'), \quad \overleftarrow{Y}(z') = 1/\overleftarrow{Z}(z').\end{aligned}\quad (1.86)$$

Using (1.86) and the circuit theory, we derive the currents and voltages at the source point:

$$V_i^-(z') = V_i^+(z') = \frac{J_0}{\overleftarrow{Y}(z')}, \quad I_i^+(z') = J_0 \frac{\overrightarrow{Y}(z')}{\overleftarrow{Y}(z')}, \quad I_i^-(z') = -J_0 \frac{\overleftarrow{Y}(z')}{\overleftarrow{Y}(z')}. \quad (1.87)$$

The condition $V_u(z' + \varsigma, z') - V_u(z' - \varsigma, z') = 1$ in (1.84) may be interpreted as a lumped voltage source $V_0 = 1$ V included longitudinally at the point z' , in which case, the equivalent circuit shown in Fig. 1.4d may be applied to the derivation of the voltage and current at the source point. This equivalent circuit introduces the following notations: $V_u^-(z')$ and $V_u^+(z')$ are the voltages before and after the source point, $I_u^-(z')$ and $I_u^+(z')$ are the currents before and after the source point. Using already introduced notations (1.86) and the circuit theory, we derive the currents and voltages at the source point:

$$I_u^-(z') = I_u^+(z') = \frac{V_0}{\overleftarrow{Z}(z')}, \quad V_u^+(z') = V_0 \frac{\overrightarrow{Z}(z')}{\overleftarrow{Z}(z')}, \quad V_u^-(z') = -V_0 \frac{\overleftarrow{Z}(z')}{\overleftarrow{Z}(z')}. \quad (1.88)$$

Since the currents and voltages of the transmission line at different points z and z' are related through (1.78), the voltage and current responses at the observation point z may be derived from their values at the source point given by (1.87) and (1.88). Finally, we obtain the following expressions for the transmission-line Green's functions:

$$V_u(z, z') = \begin{cases} \frac{\overrightarrow{Z}(z')}{\overleftarrow{Z}(z')} \cosh jk(z - z') - \frac{Z_w}{\overleftarrow{Z}(z')} \sinh jk(z - z'), & z > z', \\ -\frac{\overleftarrow{Z}(z')}{\overleftarrow{Z}(z')} \cosh jk(z' - z) + \frac{Z_w}{\overleftarrow{Z}(z')} \sinh jk(z' - z), & z < z', \end{cases} \quad (1.89)$$

$$V_i(z, z') = \begin{cases} \frac{1}{\overleftarrow{Y}(z')} \cosh jk(z - z') - \frac{Z_w \overrightarrow{Y}(z')}{\overleftarrow{Y}(z')} \sinh jk(z - z'), & z > z', \\ \frac{1}{\overleftarrow{Y}(z')} \cosh jk(z' - z) - \frac{Z_w \overleftarrow{Y}(z')}{\overleftarrow{Y}(z')} \sinh jk(z' - z), & z < z', \end{cases} \quad (1.90)$$

$$I_i(z, z') = \begin{cases} -\frac{1}{Z_w \overleftarrow{Y}(z')} \sinh jk(z - z') + \frac{\overrightarrow{Y}(z')}{\overleftarrow{Y}(z')} \cosh jk(z - z'), & z > z', \\ \frac{1}{Z_w \overleftarrow{Y}(z')} \sinh jk(z' - z) - \frac{\overleftarrow{Y}(z')}{\overleftarrow{Y}(z')} \cosh jk(z' - z), & z < z', \end{cases} \quad (1.91)$$

$$I_u(z, z') = \begin{cases} -\frac{\overrightarrow{Z}(z')}{\overleftarrow{Z}(z')Z_w} \sinh jk(z - z') + \frac{1}{\overrightarrow{Z}(z')} \cosh jk(z - z'), & z > z', \\ -\frac{\overleftarrow{Z}(z')}{\overrightarrow{Z}(z')Z_w} \sinh jk(z' - z) + \frac{1}{\overleftarrow{Z}(z')} \cosh jk(z' - z), & z < z'. \end{cases} \quad (1.92)$$

1.5.3 Reciprocity of the transmission-line Green's functions

The reciprocity relations for the transmission-line Green's functions are derived analogous to the ones for the vector wave equation in § 1.2.3. We consider the piecewise uniform transmission line shown in Fig. 1.4a excited by two independent sets of voltage and current sources $\{V_s^{(1)}(z), I_s^{(1)}(z)\}$ and $\{V_s^{(2)}(z), I_s^{(2)}(z)\}$. The voltage and current distributions caused by these two sets of sources denoted by $\{V^{(1)}(z), I^{(1)}(z)\}$ and $\{V^{(2)}(z), I^{(2)}(z)\}$, respectively, satisfy the transmission-line equations:

$$-\frac{\partial}{\partial z}V^{(1)}(z) = jkZ_w I^{(1)}(z) + V_s^{(1)}(z), \quad (1.93)$$

$$-\frac{\partial}{\partial z}I^{(1)}(z) = \frac{jk}{Z_w}V^{(1)}(z) + J_s^{(1)}(z), \quad (1.94)$$

$$-\frac{\partial}{\partial z}V^{(2)}(z) = jkZ_w I^{(2)}(z) + V_s^{(2)}(z), \quad (1.95)$$

$$-\frac{\partial}{\partial z}I^{(2)}(z) = \frac{jk}{Z_w}V^{(2)}(z) + J_s^{(2)}(z). \quad (1.96)$$

The integral over the solution region from the function composed as (1.93)· $I^{(2)}(z)$ + (1.96)· $V^{(1)}(z)$ - (1.94)· $V^{(2)}(z)$ - (1.95)· $I^{(1)}(z)$ is written below:

$$\begin{aligned} & (V^{(1)}(z)I^{(2)}(z) - I^{(1)}(z)V^{(2)}(z))\Big|_{z_0}^{z_n} = \\ & \int_{z_0}^{z_n} (I^{(2)}(z)V_s^{(1)}(z) + V^{(1)}(z)I_s^{(2)}(z) - I^{(1)}(z)V_s^{(2)}(z) - V^{(2)}(z)I_s^{(1)}(z)) dz \end{aligned} \quad (1.97)$$

The left-hand side of (1.97) yields zero, since the voltage and currents at the terminations of the loaded line Fig. 1.4a are related via the same load impedances: $\overleftarrow{Z}_0 I^{(1)}(z_0) = V^{(1)}(z_0)$, $\overleftarrow{Z}_0 I^{(2)}(z_0) = V^{(2)}(z_0)$, $\overrightarrow{Z}_n I^{(1)}(z_n) = V^{(1)}(z_n)$, and $\overrightarrow{Z}_n I^{(2)}(z_n) = V^{(2)}(z_n)$. Thus, (1.97) yields the general reciprocity theorem for the loaded transmission line:

$$\int_{z_0}^{z_n} (I^{(2)}(z)V_s^{(1)}(z) + V^{(1)}(z)I_s^{(2)}(z) - I^{(1)}(z)V_s^{(2)}(z) - V^{(2)}(z)I_s^{(1)}(z)) dz = 0. \quad (1.98)$$

The reciprocity relations for the Green's functions may be derived from (1.98) applying some particular sets of sources:

1. The substitution of $V_s^{(1)}(z) = 0$, $V_s^{(2)}(z) = 0$, $I_s^{(1)}(z) = -\delta(z - z')$, and $I_s^{(2)}(z) = -\delta(z - z'')$ in (1.98) results in $V_i(z'', z') - V_i(z', z'') = 0$.
2. The substitution of $I_s^{(1)}(z) = 0$, $I_s^{(2)}(z) = 0$, $V_s^{(1)}(z) = -\delta(z - z')$, and $V_s^{(2)}(z) = -\delta(z - z'')$ in (1.98) results in $I_u(z', z'') - I_u(z'', z') = 0$.
3. The substitution of $I_s^{(1)}(z) = -\delta(z - z')$, $I_s^{(2)}(z) = 0$, $V_s^{(1)}(z) = 0$, and $V_s^{(2)}(z) = -\delta(z - z'')$ in (1.98) results in $-I_i(z'', z') - V_u(z', z'') = 0$.

Finally, the reciprocity relations between the transmission-line Green's functions are summarized as follows:

$$\begin{aligned}
 V_i(z', z'') &= V_i(z'', z'), \\
 I_u(z', z'') &= I_u(z'', z'), \\
 V_u(z', z'') &= -I_i(z'', z').
 \end{aligned} \tag{1.99}$$

1.6 Causality

Since this work deals with the time-domain analysis of the passive interconnection structures, a short summary devoted to the *causality* of the time-domain models is made in this section. In the following, we consider a frequency-domain transfer function $H(j\omega)$, which relates the signals at the input and output ports denoted by $X(j\omega)$ and $Y(j\omega)$, respectively:

$$Y(j\omega) = H(j\omega) X(j\omega). \tag{1.100}$$

The inverse Fourier transformation of (1.100) leads to the relation between the input and output functions $x(t)$ and $y(t)$ through the convolution integral (3.19).

The frequency response $H(j\omega)$ is causal if the time response $y(t)$ appears not earlier than the excitation $x(t)$. The consideration of the convolution-integral (3.19) structure tells one that the transfer function is causal if $g(t) = 0$ for $t < 0$, where $g(t)$ is the impulse response for this transfer function computed as its inverse Fourier transformation $g(t) = \mathfrak{F}^{-1}\{H(j\omega)\}$. This definition may be expanded if there is a priori information that the transfer response has a time delay τ . In this case, the system is causal if $g(t) = 0$ for $t < \tau$. Obviously, the non-causal frequency responses cannot exist or be realized physically, while a large number of computational methods in electromagnetics apply them in the frequency-domain analysis (e.g., the fast-multipole method [127]). The transformation of these methods in the time domain requires the careful consideration of their causality. The causal and non-causal frequency responses have to be separated via suitable criteria given below.

The impulse response $g(t)$ for $H(j\omega)$, which has the time delay τ may be calculated as follows:

$$g(t) = \mathfrak{F}^{-1}\{H(j\omega)\} = \frac{1}{2\pi} \int_{-\infty}^{+\infty} \tilde{H}(j\omega) e^{j\omega(t-\tau)} d\omega, \tag{1.101}$$

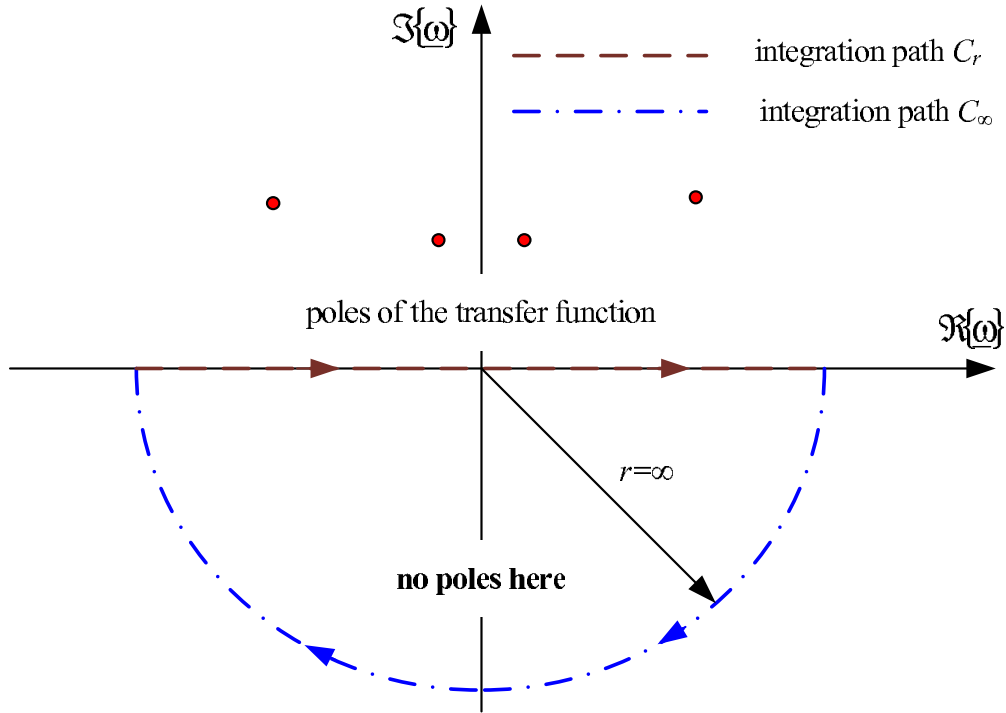


Figure 1.5: The Fourier-integration path.

where $\tilde{H}(j\omega) = H(j\omega) e^{j\omega\tau}$ is the transfer function with the extracted time-delay part. This Fourier integral may be calculated using the contour integration rules [86]. The residue theorem [86] is formulated as

$$\int_C \tilde{H}(j\underline{\omega}) e^{j\underline{\omega}(t-\tau)} d\underline{\omega} = -2\pi j \sum_{n=1}^p \text{res}\{\tilde{H}(\underline{\omega}_n) e^{j\underline{\omega}_n(t-\tau)}\}, \quad (1.102)$$

where $C = C_\infty \cup C_r$ is the closed integration contour, which consists of the initial integration path C_r and the semicircle C_∞ with a radius $r = \infty$ as shown in Fig. 1.5. Assuming $t < \tau$, we obtain $\Re\{j\underline{\omega}(t-\tau)\} < 0$ if $\Im\{\underline{\omega}\} < 0$. Consequently, the integral over C_∞ yields zero, and, thus, (1.102) results in

$$\int_{-\infty}^{+\infty} \tilde{H}(j\omega) e^{j\omega(t-\tau)} d\omega = -2\pi j \sum_{n=1}^p \text{res}\{\tilde{H}(\underline{\omega}_n) e^{j\underline{\omega}_n(t-\tau)}\}, \quad (1.103)$$

where $\text{res}\{\tilde{H}(\underline{\omega}_n) e^{j\underline{\omega}_n(t-\tau)}\}$ are the residues (see [86]) of the integrand at the poles $\underline{\omega}_n$ located inside the closed integration path C , i.e., on the lower half-plane $\underline{\omega}$. Therefore, the integral is zero if $\tilde{H}(j\omega)$ has no poles and branch-points on the lower half-plane $\underline{\omega}$. This may be formulated as a rigorous criterion given in [30] for a delay-loss transfer function:

The time-delay transfer function $H(j\omega)$ is causal ($g(t) = 0$ for $t < \tau$), if the function $\tilde{H}(j\underline{\omega}) = H(j\underline{\omega}) e^{j\underline{\omega}\tau}$ is regular at all points $\underline{\omega}$ with $\Im\{\underline{\omega}\} < 0$.

Another criterion for the causality of frequency responses is in use in the circuit theory [94]. The proposed in [118] Paley-Wiener criterion provides the necessary and sufficient condition for the causality in the frequency domain.

The transfer function $H(j\omega)$ is causal if and only if

$$\int_{-\infty}^{+\infty} \frac{|\ln |H(j\omega)||}{1 + \omega^2} d\omega < \infty, \quad (1.104)$$

i.e., if the magnitude of the transfer function decreases towards the increase of the frequency in logarithmic scale slower than $1/\omega^2$.

Of course, this criterion may be applied only if the inverse Fourier integral of $H(j\omega)$ converges, which is formulated as

$$\int_{-\infty}^{+\infty} |H(j\omega)|^2 d\omega < \infty. \quad (1.105)$$

Chapter 2

Computational methods for circuit analysis

One of the most important matters considered in this monograph is the simultaneous modeling of the passive interconnection structures in their circuit environment. This is reached by the application of the PEEC models, which have an equivalent circuit formulation. These equivalent circuits are computed in the time and frequency domain using a universal circuit-simulator software. In particular, the author applies the slightly modified wide-spread Berkeley SPICE 3f4 for the simulation with the simplest free- and half-space PEEC models, while more advanced PEEC models are implemented in the special-purpose circuit simulator NEAN (Networks and Electromagnetics Analyzer). This code programed by the author works only in the time-domain.

This chapter presents the short summary of the computational methods for circuit analysis, which are required for understanding the questions concerning the implementation of the interconnection-structure models in the circuit simulators. § 2.1 defines the basic concepts of the modified nodal analysis (MNA) used as the general-formulation method in both Berkeley SPICE 3f4 and NEAN codes. Since the MNA method is applied in the frequency as well as in the time domains, its main principles in both solution domains are studied. § 2.2 explains the approaches applied to the transient analysis in the both circuit simulators and gives several definitions required in the following.

2.1 Modified nodal analysis (MNA)

2.1.1 General formulation

The *modified nodal analysis* is the most wide-spread general-formulation method used in the analysis of circuits. It may be applied to an arbitrary active or passive network, which must be a *connected circuit*, i.e., a circuit composed by connected subcircuits. In general, the topology of a circuit with $N + 1$ nodes and M branches is described in terms of the graph theory that is omitted here (see, e.g., [33], [156]). The direction of currents in branches

may be chosen arbitrary except for the voltage and current sources, whose currents have the predefined directions. The connections between nodes and branches in the circuit are described using the *incidence matrix* $\mathbb{A} = \{A_{n,m}\}$, which has $N + 1$ rows and M columns. The element of the incident matrix $\{A_{n,m}\}$ is 1 if the current of the branch m flows away from the node k , -1 if the current of the branch m flows into the node k , and otherwise is zero. One may resume that each column of \mathbb{A} has only two nonzero elements, as every branch is connected with only two nodes.

At the beginning of the MNA algorithm, one node has to be denoted by the common node or ground, this node becomes the index 0. Then, we introduce the *nodal voltages* calculated as the potentials with respect to the ground and denoted $U_{n,0}$, $n = \overline{1, N}$. The branch voltages are related to the nodal ones as follows:

$$\mathbf{U} = \mathbb{A}^T \mathbf{U}_n, \quad (2.1)$$

where \mathbf{U} and \mathbf{U}_n are vectors with branch and nodal voltages. Further, the branches have to be rearranged in the following three groups:

1. The branches, which have an admittance representation (finite admittance, e.g., the circuit in Fig. 2.1a) and branches, whose currents do not need to be calculated. The currents and voltages of these branches are assembled in vectors \mathbf{I}_1 and \mathbf{U}_1 , respectively. The relations between currents and voltages are:

$$\mathbf{I}_1 = \mathbb{Y}_1 \mathbf{U}_1, \quad (2.2)$$

where \mathbb{Y}_1 is the diagonal matrix with branch admittances.

2. The branches without an admittance representation except for the independent current sources (see, e.g., Fig. 2.1b) and branches, whose currents have to be computed. These currents and voltages are assembled in \mathbf{I}_2 and \mathbf{U}_2 , respectively. The constitutive relations for these branches may be formulated as following matrix equation:

$$\mathbb{Y}_2 \mathbf{U}_2 + \mathbb{Z}_2 \mathbf{I}_2 = \mathbf{W}_2, \quad (2.3)$$

3. The branches with independent current sources (see Fig. 2.1c), whose voltages and currents are assembled in \mathbf{U}_3 \mathbf{J}_3 , respectively.

With respect to these three groups of branches, the incidence matrix is sorted and partitioned into three blocks:

$$\mathbb{A} = [\mathbb{A}_1 \ \mathbb{A}_2 \ \mathbb{A}_3]. \quad (2.4)$$

The solution for all unknown branch currents and voltages of the network is calculated by the solution of the algebraic equation system, which is presented below in matrix form:

$$\mathbb{S} \begin{bmatrix} \mathbf{U}_n \\ \mathbf{I}_2 \end{bmatrix} = \mathbf{R}, \quad \mathbb{S} = \begin{bmatrix} \mathbb{Y}_n & \mathbb{A}_2 \\ \mathbb{Y}_2 \ \mathbb{A}_2^T & \mathbb{Z}_2 \end{bmatrix}, \quad \mathbf{R} = \begin{bmatrix} \mathbf{J}_n \\ \mathbf{W}_2 \end{bmatrix}, \quad (2.5)$$

where

$$\mathbb{Y}_n = \mathbb{A}_1 \mathbb{Y}_1 \mathbb{A}_1^T \quad (2.6)$$

is the nodal admittance matrix and

$$\mathbf{J}_n = -\mathbb{A}_3 \mathbf{J}_3 \quad (2.7)$$

is the nodal current-source vector. \mathbb{S} is called *system matrix*, \mathbf{R} is called *right-hand-side (RHS) vector*. Obviously, the vector of unknowns in the matrix equation (2.5) consists of all nodal voltages \mathbf{U}_n and, additionally, the currents in branches of the second group \mathbf{I}_2 . The remaining branch currents and voltages may be calculated using the solution of (2.5):

$$\begin{aligned} \mathbf{U}_1 &= \mathbb{A}_1^T \mathbf{U}_n, & \mathbf{I}_1 &= \mathbb{Y}_1 \mathbf{U}_1, \\ \mathbf{U}_2 &= \mathbb{A}_2^T \mathbf{U}_n, & \mathbf{U}_3 &= \mathbb{A}_3^T \mathbf{U}_n. \end{aligned} \quad (2.8)$$

2.1.2 MNA formulation by inspection

The MNA algorithm presented in § 2.1.1 has a significant disadvantage. The calculation of the system-matrix elements in (2.5) involves several auxiliary matrices, which are large and sparse. Alternatively, the MNA matrix equation (2.5) may be set up using the MNA formulation by inspection, which avoids these auxiliary matrix operations. This algorithm provides two main steps for the set up of (2.5).

1. The first inspection of the branches list provides the same partitioning and sorting of the branches as in § 2.1.1, while the auxiliary matrices are not allocated. The size of the system matrix is determined, the system matrix and right-hand-side vector in (2.5) are initialized as zero.
2. The list of branches is inspected a second time. For each branch in the list, the system matrix and the right-hand-side vector are augmented by the contributions of this branch using the so-called *MNA-stamp* associated with the branch type.

Since all matrix multiplications used in § 2.1.1 involve only the topological matrices, they introduce only the superposition of contributions from different branches. This makes possible consequential filling the system matrix and the right-hand-side vector.

The applications of the MNA method for the DC and AC circuit simulation do not differ significantly, as opposed to the transient analysis introduced in § 2.2. In the following, we consider the MNA formulation for the frequency-domain simulation and explain the MNA-stamps in three examples with branches, which belong to each of the three aforementioned groups. The first one is the complex impedance connected between nodes n_1 and n_2 as shown in Fig. 2.1a. The branch-current direction is assumed from n_1 to n_2 . This branch may represent a resistance $Z(j\omega) = R$, an inductance $Z(j\omega) = j\omega L$ or a capacitance $Z(j\omega) = 1/j\omega C$. The constitutive relation for this element according to (2.2) is $(U_{n_1,0} - U_{n_2,0})/Z(j\omega) = I$. Assuming the absence of all other branches and applying (2.6) and (2.7), one obtains the zero RHS vector and the system matrix with only four nonzero elements: $S_{n_1,n_1} = S_{n_2,n_2} =$

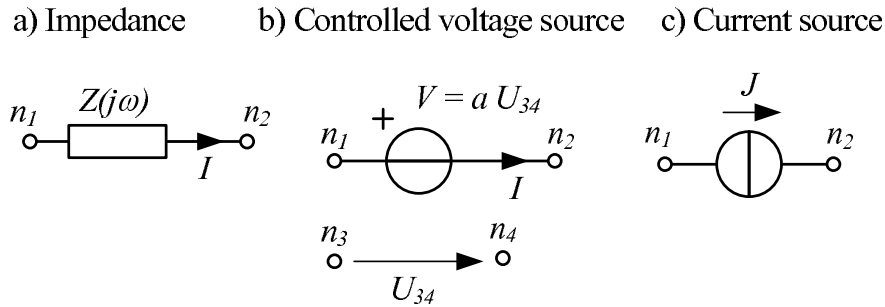


Figure 2.1: Circuit branches from three groups (a), (b), and (c).

$1/Z(j\omega)$ and $S_{n_1, n_2} = S_{n_2, n_1} = -1/Z(j\omega)$. This may be written in the compact form of a MNA-stamp as:

	n_1	n_2	RHS
n_1	$1/Z(j\omega)$	$-1/Z(j\omega)$	
n_2	$-1/Z(j\omega)$	$1/Z(j\omega)$	

The first row and column of the stamp provides the indexes of columns and rows of \mathbb{S} and corresponding rows of \mathbf{R} , where the contributions from this branch are added.

The second example is the voltage controlled voltage source (VCVS), which belongs to the second group of branches, shown in Fig. 2.1b. The voltage between the nodes n_1 and n_2 is calculated as the voltage between other two nodes n_3 and n_4 multiplied by the factor a : $U_{n_1,0} - U_{n_2,0} = a (U_{n_3,0} - U_{n_4,0})$, which is the constitutive relation for this branch. Since the voltage source has no finite admittance, its current is included in the vector \mathbf{I}_2 as an additional variable. We suppose that the index of this current in the total vector of unknowns is i . The MNA-stamp related to the five used unknowns is presented below:

	n_1	n_2	n_3	n_4	i	RHS
n_1					1	
n_2					-1	
n_3						
n_4						
i	1	-1	-a	a		

One may notice that the stamp contribution in the row i provides the constitutive relation of the branch, while ± 1 in the rows n_1 and n_2 are the contributions of the VCVS current in the Kirchhoff's current law (KCL) equations in the nodes n_1 and n_2 .

The third example is the independent current source, which belongs to the third group of branches (see Fig. 2.1c). This branch does not introduce additional unknowns and makes a contribution in the RHS vector, which is calculated using (2.7):

	n_1	n_2	RHS
n_1			$-J$
n_2			J

In general, MNA-stamps are developed for all important classes of circuit elements (see, e.g., [156]). The consequential inspection of the branches and addition of the required MNA-stamps produces the equation system (2.5) simply for programming and efficiently with respect to the run time.

2.2 Time-domain simulation of linear circuits

The simulation of arbitrary circuits in the time domain is an important issue in the network theory discussed in many books. This section considers the modeling of only linear circuits because the equivalent-circuit models developed in this monograph for passive interconnections are realized with only linear elements. The approach presented here is applied in usual network simulators for modeling the linear part of the network. Thus, the information given by this chapter is enough for the implementation of the PEEC model in a non-linear network simulator, e.g., in SPICE.

Since the time-domain constitutional relations for branches may consist time derivatives and integrals, the general formulation methods result in differential equation systems. This equation system may be solved in the state variable form [156], but this possibility is not used in the SPICE-like codes, since the description of an arbitrary network in the canonical state-variable form is algorithmically sophisticated. Thus, the state-variable approach needs a complex preprocessing step before the numerical solution of the differential equation system. Another approach is used in SPICE as well as in NEAN, it is based on the concept of so-called *associated discrete circuits* (ADC) (see [33]) also known as *companion circuits* (see [156]). The study of this approach requires a short summary about the methods of the numerical integration given below.

2.2.1 Numerical integration of differential equations

An *initial value problem* (IVP) for an ordinary differential equation system is considered. Its canonical formulation of the ODE system is

$$\dot{\mathbf{x}} = \mathbf{f}(\mathbf{x}, t), \quad \mathbf{x}(t_0) = \mathbf{x}_0, \quad (2.9)$$

where $\mathbf{x}(t)$ is an unknown vector function of time, $\mathbf{f}(\mathbf{x}, t)$ is a vector function, $\mathbf{x}(t_0) = \mathbf{x}_0$ is the initial value, i.e., the value of $\mathbf{x}(t)$ at the initial time t_0 . In order to obtain a numerical solution, the continuous time axis may be replaced by a set of discrete points t_n , $n = \overline{0, \infty}$. For simplification, we apply the uniform discretization and define the discrete time points as $t_n = n \Delta t$. The numerical solution provides the values of $\mathbf{x}(t)$ at points t_n denoted by \mathbf{x}_n , i.e., $\mathbf{x}_n = \mathbf{x}(t_n)$.

In general, the approximated solution for (2.9) may be calculated using the *difference quotients* or *numerical integration*. The numerical integration may be applied to the integral

equation, which is equivalent to (2.9):

$$\mathbf{x}(t) = \mathbf{x}(t_0) + \int_{t_0}^t \mathbf{f}(\mathbf{x}, \tau) d\tau. \quad (2.10)$$

The setting $t_0 = t_n$ and $t = t_{n+1}$ leads to

$$\mathbf{x}_{n+1} = \mathbf{x}_n + \int_{t_n}^{t_{n+1}} \mathbf{f}(\mathbf{x}, \tau) d\tau. \quad (2.11)$$

Since the step of the discretization is short, the integral in (2.11) can be interpolated by polynomials of power k . One may derive for (2.11):

$$\mathbf{x}_{n+1} = \mathbf{x}_n + \Delta t \sum_{i=0}^k a_i \mathbf{f}_{n+1-k} \quad \text{with } \mathbf{f}_{n+1-k} = \mathbf{f}(\mathbf{x}_{n+1-k}, t_{n+1-k}). \quad (2.12)$$

The general formulation (2.12) provides the family of k -step *Adams methods* [95]. The *local truncation error* resulted by the numerical integration rule is proportional to $C_{p+1} \Delta t^{p+1}$, where p is the *order of the method* and C_{p+1} is the *error constant*. The most wide-spread Adams method is also known as the method of trapezoids:

$$\mathbf{x}_{n+1} = \mathbf{x}_n + \frac{\Delta t}{2} (\mathbf{f}_{n+1} + \mathbf{f}_n). \quad (2.13)$$

The order of the method of trapezoids is 2, the error constant is $-1/12$ (see, e.g., [156]). Alternatively to Adams methods, the family of the backward differentiation (BD) formulas [95] also known as the Gear's methods [33] may be derived using the interpolation of the derivative in (2.9). The k -step BD formulas are expressed as

$$\sum_{i=0}^k a_i \mathbf{x}_{n+1-k} = \Delta t b_0 \mathbf{f}_{n+1}. \quad (2.14)$$

The Berkeley SPICE 3f4 applies the method of trapezoids and the BD formulas with the variable order. Another solver developed by the author (NEAN) is based on the 2-step backward differentiation formula (BD2):

$$\mathbf{x}_{n+1} - \frac{4}{3} \mathbf{x}_n + \frac{1}{3} \mathbf{x}_{n-1} = \frac{2}{3} \Delta t \mathbf{f}_{n+1}, \quad (2.15)$$

which choice is explained in § 4.3. The order of BD2 is 2, the error constant is $-2/9$ (see [95]).

Of course, the mentioned-above simple numerical integration rules cannot be considered as the complete summary of the numerical integration of differential equations. The families of Taylor methods (see, e.g., [33]), predictor-corrector methods (see, e.g., [33]), Runge-Kutta

methods (see, e.g., [95]), etc. are omitted in this monograph as have not been applied. We consider here only the basic theory necessary for understanding the next chapters.

In the following, some important definitions related to the methods of the numerical integration are introduced. As this definitions in a rigorous mathematical form require a large number of auxiliary theory, which can essentially inflate this monograph, the definitions given here are more heuristic than rigorous. The proofs are omitted.

The numerical method, which provides an exact solution for any ODEs satisfying the Lipschitz condition [95] with an infinitesimal step of discretization, is called *consistent*.

The numerical method is called *A-stable* if it shows a stable solution using an arbitrary step of discretization for an arbitrary linear ODE system, whose exact solution is stable. A numerical rule, which is A-stable and consistent, guarantees the convergence of the numerical solution to the exact one if the discretization step is small enough. The method of trapezoids and BD2 are A-stable and consistent in contrast to the most of other approaches that explains their wide application. E.g., SPICE applies the method of trapezoids for the most of circuits, as it is simple effective and produce a stable and precise solution if the time step is small enough. However, SPICE applies also the BD methods. It is motivated by a special class of problems, whose calculation using the method of trapezoids leads to a correct solution, but the time step has to be chosen extremely short with respect to the simulation time. Thus, the total number of time steps is huge. The class of problems causing this phenomenon are called *stiff* problems.

The correct solution of stiff problems by the numerical methods is a hard and important problem studied in the literature, e.g., see [87], [88]. A simplified definition of the stiffness can be formulated for an ODE system with constant coefficients. The ratio between the largest and the smallest real-part magnitude of the ODE eigenvalues is called the *stiffness ratio*. The system is stiff if the stiffness ratio is much larger than 1, i.e., the ODE system yields the fast and slow transients in the same solution. In electromagnetics, such problems are denoted also as *multiscale problems*.

The numerical method is called *L-stable* if

1. it is A-stable and
2. it is *stiffly stable*, i.e., this method applied to the test equation $\dot{x}(t) = \lambda x(t)$, where λ is a complex constant with $\Re\{\lambda\} < 0$, yields a zero solution as $(\Re\{\lambda\} \Delta t) \rightarrow -\infty$.

The condition $(\Re\{\lambda\} \Delta t) \rightarrow -\infty$ matters that the time step is large as compared to the short time constant $\tau = -1/\Re\{\lambda\}$. Thus, a multiscale problem may be solved with a small time step (the solution for fast and slow transients is inefficient) or with a large time step (the fast and correct solution only for the slow transients, while the fast transients are excluded).

The group of the backward differentiation formulas are stiffly stable, while BD1 (also known as the backward Euler method) and BD2 are L-stable. Hence, SPICE applies the backward differentiation formulas as well as the NEAN code.

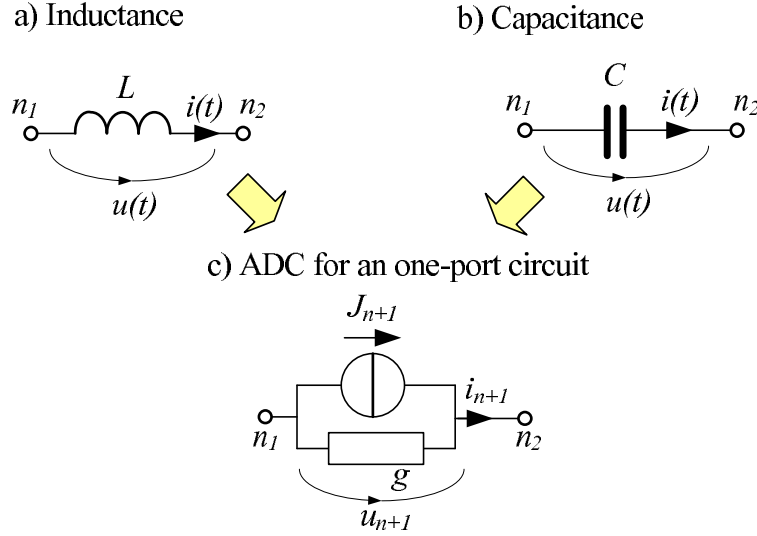


Figure 2.2: An inductance (a), a capacitance (b), and their associated discrete circuit (c).

2.2.2 Associated discrete circuits for the time-domain analysis

After the short summary devoted to the methods of the numerical integration, the ADC models may be studied. Since ADCs are developed using a numerical method, a particular numerical rule has to be chosen. In the following, we apply BD2, as it is used for programming the ADC models in the NEAN code.

The concept of the associated discrete circuits may be well explained by examples of the inductance and capacitance included between nodes n_1 and n_2 as shown in Fig. 2.2. The constitutive relation for the inductance is

$$\frac{d}{dt}i(t) = \frac{1}{L} u(t). \quad (2.16)$$

The time axis is assumed to be discretized with a constant step Δt . The voltage and current at the discrete points are denoted by $i_n = i(t_n)$ and $u_n = u(t_n)$ as in the previous section. Application of the BD2 rule (2.15) to (2.16) leads to

$$i_{n+1} - \frac{4}{3}i_n + \frac{1}{3}i_{n-1} = \frac{2\Delta t}{3L} u_{n+1}.$$

This equation may be rewritten in the following form:

$$i_{n+1} = g u_{n+1} + J_{n+1} \quad \text{with} \quad g = \frac{2\Delta t}{3L} \quad \text{and} \quad J_{n+1} = \frac{4}{3}i_n - \frac{1}{3}i_{n-1}. \quad (2.17)$$

where g is an equivalent ohmic admittance and J_{n+1} is the independent current source, whose value is calculated using the inductance current at two previous time points. Consequently, the shown in Fig. 2.2a inductance between the nodes n_1 and n_2 at the time point t_{n+1} may be represented with the circuit shown in Fig. 2.2c. Considering (2.17), one may observe that the parameters of the ADC depend on Δt and the numerical rule used. The equivalent

admittance does not change if the time step is constant, while J_{n+1} has to be calculated at each new time point. The presented here ADC for the inductance is a Norton generator, of course, it may be equivalently transformed into a Thevenin-generator form, which is less suitable for the NMA formulation and not considered here.

The analogous derivation may be applied to the capacitance in Fig. 2.2b, whose constitutive relation is

$$\frac{d}{dt}u(t) = \frac{1}{C} i(t). \quad (2.18)$$

The application of the BD2 rule (2.15) to (2.18) yields:

$$i_{n+1} = g u_{n+1} + J_{n+1} \quad \text{with} \quad g = \frac{3C}{2\Delta t} \quad \text{and} \quad J_{n+1} = -g \left(\frac{4}{3}u_n - \frac{1}{3}u_{n-1} \right). \quad (2.19)$$

This equation may be interpreted as the same Norton generator (see Fig. 2.2c) as for the inductance, whose parameters are calculated by another expressions given in (2.19).

Since the ADC for an one-port circuit in the Norton-generator form consists of only the ohmic admittance and the independent current source, it is very suitable for the description using the MNA formulation studied in § 2.1.2. The MNA-stamp for an one-port ADC circuit is very simple.

	n_1	n_2	RHS
n_1	g	$-g$	$-J_{n+1}$
n_2	$-g$	g	J_{n+1}

Thus, the transient analysis of linear circuits does need to set up the differential equation system. Instead, the parameters of the associated discrete circuits are calculated at each discrete time point. The MNA formulation set up at a time point is an algebraic equation system, which may be solved. This yields a consequential solution at discrete time points, which is equivalent to the numerical integration.

This monograph does not consider a large number of questions related to the error estimation, the choice of the time step, taking into account non-linear circuits, and the possibility for using a predictor/corrector numerical method. These topics can be read in the references [33] and [156], while this section gives only the theory required for the development of the time-domain models for passive interconnection structures in § 4.3, § 4.5, and § 5.4.

Chapter 3

Computational methods in electrodynamics

The main subject of this monograph is the accurate electromagnetic modeling of passive interconnection structures, whose dynamics are governed by Maxwell's equations (1.1). The direct closed-form solution for electromagnetic problems exists only in a few simple cases, while in general case, only an approximate solution can be obtained. The electrodynamic problem is formulated as a partial differential equation system (1.1) completed with boundary conditions, i.e., it is a boundary-value problem. The computational methods, which may be applied to solution of the boundary-value problems, are classified as *analytical*, *semi-analytical*, and *numerical*.

The analytical techniques allow one to derive a closed-form solution, which may be calculated explicitly with minor computational efforts. Usually, the application of analytical techniques is possible only under strict assumptions and for very simple structures. As an example of analytical techniques, one can consider the *separation of variables* (see, e.g., [136]) that gives the closed-form solutions for some particular problems.

In contrast, the pure numerical methods (also known as *differential methods*) involve no analytical solutions for electromagnetic problems, instead, the volume is divided into a number of grid cells that allows one to approximate the PDE at local cell volumes. The differential methods lead to a large number of algebraic equations for three-dimensional problems, since the number of discretization cells is proportional to the ratio between the volume of the solution region and the third power of the wave length of the excitation. However, they may be simply applied to the simulation of problems in anisotropic non-uniform and non-linear media, which is possible if assuming the medium isotropic uniform and piecewise linear locally at discretization cells. The short summary of the differential methods in application to the simulation of interconnections is presented in § 3.2.

The semi-analytical methods provide an implicit analytical solution for the initial boundary-value problem that can be solved numerically involving a significantly lower number of unknowns as compared to differential methods. The most significant family of semi-analytical methods in electrodynamics are based on the numerical solutions of integral equations derived

from Maxwell's equations. These methods are referenced as *integral equation techniques*. For example, this work uses the electric-field integral equation (1.56) and the mixed-potential integral equation (1.65), whose numerical solutions may be achieved by the method of moments explained in § 3.3 (see also [60], [19], [140]) and the partial element equivalent circuit method discussed in § 3.5 and thoroughly explained in Chapter 4. Since the two aforementioned methods as well as some other methods are based on the weighed residual method, their fundamentals are introduced in § 3.1 in order to simplify the understanding of the following sections.

The methods based on Maxwell's equations and on the field integral equations are also classified as the *full-wave* methods. This means that they do not introduce some principle assumptions with respect to the wave-propagation modes. The full-wave methods take into account the radiation of electromagnetic energy and are correct at any frequency if the discretization is precise enough. In contrast, the numerical methods based on the transmission-line equations account for only TEM-wave propagation and may be applied only in a limited frequency range. However, these methods are often applied, as they are very simple and efficient. A short comparative review of the transmission-line based methods as well as the *generalized transmission-line models* is given in § 3.4.

Another alternative for the analysis of passive interconnection structures is discussed in § 3.6. This is the behavioral modeling of linear systems, which is also referenced in the literature as *macromodeling* (e.g., in [114]), *model order reduction* (e.g., in [113]) or *black-box modeling* as the general notation for linear and non-linear devices in electrical engineering. The main idea here is the precise full-wave description of the linear interconnection structure using one of the aforementioned direct approaches, whose result is used to set up a low-order time-domain *macromodel*. This macromodel does not represent the internal structure of the interconnections, but instead models their behavior from the out side as a "black-box". A separation of a complex system into a number of such macromodels allows one to analyze a problem that needs too much computation effort for the direct solution.

3.1 Weighted residual method

The method of weighted residuals is an important fundamental mathematical technique used for the approximate solution of boundary-value problems written in the canonical linear-operator form. As partial differential and integral equations of classical electrodynamics can be represented in this form, the majority of computational methods apply the principles of the weighted residual method in their base [91], [136]. E.g., finite element method (FEM), boundary element method (BEM), method of moments, and the PEEC method are derived from the method of weighted residuals. This section introduces the general abstract formulation of the weighted residual method, used further for the derivation of particular numerical approaches, and presents the relations between the above-listed methods.

Let the boundary-value problem be formulated in a linear-operator form as in (1.28):

$$\begin{aligned}\mathfrak{L}\{f(x)\} &= g(x), & x \in V, \\ f(x) &= \alpha(x), \quad \frac{\partial f(x)}{\partial n} = \beta(x), & x \in \partial V,\end{aligned}\tag{3.1}$$

where V is the solution region, $\alpha(x)$ and $\beta(x)$ are Dirichlet and Neumann boundary conditions. The method of weighted residuals proposes the following approximated solution of (3.1):

$$\tilde{f}(x) = \sum_{k=1}^N a_k b_k(x),\tag{3.2}$$

where $b_k(x)$ and a_k are called *basis functions* (BF) and *expansion coefficients*, respectively. The choice of the predefined basis functions governs the below given modification of the weighted residual method. The expansion coefficients are unknown. Thus, the numerical solution is obtained if the expansion coefficients are calculated. The method of weighted residuals does it as follows. As $\tilde{f}(x)$ has to satisfy the given boundary conditions and to approximate $f(x)$ with a finite precision, the substitution of $\tilde{f}(x)$ in (3.1) results in a residual error in all points of the solution region:

$$R(x) = \mathfrak{L}\{\tilde{f}(x)\} - g(x).\tag{3.3}$$

We obtain N algebraic equations through an inner product of $R(x)$ and N *weighting functions*:

$$\langle w_m(x), R(x) \rangle_V = 0, \quad m \in \overline{1, N}.\tag{3.4}$$

Eq. (3.4) demands that the weighted summary residual error of the approximation is equal to zero. The substitution (3.2) in (3.4) results in the general formulation of the method:

$$\sum_{k=1}^N a_k \langle w_m(x), \mathfrak{L}\{b_k(x)\} \rangle_V = \langle w_m(x), g(x) \rangle_V, \quad m \in \overline{1, N}.\tag{3.5}$$

Since the inner products of known functions in (3.5) result in scalar values, (3.5) yields an algebraic equation system with respect to the unknown expansion coefficients. Because (3.5) applies inner products of functions, the both basis and weighting functions belong to a functional space with an inner product defined as follows

$$\langle w(x), b(x) \rangle_V = \int_V w(x)b(x)dx.\tag{3.6}$$

The weighted residual method has several important modifications related to the weighting and basis functions. The methods used in this book require considering three wide-spread techniques: *collocation*, *subdomain*, and *Galerkin's* approaches.

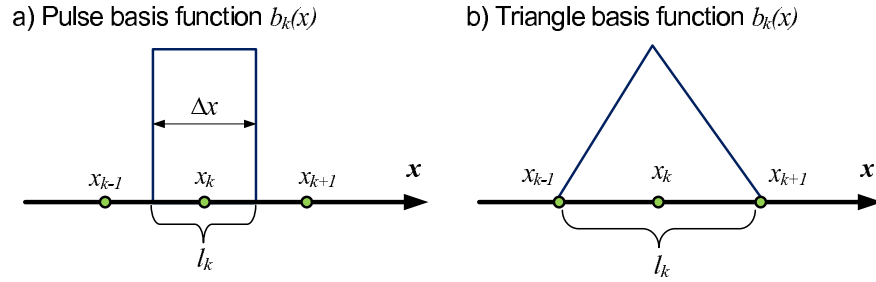


Figure 3.1: One-dimensional basis functions.

The main idea of the subdomain approach consists in the application of only *local basis and weighting functions*, i.e., the functions, which are non zero over a small subregion of the solution region. Practically, this approach results in a piecewise approximation of the solution through the basis functions over their definition areas. This leads to a significant acceleration of the procedure for calculation of the inner product integrals in (3.4). The local basis functions are invariant with regard to the geometry of the solution region and to the boundary conditions, while *global basis* functions defined over the total solution region are suitable only for some particular problems.

As the local basis functions are defined with regard to some local subregions, they have to be related to a *discretization grid*. The grid consists of *grid nodes* and *grid segments*. Usually, the grid nodes are located in geometrical centers of subregions, and the grid segments are subregions between the grid nodes.

The numerical models developed in this book involve four of one-dimensional basis and weighting functions. If the solution region (denoted by l) is one-dimensional, we assume it as a line in three-dimensional space with a local coordinate x . The *pulse or rectangular basis function* (see Fig. 3.1a) is defined as follows:

$$b_k(x) = \begin{cases} 1, & x \in l_k \\ 0, & x \notin l_k \end{cases}, \quad (3.7)$$

where Δx is the length of the grid segment. The function (3.7) differs from zero only in the subregion l_k of the solution region defined as $l_k = \{x \mid x_k - \Delta x/2 < x < x_k + \Delta x/2\}$. Obviously, the application of the pulse basis functions leads to a staircase approximation of $f(x)$, i.e., we obtain a discontinuous and not differentiable solution of the problem.

The *triangular basis function* (see Fig. 3.1b) can be defined as follows:

$$b_k(x) = \begin{cases} \frac{\Delta x - |x - x_k|}{\Delta x}, & x \in l_k \\ 0, & x \notin l_k \end{cases}. \quad (3.8)$$

The subregion of a triangular BF consists of two grid segments, which are adjacent to the grid node associated with the basis function. The triangle basis functions yield a piecewise (i.e., not smooth but differentiable) approximation of the solution.

A special type of global basis function, defined as

$$b_k(x) = \frac{a^2}{(a^2 + x^2)^{3/2}} \quad (3.9)$$

with a nonzero constant a , is used in § 5.4. This function has been proposed in [49] for the approximation of the Green's functions for microstrips.

The next kind of local weighting function defines a special modification of the weighted residual method, namely, the collocation approach. The definition of the weighting functions by the Dirac function

$$w_m(x) = \delta(x - x_m) \quad (3.10)$$

leads to an essential simplification of the method. Using the properties of the weighting function, one can simplify (3.5) to the formulation of the collocation approach:

$$\sum_{k=1}^N a_k \mathfrak{L}\{b_k(x_m)\} = g(x_m), \quad m \in \overline{1, N}. \quad (3.11)$$

These equations guarantee the correct approximation at grid nodes. However, the collocation approach can be very inaccurate at points beyond the grid nodes. However, the simplicity of this approach makes its usage reasonable in some cases. The collocation method is especially useful in the *least-square* modification of the weighted residual method, i.e., if the number of weighting functions exceeds the number of basis functions. The resulted non-square system of algebraic equations (3.11) may be solved by the least-square algorithm [62]. This is more exact than the simple collocation approach, but is simpler than the general formulation (3.5).

The method of weighted residuals with the same basis and weighting functions is called the Galerkin's approach. The Galerkin's approach is considered here only with regard to the PEEC method, which can be derived purely on its base.

It has been already mentioned that the most of direct full-wave numerical methods used in electrodynamics are derived on the basis of the weighted residual method. They differ only in the modification of weighted residual method, and in the linear operator in (3.1), i.e., in the initial mathematical model. The general classification of the most wide-spread universal approaches using the principles of the weighted residual method is shown in Fig. 3.2.

Often, the method of moments is used as a synonym for the weighted residual technique. However, in computational electromagnetics, one understands under MoM the weighted residual technique applied to the EFIE (1.56) or the MPIE (1.65) as it was introduced in [60]. The method of moments may use different types of the subdomain basis and weighting functions, which are considered in [36], [61], and [91].

The PEEC method [129] is derived through the application of the Galerkin's approach with pulse basis functions to the MPIE. As the PEEC method produces an equivalent circuit, the choice of the basis functions is limited, and the EFIE cannot be used. However, its characteristics are very similar to the method of moments because the mathematical model in both cases is the same.

The most wide-spread differential method is the finite element method based on the second order PDEs. Laplace or Poisson equations can be the mathematical models for FEM in electrostatics, the wave equation (1.13) in electrodynamic. There are two alternative derivations for the FEM formulation, the first is based on the calculus of variations, the second is based on the application of the Galerkin's approach with triangular (in 3D-space with tetrahedron) basis functions to the given differential equation [91].

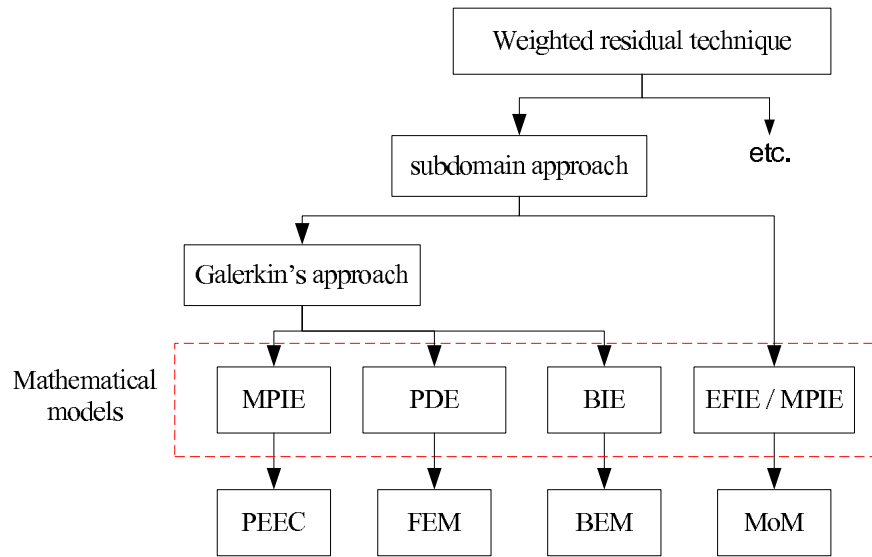


Figure 3.2: Numerical methods in electrodynamics based on the weighted residual method.

An application of the Galerkin's approach with triangular basis functions to the boundary integral equation leads to the boundary element method [25], [34], and [30]. In contrast to FEM, BEM requires the discretization only of boundaries between the uniform subdomains of the solution region.

3.2 Differential methods

Finite difference method

The Finite difference method derived from Maxwell's equations in differential form, which are locally approximated using a difference quotients (usually the central difference formula). The most important modification of the finite difference method in electromagnetics is named finite difference time domain (FDTD) method. It has been introduced by Kane Yee [163] in 1966. The approximation of curl operators in Maxwell's equations via the central difference formula requires introduction of two discretization grids that are used for the calculation of electric and magnetic field intensities [24], [93], [139]. Initially, these grids were only orthogonal and uniform, the more advanced modifications of the FDTD method [136], [144] apply non-orthogonal and nonuniform grids.

The grid step used for the spatial discretization has to be chosen according to the following criterion:

$$\Delta l \leq \frac{\lambda_m}{20}, \quad (3.12)$$

where λ_m is the wavelength related to the maximum frequency of interest. Thus, Δl is defined by the excitation, which can have only a limited spectrum. The second factor, which may influence Δl is the inhomogeneity of the medium. Hence, Δl has to be chosen small

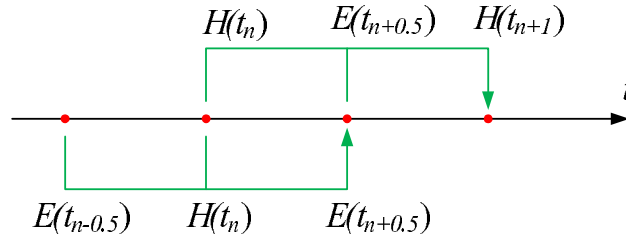


Figure 3.3: The "leap-frog" scheme.

enough, in order to make it possible the assumption that the medium is locally homogeneous in elementary volumes with a side Δl . The FDTD method models the time dependence using the efficient "leap-frog" scheme (see Fig. 3.3). The time derivations in Maxwell's equations are approximated with the central difference formula. This shifts the time axes for the electric and magnetic fields by a half of the time step. As shown in Fig. 3.3, the electric field intensity at a new time point $E(t_{n+0.5})$ is calculated using the already known values $E(t_{n-0.5})$ and $H(t_n)$, while the magnetic field at the new time point $H(t_{n+1})$ is calculated using the already calculated values $E(t_{n+0.5})$ and $H(t_n)$. This scheme is completely explicit, consequently, the FDTD method does not need to solve a system of algebraic equations at each time step, but needs to calculate only explicit formulas. In addition, the stability of this explicit algorithm is guaranteed by the Courant criterion:

$$\Delta t \leq \frac{\Delta l}{v_{max}}, \quad \Delta l = \frac{1}{\sqrt{\frac{1}{\Delta x_{min}^2} + \frac{1}{\Delta y_{min}^2} + \frac{1}{\Delta z_{min}^2}}}, \quad (3.13)$$

where v_{max} is the maximum propagation velocity, x_{min} , y_{min} , and z_{min} are minimal spatial grid steps.

Finite integration technique

The finite integration technique (FIT) is a further generalization of the FDTD method developed by Weiland [158] in 1977. As well as the FDTD method, the FIT is based on Maxwell's equations but, in contrast to FDTD, Maxwell's equations are in integral form [107], [155]. It holds all advantages of the FDTD method, i.e., simplicity, more sparse matrices as compared to FEM, and the efficient explicit time-domain algorithm. At the same time, it possesses one additional advantage. FIT is a consistent numerical method (see [155]), in contrast to FDTD. This means that the FIT formulation satisfies the curl Maxwell's equations in integral form exactly.

Since the characteristics of the FDTD and FIT methods are similar, we classify these approaches conjointly. Their advantages are

- very efficient explicit time-domain algorithm,
- trivial consideration of anisotropic non-uniform and non-linear media,

- inclusion of simple lumped circuit elements [144].

The main disadvantage of the FDTD and FIT methods in the past is that there were only orthogonal grids, while non-orthogonal ones developed in [144] were difficult to implement. This was a disadvantage for the solution of problems with essentially non-orthogonal geometries as compared to the finite element method, which is based on the tetrahedron grid. However, recently, the so-called *perfect boundary condition* (PBC) was developed for the FDTD in [126] and for the FIT in [115]. PBCs make it possible to model the smooth boundaries that cross the orthogonal grid cells. Thus, the modern commercial codes apply the simple orthogonal grids and take into account the non-orthogonal boundaries on these grid precisely.

The number of unknowns used in the FDTD method is large, it can be estimated as a value proportional to $V/\Delta l^3$ and can be huge. Fortunately, the matrix formulation of the FIT method involves huge but sparse matrices and is very efficient as compared to other differential methods.

Finite element method

The finite element method is the most wide-spread numerical method for the solution of boundary-value problems. As mentioned in § 3.1, the FEM is based on the calculus of variations, but it may be alternatively formulated as an application of the weighted residual method to partial differential equations [91]. The finite element method expands the unknown functions using the local basis functions (usually linear basis functions). The typical discretization grid applied in the FEM is triangular, thus, the grid cells (so-called finite elements) are tetrahedrons, although quadrilateral grids may also be used. The most important advantage of the FEM is a very flexible non-uniform triangular grid, which allows one to analyze non-uniform objects and change the grid step smoothly. The numerical solution for the FEM is calculated via algebraic equation systems, whose system matrix is sparse as with other differential methods. The time-domain formulation of the FEM leads to an ODE system, whose explicit numerical solution can be instable. Thus, an implicit method of the numerical integration has to be applied. Therefore, the efficiency of a time-domain FEM model is lower than that of an equivalent FDTD/FIT model, which uses the efficient "leap-frog" scheme.

Differential methods: application area

The differential methods provide full-wave numerical solutions of Maxwell's equations, which are valid in the general electromagnetic problem with inhomogeneous and anisotropic medium. Of course, no other methods may be efficiently applied in this case. The applicability of the differential methods is limited only with the maximal number of unknowns, which can be saved in the computer memory. The ratio between the size of the solution region and the minimal wave length of the excitation cannot exceed several tenfold. Thus, the open problems can be solved by differential methods only by applying the open or PML

boundary conditions [144], the approach of which can be less efficient than the application of methods based on the integral equation techniques. The natural application area of the differential methods is the simulation of closed problems with an inhomogeneous medium.

3.3 Method of moments

The method of moments introduced by Harrington [60] is the most wide-spread alternative for full-wave modeling passive interconnections by the differential methods discussed in § 3.2. MoM is the classical weighted residual method (see § 3.1) applied to field integral equations, e.g., to the electric-field integral equation (1.56) or to the mixed-potential integral equation (1.65), which may be written in the linear-operator form as in (3.1). E.g., (1.56) for perfect conductors yields in the linear-operator form:

$$\begin{aligned} -\hat{\mathbf{n}} \times \hat{\mathbf{n}} \times \mathbf{E}^i(\mathbf{r}) &= \mathcal{L}\{\mathbf{J}_s(\mathbf{r})\}, \\ \mathcal{L}\{\mathbf{J}_s(\mathbf{r})\} &= -\hat{\mathbf{n}} \times \hat{\mathbf{n}} \times \iint_{S'} \overline{\overline{\mathbf{G}}}_J^E(\mathbf{r}, \mathbf{r}') \cdot \mathbf{J}_s(\mathbf{r}') dS'. \end{aligned} \quad (3.14)$$

At the beginning, the passive interconnection structure is divided into a number of segments, which may be one-dimensional for wires and two-dimensional, usually, triangle elements for surfaces. The geometrical sizes of these segments have to be electrically small, i.e., the discretization of interconnections is done with respect to the criterion (3.12) given for the differential methods. Since currents flow only on the conductor surface S , the current density is expanded with local basis functions associated with the segments according to (3.2). The usually applied basis functions for one-dimensional discretization are the pulse basis functions (3.7), the triangle functions (3.8), and the piecewise sinusoidal functions (see [36]), while the linear two-dimensional basis functions proposed by Glisson [51] are used for surfaces. An algebraic equation system is derived according to (3.5) in the following conventional form:

$$\begin{bmatrix} Z_{1,1} & Z_{1,2} & \cdots & Z_{1,N} \\ Z_{2,1} & Z_{2,2} & \cdots & Z_{2,N} \\ \cdots & \cdots & \cdots & \cdots \\ Z_{N,1} & Z_{N,2} & \cdots & Z_{N,N} \end{bmatrix} \begin{bmatrix} I_1 \\ I_2 \\ \cdots \\ I_N \end{bmatrix} = \begin{bmatrix} U_1 \\ U_2 \\ \cdots \\ U_N \end{bmatrix}, \quad (3.15)$$

where the expansion coefficients I_m are currents in the segments. In general, the constant matrix elements $Z_{k,m}$ have Ω units and are calculated as

$$Z_{k,m} = - \iint_S \iint_{S'} \mathbf{w}_k(\mathbf{r}) \cdot \hat{\mathbf{n}} \times \hat{\mathbf{n}} \times \overline{\overline{\mathbf{G}}}_J^E(\mathbf{r}, \mathbf{r}') \cdot \mathbf{b}_m(\mathbf{r}') dS' dS, \quad (3.16)$$

where $\mathbf{w}_k(\mathbf{r})$ and $\mathbf{b}_m(\mathbf{r}')$ are vector weighting and basis functions. The elements of the right-hand side vector are computed as

$$U_k = - \iint_S \mathbf{w}_k(\mathbf{r}) \cdot \hat{\mathbf{n}} \times \hat{\mathbf{n}} \times \mathbf{E}^i(\mathbf{r}) dS. \quad (3.17)$$

Obviously, the equation system (3.15) provides a full-wave solution of the problem with respect to surface currents on interconnections. The electric and magnetic field intensities in the total solution region can be calculated using this MoM solution in a post-processing step through (1.49). Thus, the main qualitative difference between the MoM and the differential methods is the discretization. While the differential methods divide the total space of the solution region, the MoM needs to discretize only conductors and, therefore, involves much fewer unknowns in the resulted equation system. However, the MoM system matrix in (3.15) is fully-filled, while the differential methods result in sparse system matrices. Hence, the run time of a MoM code increases as power three of the unknown number. This important disadvantage of the method of moments can be improved using the *multilevel fast-multipole method* (FMM), which has been introduced in [143] based on the fast-multipole method developed by Rokhlin [127]. The MoM models based on the multilevel fast-multipole technique produce sparse (but sometimes bad conditioned) matrices in contrast to the standard algorithm.

In summary, the method of moments has a more limited application area as compared to the differential methods. It may be applied only to problems that may be analyzed using field integral equations, i.e, in only linear media with several particular geometries: free-space, half-space, multilayer media, etc. As a rule, the method of moments is more efficient than the differential methods for the solution of open problems, since it takes into account the open solution region analytically, while differential methods discretize it. The method of moments may be applied to the solution of closed problems, but it can be inefficient in comparison to differential methods, in this case.

3.4 Numerical modeling of transmission lines

The general-purpose full-wave methods discussed above solve Maxwell's equations or integral equations in three-dimensional space, which can be computationally expensive. A large and wide-spread class of interconnections does not require so precise three-dimensional models and may be analyzed on the basis of simpler equations. At relatively low frequencies, transmission lines, twisted wires, cables, traces on PCB boards, etc. are governed by the transmission-line equations, whose simplest formulation for the two-wire transmission line is given in § 1.5. In general, the voltage and currents in the mentioned interconnections may have the *differential* and *common* modes. Usually, the differential modes (TEM waves) are fundamental propagation modes, while the common modes are parasitic and should be avoided. If the longitudinal dimension of the interconnection structure is electrically large and its transversal dimension is electrically small, one may assume the existence of only differential modes and describe it using the conventional transmission-line theory.

The finite difference method can be applied to the Telegrapher's equations (1.70) that depend on the time and a space coordinate [147]. The length of the transmission line is discretized with the grid step defined as in the FDTD method via (3.12) based on the maximum frequency of interest. Applying the difference quotients, one obtains a Π - or T -like equivalent-circuit model of the transmission line, which consists of inductances, capacitances,

and resistances. This approach has a benefit related to the simplicity of the inclusion into circuit-simulator codes and a drawback that is the inconsistency of the FDTD method. The practical consequence from this inconsistency is the distortion of the time-domain solution through high-frequency oscillations, which are the methodical error of this method. The frequency of these false oscillations is higher than the maximum frequency of interest and depends on the discretization step. Paul [121] has shown that the decrease of the discretization step cannot completely eliminate this error, while Korovkin and Selina [90] proved that introduction of high-order difference quotients at the ends of transmission lines allows one to avoid this drawback although the equivalent circuit becomes more complex.

The second wide-spread numerical method developed by Bergeron [21] is called Bergeron's method. The numerical method is based on the closed-form solution of the Telegrapher's equations for an infinite line [147]. Using the decomposition on *natural propagation modes*, the Bergeron's method may also be applied to multiconductor transmission lines. As with the equivalent circuits for transmission lines, the Bergeron's model is very simple for inclusion into a circuit-simulator code. The main advantage of the Bergeron's method is its consistency with the Telegrapher's equations and, thus, absence of false high-frequency oscillations.

In general, the numerical methods related to the transmission-line theory are very fast as compared to full-wave methods, but their application area is strictly limited to uniform transmission lines. They assume only traveling TEM-waves and, thus, cannot take into account several high-frequency phenomena associated with modern switching rates. The models based on the conventional transmission-line theory can not account for the radiation, the effect of a two dimensional current distribution, inhomogeneity of transmission lines, dielectric losses, etc. Consideration of these phenomena requires the application of more sophisticated models.

Models based on generalized transmission-line theories

The aforementioned drawbacks of transmission-line models prevent their use in many cases, even though, they seem to be very fast and suitable models. This encourages scientists in the development of so-called *generalized transmission-line* (GTL) theories. The generalization may be related to the expansion of the theory on non-uniform transmission-lines or to accounting for the electromagnetic-energy radiation. Applying the conformal mappings, Collin [34] has formulated a general transmission-line theory for non-uniform lines. The theory is very suitable for the modeling of cable systems with arbitrary geometry if the radiation is not significant. A model for finite-length transmission lines accounting for skin and radiation effects has been developed by Kochetov and Korovkin [71]. This approach provides Telegrapher-like equations derived from the mixed-potential integral equation (1.63). The radiation is considered via the frequency dependence of the per-unit-length inductance and capacitance of the line. A more advanced variant of the GTL theory has been developed by Haase and Nitsch [57]. This formulation known as *transmission-line super theory* is also based on the MPIE and accounts for the radiation effect as well as for the inhomogeneity of the transmission line.

Although the list of generalized transmission-line models presented above is not complete,

we may summarize the main characteristics of such models. The derivation of GTL models is sophisticated with respect to the conventional transmission-line model, but they do not require a solution of three-dimensional electromagnetic problems and, thus, are much more efficient than the full-wave methods. At the same time, the GTL models show results much more accurate than the conventional transmission-line models but less accurate than the integral equation based methods. For example, see the comparison between the transmission-line super theory and the full-wave PEEC method provided by Haase and Kochetov [56]. Despite this, the GTL models are forward-looking techniques, which are especially suitable for the modeling of curved cables, twisted wires, and other non-uniform transmission-line structures.

3.5 PEEC method: motivation and state of development

The partial element equivalent circuit (PEEC) method is one of the most wide-spread approaches for the time- and frequency-domain modeling of passive interconnection structures. It is derived from the mixed-potential integral equation (1.65) and may provide the full-wave and quasi-static models for arbitrary conducting structures as the method of moments. In general, the PEEC model has similar characteristics and the same application area as the method of moments. It is derived from the MPIE using the Galerkin's approach with pulse basis functions (3.7) analogous to MoM. In contrast to MoM, the PEEC method provides some additional derivation steps leading to an equivalent-circuit model, while MoM results in an algebraic equation system. This is the principle difference between the two methods. The PEEC model may be directly included in a circuit-simulator code. Thus, the simultaneous modeling of passive interconnection structures with the lumped active devices is possible, while MoM accounts for only very simple one-port lumped elements as resistances, inductances, capacitances.

The PEEC method has a number of merits and drawbacks, which are summarized below.

- The reasonable application area of the PEEC method (as well as the MoM) is limited by interconnections in either homogeneous or inhomogeneous media with specific features, e.g., a piecewise homogeneous layered medium that can be described using the MPIE (1.65). The PEEC modeling is possible for a completely non-uniform general medium, but involves the volume discretization of the solution region and, thus, is inefficient as compared to differential methods.
- The PEEC method provides the full-wave equivalent circuits in the time as well as in the frequency domain. These circuits may be included in commonly used circuit-simulator codes, e.g., in SPICE, which allows the direct connection of the circuit and electromagnetic levels of simulation.
- In contrast to transmission-line theory based models, the PEEC method is able to model arbitrary shaped wires, conducting surfaces discretized with orthogonal and non-orthogonal grids, traces and vias on PCB boards, and antennas.

- The efficiency of the PEEC method is slightly lower than that of an equivalent MoM model because PEEC introduces more unknowns than MoM.

State-of-the-art in the PEEC method

In 1974, A. E. Ruehli published in [129] the concept of a novel numerical approach for analysis of interconnections in integrated circuits, which was named the partial element equivalent circuit method. Until now, this fundamental concept has served as the basis for all further improvements and modifications of the method. This original formulation is referenced in this monograph as the standard full-wave PEEC method and is explained in § 4.2. In the following, we systematically classify the further extensions and modifications of the PEEC method.

Dielectrics in the PEEC method

Ruehli and Heeb [132] have introduced an extension of the PEEC method for the considering of arbitrary finite inhomogeneous dielectric media. This approach applies the *volume equivalence principle* (see, e.g., in [18]). Its key idea is the three-dimensional discretization of dielectrics with $\epsilon_r > 1$ into so-called *dielectric cells* and the calculation of the displacement current in these cells. This allows one to apply a free-space PEEC model with a large number of additional variables. The further extension of this approach on lossy dielectrics has been added by Garrett and Ruehli [46], while the thorough explanation is given in the PhD thesis of Garrett [45].

Recently, a novel concept for the modeling of dielectric substrates in PCB boards with the PEEC method was developed by Kochetov, Wollenberg, and Leone [82], [74], [72], [73], and [75]. This concept is based on the generalization of the PEEC method on the MPIE with dyadic Green's functions for the vector magnetic and scalar electric potentials. In contrast to the approach based on the volume equivalence principle, the novel formulation does not require the volume discretization of the dielectric, instead the Green's functions account for it. Thus, the additional variables for the displacement current are not necessary. Hence, all advantages of the PEEC method are preserved, and the substrate is taken into account in closed-form. In this monograph, § 5.4 is devoted to the detailed derivation and investigation of this method.

Skin effect

Skin effect is a well known phenomenon (see [58], [147], and [123]), it manifests itself in the non-uniform distribution of the current in the conductor cross-section. At high frequencies, the currents are shifted to the exterior surface of conductors, which increases the ohmic losses, and decreases the internal inductance in conductors. Generally, the conductor losses and the internal inductance are frequency dependent functions. The standard time-domain PEEC model does not account for this phenomenon.

An enhanced skin effect model for the PEEC method has been proposed by Coperich, Ruehli, and Cangellaris [35]. This method is based on the introduction of the global surface impedance (GSI), which accurately and efficiently models the quasi-static electromagnetic behavior of a 2D lossy conductor (interior Problem). Since the interior of the conductor cross section is discretized and incorporated into the formulation of the GSI model, it eliminates the need for a high-frequency volume filament approach. The GSI representation has to be integrated in the MPIE and, finally, in the PEEC model to solve the exterior problem.

Another approach has been proposed by Wollenberg and Kochetov [161]. It approximately considers the skin effect for arbitrary cross sections of wire-like structures in the time and frequency domain. This PEEC modification replaces the partial resistance in the standard PEEC model by the mean surface impedance (MSI) representing the frequency dependent resistance and the internal inductance of the wire segment. The MSI can be calculated in closed-form or numerically. In the time domain, its frequency dependence is approximated using an equivalent RL stair-case circuit. The thorough explanation of this approach is given in § 4.4.1 and § 4.4.2.

Recently, the approach based on the stair-case circuits was further developed by Magdowski, Kochetov, and Leone [105]. The approach explained in § 4.4.3 uses the same concept of the mean surface impedance, but the frequency response of the MSI is modeled by the efficient full-spectrum convolution macromodeling, the concept of which is presented in § 3.6 of this work.

Efficiency

The efficiency is the critical characteristic of the PEEC method. Since the number of grid cells in a PEEC models may not be significantly reduced, the only way (except for programming techniques) for the efficiency improvement is the development of alternative formulations with a not fully-filled system matrix in the corresponding MNA problem. This may be performed by two approaches.

Antonini [8], [10], [9] has applied the fast-multipole method, which has been developed by Rokhlin [127] for the method of moments. Exactly as for the MoM, the fast-multipole method decouples the remote cells and makes the system matrix sparse.

Another approach leading to a sparse system matrix is the concept of reluctances formulated by Krauter and Pileggi [92] and Devgan et al. [38]. The standard PEEC method formulates the inductive and capacitive couplings between cells in terms of partial inductances and potential coefficients. These couplings may be alternatively represented in terms of *partial reluctances* and *partial capacitances*. The advantage of this modeling technique is caused by the dominance of the diagonal partial-reluctance and partial-capacitance matrix elements, so that very small non-diagonal values can be ignored under reservation of the interconnection-structure passivity. Furthermore, one can derive a SPICE compatible circuit dispensing with extra tools. The drawback of this method is its applicability to only quasi-static PEEC models (see § 4.2.4) due to causality. Moreover, this approach is suitable for PEEC models in power electronics, see Thamm, Kochetov et al. in [148].

An approach for the improvement of the topology of PEEC circuits has been proposed by Vahrenholt, Bruns, and Singer [152]. The authors reduce the number of unknowns by exploiting the connectivity of cells in the PEEC model.

Excitation by an incident field

The extension of the standard PEEC formulation to the three-dimensional structures excited by non-homogeneous incident electric fields has been provided by Ruehli, Garrett, and Paul [131]. The incident fields are included in the PEEC circuit in the form of independent voltage sources, which are completely compatible with the standard SPICE-like codes.

Stability

Although the interconnection structures are passive and, thus, physically stable systems, their time-domain solutions may show instability. This problem is typical for the integral-equation techniques, e.g., for the marching-on in time MoM solution [135] as well as for the time-domain PEEC models. Since the discussion about the stability of the PEEC method requires some additional definitions, the complete summary of this topic is included in § 4.5.3, which deals with the stability.

Discretization grid

Initially, the PEEC method was derived for an orthogonal discretization grid, which was its significant drawback, as a large number of interconnections are smooth-shaped and can be explained more precisely by non-orthogonal grids. The attempt to improve this problem has been undertaken by several teams of researchers.

Ruehli, Antonini et al. [130] have extended the PEEC formulation to non-orthogonal geometries, especially to 2D quadrilateral and 3D hexahedral meshing. This more general formulation retains all properties of the orthogonal PEEC method but is more flexible with respect to the geometry of interconnections.

Rong and Cangellaris [128] and Jandhyala, Wang, Gope, and Shi [67] have developed the PEEC models using triangular cells and prisms as fundamental elements for the modeling of arbitrary conductor surfaces and conductor and dielectric volumes. The PEEC method with a triangular grid applies the flexible Rao-Wilton-Glisson expansion functions [125].

Kochetov and Wollenberg [76], [80] have introduced the PEEC model with multipoint difference quotients. This modification improves the static accuracy of the method without changing the discretization grid via increasing the difference-quotient approximation order (see § 4.5.1).

PEEC for power electronics

One additional benefit of the PEEC method is the simplicity of its application for power electronics. Since the maximum frequency of interest in power-electronics applications is

relatively low, the quasi-static PEEC model is usually a suitable tool for the simulation of parasitic interconnections. Kochetov, Wollenberg et al. [84], [83], and [85] have implemented a quasi-static PEEC model in the code SIMPLORERTM (Ansoft Corporation), which is one of the best tools for the numerical simulation of power electronic circuits. Initially, this code did not have the models for power buses, wires, conducting planes, cases, and other passive interconnections used in power supplies. The additional PEEC model for SIMPLORER, which is programmed in C++ and integrated in SIMPLORER as a DLL file, has improved this drawback and allows the user to simulate arbitrary passive interconnection as "user defined elements" in the SIMPLORER interface.

Other contributions

The application of the PEEC method for the simulation of lightning protection systems has been provided by Antonini et al. [13]. The PEEC method has been applied to the modeling of skin effect in conductors of rectangular cross section by Antonini et al. [16]. The wavelet-based time-domain solution for a PEEC circuit has been proposed by Antonini and Orlandi [15]. Vahrenholt, Bruns, Singer, and Rimolo-Donaldo [153] have developed an efficient model for the microstrip lines using the hybrid MoM-PEEC formulation.

3.6 Black-box modeling of passive interconnections

The next important family of methods describing the passive interconnection structures is related to the concept of the model order reduction (MOR). These methods are especially suitable for the solution of problems that have complex interconnection structures connected to complex electronic circuits. Since the active electronic components influence the system behavior principally, they have to be considered, while interconnections make some parasitic influences on the functional behavior of the system and have to be considered as well. The simultaneous time-domain simulation of these complex and multi-scale problems by a direct method may need a huge run time of the code. The concept of the model order reduction divides the problem into linear passive-interconnections and active lumped circuits. The parasitic behavior of the linear interconnection structure can be extracted using a direct numerical method or from measurements. In either case, the interconnections are described in the frequency domain through scattering, admittance or impedance parameters. Further, the interconnection structure may be represented as a multi-port black-box model (also known as a macromodel), which simulates its behavior at the input-output ports. Usually, the order of the macromodel is incomparably lower than that of the full-wave model. This reduced-order time-domain model may be used for a time-domain simulation of the complete problem that leads to low-order models for the circuit-level simulation. Thus, one obtains a precise and efficient solution.

Over the last few decades, several methods for the time-domain macromodeling of frequency responses have been developed. In general, they may be classified into the techniques which approximate frequency responses and the related impulse response. The majority of

methods approximate the frequency response and are based on the Pade approximation Pillage and Rohrer [124], orthogonal polynomials Beyene [23], the piecewise approximation Korovkin et al. [89], and the *vector fitting technique* (VFT) Gustavsen and Semlyen [55]. The VFT is referenced as the most wide-spread and developed approach for the rational-function macromodeling, which is enforced by Min and Swaminathan [114], Antonini [12], et al. The further development of the VFT approach provided by Deschrijver et al. [37] is named *orthonormal vector fitting technique*. It uses orthonormal rational functions for the improvement of the numerical stability of the algorithm. The rational approximation for frequency responses resulted by the vector fitting technique may be represented in terms of passive RLC circuits that can be included in SPICE-like codes and simulated in the time domain with the active-devices environment. Substantial contributions in this area have been made by Antonini [11] and Min and Swaminathan [114].

The second alternative for methods based on the approximation of frequency responses is the *generalized pencil of function* (GPOF) method developed by Huo and Sarkar [66], [113] and the Prony method (see, e.g., [154], [68]). These methods approximate the impulse response with a sum of complex exponential functions, whereby the Fourier transformation is a rational function. Thus, these methods provide the same kind of approximation as the vector fitting technique and the same equivalent circuit description, but the algorithms for the macromodel parameters estimation are different.

In general, the vector fitting technique is more efficient for the modeling of narrow band frequency responses, while the GPOF method is preferable for broad-band pulses, which have short-pulse impulse responses in the time domain. Moreover, all these methods may be successfully applied to the modeling of arbitrary frequency responses.

Full-spectrum convolution macromodeling

The only disadvantage of the above considered macromodels is the correct representation of the initial frequency response at a limited spectrum. They are based on the assumption that the excitation has a limited spectrum from DC up to a finite frequency f_m . The asymptotic behavior of the initial frequency response at frequencies $f \gg f_m$ is not considered. However, the frequency spectrum of the excitation cannot be strictly limited. Thus, a time domain macromodel treats a minor part of the signal spectrum at $f > f_m$ with errors. Usually, this inaccuracy is acceptable, and only in a few cases can this error be decisive. § 4.5.3 presents such a problem, the full-wave time-domain PEEC model applies time-delay voltage sources as an approximation correct at frequencies $f < f_m$, however, the asymptotic behavior of the model, and the initial physical function are different. The seemingly negligible inaccuracy leads, however, to instability of the solution. The second characteristic of the VFT macromodels is the introduction of additional circuit elements, and nodes. This is an advantage if we use a few macromodels, but it is a disadvantage if the number of such macromodels is huge (see, e.g., § 4.5.4).

We develop this novel kind of macromodels satisfying two conditions:

- asymptotically correct approximation of the initial frequency response at $f \gg f_m$,

- no additional nodes in the MNA-formulation.

The full-spectrum convolution macromodeling (FSCM) is a strategy for the development of special macromodels with both of the aforementioned features and applicable to particular families of frequency responses. In this monograph, we develop the FSCM descriptions for several families of frequency responses: the generalized partial elements for the free-space PEEC method used in § 4.5.5, the mean surface impedance of the conductor used in § 4.4, and the generalized partial elements for the DGFLM-PEEC method derived in § 5.4.5.

The general strategy of FSCM consists of following steps:

- The initial frequency response $F(j\omega)$ is approximated by a function or a linear combination of functions, whose inverse Fourier transformation exists in closed form. For simplicity, we approximate here only by one function $F(j\omega) \approx \tilde{F}(j\omega)$.
- The time response of the system with the impulse and step responses $g(t)$ and $s(t)$ respectively on an arbitrary excitation $x(t)$ may be calculated using Duhamel integral [123]:

$$y(t) = s(0)x(t) + \int_0^t g(t - \vartheta)x(\vartheta)d\vartheta, \quad (3.18)$$

where $g(t) = \mathfrak{F}^{-1}\{F(j\omega)\}$ and $s(t) = \mathfrak{F}^{-1}\{F(j\omega)/(j\omega)\}$. Since for a causal impulse response $s(0) = 0$, (3.18) may be simplified as follows:

$$y(t) = \int_0^t g(t - \vartheta)x(\vartheta)d\vartheta. \quad (3.19)$$

- Since SPICE-like circuit simulators apply in the time domain a discrete time axis (see § 2.2), a time-domain macromodel has to calculate the values of the time response $y(t)$ only at discrete time points. In order to simplify, a constant time step Δt is assumed. Thus, we can introduce the notations $n\Delta t = t_n$, $x(t_n) = x_n$, and $y(t_n) = y_n$. The input function between the time points may be approximated as a linear function:

$$x(t) = a_{n+1}(t - t_n) + b_{n+1}, \quad t \in [t_n, t_{n+1}], \quad a_{n+1} = \frac{x_{n+1} - x_n}{\Delta t}, \quad b_{n+1} = x_n, \quad (3.20)$$

- Using (3.20), the convolution integral (3.19) at a time step may be calculated in closed-form. Further, a moving average formula for y_{n+1} can be developed:

$$y_{n+1} = \sum_{k=p}^q \Omega_k x_k, \quad 0 \leq p \leq q \leq n + 1, \quad (3.21)$$

which coefficients Ω_k are computed in closed form.

The moving average (3.21) can be represented in the form of an associated discrete circuit for a SPICE-like circuit simulator (see § 2.2). The particular derivation of (3.21) and its ADC models can be different, the particular examples are given in § 4.4, § 4.5.5, and § 5.4.5.

Chapter 4

Partial Element Equivalent Circuit method

The classical full-wave formulation of the PEEC method has been derived from the mixed-potential integral equation for the free space by A.E. Ruehli [129] in 1974. The later perfections and modifications of the PEEC method use same derivation principles regarding to basis and weighting functions, partial elements, and an equivalent circuit representation. The generalized formulation of the PEEC method, which has been initially developed by Kochetov, Wollenberg, and Leone [82], is based on the mixed-potential integral equation involving the dyadic Green's function for the vector magnetic potential and the scalar Green's function for the scalar potential. The DGF-PEEC method expands the application area of the PEEC method to every nonuniform medium that may be described using the MPIE formulated in (1.65). Since the PEEC formulation for the free and half space may be derived from the DGF-PEEC formulation, this book has the following structure. First, the generalized formulation is studied. Whence the classical PEEC models for the free and half space, and the advanced DGFLM-PEEC formulation for stratified media (see Chapter 5) are derived.

4.1 Generalized formulation of the PEEC method

In the following, we derive the DGF-PEEC model in the frequency domain, which is converted into the time domain using the inverse Fourier transformation.

The starting point for the derivation is the MPIE given by (1.65). This integrodifferential equation may be rewritten in operator form analogous to the basic formulation of the weighted residual technique (3.1). Since (1.65) contains two unknown functions $\mathbf{J}_s(\mathbf{r})$ and

$\rho_s(\mathbf{r})$, the following linear integro-differential operator should be applied:

$$\begin{aligned} \mathfrak{L}\{\mathbf{J}_s(\mathbf{r}), \rho_s(\mathbf{r})\} = \\ - \hat{\mathbf{n}} \times \hat{\mathbf{n}} \times \left(\frac{\mathbf{J}(\mathbf{r})}{\sigma} + j\omega\mu_0 \iint_{S'} \overline{\mathbf{G}}^A(\mathbf{r}, \mathbf{r}') \cdot \mathbf{J}_s(\mathbf{r}') dS' + \frac{\nabla}{\epsilon} \iint_{S'} K^\varphi(\mathbf{r}, \mathbf{r}') \rho_s(\mathbf{r}') dS' \right), \end{aligned} \quad (4.1)$$

The third unknown in the operator (4.1) is the current density $\mathbf{J}(\mathbf{r})$. Since it is related to the surface current density $\mathbf{J}_s(\mathbf{r})$, the introduction of additional basis functions for $\mathbf{J}(\mathbf{r})$ is not required. Finally, the MPIE is rewritten in the operator form:

$$\mathfrak{L}\{\mathbf{J}_s(\mathbf{r}), \rho_s(\mathbf{r})\} = -\hat{\mathbf{n}} \times \hat{\mathbf{n}} \times \mathbf{E}^i(\mathbf{r}). \quad (4.2)$$

The linear-operator equation (4.2) may be transformed into a system of algebraic equations using the Galerkin's approach, which needs the discretization and the introduction of basis functions.

4.1.1 Discretization and basis functions

The standard PEEC method [129] is set up applying the Galerkin's approach with the pulse basis functions (3.7) to the free-space MPIE. Since the local basis functions are related to a discretization grid, the interconnection system is discretized into two grids associated to both unknown functions $\mathbf{J}_s(\mathbf{r})$ and $\rho_s(\mathbf{r})$. The grid step is defined via the criterion (3.12), namely, $\Delta l \leq \lambda_m/20$, where λ_m is the wave length corresponding to the maximum frequency of interest.

In general, the conductor can be discretized using one-, two-, or three-dimensional grids. The discretization of a conductor using a three-dimensional grid leads to the computation of the volume current distribution, which can be necessary only for massive nonuniform interconnections or for considering skin effect. The three-dimensional PEEC (3D-PEEC) models are highly inefficient because, in general case, they produce an equation system with a large fully-filled system matrix, while the differential methods have a sparse system matrix. Thus, the simulation by the 3D-PEEC method can be inefficient as compared with differential methods. Moreover, skin effect can be considered avoiding the three-dimensional discretization (see § 4.4). Practically, the application of the PEEC method is reasonable only for the one- or two-dimensional discretization.

In order to simplify derivations, the DGF-PEEC model for the one-dimensional discretization of conductors (1D-PEEC) is developed in this monograph. The 2D-PEEC model differs from the 1D-PEEC model only in details. The 1D-PEEC models have large practical significance, as they are used for the simulation of the thin (with regard to λ_m) interconnection systems in the three-dimensional space, e.g., wire systems, printed circuit boards, non uniform transmission lines, etc.

An arbitrary conductor shown in Fig. 4.1a is divided into two grids. The primary grid (see Fig. 4.1b) is related to basis functions used for the approximation of currents, while the

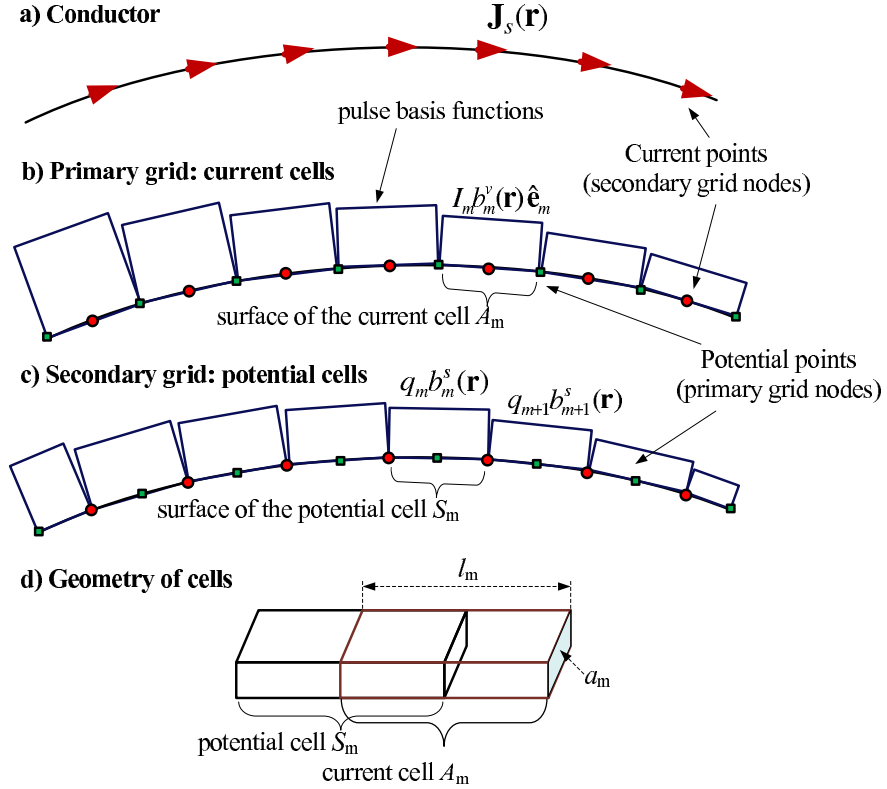


Figure 4.1: Discretization of a conductor in the PEEC method.

secondary grid (see Fig. 4.1c) is related to basis functions used for approximation of charges. The primary and secondary grid nodes are shown in Fig. 4.1 by the rectangular and round marks, respectively. Conventionally, the primary and secondary grid segments are named *current cells* and *potential cells*. As shown in Fig. 4.1 the geometrical centers of the currents cells serve as the boundaries for the potential cells and v.v. Thus, the current and potential cells are shifted from each other by a half of their length. Such a shift of the primary and secondary grids is sequent from using differential quotients as in some differential methods (e.g., FDTD, FIT).

$\mathbf{J}_s(\mathbf{r})$ is expanded on the total surface of the interconnection structure by the pulse basis functions as follows:

$$\mathbf{J}_s(\mathbf{r}) = \sum_{m \in M} I_m b_m^v(\mathbf{r}) \hat{\mathbf{e}}_m, \quad b_m^v(\mathbf{r}) = \begin{cases} 1/d_m, & \mathbf{r} \in A_m \\ 0, & \mathbf{r} \notin A_m \end{cases}, \quad (4.3)$$

where A_m and d_m are the surface and perimeter of the current cell m respectively (see Fig. 4.1d), $\hat{\mathbf{e}}_m$ is the unit vector giving the direction of the cell current, M is the set of current cells. The expansion coefficient I_m can be interpreted as the cell current, thus, introduction of (4.3) assumes that the currents in cells are constant, and the current distribution is approximated as a stair-case function (see Fig. 4.1b). Assuming that the current distribution over the conductor cross section is uniform, $\mathbf{J}(\mathbf{r})$ can be expanded by the same basis functions

and expansion coefficients as $\mathbf{J}_s(\mathbf{r})$:

$$\mathbf{J}(\mathbf{r}) = \sum_{m \in M} I_m b_m^v(\mathbf{r}) \frac{d_m}{a_m} \hat{\mathbf{e}}_m, \quad (4.4)$$

where a_m is the cross section of the current cell m .

The charges are distributed on the conductor surface and may be represented with the pulse basis functions:

$$\rho_s(\mathbf{r}) = \sum_{i \in M_c} q_i b_i^s(\mathbf{r}), \quad b_i^s(\mathbf{r}) = \begin{cases} 1/S_i, & \mathbf{r} \in S_i \\ 0, & \mathbf{r} \notin S_i \end{cases}, \quad (4.5)$$

where S_i is the surface of the potential cell i , M_c is the set of potential cells. The expansion coefficient q_i can be interpreted as the charge on the potential cell i . Thus, the charge density distribution is also approximated by a stair-case function (see Fig. 4.1c).

4.1.2 Derivation of the generalized partial elements

According to the Galerkin's approach, the weighting functions are equal to the basis functions, hence, we assign

$$\mathbf{w}_\alpha(\mathbf{r}) = b_\alpha^v(\mathbf{r}) \hat{\mathbf{e}}_\alpha, \quad (4.6)$$

and set up the algebraical equations for current cells:

$$\iint_S \mathbf{w}_\alpha(\mathbf{r}) \cdot \mathfrak{L}\{\mathbf{J}_s(\mathbf{r}), \rho_s(\mathbf{r})\} dS = - \iint_S \mathbf{w}_\alpha(\mathbf{r}) \cdot (\hat{\mathbf{n}} \times \hat{\mathbf{n}} \times \mathbf{E}^i(\mathbf{r})) dS. \quad (4.7)$$

The algebraic equations (4.7) should be converted into the Kirchhoff's voltage law (KVL) equation as in the standard PEEC method [129]. Thus, (4.7) should be simplified into a simple scalar form.

Since the weighting function is selective, we write

$$- \iint_S \mathbf{w}_\alpha(\mathbf{r}) \cdot (\hat{\mathbf{n}} \times \hat{\mathbf{n}} \times \mathbf{E}^i(\mathbf{r})) dS = - \frac{1}{d_\alpha} \iint_{A_\alpha} \hat{\mathbf{e}}_\alpha \cdot (\hat{\mathbf{n}} \times \hat{\mathbf{n}} \times \mathbf{E}^i(\mathbf{r})) dA_\alpha. \quad (4.8)$$

Using the vector identity (A.3) and in view that $\hat{\mathbf{e}}_\alpha$ is orthogonal to the outward normal vector $\hat{\mathbf{n}}$ at all points of A_α , we can write for an arbitrary vector \mathbf{b} located on A_α

$$-\hat{\mathbf{e}}_\alpha \cdot (\hat{\mathbf{n}} \times \hat{\mathbf{n}} \times \mathbf{b}) = \hat{\mathbf{e}}_\alpha \cdot \mathbf{b}. \quad (4.9)$$

The cross and dot products in (4.8) may be simplified using (4.9):

$$-\frac{1}{d_\alpha} \iint_{A_\alpha} \hat{\mathbf{e}}_\alpha \cdot (\hat{\mathbf{n}} \times \hat{\mathbf{n}} \times \mathbf{E}^i(\mathbf{r})) dA_\alpha = \frac{1}{d_\alpha} \iint_{A_\alpha} \hat{\mathbf{e}}_\alpha \cdot \mathbf{E}^i(\mathbf{r}) dA_\alpha. \quad (4.10)$$

Thus, the right-hand side of (4.7) becomes:

$$U_\alpha^i = \frac{1}{d_\alpha} \iint_{A_\alpha} \hat{\mathbf{e}}_\alpha \cdot \mathbf{E}^i(\mathbf{r}) dA_\alpha, \quad (4.11)$$

where U_α^i is the voltage induced by the incident field in the current cell α as in the standard PEEC formulation [129].

As the linear operator (4.1) consists of three summands, the left-hand side of (4.7) has three terms. First, the first term is simplified analogous to the right-hand side (4.8):

$$\begin{aligned} & - \iint_S \mathbf{w}_\alpha(\mathbf{r}) \cdot \left(\hat{\mathbf{n}} \times \hat{\mathbf{n}} \times \frac{\mathbf{J}(\mathbf{r})}{\sigma} \right) dS = - \iint_{A_\alpha} \hat{\mathbf{e}}_\alpha \cdot \left(\hat{\mathbf{n}} \times \hat{\mathbf{n}} \times \hat{\mathbf{e}}_\alpha \frac{I_\alpha}{d_\alpha a_\alpha \sigma} \right) dA_\alpha \\ & = \iint_{A_\alpha} \frac{I_\alpha}{d_\alpha a_\alpha \sigma} dA_\alpha = \frac{l_\alpha}{\sigma a_\alpha} I_\alpha. \end{aligned} \quad (4.12)$$

Denoting the ohmic resistance of the conductor segment α as R_α , (4.12) is rewritten in the compact final form:

$$R_\alpha I_\alpha \quad \text{with} \quad R_\alpha = \frac{l_\alpha}{\sigma a_\alpha}. \quad (4.13)$$

The second term of the left-hand side in (4.7) becomes:

$$-j\omega\mu_0 \iint_S \mathbf{w}_\alpha(\mathbf{r}) \cdot \left(\iint_{S'} \hat{\mathbf{n}} \times \hat{\mathbf{n}} \times \overline{\mathbf{G}}^A(\mathbf{r}, \mathbf{r}') \cdot \mathbf{J}_s(\mathbf{r}') dS' \right) dS. \quad (4.14)$$

Using (4.3), (4.6), and (4.9), we can rewrite (4.14) as follows:

$$j\omega \sum_{m \in M} L_{\alpha,m}(j\omega) I_m. \quad (4.15)$$

The coefficients $L_{\alpha,m}(j\omega)$ are called *generalized partial inductances*, they have the inductance units analogous to partial inductances of the standard PEEC method [129]. The generalized partial inductance yields:

$$L_{\alpha,m}(j\omega) = \frac{\mu_0}{d_m d_\alpha} \iint_{A_\alpha} \iint_{A'_m} \left(\hat{\mathbf{e}}_\alpha \cdot \overline{\mathbf{G}}^A(\mathbf{r}, \mathbf{r}') \cdot \hat{\mathbf{e}}_m \right) dA'_m dA_\alpha. \quad (4.16)$$

The generalized partial inductances are scalar frequency dependent functions, which can be simplified to the usual partial inductances [129] for the free space. Generally, the frequency dependent generalized partial inductances take into account the inhomogeneous medium and directions of currents in cells with respect to medium inhomogeneities and to each other. The calculation of the integrals in (4.16) depends on the structure of the Green's function and on the cell geometry. In some practical cases, the generalized partial inductances may

be derived in closed form as in the standard PEEC model. In the worst case, the integrals have to be computed numerically that essentially decreases the efficiency of the method.

The third part of the left-hand side of (4.7) is the starting point for the next derivation:

$$- \iint_S \mathbf{w}_\alpha(\mathbf{r}) \cdot (\hat{\mathbf{n}} \times \hat{\mathbf{n}} \times \nabla \varphi(\mathbf{r})) dS \quad \text{with} \quad \varphi(\mathbf{r}) = \frac{1}{\epsilon} \iint_{S'} K^\varphi(\mathbf{r}, \mathbf{r}') \rho_s(\mathbf{r}') dS'. \quad (4.17)$$

Using (4.9) we can write

$$-\hat{\mathbf{e}}_\alpha \cdot (\hat{\mathbf{n}} \times \hat{\mathbf{n}} \times \nabla \varphi(\mathbf{r})) = \frac{\partial}{\partial l_\alpha} \varphi(\mathbf{r}), \quad (4.18)$$

where $\partial/\partial l_\alpha = \hat{\mathbf{e}}_\alpha \cdot \nabla$ is the projection of the gradient vector on the cell current direction. The next equation is obtained by substitution (4.6) and (4.18) in (4.17):

$$\frac{1}{d_\alpha} \iint_{A_\alpha} \frac{\partial}{\partial l_\alpha} \varphi(\mathbf{r}) dA_\alpha. \quad (4.19)$$

The directional derivative of the scalar potential on the surface dA_α can be approximated by a difference quotient:

$$\frac{\partial}{\partial l_\alpha} \varphi(\mathbf{r}) \approx \frac{\varphi(\mathbf{r} + \hat{\mathbf{e}}_\alpha \frac{l_\alpha}{2}) - \varphi(\mathbf{r} - \hat{\mathbf{e}}_\alpha \frac{l_\alpha}{2})}{l_\alpha}. \quad (4.20)$$

The questions related to the accuracy of this approximation and the possibilities for its improvement are discussed in § 4.5. Substituting (4.20) in (4.19) we write:

$$\frac{1}{d_\alpha} \iint_{A_\alpha} \frac{\partial}{\partial l_\alpha} \varphi(\mathbf{r}) dA_\alpha \approx \frac{1}{d_\alpha l_\alpha} \iint_{A_\alpha} \varphi(\mathbf{r} + \hat{\mathbf{e}}_\alpha \frac{l_\alpha}{2}) dA_\alpha - \frac{1}{d_\alpha l_\alpha} \iint_{A_\alpha} \varphi(\mathbf{r} - \hat{\mathbf{e}}_\alpha \frac{l_\alpha}{2}) dA_\alpha. \quad (4.21)$$

Based on the fact that the current and potential cells are shifted by a half of their length (see Fig. 4.1), the integration over the surface A_α is replaced by the integrations over S_α and $S_{\alpha+1}$. In the case of the uniform discretization, we can write $S_{\alpha+1} = S_\alpha = d_\alpha l_\alpha$ and simplify (4.21) as follows:

$$\frac{1}{S_{\alpha+1}} \iint_{S_{\alpha+1}} \varphi(\mathbf{r}) dS_{\alpha+1} - \frac{1}{S_\alpha} \iint_{S_\alpha} \varphi(\mathbf{r}) dS_\alpha. \quad (4.22)$$

Using the basis-function expansion (4.5), the scalar potential in (4.22) yields:

$$\varphi(\mathbf{r}) = \frac{1}{\epsilon} \iint_{S'} K^\varphi(\mathbf{r}, \mathbf{r}') \sum_{i \in M_c} q_i b_i^s(\mathbf{r}) dS' = \sum_{i \in M_c} \frac{q_i}{S_i \epsilon} \iint_{S'_i} K^\varphi(\mathbf{r}, \mathbf{r}') dS'_i. \quad (4.23)$$

The substitution of (4.23) in (4.22) leads to the compact formulation developed with respect to the expansion coefficients, i.e., charges on potential cells:

$$\varphi_{\alpha+1} - \varphi_\alpha, \quad \varphi_\alpha = \sum_{i \in M_c} p_{\alpha,i}(j\omega) q_i, \quad (4.24)$$

where φ_α and $\varphi_{\alpha+1}$ are the potentials on the cells α and $\alpha + 1$. The coefficients $p_{\alpha,i}(j\omega)$ are called *generalized potential coefficients*, they are computed via the following general formula:

$$p_{\alpha,i}(j\omega) = \frac{1}{\epsilon S_\alpha S'_i} \iint_{S_\alpha} \iint_{S'_i} K^\varphi(\mathbf{r}, \mathbf{r}') dS'_i dS_\alpha. \quad (4.25)$$

The expression (4.24) differs from the corresponding term in the standard PEEC formulation only in the Green's function $K^\varphi(\mathbf{r}, \mathbf{r}')$ used instead of the free-space Green's function [129].

Using (4.11), (4.13), (4.15), and (4.24), an algebraic equation for the weighting function $\mathbf{w}_\alpha(\mathbf{r})$ (or for the current cell α) is set up:

$$U_\alpha^i = R_\alpha I_\alpha + j\omega \sum_{m \in M} L_{\alpha,m}(j\omega) I_m + \varphi_{\alpha+1} - \varphi_\alpha \quad (4.26)$$

with $\varphi_\alpha = \sum_{i \in M_c} p_{\alpha,i}(j\omega) q_i.$

Since our goal is the development of an equivalent circuit for this equation, the charges on the surface of potential cells have to be replaced by integrals of displacement currents with regard to the ground:

$$q_i = \frac{I_i^c}{j\omega}, \quad i \in M_c. \quad (4.27)$$

Finally, (4.26) is rewritten as a KVL equation analogous to the standard PEEC model:

$$U_\alpha^i = R_\alpha I_\alpha + j\omega \sum_{m \in M} L_{\alpha,m}(j\omega) I_m + \varphi_{\alpha+1} - \varphi_\alpha \quad (4.28)$$

with $\varphi_\alpha = \frac{1}{j\omega} \sum_{i \in M_c} p_{\alpha,i}(j\omega) I_i^c.$

4.1.3 Equivalent circuit for the DGF-PEEC method

The KVL-equation (4.28) can be interpreted as an equivalent Π -like circuit shown in Fig. 4.2, where the conductor segment discretized into the current cell α is represented by an equivalent circuit with three branches. The longitudinal branch approximates the potential drop along the conductor segment. It includes the voltage source U_α^i accounting for the voltage induced in this segment by the incident electric field. The resistance R_α approximates the ohmic losses in the conductor. The set of controlled voltage sources describes the inductive coupling between currents in segments. The transversal branches consist of only controlled voltage sources, which represent the capacitive couplings between the segments of conductors that are discretized into potential cells. The potentials and currents in Fig. 4.2 are related to the geometry: φ_α is the potential at the geometrical center of the potential cell α , I_α is the current between two adjacent potential points located at geometrical centers of potential cells, I_α^c is the displacement current from the center of the potential cell. The

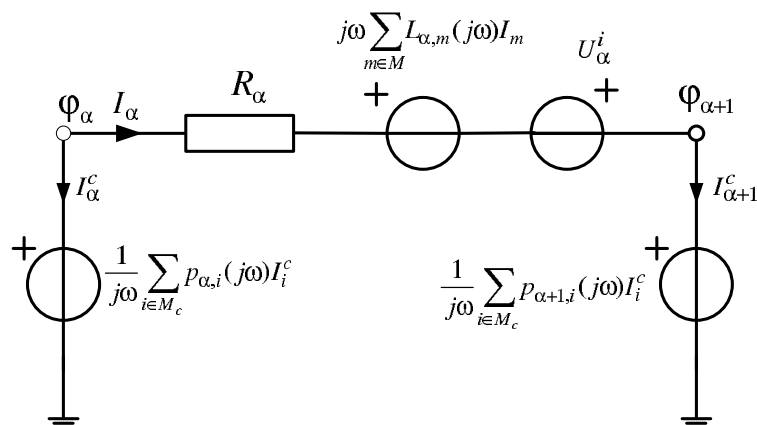


Figure 4.2: DGF-PEEC model for a conductor segment in the frequency domain.

complete DGF-PEEC model of an arbitrary interconnection system can be composed by cascaded equivalent circuits for conductor segments.

Obviously, all elements of the equivalent circuit are related to the *generalized partial elements*, i.e., generalized partial inductances and potential coefficients. This yields the acronym PEEC (Partial Element Equivalent Circuit) method.

As a usual circuit, the above-developed PEEC model may be directly transformed into the time domain. This transformation depends strongly on the Green's functions used for the partial-element derivation. In several practical cases, it is simple (see § 4.2). If the Green's functions are sophisticated (see Chapter 5) the time-domain model of the controlled voltage sources with frequency dependent coefficients may be set up via the black-box modeling, which is explained in § 3.6.

4.2 PEEC models for free- and half-space problems

The PEEC model for the free-space problems is the most wide-spread in the practice. We denote it also as the *standard PEEC method* because it has been initially proposed by Ruehli [129]. This section presents the derivation of the standard PEEC model from the more general DGF-PEEC formulation derived in the previous section and its important modifications. The half-space PEEC (HS-FW-PEEC) model differs from the free-space one only in a minor modification of the Green's function. Therefore, the half-space PEEC model is introduced in this monograph with regard to the standard PEEC method.

4.2.1 Derivation of the standard PEEC model in the frequency domain

Since an arbitrary interconnection system is located in the free space, the dyadic Green's function for the vector magnetic potential and the scalar Green's function for the scalar electric potential are defined by (1.66) and (1.67), respectively. The interconnection structure

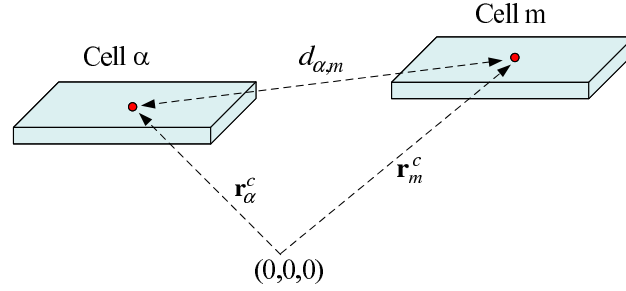


Figure 4.3: Approximation of the time delay between cells.

is discretized according to the concept given in § 4.1.1. The DGF-PEEC model can be applied to this particular variant of Green's functions. The generalized partial inductances are derived by the substitution (1.66) in (4.16):

$$L_{\alpha,m}(j\omega) = \frac{\mu_0}{d_m d_\alpha} \iint_{A_\alpha} \iint_{A'_m} \hat{\mathbf{e}}_\alpha \cdot \bar{\bar{\mathbf{I}}} \cdot \hat{\mathbf{e}}_m g(\mathbf{r}, \mathbf{r}') dA'_m dA_\alpha. \quad (4.29)$$

Using the definition for the scalar Green's function (1.41), and the vector identity $\hat{\mathbf{e}}_\alpha \cdot \bar{\bar{\mathbf{I}}} \cdot \hat{\mathbf{e}}_m = \hat{\mathbf{e}}_\alpha \cdot \hat{\mathbf{e}}_m$, (4.29) may be simplified:

$$L_{\alpha,m}(j\omega) = \frac{\mu_0}{4\pi d_m d_\alpha} \cos \phi_{\alpha,m} \iint_{A_\alpha} \iint_{A'_m} \frac{e^{-jk|\mathbf{r}-\mathbf{r}'|}}{|\mathbf{r}-\mathbf{r}'|} dA'_m dA_\alpha \quad (4.30)$$

with $\cos \phi_{\alpha,m} = \hat{\mathbf{e}}_\alpha \cdot \hat{\mathbf{e}}_m$. Then, the standard PEEC method provides a simplification of (4.30) via the following assumption:

$$L_{\alpha,m}(j\omega) \approx \tilde{L}_{\alpha,m}(j\omega) = L_{\alpha,m} e^{-j\omega\tau_{\alpha,m}} \quad (4.31)$$

with

$$L_{\alpha,m} = \frac{\mu_0}{4\pi d_m d_\alpha} \iint_{A_\alpha} \iint_{A'_m} \frac{dA'_m dA_\alpha}{|\mathbf{r}-\mathbf{r}'|} \cos \phi_{\alpha,m}. \quad (4.32)$$

The space-convolution integrals in (4.30) are approximated by functions $\tilde{L}_{\alpha,m}(j\omega)$, which consist of their static analogs $L_{\alpha,m}$ called *partial inductances* and ideal delay functions with time delays $\tau_{\alpha,m} = d_{\alpha,m}/c$ computed between geometric centers of cells. This approach is explained in Fig. 4.3, where \mathbf{r}_m^c , and \mathbf{r}_α^c are geometrical centers of cells, $d_{\alpha,m} = |\mathbf{r}_\alpha^c - \mathbf{r}_m^c|$. Thus, the static behavior of the generalized partial inductance is taken into account exactly, while its dynamic behavior is approximated. The most important advantage of this approach is simplicity. The space-convolution integrals (4.32) may be calculated in closed form for many practically important cell geometries, e.g., for nonorthogonal coplanar quadrilaterals see [17] and for rectangular cells see [63]. Hence, the efficiency increases many times, as the partial elements have to be calculated only one time, and then, recomputed for other frequencies using (4.31). The only disadvantage of this approach concerns the stability of the time-domain solution, the thorough investigation of this issue is presented in § 4.5.3.

The generalized potential coefficient in the free space is derived by the substitution of (1.67) in (4.25):

$$p_{\alpha,i}(j\omega) = \frac{1}{4\pi\epsilon_0 S_\alpha S'_i} \iint_{S_\alpha} \iint_{S'_i} \frac{e^{-jk|\mathbf{r}-\mathbf{r}'|}}{|\mathbf{r}-\mathbf{r}'|} dS'_i dS_\alpha. \quad (4.33)$$

(4.33) is simplified via the assumption analogous to (4.31):

$$p_{\alpha,i}(j\omega) \approx \tilde{p}_{\alpha,i}(j\omega) = p_{\alpha,i} e^{-j\omega\tau_{\alpha,i}^c} \quad (4.34)$$

with

$$p_{\alpha,i} = \frac{1}{4\pi\epsilon_0 S_\alpha S'_i} \iint_{S_\alpha} \iint_{S'_i} \frac{dS'_i dS_\alpha}{|\mathbf{r}-\mathbf{r}'|}. \quad (4.35)$$

The real constants $p_{\alpha,i}$ are named *potential coefficients*, $\tau_{\alpha,i}^c$ is the time delay between geometrical centers of the potential cells α and i . The above given standard partial inductances and potential coefficients have been defined by Ruehli [129] in 1974. The above described rigorous derivation for partial elements from the more general DGF-PEEC model is an alternative for the standard PEEC derivation acting only in the free space.

Since $\tau_{\alpha,\alpha} = 0$ and $\tau_{\alpha,\alpha}^c = 0$, the self partial inductances and potential coefficients may be considered as usual inductances $L_{\alpha,\alpha}$ and capacitances $C_{\alpha,\alpha} = 1/p_{\alpha,\alpha}$. The voltage drops on the self partial inductance and on the self capacitance are denoted by U_α^L and U_α^c , respectively. The relations between the currents and voltages for these elements are trivial:

$$U_\alpha^L = j\omega L_{\alpha,\alpha} I_\alpha, \quad I_\alpha^c = j\omega C_{\alpha,\alpha} U_\alpha^c = \frac{j\omega}{p_{\alpha,\alpha}} U_\alpha^c. \quad (4.36)$$

After the substitution of (4.31), (4.34), and (4.36) in the algebraic equation for a conductor segment (4.28), one obtains the standard full-wave free-space PEEC formulation with voltage sources:

$$U_\alpha^i = R_\alpha I_\alpha + j\omega L_{\alpha,\alpha} I_\alpha + \hat{U}_\alpha^L + U_{\alpha+1}^c + \tilde{U}_{\alpha+1}^c - U_\alpha^c - \tilde{U}_\alpha^c, \quad (4.37)$$

where \hat{U}_α^L , \tilde{U}_α^c , and $\tilde{U}_{\alpha+1}^c$ are controlled voltage sources with the time delay:

$$\begin{aligned} \hat{U}_\alpha^L &= \sum_{\substack{m \in M \\ m \neq \alpha}} \frac{L_{\alpha,m}}{L_{m,m}} U_m^L e^{-j\omega\tau_{\alpha,m}}, \\ \tilde{U}_\alpha^c &= \sum_{\substack{i \in M_c \\ i \neq \alpha}} \frac{p_{\alpha,i}}{p_{i,i}} U_i^c e^{-j\omega\tau_{\alpha,i}}. \end{aligned} \quad (4.38)$$

The KVL equation (4.37) can be represented as an equivalent circuit (see Fig. 4.4a) composed of resistances, inductances, capacitances, and controlled voltage sources. The circuit in Fig. 4.4a realizes the couplings between cells using Thevenin generators, i.e. the series connection of a voltage source and an impedance. Since the Thevenin generators can be transformed in Norton generators, the equivalent circuit with the voltage sources can be

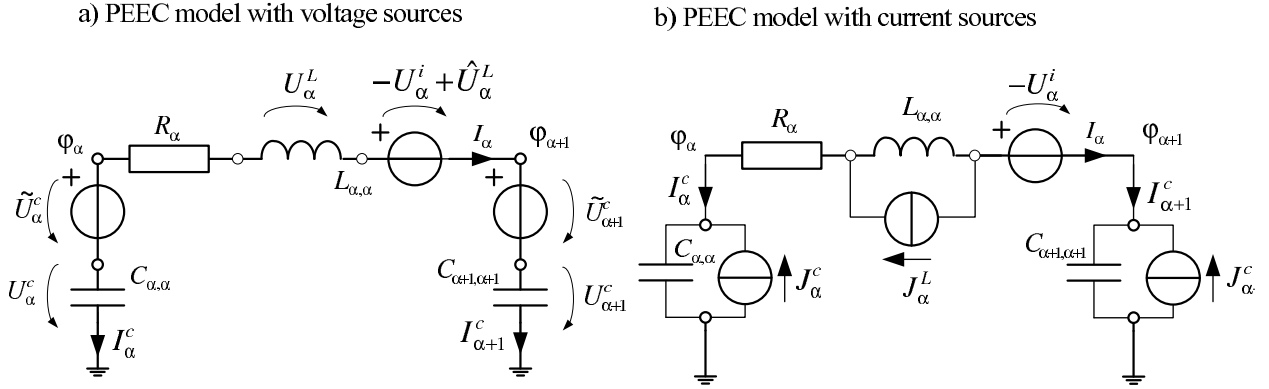


Figure 4.4: PEEC models in the free space with voltage (a) and current (b) sources.

replaced by an alternative one using the current sources (see Fig. 4.4b) that are computed as follows:

$$\begin{aligned}
 J_\alpha^L &= \sum_{\substack{m \in M \\ m \neq \alpha}} \frac{L_{\alpha,m}}{L_{\alpha,\alpha}} I_m e^{-j\omega\tau_{\alpha,m}}, \\
 J_\alpha^c &= \sum_{\substack{i \in M_c \\ i \neq \alpha}} \frac{p_{\alpha,i}}{p_{\alpha,\alpha}} I_i e^{-j\omega\tau_{\alpha,i}}.
 \end{aligned} \tag{4.39}$$

The both equivalent circuits for the PEEC method may be implemented in a universal circuit simulator, they have advantages and disadvantages, which are discussed in § 4.3.

4.2.2 Standard half-space PEEC model in the frequency domain

The above-developed PEEC model for the free space may be simply transformed into the half-space one. This monograph understands under the half space an half-infinite vacuum-filled space, which is bounded by an infinite perfectly conductive ground. For distinctness, the ground is placed in the (x, y) plane at the point $z = 0$, as shown in Fig. 4.5. This half-space geometry has a large number of practical applications, e.g., antennas or transmission lines in the proximity of conducting surfaces, PCB boards, etc.

The Green's functions for the vector and scalar potentials for a half-space medium may be constructed using the image theory that is explained in § 1.2.4. The half-space geometry may be replaced by a free-space geometry, where all current and charge sources are complemented by their reflected counterparts (or images). The location of the image of the source point with the coordinate \mathbf{r}' (see Fig. 4.5) is calculated as follows:

$$\mathbf{r}'_i = \bar{\bar{\mathbf{I}}}_i \cdot \mathbf{r}', \tag{4.40}$$

where $\bar{\bar{\mathbf{I}}}_i$ is the reflection dyadic (see [104]) defined in Cartesian coordinates as follows:

$$\bar{\bar{\mathbf{I}}}_i = \hat{\mathbf{x}}\hat{\mathbf{x}} + \hat{\mathbf{y}}\hat{\mathbf{y}} - \hat{\mathbf{z}}\hat{\mathbf{z}}. \tag{4.41}$$

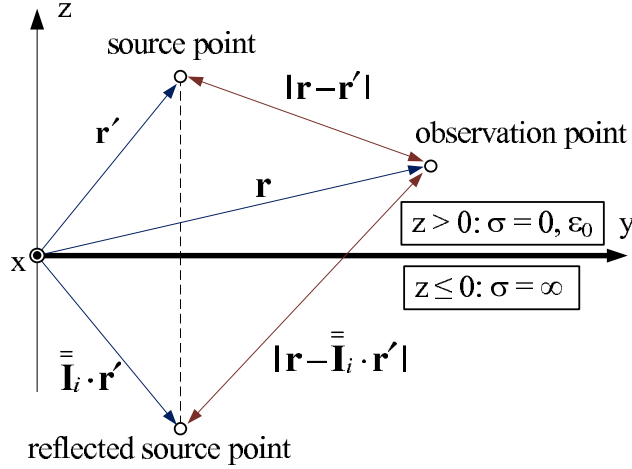


Figure 4.5: Image theory in application to PEEC models in the half space.

According to the image theory, charge sources and horizontal currents are reflected with the opposite sign, while vertical currents are reflected with the same signs. These rules can be included in the dyadic Green's function for the vector potential:

$$\overline{\overline{\mathbf{G}}}^A(\mathbf{r}, \mathbf{r}') = g(\mathbf{r}, \mathbf{r}') \overline{\overline{\mathbf{I}}} - g(\mathbf{r}, \overline{\overline{\mathbf{I}}}_i \cdot \mathbf{r}') \overline{\overline{\mathbf{I}}}_i \quad (4.42)$$

and in the Green's function for the scalar potential:

$$K^\varphi(\mathbf{r}, \mathbf{r}') = g(\mathbf{r}, \mathbf{r}') - g(\mathbf{r}, \overline{\overline{\mathbf{I}}}_i \cdot \mathbf{r}') \quad (4.43)$$

These Green's functions can be substituted in the equations for the generalized partial elements (4.16), and (4.25). Applying the same derivation as for the free-space Green's function, one obtains for the generalized partial inductance:

$$L_{\alpha,m}(j\omega) \approx L_{\alpha,m} e^{-j\omega\tau_{\alpha,m}} - L_{\alpha,m}^{(i)} e^{-j\omega\tilde{\tau}_{\alpha,m}}, \quad (4.44)$$

where $L_{\alpha,m}$ is the partial inductance between cells in the free space calculated using (4.32), while $L_{\alpha,m}^{(i)}$ is the partial inductance between the image of the cell m and the cell α calculated as follows:

$$L_{\alpha,m}^{(i)} = \frac{\mu_0}{4\pi d_m d_\alpha} \iint_{A_\alpha} \iint_{A'_m} \frac{dA'_m dA_\alpha}{|\mathbf{r} - \overline{\overline{\mathbf{I}}}_i \cdot \mathbf{r}'|} \cos \phi_{\alpha,m}^{(i)} \quad (4.45)$$

with $\cos \phi_{\alpha,m}^{(i)} = \hat{\mathbf{e}}_\alpha \cdot \overline{\overline{\mathbf{I}}}_i \cdot \hat{\mathbf{e}}_m$. $\tau_{\alpha,m}$ is the time delay between the cell centers as in the free space, $\tilde{\tau}_{\alpha,m} = |\mathbf{r}_\alpha^c - \overline{\overline{\mathbf{I}}}_i \cdot \mathbf{r}_m^c|/c$ is the time delay between the geometrical centers of the cell α , and the image of the cell m .

A suitable formulation for the generalized potential coefficients is derived analogously to the generalized partial inductances via the substitution of (4.43) in (4.25):

$$p_{\alpha,i}(j\omega) \approx p_{\alpha,i} e^{-j\omega\tau_{\alpha,i}^c} - p_{\alpha,i}^{(i)} e^{-j\omega\tilde{\tau}_{\alpha,i}^c}, \quad (4.46)$$

where $p_{\alpha,i}$ is the potential coefficient between the cells in the free space calculated using (4.35), $p_{\alpha,i}^{(i)}$ is the potential coefficient between the image of the cell i and the cell α :

$$p_{\alpha,i}^{(i)} = \frac{1}{4\pi\epsilon_0 S_\alpha S'_i} \iint_{S_\alpha} \iint_{S'_i} \frac{dS'_i dS_\alpha}{|\mathbf{r} - \bar{\mathbf{I}}_i \cdot \mathbf{r}'|}. \quad (4.47)$$

Using the same derivation as for the free-space PEEC model (see § 4.2.1) and applying the generalized partial elements given by (4.44), (4.46), the KVL equation for DGF-PEEC (4.28) can be simplified to the form (4.37). However, the controlled voltage sources \hat{U}_α^L , \tilde{U}_α^c , and $\tilde{U}_{\alpha+1}^c$ are computed differently:

$$\begin{aligned} \hat{U}_\alpha^L &= \sum_{\substack{m \in M \\ m \neq \alpha}} \frac{L_{\alpha,m}}{L_{m,m}} U_m^L e^{-j\omega\tau_{\alpha,m}} - \sum_{m \in M} \frac{L_{\alpha,m}^{(i)}}{L_{m,m}} U_m^L e^{-j\omega\tilde{\tau}_{\alpha,m}}, \\ \tilde{U}_\alpha^c &= \sum_{\substack{i \in M_c \\ i \neq \alpha}} \frac{p_{\alpha,i}}{p_{i,i}} U_i^c e^{-j\omega\tau_{\alpha,i}} - \sum_{i \in M_c} \frac{p_{\alpha,i}^{(i)}}{p_{i,i}} U_i^c e^{-j\omega\tilde{\tau}_{\alpha,i}}. \end{aligned} \quad (4.48)$$

As the KVL equations for the PEEC models in the free and half space are identical, we use for both solution domains the same equivalent circuits shown in Fig. 4.4. The controlled voltage sources in Fig. 4.4a can be transformed in current sources in Fig. 4.4b as follows:

$$\begin{aligned} J_\alpha^L &= \sum_{\substack{m \in M \\ m \neq \alpha}} \frac{L_{\alpha,m}}{L_{\alpha,\alpha}} I_m e^{-j\omega\tau_{\alpha,m}} - \sum_{m \in M} \frac{L_{\alpha,m}^{(i)}}{L_{\alpha,\alpha}} I_m e^{-j\omega\tilde{\tau}_{\alpha,m}}, \\ J_\alpha^c &= \sum_{\substack{i \in M_c \\ i \neq \alpha}} \frac{p_{\alpha,i}}{p_{\alpha,\alpha}} I_i^c e^{-j\omega\tau_{\alpha,i}} - \sum_{i \in M_c} \frac{p_{\alpha,i}^{(i)}}{p_{\alpha,\alpha}} I_i^c e^{-j\omega\tilde{\tau}_{\alpha,i}}. \end{aligned} \quad (4.49)$$

In summary, the PEEC models for the half- and free-space problems differ only in additional summands in the controlled sources caused by the presence of the image cells.

4.2.3 PEEC method in the time domain

The above-developed frequency-domain PEEC models may be trivially transformed into the time domain using the IFT transformation (A.21). The resulted equivalent circuit is shown in Fig. 4.6a. We denote in the time domain: $u_m^i(t) = \mathfrak{F}^{-1}\{U_m^i\}$, $i_m(t) = \mathfrak{F}^{-1}\{I_m\}$, $i_m^c(t) = \mathfrak{F}^{-1}\{I_m^c\}$, $\varphi_m(t) = \mathfrak{F}^{-1}\{\varphi_m\}$, $u_m^L(t) = \mathfrak{F}^{-1}\{U_m^L\}$, $u_m^c(t) = \mathfrak{F}^{-1}\{U_m^c\}$, $\tilde{u}_m^c(t) = \mathfrak{F}^{-1}\{\tilde{U}_m^c\}$, $\tilde{u}_m^L(t) = \mathfrak{F}^{-1}\{\tilde{U}_m^L\}$, $J_m^c(t) = \mathfrak{F}^{-1}\{J_m^c\}$, and $J_m^L(t) = \mathfrak{F}^{-1}\{J_m^L\}$. The circuit in the time domain consists of the same resistances, inductances, and capacitances as the circuits in Fig. 4.4. The inverse Fourier transformation of the controlled sources is done in

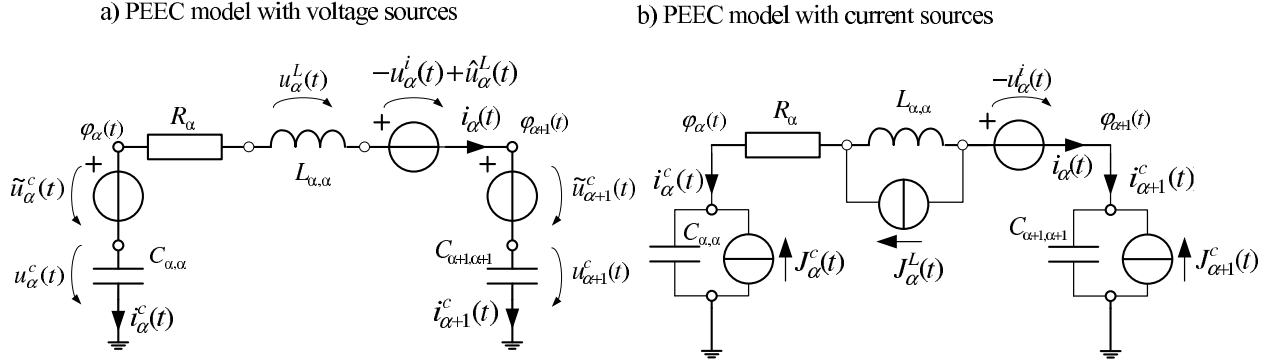


Figure 4.6: PEEC models with voltage (a) and current (b) sources in the time domain.

view of the identity: $f(t - \tau) = \mathfrak{F}^{-1}\{F(j\omega) e^{-j\omega\tau}\}$ with $f(t) = \mathfrak{F}^{-1}\{F(j\omega)\}$. Thus, the formulations for the time delay controlled voltage sources (4.38) yield:

$$\begin{aligned} \mathfrak{F}^{-1}\{\hat{U}_\alpha^L\} &= \hat{u}_\alpha^L(t) = \sum_{\substack{m \in M \\ m \neq \alpha}} \frac{L_{\alpha,m}}{L_{m,m}} u_m^L(t - \tau_{\alpha,m}), \\ \mathfrak{F}^{-1}\{\tilde{U}_\alpha^c\} &= \tilde{u}_\alpha^c(t) = \sum_{\substack{i \in M_c \\ i \neq \alpha}} \frac{p_{\alpha,i}}{p_{i,i}} u_i^c(t - \tau_{\alpha,i}), \end{aligned} \quad (4.50)$$

while the formulations for the time delay controlled current sources (4.39) are

$$\begin{aligned} \mathfrak{F}^{-1}\{J_\alpha^L\} &= J_\alpha^L(t) = \sum_{\substack{m \in M \\ m \neq \alpha}} \frac{L_{\alpha,m}}{L_{\alpha,\alpha}} i_m(t - \tau_{\alpha,m}), \\ \mathfrak{F}^{-1}\{J_\alpha^c\} &= J_\alpha^c(t) = \sum_{\substack{i \in M_c \\ i \neq \alpha}} \frac{p_{\alpha,i}}{p_{\alpha,\alpha}} i_i^c(t - \tau_{\alpha,i}). \end{aligned} \quad (4.51)$$

4.2.4 Quasi-static formulation of the standard PEEC method

The above-considered PEEC models for the free- and half-space problems are classified as full-wave PEEC (FW-PEEC) models. This means that they take into account the radiation of the electromagnetic energy. Since these models are composed of the time-delay controlled sources, their direct implementation in a general-purpose circuit simulator produces several minor problems. The time-delay sources are present as a standard element not in all codes, e.g., in SPICE 3f4. The time-delay sources provided by modern codes are not ever enough efficient for the application in PEEC models, since the number of such sources can exceed millions. Additionally, the FW-PEEC model can produce instable time-domain solutions discussed in § 4.5.3. Thus, the development of a PEEC model without time delay sources can be useful with respect to efficiency and stability.

The quasi-static PEEC (QS-PEEC) model is derived from the full-wave one assuming all time delays equal to zero. This assumption is applicable in the limited frequency range

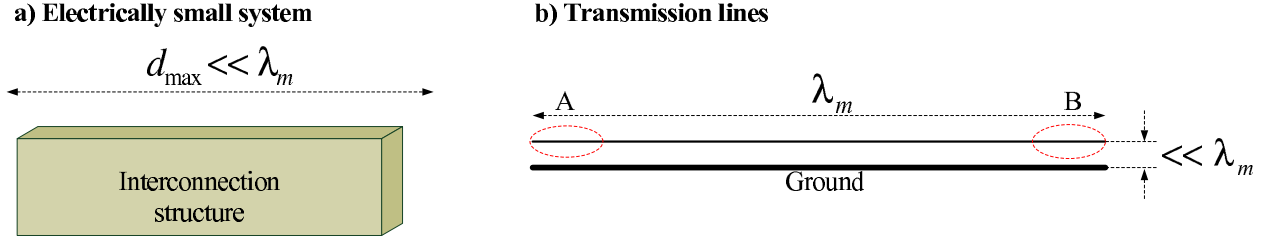


Figure 4.7: The interconnection systems modeled by the quasi-static PEEC method.

only for few kinds of interconnection structures with negligible radiation: electrically small systems [147] and non-uniform transmission lines. The electrically small systems have the maximal geometrical size d_{max} much less than the minimal wavelength of interest λ_m (see Fig. 4.7a). Since the maximal time delay in controlled sources is computed as $\tau_{max} = d_{max}/c$ and $\omega_m = 2\pi/\lambda_m$, the exponent term in the time-delay sources may be represented as:

$$\omega\tau_{max} = 2\pi d_{max}/\lambda_m \ll 2\pi \Rightarrow e^{-j\omega\tau_{max}} \approx 1.$$

The same rule may be applied to all controlled sources, since their time delays are less than τ_{max} .

Another situation can be observed by non-uniform transmission lines. The lengths of lines can be electrically large, but their transverse sizes are electrically small (see Fig. 4.7b). Thus, the time delay between remote cells located in areas shown in Fig. 4.7b as A and B seems to be important. However, it is wrong because of the Green's function selectivity. As an example, a generalized potential coefficient between cells from areas A and B computed by (4.46) is considered. Since the distance from the wire to the ground is tiny as compared to the distance between cells, one assumes $\tau_{\alpha,i}^c \approx \tilde{\tau}_{\alpha,i}^c$ and $p_{\alpha,i} \approx p_{\alpha,i}^{(i)}$. Hence, (4.46) yields:

$$p_{\alpha,i}(j\omega) \approx (p_{\alpha,i} - p_{\alpha,i}^{(i)}) e^{-j\omega\tau_{\alpha,i}^c} \approx 0.$$

Thus, the time delay for remote cells is not negligible, but the couplings between these cells do not influence the solution. In fact, the quasi-static PEEC model produces for lines similar results as Π - or T -like equivalent circuits derived from the transmission line theory, but the PEEC method is more flexible with respect to the geometry of conductors. The typical application of the QS-PEEC is modeling PCBs at relatively low frequencies.

The quasi-static formulation of PEEC method is based on the KVL equation (4.37), which applies the controlled sources without time delays:

$$\begin{aligned} \hat{U}_\alpha^L &= \sum_{\substack{m \in M \\ m \neq \alpha}} j\omega L_{\alpha,m} I_m, \\ \tilde{U}_\alpha^c &= \sum_{\substack{i \in M_c \\ i \neq \alpha}} p_{\alpha,i} \frac{I_i^c}{j\omega}. \end{aligned} \quad (4.52)$$

Obviously, the controlled sources for inductive cells are equivalent to the inclusion of mutual inductances $L_{\alpha,m}$ between these cells. Thus, the equivalent circuit for current cells can be

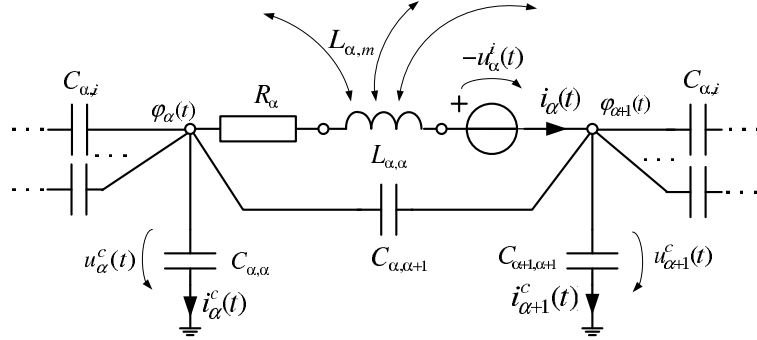


Figure 4.8: Quasi-static PEEC model for a conductor segment.

set up by self and mutual inductances existing in all usual circuit simulators. The controlled sources for capacitive couplings may be alternatively represented by usual circuit elements using the *partial capacitances*. All potential coefficients fill a square matrix denoted by $\mathbb{P} = \{p_{i,j}\}$, with $i, j \in M_c$. According to (4.28) the vector of scalar potentials on cells $\boldsymbol{\varphi} = \{\varphi_i\}$ is related to charges on the cells $\boldsymbol{q} = \{q_i\}$ as $\boldsymbol{\varphi} = \mathbb{P}\boldsymbol{q}$. The matrix \mathbb{P}^{-1} holds the *capacitive coefficients* denoted here as $c_{\alpha,i}$ (see [147]). The partial capacitances $C_{\alpha,i}$ between potential cells are computed from the capacitive coefficients as follows:

$$C_{\alpha,i} = \begin{cases} \sum_{j \in M_c} c_{\alpha,j}, & \alpha = i \\ -c_{\alpha,i}, & \alpha \neq i \end{cases}, \quad \mathbb{P}^{-1} = \{c_{i,j}\}, \quad i, j \in M_c. \quad (4.53)$$

The inclusion of the mutual inductances and partial capacitances instead of controlled sources allows one to transform the equivalent circuit for the full-wave PEEC model Fig. 4.6 into the circuit shown in Fig. 4.8, which is applicable in the time and frequency domain. The most important advantage of this model is its realization only by usual passive elements: resistances, inductances, and capacitances. On the one hand, this simplifies the inclusion of the model into circuit-simulator codes, on the other hand, the stability of the time-domain solution for this passive circuit is guaranteed by a simple criterion. This criterion is based on the partial capacitances and so-called *partial reluctances* $K_{\alpha,m}$, which are defined as follows:

$$K_{\alpha,m} = \begin{cases} \sum_{j \in M} \mathfrak{K}_{\alpha,j}, & \alpha = m \\ -\mathfrak{K}_{\alpha,m}, & \alpha \neq m \end{cases}, \quad \mathbb{L}^{-1} = \{\mathfrak{K}_{i,j}\}, \quad i, j \in M, \quad (4.54)$$

where $\mathbb{L} = \{L_{\alpha,m}\}$ is the matrix with the partial inductances. Thus, the QS-PEEC model is stable if and only if

$$\begin{aligned} K_{\alpha,m} &> 0, & \alpha, m \in M. \\ C_{\alpha,i} &> 0, & \alpha, i \in M_c. \end{aligned} \quad (4.55)$$

4.3 Inclusion of PEEC models in circuit simulators

The general DGF-PEEC model as well as the PEEC models for the free and half space have an equivalent circuit formulation. The time- and frequency-domain solutions for the

PEEC models may be computed using a circuit-simulator software. The computational models developed in this monograph are programmed in two codes. The first one is the Berkeley SPICE3f4, which is used for the inclusion of

- the QS-PEEC model and
- the FW-PEEC model

for the free and half space in the frequency and time domain (see § 4.2). The above-mentioned models are composed by the standard circuit elements except for the time-delay controlled sources and are realized in the form of SPICE netlists. The required time-delay controlled sources are added through a minor modification of the SPICE source code.

The special-purpose circuit simulator NEAN has been developed by the author for the simulation of the following advanced time-domain PEEC models:

- standard free-space FW-PEEC model,
- S-FW-PEEC model (see § 4.5.5), and
- QD-DGFLM-PEEC model (see § 5.4).

The next two subsections consequently explain the questions related to inclusion of the standard QS- and FW-PEEC models in both codes. The modifications of these approaches used for advanced models are given in the sections, where these models are explained. The matter of this section requires preliminary reading Chapter 2.

4.3.1 PEEC models in Berkeley SPICE3f4

The QS-PEEC model in the time and frequency domain

The QS-PEEC model is developed in § 4.2.4, the corresponding equivalent circuit for a conductor segment is shown in Fig. 4.8. Initially, this model has been included in SPICE in [52] and [160]. Obviously, this model is composed of only resistances, capacitances, self and mutual inductances, and independent voltage sources. All these elements are present in every version of SPICE, hence, the total equivalent circuit for the interconnection system may be written as a SPICE-netlist (see, e.g., [157] and [151]). Since the generation of a netlist is a trivial task, it is not discussed more in this monograph.

The FW-PEEC model in the frequency domain

The frequency-domain FW-PEEC model is developed in § 4.2.1, its equivalent circuit with voltage sources (see Fig. 4.4a) has been included in SPICE in [52] and [160]. Obviously, the circuit in Fig. 4.4a consists of only resistances, capacitances, inductances, independent voltage sources, and the time-delay VCVS sources \hat{U}_α^L and \tilde{U}_α^c (4.38), which represent the mutual partial elements. These VCVS sources are not standard elements of SPICE and have

been added through a minor modification of its source code for the standard VCVS source, while other mentioned elements are standard and realized using the usual SPICE netlist.

The MNA-stamp for a simple VCVS source with a single control variable shown in Fig. 2.1b is explained in § 2.1.2. It may be expanded on the VCVS sources \hat{U}_α^L and \tilde{U}_α^c controlled by many variables. For simplicity, in the following, the VCVS source \hat{U}_α^L with only two summands is considered. In this case, (4.38) yields

$$\hat{U}_\alpha^L = a_{\alpha,q}(j\omega) U_p^L + a_{\alpha,p}(j\omega) U_q^L, \quad a_{\alpha,p}(j\omega) = \frac{L_{\alpha,p}}{L_{p,p}} e^{-j\omega\tau_{\alpha,p}}, \quad a_{\alpha,q}(j\omega) = \frac{L_{\alpha,q}}{L_{q,q}} e^{-j\omega\tau_{\alpha,q}}, \quad (4.56)$$

where α , p , and q are indexes of the current cells. $a_{\alpha,q}(j\omega)$ and $a_{\alpha,p}(j\omega)$ are linear frequency dependent factors of the controlled sources. We assume that the VCVS is included between the nodes n_1 and n_2 , while $L_{p,p}$ is located between nodes n_3 and n_4 , and $L_{q,q}$ between n_5 and n_6 . It is set that the current through $L_{\alpha,\alpha}$ has an index i . In this case, (4.56) obtains the following MNA-stamp formulation:

	n_1	n_2	n_3	n_4	n_5	n_6	i	RHS
n_1							1	
n_2							-1	
n_3								
n_4								
n_5								
n_6								
i	1	-1	$-a_{\alpha,p}(j\omega)$	$a_{\alpha,p}(j\omega)$	$-a_{\alpha,q}(j\omega)$	$a_{\alpha,q}(j\omega)$		

In general, the similar stamp may be applied to the VCVS for potential cells. The difference is only in the calculation of the factors $a_{\alpha,p}(j\omega)$. The increase of the number of summands in (4.38) does not change the structure of the stamp, but adds nonzero elements in i^{th} row of the system matrix. If the FW-PEEC model is not reduced, all cells are coupled to each other. Hence, the rows of the system matrix corresponding to the currents in self partial elements are filled with nonzero elements, which leads to a fully-filled system matrix. This changes significantly the run time of the solver. SPICE 3f4 considers the MNA system matrix as a sparse matrix, which is typical for circuits but wrong for the frequency-domain PEEC model. The application of sparse-matrix algorithms to the full-filled matrix leads to decrease of efficiency.

The FW-PEEC model in the time domain

The frequency-domain FW-PEEC model is developed in § 4.2.3, its equivalent circuit with voltage sources (see Fig. 4.6a) has been included in SPICE. It consists of resistances, capacitances, inductances, independent voltage sources, and the given by (4.50) time-delay VCVS (TDVCVS) sources $\hat{u}_\alpha^L(t)$ and $\tilde{u}_\alpha^c(t)$, which represent the mutual partial elements. While all other elements are realized using the usual netlist, the time-delay sources are set up through a minor modification of the SPICE source code.

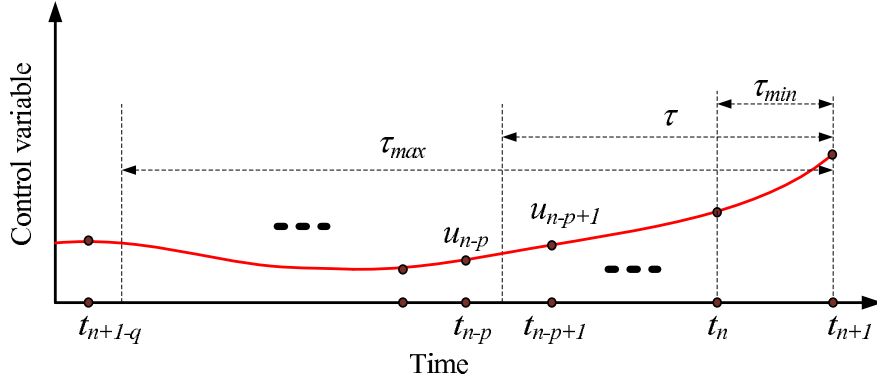


Figure 4.9: Calculation of the retarded control variable.

The TDVCVS sources for the current and potential cells (4.50) may be rewritten in the generalized form:

$$u_s(t) = a u(t - \tau), \quad (4.57)$$

where $u_s(t)$ is the instantaneous value of the voltage source, which is $\hat{u}_\alpha^L(t)$ for current cells and $\tilde{u}_\alpha^c(t)$ for potential cells. a is a constant coefficient, which is $\frac{L_{\alpha,m}}{L_{m,m}}$ for current cells and $\frac{p_{\alpha,i}}{p_{i,i}}$ for potential cells. $u(t - \tau)$ is the control variable, i.e., the voltage on the self partial element. τ is the delay time.

The time step is chosen from the condition $\Delta t \leq \tau_{min}$, which is the minimal delay time in the PEEC model. Thus, the value $u_s(t)$ at the discrete time point $t = t_{n+1}$ does not depend on the control variable at the same time point and may be represented using the MNA-stamp for an independent voltage source:

	n_1	n_2	i	RHS
n_1			1	
n_2			-1	
i	1	-1		$u_s(t_{n+1})$

where the time-delay voltage source is connected between nodes n_1 and n_2 , and i is the index of the TDVCVS current. Thus, every TDVCVS source introduces in the system matrix only four nonzero elements independent of the number of summands in (4.50). Consequently, although all cells are coupled, the system matrix is sparse and the MNA problem may be solved very efficiently. Since the system matrix is sparse, the increase of the number of nodes in the PEEC circuit does not lead to fast growing run time.

The most of the run time is spent on the calculation of the RHS vector that operation has an $O(N^2)$ complexity, where N is the number of current cells.

The calculation of a TDVCVS source at the actual time point $u_s(t_{n+1})$ is realized using a table with delayed values of the control variable. We denote the minimum and maximum time delays of the TDVCVS source by τ_{min} and τ_{max} , respectively. Since SPICE changes the time step during the solution, the discrete time points are located non-uniformly as shown in Fig. 4.9. However, the time step is limited by τ_{min} , and the automatically estimated time

step may not exceed the boundary. At the time t_{n+1} , only q last values of the control variable are required, where the value q is defined as $t_{n+1-q} \leq t_{n+1} - \tau_{max} \leq t_{n+2-q}$ (see Fig. 4.9). As it is illustrated in Fig. 4.9, the delayed value of the control variable is interpolated piecewise using the two nearest saved values:

$$u(t_{n+1}) = u_{n-p} + \delta (u_{n+1-p} - u_{n-p}) \quad \text{with} \quad \delta = \frac{t_{n+1} - \tau - t_{n-p}}{t_{n+1-p} - t_{n-p}}. \quad (4.58)$$

Then, the value $u(t_{n+1})$ is substituted in (4.57), and the result is added to the RHS vector using the MNA stamp of the independent voltage source.

4.3.2 Standard full-wave PEEC model in the NEAN code

The special-purpose circuit simulator NEAN is programmed especially for the time-domain simulation of the advanced PEEC models developed in this monograph. All these models use the time-domain macromodels based on the FSCM concept, whose programming in SPICE is possible but requires a significant modification of its code. Additionally, the general-purpose code as SPICE is not optimal for the analysis of PEEC circuits, which have several particular features.

- The time step required for the time-domain simulation of the interconnection system is constrained not only by the local truncation error of the numerical integration as usual circuit, but also by the maximum frequency of interest f_m , which is related to the grid step Δl used for the spatial discretization. As the correct spatial discretization is expressed by (3.12), the correct time discretization is constrained by the following criterion:

$$\Delta t \leq \frac{T_{min}}{40}, \quad T_{min} = \frac{1}{f_m}, \quad (4.59)$$

i.e., more than 40 discrete points per period of the highest harmonic of interest. Otherwise, the excitation waveform will be significantly distorted because of too rough discretization. One more factor limits the time step only for the standard FW-PEEC model (but not for advanced models based on the FSCM) is the minimal time delay τ_{min} . As it is agreed in § 4.3.1,

$$\Delta t \leq \tau_{min}. \quad (4.60)$$

- Decrease of the time step below the strictest constraints (4.59) and (4.60) is not necessary because the solution of the problem has a spectrum limited by f_m .
- The time-domain FW-PEEC circuit yields the MNA formulation with a sparse system matrix. Hence, the bottle neck of the algorithm is the computation of the RHS vector, which is an $O(N^2)$ operation.

The aforementioned facts show that the numerical integration with the variable time step as in Berkeley SPICE is inefficient in the case of the PEEC model. On the one hand, SPICE estimates Δt at each time point, but may not increase it because of the constraints (4.59) and

(4.60). On the other hand, the decrease of the time step leads to high-frequency oscillations in the solution, which are not supported by the spatial discretization. Thus, SPICE produces a large number of redundant operations.

The NEAN code is set up on the basis of the backward differentiation formula of the second order (BD2) (2.15) with a constant time step, which is chosen according to the constraints (4.59) and (4.60). Since the numerical rule used is L-stable, it produces a correct solution at the frequency range of the interest, which is caused by the constraints on the time step, and filter out the oscillations at $f \gg f_m$. The BD2 rule has the order 2, its error constant is $-2/9$, i.e., BD2 is slightly less exact than the method of trapezoids (see § 2.2.1) applied in SPICE, but the order of both methods is the same. This approach causes several advantages as compared to the numerical integration with the variable time step.

- No redundant operations for the time-step estimation are required.
- No unnecessary decreasing of the time step may appear.
- The system matrix of the MNA problem does not change in time, since the matrix contributions of ADC circuits are constants if the time step is constant (see § 2.2.2). Consequently, the matrix may be one time decomposed on the sub- and superdiagonal matrices that are applied at all following time steps for the solution of the MNA problem. This reduces the run time for the matrix operations significantly.

In general, the NEAN code applies the same MNA formulation as the Berkeley SPICE, but uses another strategy for the control of the time step and a more suitable numerical rule. Consequently, the MNA-stamp for the time-delay VCVS source presented in § 4.3.1 for SPICE is also valid for NEAN. The standard circuit elements of SPICE are realized in NEAN using their conventional MNA-stamps given, e.g., in [156] and their ADC circuits for the BD2 rule.

The advanced PEEC models apply the time-domain FSCM macromodels (see § 3.6) that are developed in terms of ADC circuits. The ADC formulations and MNA-stamps for these special elements may be found in the corresponding sections of this work (see § 4.4.3, § 4.5.5, and § 5.4).

4.4 Skin effect in PEEC models

The above-considered time-domain PEEC models may be applied for the analysis of interconnections excited by broad-band signals, i.e., at frequencies from DC up to f_m . This maximum frequency of interest can be so high that the skin effect is not negligible, and conductor losses can essentially exceed the DC losses included in the standard PEEC model using the formulation (4.13).

The analysis of interconnections, where the skin and proximity effects are significant with the conventional PEEC method needs a transversal discretization of the conductor cross-section as proposed in [35]. This approach increases the number of unknowns dramatically, since the skin depth can be much less than the transversal dimension of the conductor.

This section considers a more efficient approach to the inclusion of skin effect in the PEEC model. While the approach [35] models the physical distribution of the current in the cross-section of conductors numerically, the alternative is the behavioral macromodeling of the skin-effect influence. Since skin effect causes a frequency dependence of the longitudinal impedance of the conductor, its influence can be modeled in the integral form by including a serial impedance in current cells. This technique has been initially applied to transmission-line models, sorting historically, in [90], [70], [89], and [28]. The authors simulate the frequency dependence of the transmission-line longitudinal impedance with stair-case equivalent circuits. These circuits have a predefined structure and parameters computed for a particular wire geometry. Thus, the stair-case circuits are *parametric macromodels*.

The first heuristic application of the stair-case circuits to the standard PEEC model has been presented in [53] and [52]. The rigorous derivation of a PEEC formulation in the frequency domain involving the *mean surface impedance* (MSI) of the conductor has been developed by the author in [161]. The time-domain representation of this model requires macromodeling the frequency dependent surface impedance. This may be realized through the usual stair-case circuits [161] and by applying the full spectrum convolution macromodeling. This section studies and compares both possibilities.

The derivation of the approach is based on the revision of (4.12), where we assume the uniform distribution of the current in the cross-section. The exact expression is kept instead of the approximation in (4.12):

$$-\iint_S \mathbf{w}_\alpha(\mathbf{r}) \cdot \left(\hat{\mathbf{n}} \times \hat{\mathbf{n}} \times \frac{\mathbf{J}(\mathbf{r})}{\sigma} \right) dS = \frac{1}{d_\alpha} \iint_{A_\alpha} \hat{\mathbf{e}}_\alpha \cdot \mathbf{E}(\mathbf{r}) dA_\alpha. \quad (4.61)$$

The mean surface impedance for the current cell can be defined as follows:

$$Z_\alpha^s(j\omega) = \frac{1}{d_\alpha I_\alpha} \iint_{A_\alpha} \hat{\mathbf{e}}_\alpha \cdot \mathbf{E}(\mathbf{r}) dA_\alpha, \quad (4.62)$$

which allows one to write instead of (4.13) the following formula:

$$Z_\alpha^s(j\omega) I_\alpha. \quad (4.63)$$

Since the inclusion of (4.63) in the DGF-PEEC model does not change the derivation of partial elements, the equivalent circuit is similar to the standard one. The only difference is in the replacement of the resistance R_α by $Z_\alpha^s(j\omega)$. Thus, the standard PEEC models in the frequency (see Fig. 4.4a) and time domain (see Fig. 4.6a) are transformed in the form shown in Fig. 4.10. The following section is devoted to the calculation of $Z_\alpha^s(j\omega)$ for different types of wire cross-sections. This frequency responses may be directly included in the computation for the frequency domain models in Fig. 4.10a. § 4.4.2 and § 4.4.3 give two approaches for the time-domain macromodeling of $Z_\alpha^s(j\omega)$ used in Fig. 4.10b.

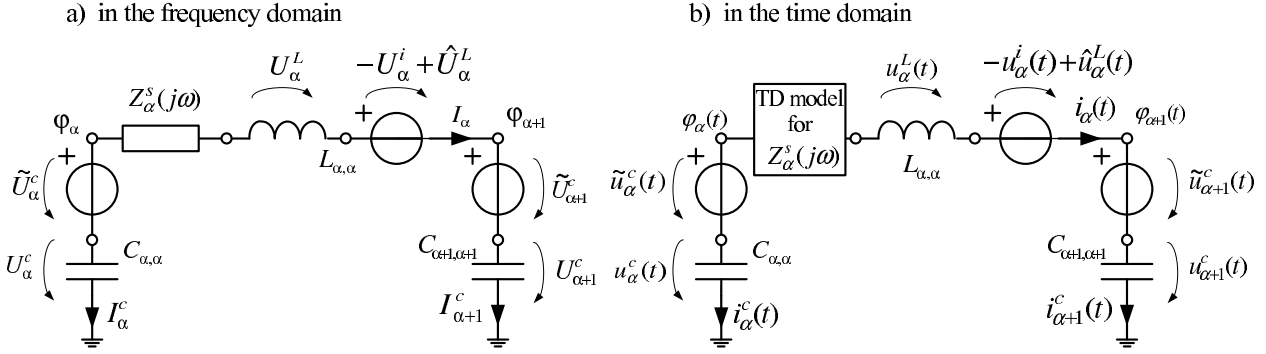


Figure 4.10: PEEC models with skin effect.

4.4.1 Calculation of the mean surface impedance

The defined by (4.62) mean surface impedance describes a relation between the current in the cell and the mean electric field intensity on the surface of this cell. Since this relation is determined through the geometry and material of the conductor, the MSI may be computed using an auxiliary problem. An infinitely long transmission line with the same material and cross section as the current cell is considered. The distance between the direct and return wires is set so large that the proximity effect does not influence the results. An incident electric field E^i is impressed at all points of the wire surface (see Fig 4.11a). Since the electric field intensity and the current density distributions can be calculated over the cross-section, the mean surface impedance can be obtained directly through (4.62):

$$Z_\alpha^s(j\omega) = l_\alpha Z'_s(j\omega) \quad \text{with} \quad Z'_s(j\omega) = \frac{1}{sI} \oint_s E(x, y) ds, \quad (4.64)$$

where $Z'_s(j\omega)$ is the per unit length MSI, s is the perimeter of the cross-section, I is the current in the conductor. The particular approach for the calculation of $Z_\alpha^s(j\omega)$ with (4.64) depends on the cross-section of the conductor. The solutions in closed form can be derived for round and rectangular cross-sections (see (B.1) and (B.2) respectively). A very useful approximated closed-form solution for microstrip lines with a rectangular cross-section is developed in [39].

The mean surface impedance for the conductor with an arbitrary cross-section can be calculated numerically by different methods. Generally, we have to compute the electric field intensity in the discrete points over the perimeters of the cross-section and, then, calculate the integral (4.64) as a sum. The most suitable numerical method is the boundary element method [91], since it requires the discretization of only the boundary between the conductor and dielectric. Alternatively, the two-dimensional realizations of differential methods may be applied, they need discretization of the total conductor cross-section. In contrast to the BEM, the differential methods produce a sparse system matrix, and their efficiency can be comparable with the BEM.

An original approach for the numerical computation of MSI (see [161]) using the PEEC method is presented below. The conductor is divided into the current filaments as shown

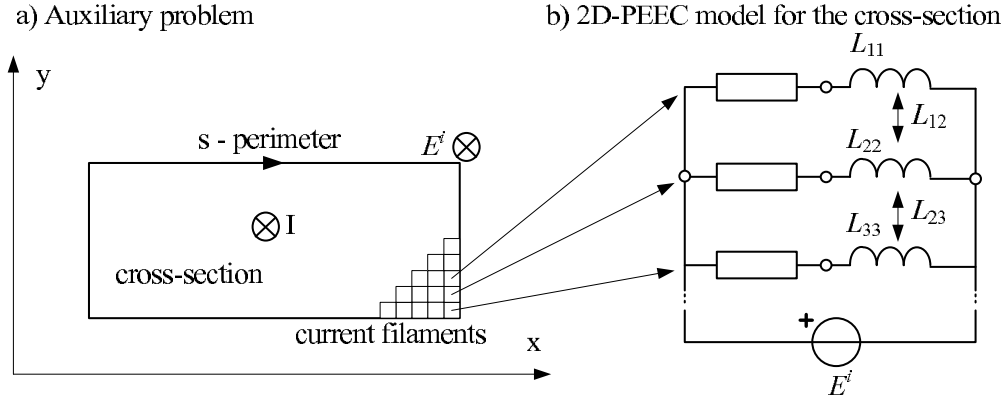


Figure 4.11: Calculation of the mean surface impedance.

in Fig 4.11a. The filaments are assumed as thin wires characterized by per unit length resistances, partial self and mutual inductances. The capacitive couplings between filaments are neglected. This simplified quasi-static inductive PEEC model can be derived from the MPIE with the two-dimensional quasi-static free-space Green's function. The equivalent circuit becomes a set of parallel connected branches that model the filaments (see Fig 4.11b). Finally, the partial inductances can be computed in the terms of geometrically mean distances (GMD), which are described in [147], as follows:

$$L'_{k,k} = \frac{\mu_0}{2\pi} \ln \frac{g'_{k,k}}{g_{k,k}}, \quad L'_{k,m} = \frac{\mu_0}{2\pi} \ln \frac{g'_{k,m}}{g_{k,m}}. \quad (4.65)$$

where $g_{k,k}$ is the geometrically mean size of the k^{th} filament, $g'_{k,k}$ is the GMD between the k^{th} filament and its return filament, $g_{k,m}$ is the GMD between the k^{th} and m^{th} filaments, $g'_{k,m}$ is the GMD between the k^{th} and return m^{th} filaments [147]. The current distribution over the cross-section can be found from the following matrix equation:

$$\begin{aligned} \mathbb{Z} \mathbf{I} &= \mathbf{u} \Rightarrow \mathbf{I} = \mathbb{Z}^{-1} \mathbf{u}, \\ \mathbb{Z} &= \{z_{k,m}\}, \quad z_{k,m} = \begin{cases} R'_k + j\omega L'_{k,k}, & k = m \\ j\omega L'_{k,m}, & k \neq m \end{cases}, \\ \mathbf{I} &= \{I_k\}, \quad \mathbf{u} = \{u_k\}, \quad R'_k = \frac{1}{\sigma a_k} \quad k, m = \overline{1, N}, \end{aligned} \quad (4.66)$$

where R'_k , a_k , and I_k are resistances, cross-section surfaces, and currents in filaments. N is the number of filaments. $u_k = E^i$ is the equal for all filaments electric field used for the excitation. The current in the total conductor is the sum of all currents in filaments, the MSI is calculated as a sum instead of the integral in (4.64) follows:

$$Z'_s(j\omega) = \frac{1}{sI} \sum_{k \in s} \frac{I_k}{a_k \sigma}, \quad \text{with } I = \sum_{k=1}^N I_k, \quad (4.67)$$

where $k \in s$ means the filaments on the surface of the wire.

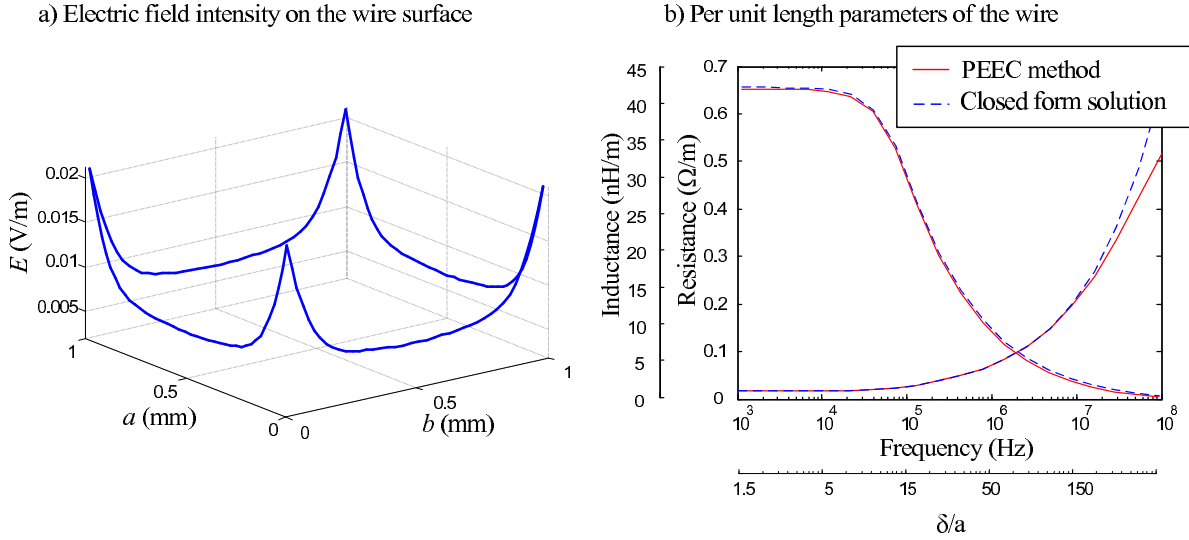


Figure 4.12: Mean surface impedance of the wire with the rectangular cross-section.

E.g., the distribution of the current in the copper wire with a square cross-section of 1 mm^2 is calculated with the help of the closed form solution shown in (B.2) and numerically by (4.67). The computation is done at $f=1 \text{ MHz}$, the skin depth (1.53) for this frequency is 0.066 mm . The distribution of the electric field intensity on the conductor surface computed by the PEEC method is shown in Fig. 4.12a. The frequency response of the internal inductance and resistance are presented in Fig. 4.12b. Obviously, both solutions are same at low frequencies. At high frequencies, the difference between solutions increases, since the numerical solution has not enough currents filaments for the correct modeling of the current distribution, and the closed-form solution uses an assumption, which is wrong at high frequencies. It may be resumed that both approaches give only an approximate solution at high frequencies.

4.4.2 Time-domain modeling of skin effect using the stair-case circuits

As mentioned above, the PEEC model in the frequency domain may include $Z_s(j\omega)$ directly, according to Fig. 4.10a. Another situation appears in the time domain. $Z_s(j\omega)$ results in a step response, which cannot be directly reproduced by a typical circuit element. The time-domain macromodeling is a natural solution for this problem.

The frequency response $Z_s(j\omega)$ may be modeled by an equivalent circuit. A number of such circuits has been introduced in the literature devoted to transmission lines. The most suitable variant (see [90]) is shown in Fig. 4.13a. It is a stair-case circuit, whose number of stairs is set between 4 and 8, usually. As the structure of the circuit is predefined, we have to find only its parameters, namely, resistances and inductances. There are several mentioned in [52] heuristical approaches for evaluation of these parameters, but we consider here a

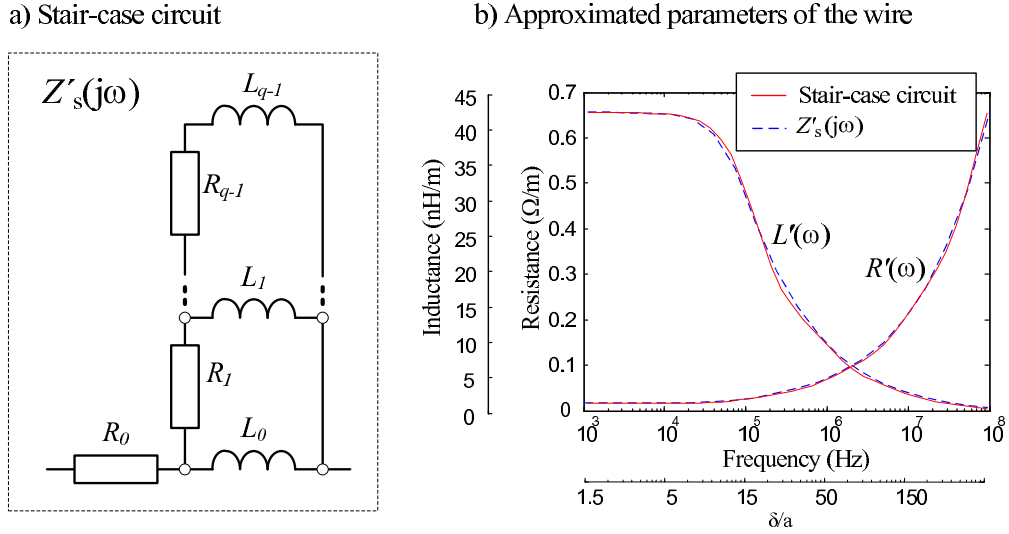


Figure 4.13: Approximation of $Z_s(j\omega)$ using the stair-case circuits.

general approach based on the solution of the following inverse problem proposed in [89]:

$$\min_{\mathbf{P}} \left(\int_{\omega_{min}}^{\omega_{max}} \left(\frac{|Z_s(j\omega) - \tilde{Z}_s(j\omega)|}{|Z_s(j\omega)|} \right)^2 d\omega \right)^{1/2}, \quad (4.68)$$

where $\tilde{Z}_s(j\omega)$ is the impedance of the stair-case circuit, \mathbf{P} is the vector with unknown parameters of the circuit. The goal function of the optimization problem is formulated so that the parameters of the circuit are optimal in the sense of the minimal least square approximation error in the frequency range from ω_{min} up to ω_{max} . Generally, the vector of parameters consists of all unknown inductances and resistances, which is a relatively large number of unknowns. The problem (4.68) can be simplified by definition the parameters of the stair-circuit as follows:

$$\begin{aligned} R_0 &= \Re \{ Z_s(\omega_{min}) \}, & L_0 &= \Im \left\{ \frac{Z_s(\omega_{min})}{\omega_{min}} \right\}, \\ R_k &= R_0 \varsigma^k, & L_k &= L_0 \nu^k, & k &= \overline{1, q-1}, \end{aligned} \quad (4.69)$$

where q is the number of stairs, R_0 and L_0 are static internal resistance and inductance of the wire. In this case, the vector of the parameters in (4.68) consists of only two components: $\mathbf{P} = [\varsigma, \nu]$. Fig. 4.13b shows the results of the solution of the inverse problem (4.68) for the wire with the rectangular cross-section, whose parameters are given in the previous subsection. Obviously, the stair-case circuit with 5 stairs represents the frequency response $Z'_s(j\omega)$ with a fair precision.

Example of application

The next example demonstrates the application of the PEEC model with stair-case circuits for the simulation of a two-wire transmission line, whose length is 40 cm. The cross-

section of the copper line is shown in Fig. 4.14a. The left termination of the transmission line is excited by a voltage source with an internal impedance of 30Ω , the right termination is open.

The problem is solved in the time and frequency domain using four kinds of models. The first couple of models is based on the transmission-line theory (Bergeron's method, see § 3.4). These models are standard elements of SPICE. The first describes the interconnection as a lossless line, the second includes frequency independent losses (DC losses). The second couple of computational models are the PEEC models with lossless conductors and with stair-case circuits.

Results in the frequency domain

The voltage-source amplitude is set 1 V at all frequencies. The current at the left termination of the transmission line is calculated at the frequency range from 1 MHz up to 1 GHz. The results (see Fig. 4.14a) show that conductor losses influence the processes in the system significantly. The both lossless models provide similar undamped frequency response of the current. The SPICE model with DC losses introduces frequency-independent damping at all frequencies. The PEEC method with skin effect models the frequency dependence of damping precisely.

Results in the time domain

The time response of the transmission line on the trapezoidal excitation waveform shown in Fig. 4.14b is calculated using the same four models. One may observe that the time-response waveform has a frequency dependent attenuation caused by skin effect. The rise time of the load pulse is lengthened, since the excitation has a rise time 250ps, whose cut-off frequency reaches the GHz-range. Certainly, this signal-integrity problem may not be computed by the three models that do not include skin effect. Additionally to damping, the frequency dependent losses may influence the wave impedance of the transmission line, which poses hard signal-integrity problems and makes important the correct analysis of skin effect.

The PEEC models with stair-case circuits have certain advantages with regard to the 3D-discretization of conductors and several disadvantages:

- This approach involves an optimization problem. Hence, the preprocessing computations can be inefficient due to numerous local extrema.
- The inclusion of stair-case circuits into the PEEC model leads to a large number of additional nodes in the circuit. The dimension of the equation system grows that increases the run time. As mentioned in § 4.3, the MNA system matrix is sparse for the FW-PEEC circuits (minor efficiency losses by additional nodes) and fully-filled for the QS-PEEC models (strong efficiency losses by additional nodes). Thus, the stair-case circuits are more efficient in application to the FW-PEEC models.

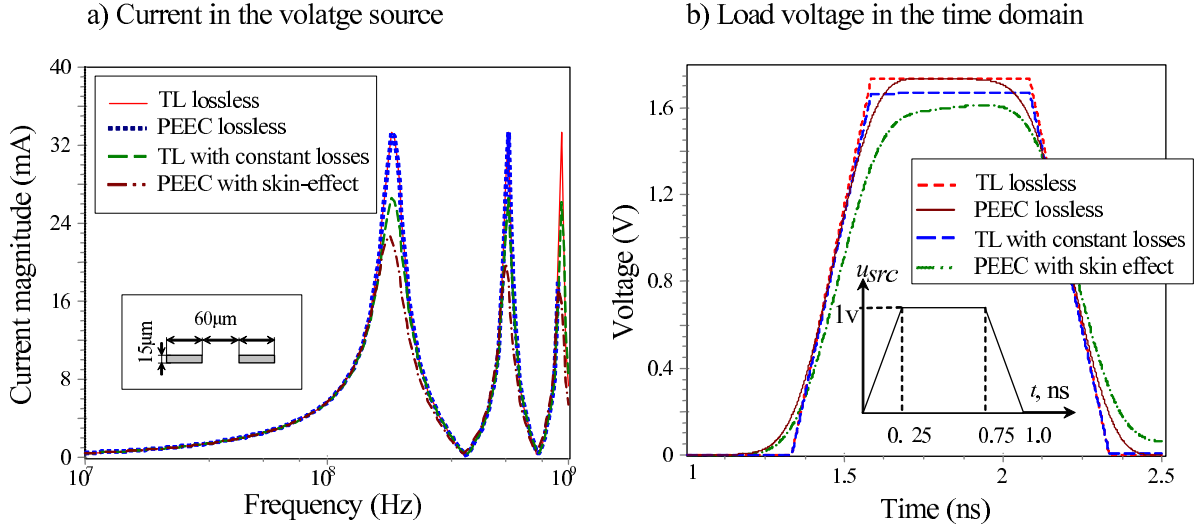


Figure 4.14: The modeling of skin effect in the time and frequency domain.

4.4.3 Time-domain modeling of skin effect using the FSCM

Both disadvantages of the stair-case circuits may be avoided using another approach developed by the author: macromodeling $Z'_s(j\omega)$ using the FSCM. According to the general strategy presented in § 3.6, we should find an approximation with the same asymptotic behavior as $Z_s(j\omega)$ and derive the impulse response for this function. Since $\lim_{\omega \rightarrow \infty} Z'_s(j\omega) = \infty$, the impulse response for the transfer function calculated as its inverse Fourier transformation cannot be computed. However, the one-port element $Z'_s(j\omega)$ (see Fig. 4.15a) may be equivalently represented in the admittance form $Y'_s(j\omega) = 1/Z'_s(j\omega) = I/U$. Analogous to $Z'_s(j\omega)$, $Y'_s(j\omega)$ is named the *mean surface admittance*, where $\Re\{Y'_s(j\omega)\}$ and $\Im\{Y'_s(j\omega)\}$ are the ohmic and reactive conductivity of the conductor, whose example frequency response is shown in Fig. 4.15b for a copper wire with a square cross-section 1×1 mm.

In contrast to $Z'_s(j\omega)$, $\lim_{\omega \rightarrow \infty} Y'_s(j\omega) = 0$. Hence, the Fourier integral of functions with the same asymptotic behavior may exist. Unfortunately, $Y'_s(j\omega)$ is computed either numerically or through a complicated closed-form expression. In both cases, the IFT in closed form is impossible. Thus, according to the FSCM strategy, we propose for $Y'_s(j\omega)$ a frequency-domain approximation $\tilde{Y}'_s(j\omega)$, which may be transformed in the time domain in closed form:

$$\tilde{Y}'_s(j\omega) = \frac{1}{R'_0} \cdot \frac{1}{\sqrt{1 + j\omega\tau_c}}. \quad (4.70)$$

$\tilde{Y}'_s(j\omega)$ has two parameters R'_0 , and τ_c . Of course, this approximation is not unique, but it has been found as optimal with respect to the ratio between the precision and simplicity. $\tilde{Y}'_s(j\omega)$ is equal to the initial frequency response at the asymptotic points $\omega = 0$ and $\omega = \infty$, and it provides an acceptably precise approximation at the total frequency range of interest.

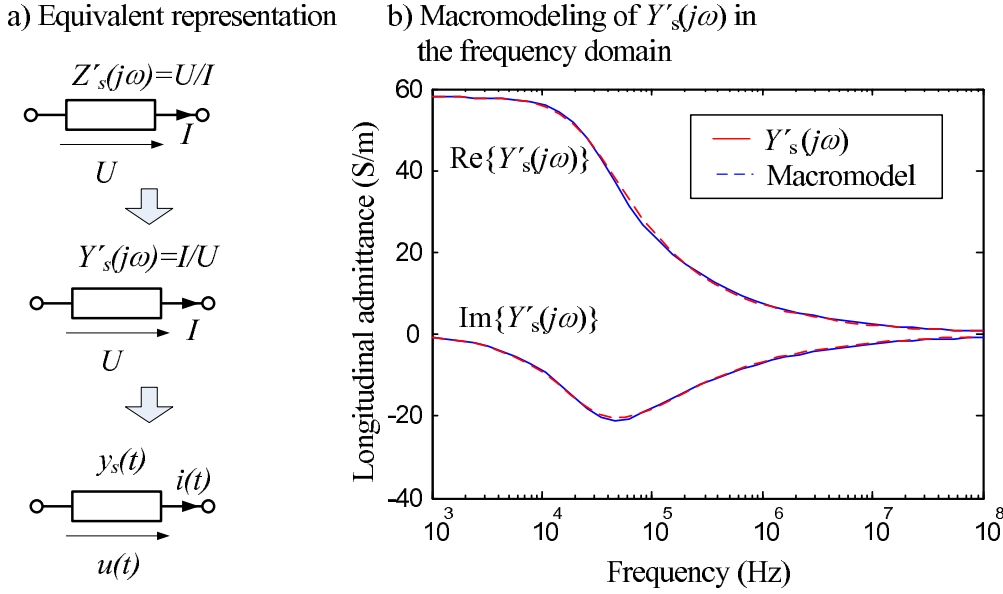


Figure 4.15: FSCM model of the mean surface impedance.

The substitution $\omega = 0$ into (4.70) leads to the formulation for R'_0 :

$$\tilde{Y}'_s(0) = \frac{1}{R'_0} \Rightarrow R'_0 = \Re \{Z'_s(0)\}, \quad (4.71)$$

which guarantees the exact approximation of the DC ohmic resistance at low frequencies. The Taylor-series expansion of $\tilde{Y}'_s(j\omega)$ at $\omega = 0$ gives:

$$\lim_{\omega \rightarrow 0} \Im \left\{ \frac{1}{\tilde{Y}'_s(0)} \right\} = R_0 \frac{\tau_c}{2} \omega + O(\omega^2). \quad (4.72)$$

Since the imaginary part of the wire impedance is $\omega L'(\omega)$, the second parameter of (4.70) may be calculated as

$$\tau_c = 2 \frac{L_0}{R_0}, \quad \text{with } L_0 = L(0). \quad (4.73)$$

This equation gives the first possible estimation of τ_c based on the accurate modeling of the static internal inductance of the wire. The asymptotic expansion for (4.70) at high frequencies shows that the real and imaginary parts of $1/\tilde{Y}'_s(j\omega)$ are equal and increase as $\sqrt{\omega}$. This guarantees the same behavior with the initial function.

The second parameter in (4.70) τ_c can be alternatively estimated more exact than by (4.73). One can prove that $\Im \left\{ \tilde{Y}'_s(j\omega) \right\}$ has the minimum (see Fig. 4.15b) at $\omega = \sqrt{3}/\tau_c$. Therefore, τ_c can be estimated as follows:

$$\tau_c = \frac{\sqrt{3}}{\omega_{min}}, \quad (4.74)$$

where ω_{min} is the extremum of the initial frequency response. This second estimation produces the best accuracy of the approximation at middle frequencies and a certain deviation

of the static inductance, while the resistance is modeled accurate at all frequencies. Since a small deviation of the wire inductance at low frequencies (at high frequencies the inductance is computed accurately) does not change the dynamic behavior of the system, we assume the estimation (4.74) better than (4.73). Its accuracy can be appreciated from Fig. 4.15b, where the comparison between $Y'_s(j\omega)$ and $\tilde{Y}'_s(j\omega)$ is shown for the copper wire with a square cross-section 1×1 mm.

Thus, we have an acceptable approximation for $Y'_s(j\omega)$ in the frequency domain, whose parameters are calculated in closed form avoiding the solution of an inverse problem as in § 4.4.2. The impulse and step responses for $Y'_s(j\omega)$ are derived as follows:

$$y(t) = \frac{1}{R_0} \frac{e^{-t/\tau_c}}{\sqrt{\pi t \tau_c}} h(t), \quad (4.75)$$

$$s(t) = \frac{1}{R_0} \operatorname{erf} \left(\frac{t}{\tau_c} \right) h(t), \quad (4.76)$$

where $h(t)$ is the Heaviside step function, $\operatorname{erf}()$ is the error function, $y(t)$ is the impulse response for the admittance. Since $s(0) = 0$, we substitute it in (3.19) and calculate instantaneous value of the current using the convolution integral:

$$i(t) = \int_0^t y(t - \vartheta) u(\vartheta) d\vartheta. \quad (4.77)$$

According to (3.20), we apply a piecewise approximation for $u(t)$ on the discrete time axis:

$$u(t) = a_{n+1}(t - t_n) + b_{n+1}, \quad t \in [t_n, t_{n+1}], \quad a_{n+1} = \frac{u_{n+1} - u_n}{\Delta t}, \quad b_{n+1} = u_n, \quad (4.78)$$

The integral (4.77) may be written as a sum of integrals over time steps:

$$i(t_{n+1}) = i_{n+1} = \sum_{k=0}^n \int_0^{\Delta t} y(t_{n+1} - t_k - \vartheta) (a_{k+1} \vartheta + b_{k+1}) d\vartheta. \quad (4.79)$$

The integrals over time steps are calculated in closed form:

$$\begin{aligned} & \int_0^{\Delta t} y(t_{n+1} - t_k - \vartheta) (a_k \vartheta + b_k) d\vartheta = \\ & + \frac{1}{R_0} \left[a_k \sqrt{\frac{\tau_c T_{n+1,k}}{\pi}} \Psi_{n+1,k} + \left(a_k T_{n+1,k} + b_k - \frac{a_k}{2} \tau_c \right) \Phi_{n+1,k} \right] \\ & - \frac{1}{R_0} \left[a_k \sqrt{\frac{\tau_c T_{n,k}}{\pi}} \Psi_{n,k} + \left(a_k T_{n+1,k} + b_k - \frac{a_k}{2} \tau_c \right) \Phi_{n,k} \right] \end{aligned} \quad (4.80)$$

$$\text{with } \Psi_{n,k} = e^{-\frac{T_{n,k}}{\tau_c}}, \quad \Phi_{n,k} = \operatorname{erf} \left(\frac{\sqrt{T_{n,k}}}{\sqrt{\tau_c}} \right), \quad T_{n,k} = t_n - t_k = (n - k) \Delta t.$$

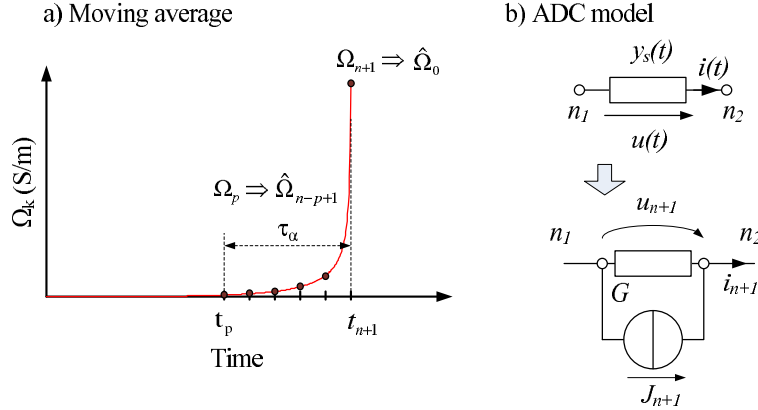


Figure 4.16: Coefficients Ω_k (a), and the ADC model for skin effect (b).

Substituting (4.80), the sum of integrals (4.79) may be compact rewritten analogous to (3.21) in a moving-average form:

$$i_{n+1} = \sum_{k=p}^{n+1} \Omega_k u_k, \quad 0 \leq p \leq n+1. \quad (4.81)$$

The sum of integrals in (4.79) involves the discrete values u_k with $0 \leq k \leq n+1$, while the sum (4.81) uses fewer points $p \leq k \leq n+1$. This difference is caused by the selectivity of $y(t)$. The coefficients for (4.81) are derived using (4.80) as follows:

$$\Omega_k = \frac{1}{R_0 \Delta t} \begin{cases} -\sqrt{\frac{\tau_c T_{n+1,k}}{\pi}} \Psi_{n+1,k} + \left(-T_{n,k} + \frac{\tau_c}{2}\right) \Phi_{n+1,k} \\ + \sqrt{\frac{\tau_c T_{n,k}}{\pi}} \Psi_{n,k} - \left(-T_{n,k} + \frac{\tau_c}{2}\right) \Phi_{n,k} & k = p \\ \\ + \sqrt{\frac{\tau_c T_{n+1,k-1}}{\pi}} \Psi_{n+1,k-1} + \left(T_{n+1,k-1} - \frac{\tau_c}{2}\right) \Phi_{n+1,k-1} \\ - \sqrt{\frac{\tau_c T_{n,k-1}}{\pi}} \Psi_{n,k-1} - \left(T_{n+1,k-1} - \frac{\tau_c}{2}\right) \Phi_{n,k-1} & k = n+1 \\ \\ - \sqrt{\frac{\tau_c T_{n+1,k}}{\pi}} \Psi_{n+1,k} + \left(-T_{n,k} + \frac{\tau_c}{2}\right) \Phi_{n+1,k} \\ + \sqrt{\frac{\tau_c T_{n,k}}{\pi}} \Psi_{n,k} - \left(-T_{n,k} + \frac{\tau_c}{2}\right) \Phi_{n,k} \\ + \sqrt{\frac{\tau_c T_{n+1,k-1}}{\pi}} \Psi_{n+1,k-1} + \left(T_{n+1,k-1} - \frac{\tau_c}{2}\right) \Phi_{n+1,k-1} \\ - \sqrt{\frac{\tau_c T_{n,k-1}}{\pi}} \Psi_{n,k-1} - \left(T_{n+1,k-1} - \frac{\tau_c}{2}\right) \Phi_{n,k-1} & \text{otherwise} \end{cases} \quad (4.82)$$

The typical dependence of these coefficients on the index is shown in Fig. 4.16a. The maximal value corresponds to the actual time point, other coefficients decrease towards the time delay with respect to t_{n+1} . Thus, the number of summands is a constant for all time steps, it is denoted by $n_\alpha = n+2-p$. The width of the moving average window is denoted by $\tau_\alpha = n_\alpha \Delta t$.

The last step for the development of a FSC macromodel is the formulation of the moving average (4.81) as an ADC, which is needed for the inclusion into the time-domain circuit

solver as all other elements of the PEEC model (see § 4.3). Thus, the MNA stamp for this ADC (see § 2.2.2) has to be developed. The moving average (4.81) giving the relation between the current and voltage may be rewritten as follows:

$$\begin{aligned} i_{n+1} &= \hat{\Omega}_0 u_{n+1} + \hat{\Omega}_1 u_n + \hat{\Omega}_2 u_{n-1} + \dots = \\ &= \hat{\Omega}_0 u_{n+1} + \sum_{k=n-n_\alpha+2}^n \hat{\Omega}_{n-k+1} u_k \quad \text{with} \quad \hat{\Omega}_k = \Omega_{n-k+1}. \end{aligned} \quad (4.83)$$

Since the modified coefficients $\hat{\Omega}_k$ do not depend on n , the formulation (4.83) is applicable at all discrete time point. It can be considered as the relation between the current and voltage for the Norton generator shown in Fig. 4.16b:

$$i_{n+1} = g u_{n+1} + J_{n+1} \quad \text{with} \quad g = \hat{\Omega}_0 \quad \text{and} \quad J_{n+1} = \sum_{k=n-n_\alpha+2}^n \hat{\Omega}_{n-k+1} u_k. \quad (4.84)$$

The MNA stamp for the ADC of the mean surface impedance given by (4.84) is trivial:

	n_1	n_2	RHS
n_1	g	$-g$	$-J_{n+1}$
n_2	$-g$	g	J_{n+1}

where the Norton generator is connected between nodes with indexes n_1 and n_2 .

Example of application: skin effect in a microstrip line

A copper microstrip line is located on the 0.1 mm thick substrate. The thickness of the microstrip is 10 μm , the width is 0.2 mm, the length is 20 mm, the relative permittivity of the substrate is 4. The left side of the line is excited by a voltage source with a ramp waveform. The left side of the line is loaded by a 50 Ω resistance. The voltage source grows from 0 up to 1 V with the rise time τ_r . Two numerical experiments with $\tau_r = 100$ ns (f_m is assumed 10 MHz) and $\tau_r = 0.1$ ns (f_m is assumed 10 GHz) has been performed. The results for both τ_r are shown in Fig. 4.17a and Fig. 4.17b. Each figure consists of three curves: the excitation, the load voltage calculated with assumption of only DC losses, and the load voltage calculated with frequency dependent losses modeled by FSCM. The frequency response of the mean surface impedance for the microstrip line is calculated by the closed form formulation given in [39]. It takes into account skin effect as well as the proximity effect. Therefore, $Z_s(j\omega)$ differs slightly from the typical frequency response of skin effect approximated by (4.70). Since the internal inductance influences on transients in microstrip lines negligibly [58], $\tilde{Z}_s(j\omega)$ approximates exactly only the ohmic losses, while the frequency dependence of the internal inductance is approximated quite rough.

The wave impedance of the line is computed about 50 Ω . The load voltage is awaited to be delayed on about 1.15 ns. The first calculation with $\tau_r = 100$ ns (see Fig. 4.17a) shows identical results for models with and without frequency dependent losses. This can be

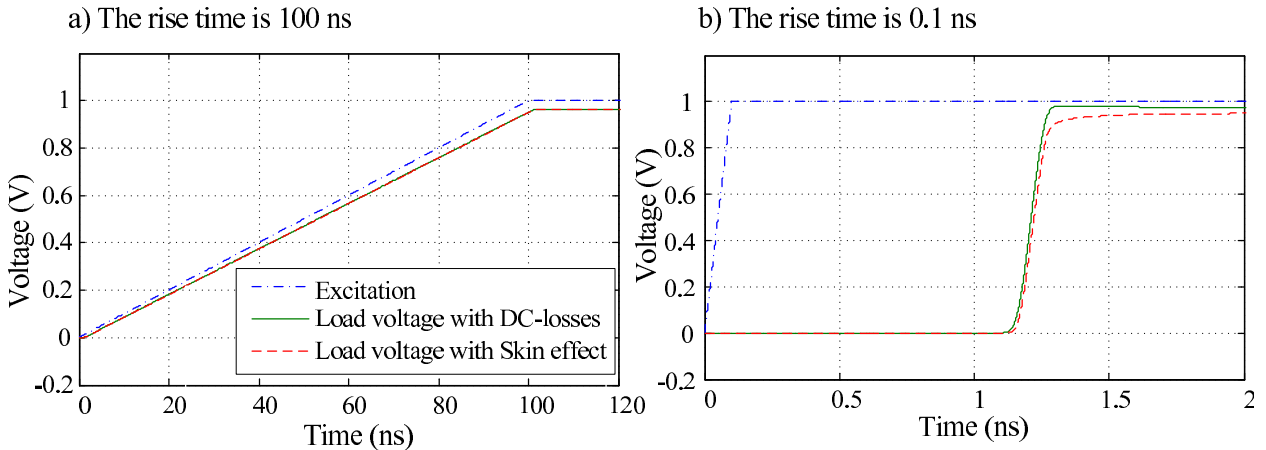


Figure 4.17: Simulation results for a microstrip line in the time domain.

explained by the fact that the excitation spectrum is limited by 10 MHz. The attenuation introduced by skin effect at these frequencies is minor, and both models yield the same results. In contrast, the calculation with $\tau_r = 0.1$ ns (see Fig. 4.17b) shows a significant difference between models. The frequency dependent attenuation introduced by skin effect has decayed the edge rate of the waveform, which is strongly rounded, as it is characteristic of conductors with skin effect.

4.5 Stability and accuracy

The DGF-PEEC method and all its simplified formulations are based on the weighted-residual method and two additional approximative techniques leading to an equivalent circuit. The two approximations introduce inaccuracies, which should be studied and improved if possible. The derivation of the DGF-PEEC method (see § 4.1) approximates the gradient of the scalar electric potential via the difference quotient as written in (4.20). This numerical approximation is used in some other numerical methods as well, e.g., in the FDTD. The typical consequence of applying this to the FDTD is the solution, which is correct at the frequency range of interest but shows small deviations for higher frequencies. In the time domain, these deviations appear in the form of non-physical damped oscillations with frequencies higher than f_m . These oscillations are caused by the difference between the physical and numerical propagation velocity in the model [144], i.e., by the inconsistency of the FDTD method. Since the equivalent-circuit models for transmission lines can be derived via the application of the one-dimensional Yee algorithm (FDTD method) to the transmission-line equations, we observe the same high frequency oscillations in the FDTD solutions [90], [121]. The improvement of this inaccuracy may be reached by the application of more accurate formulas of difference quotients. This technique has been applied to transmission lines in [90]. As the equivalent circuits for transmission lines have many similarities with PEEC models, the development of PEEC models with improved approximation of gradients seems to be possible.

The error introduced by the application of (4.20) has been studied by the author in [76] and [80]. This kind of error is named the *static inaccuracy of the PEEC method* in contrast to the *dynamic inaccuracy of the PEEC method*, which is caused by other reasons.

The dynamic inaccuracy of the PEEC method concerns the second approximation used in the standard full-wave PEEC model. On the one hand, the approximation (4.31) allows one to set up an equivalent circuit, on the other hand, it leads to an inconsistency at frequencies higher than f_m . In the time domain, this inconsistency yields late-time instability of the solution. Thus, the dynamic inaccuracy is more dangerous than the static one that results, as a rule, in convergent oscillations. A thorough investigation of the dynamic inaccuracy of the PEEC method is presented in § 4.5.3, while the approaches for improvement of this problem are proposed in § 4.5.4 and § 4.5.5.

4.5.1 Static accuracy of the PEEC method

The general DGF-PEEC formulation is considered in this section. Thus, the techniques developed in this section may be applied to all modification of the PEEC method. A simplified interconnection system modeled with several current and potential cells is shown in Fig. 4.18. Using the standard PEEC derivation, the gradient of the scalar potential is approximated by a difference quotient (4.20). Below, (4.20) is rewritten as a rigorous equality including the approximation error, which is denoted by ϵ_{∇} :

$$\dot{\varphi}_{\alpha} = \frac{\partial}{\partial l_{\alpha}} \varphi(\mathbf{r}) = \frac{\varphi(\mathbf{r} + \hat{\mathbf{e}}_{\alpha} \frac{l_{\alpha}}{2}) - \varphi(\mathbf{r} - \hat{\mathbf{e}}_{\alpha} \frac{l_{\alpha}}{2})}{l_{\alpha}} + \epsilon_{\nabla}. \quad (4.85)$$

The current and potential cells used for the discretization of interconnections have geometrical centers, which are related to the currents in current cells (CC) and the potentials in potential cells (PC), as shown in Fig. 4.18. Thus, the difference quotient (4.85) calculates the directional derivative of $\varphi(\mathbf{r})$ in the center of the CC α using the potentials at the adjacent potential-cell centers. The length of all current cells is assumed equal to Δl that means a uniform discretization. The current cell CC₇ in Fig. 4.18 is considered in the following. The directional derivative (4.85) is illustrated in Fig. 4.19a. The approximation error is calculated using the Taylor series expansion of the function φ (see, e.g., [62]):

$$\epsilon_{\nabla} = \frac{\Delta l^2}{24} \ddot{\varphi}_7, \quad (4.86)$$

where $\ddot{\varphi}_7$ is the third directional derivative of φ in the center of the current cell. This precision may be accepted as sufficient, as with other numerical methods, e.g., in the FDTD. Another situation can be observed for cells located in areas of discontinuities, e.g., ends of conductors as CC₀ or branchings of conductors as CC₁ (see Fig. 4.18). The calculation of the difference quotient for CC₀ is illustrated in Fig. 4.19b. The accuracy of this approximation may be estimated using the Taylor series expansion, the result is discouraging:

$$\epsilon_{\nabla} = \frac{\Delta l}{4} \ddot{\varphi}_0.$$

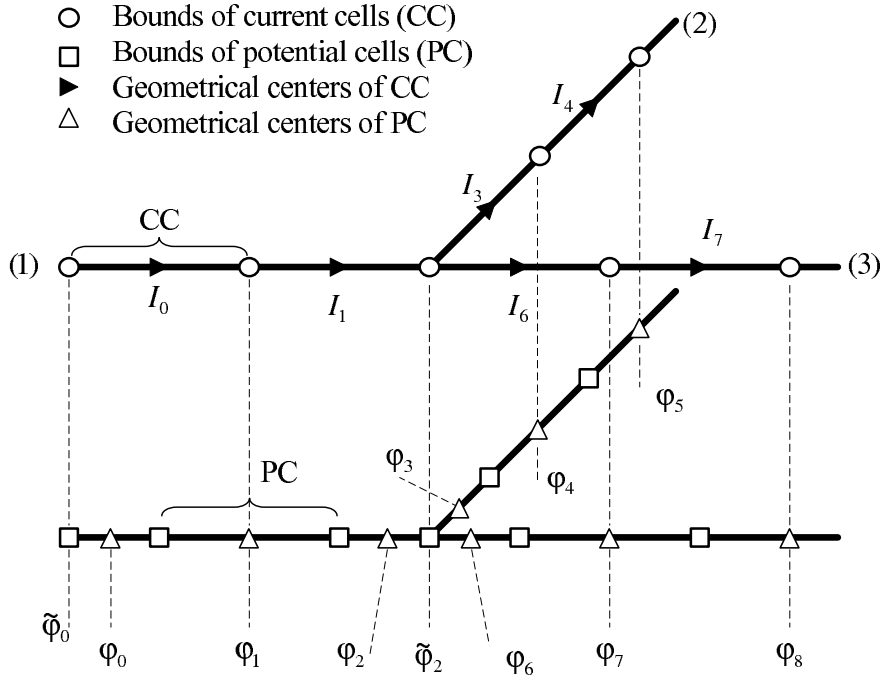


Figure 4.18: An interconnection system divided into the current and potential cells.

Thus, the error order with respect to Δl is one for cells located in discontinuities or branchings, which are named *irregular cells*, and two for other cells that are called *regular cells*.

The next special case for the difference quotient is the non-uniform grid, Fig. 4.19c shows an example for it. We consider the current cell α with the length $l_\alpha = \Delta l$. The adjacent current cells have the length: $l_{\alpha-1} = \Delta l/v$ and $l_{\alpha+1} = \Delta l v$ with $v > 1$, i.e., the length of the cell grows multiplicatively. As the geometrical centers of potential cells (triangles in Fig. 4.19c) are shifted from the bounds of current cells, the error of the approximation may be derived as follows:

$$\epsilon_\nabla = \frac{\Delta l}{8} \frac{v-1}{v} \ddot{\varphi}_0 \leq \frac{\Delta l}{8} \ddot{\varphi}_0.$$

If $v = 1$, i.e., by the uniform discretization, (4.87) yields zero. In this case, the error proportional to Δl^2 can be calculated by the expression for the uniform grid (4.86). Hence, the application of the usual formula (4.20) to non-uniform grids leads to the linear dependence between the static error and discretization step in all cells, which is not acceptable.

Resume

- The static error is acceptable only for regular cells.
- The cells at ends, edges, and branchings of interconnections are irregular. They produce a significant static error.
- All cells in the PEEC model with a non-uniform grid are irregular.

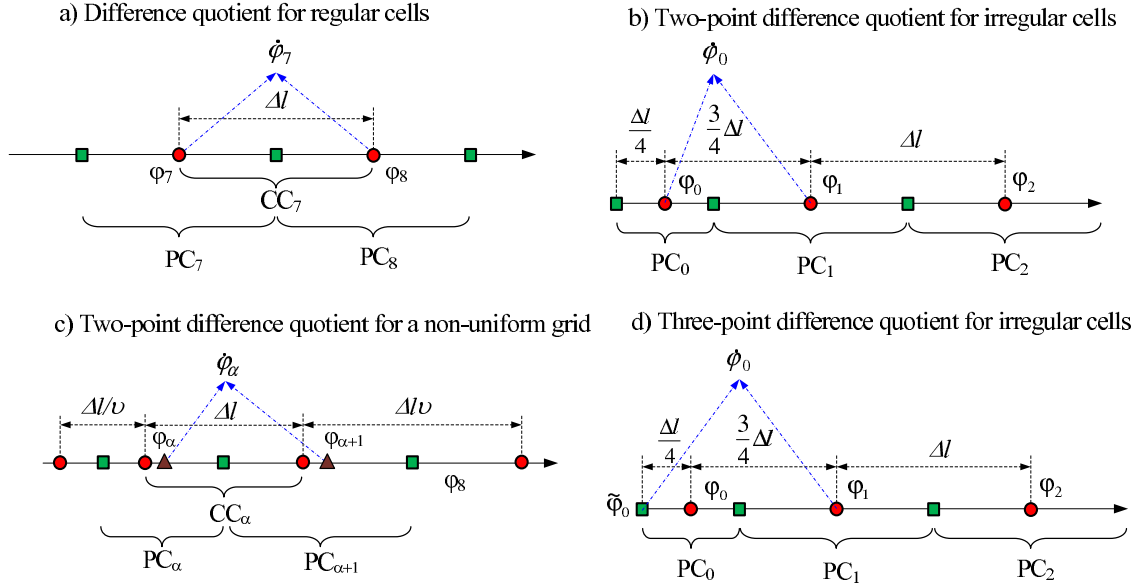


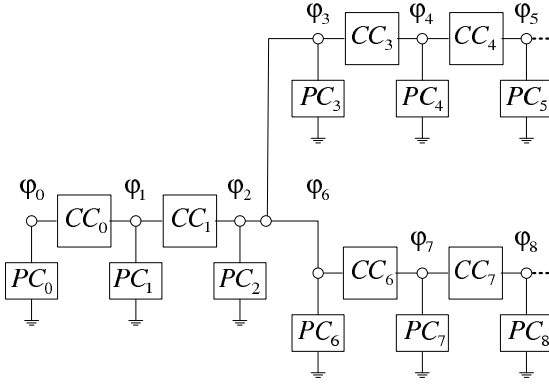
Figure 4.19: Calculation of difference quotients.

4.5.2 PEEC models with multipoint difference quotients

As a rule, the order of the difference quotient error is equal to the number of points used minus one. The exception is the two-point difference quotient for a uniform grid (4.85), whose error order is equal to two. Therefore, the accuracy of differential quotients for irregular cells may be improved via the application of multipoint formulas. There are two possible approaches for it. The first possibility is the direct calculation of the derivations with multipoint difference quotients. The second one is the interpolation of the scalar potential at points shifted in space, so as the interpolated points correspond to the uniform grid and may be used with the two-point formula (4.85).

The both approaches are discussed in the following. On the one hand, the direct application of multipoint formulas seems to be better, as it allows to reach an arbitrary accuracy, while the precision of the second approach is limited by the two-point formula for a uniform grid (4.86). On the other hand, it has a disadvantage. E.g., consider the current cells CC_1 , CC_3 , and CC_6 in Fig. 4.18, which compose a branching of three wires. The equivalent circuit for the complete interconnection system is shown in Fig. 4.20a, where the boxes CC_i denote current cells and PC_i potential cells. Obviously, three currents I_1 , I_3 , and I_6 have a common node located geometrically at ends of wires. One observes that the potentials points φ_2 , φ_3 , and φ_6 are connected together. However, geometrically, they are located in centers of potential cells PC_2 , PC_3 , and PC_6 . Hence, they may not be equal. The standard PEEC model assumes the scalar potential equal on all potential cells at the branching. According to the Taylor series expansion, these assumption leads to an error of the order one for potential approximation independent of difference quotients. The second approach based on the interpolation of the scalar potential in branching points avoids this additional inaccuracy. It leads to uniform accuracy in all regular and irregular cells.

a) Standard PEEC model



b) PEEC model with interpolated potentials

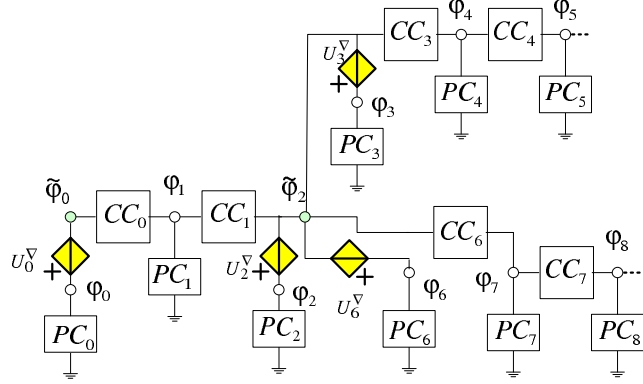


Figure 4.20: Standard and improved PEEC models of the interconnection system.

The second approach is explained in the following example. The scalar potential at the left end of the first wire $\tilde{\varphi}_0$ shown in Fig. 4.18 is interpolated by the Newton formula using the potential values at the adjacent points (see Fig. 4.19d).

$$\tilde{\varphi}_0 = \varphi_0 + \sum_{q=0}^p \zeta_q \varphi_q + \epsilon_\varphi. \quad (4.87)$$

The coefficients ζ_q depend only on the order of the approximation and the discretization step. The substitution of (4.87) into (4.85) leads to a multipoint difference quotient formula:

$$\dot{\varphi}_0 = \frac{\varphi_1 - \tilde{\varphi}_0}{\Delta l} = \frac{\varphi_1 - \varphi_0}{\Delta l} - \frac{1}{\Delta l} \sum_{q=0}^p \zeta_q \varphi_q + \epsilon_\nabla. \quad (4.88)$$

The above-given error ϵ_∇ may not be less than the error for uniform discretized conductors. However, this approximation allows the improvement of the quality of the approximation of derivatives up to the level of the uniform discretization. If $p = 1$ in (4.88), we have the coefficients $\zeta_0 = 1/3$ and $\zeta_1 = -1/3$, the errors are

$$\epsilon_\varphi = \frac{\Delta l^2}{8} \ddot{\varphi}_0, \quad \epsilon_\nabla = \frac{\Delta l}{8} \ddot{\varphi}_0.$$

For $p = 2$, the coefficients yield $\zeta_0 = 11/21$, $\zeta_1 = -2/3$, and $\zeta_2 = 1/7$, while the approximation errors are derived as follows:

$$\epsilon_\varphi = \frac{\Delta l^3}{12} \ddot{\varphi}_0, \quad \epsilon_\nabla = \frac{\Delta l^2}{24} \ddot{\varphi}_0.$$

Thus, for the difference quotient, we achieve the same precision as for regular cells. Further increasing the interpolation order improves the precision for potential approximation but cannot change ϵ_∇ . Therefore, we choose the value $p = 2$, and guarantee a uniform quality of gradient approximations on the entire interconnection system, and an error order 3 for discontinuities of potentials.

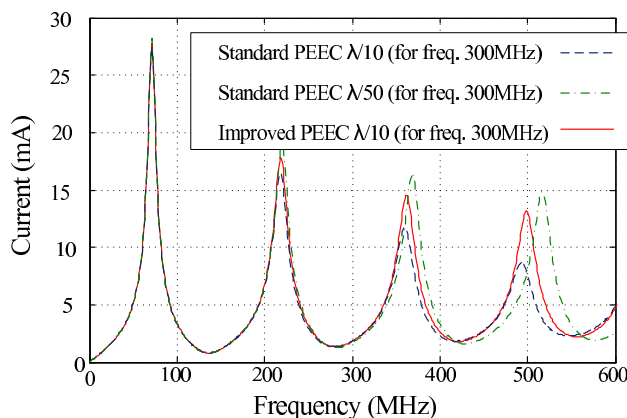


Figure 4.21: Current at the antenna base computed by different PEEC models.

The next problem, whose consideration is required, is the inclusion of the three-point difference quotient (4.88) into the equivalent circuit. Let (4.88) be substituted in (4.19) instead of (4.20). Using the same derivation as in § 4.1, a modified algebraic equation for the weighting function $w_0(\mathbf{r})$ is set up instead of (4.28):

$$\begin{aligned}
 U_0^i &= R_0 I_0 + j\omega \sum_{m \in M} L_{0,m}(j\omega) I_m + \varphi_1 - \varphi_0 + V_0^\nabla, \\
 \text{with } V_0^\nabla &= -\frac{1}{h} \sum_{q=0}^p \zeta_q \varphi_q, \quad \varphi_\alpha = \frac{1}{j\omega} \sum_{i \in M_c} p_{\alpha,i}(j\omega) I_i^c, \quad \alpha = 0, 1.
 \end{aligned}
 \tag{4.89}$$

One observes that only a difference between the standard (4.28) and modified (4.89) formulations appears. It is the voltage controlled voltage sources V_0^∇ . The modified PEEC model using (4.89) improves the approximation of the derivatives and avoids the discontinuity at branching points. Thus, current cells are correctly connected to each other. The equivalent circuit developed using the KVL equations (4.28) for regular cells and modified ones (e.g., (4.89)) for irregular cells is shown in Fig. 4.20b as compared to the standard PEEC model Fig. 4.20a. The difference between these circuits is minor, consequently, the efficiency of the standard and modified model is similar.

Example: monopole antenna

A 1-m length thin lossless monopole antenna is the first example of the application of the PEEC model with three-point differential quotients. It is excited at the base by a sinusoidal voltage source with amplitude 1 V. The antenna is discretized for the maximum frequency of interest of 300 MHz. The current at the base of the antenna is calculated at the frequency range from 1 to 600 MHz, i.e., partially out of f_m . The first curve is computed by the standard PEEC with the discretization $\lambda/10$ (see Fig. 4.21). The second curve with the discretization $\lambda/50$ is supposed as the reference. The third curve is computed by the

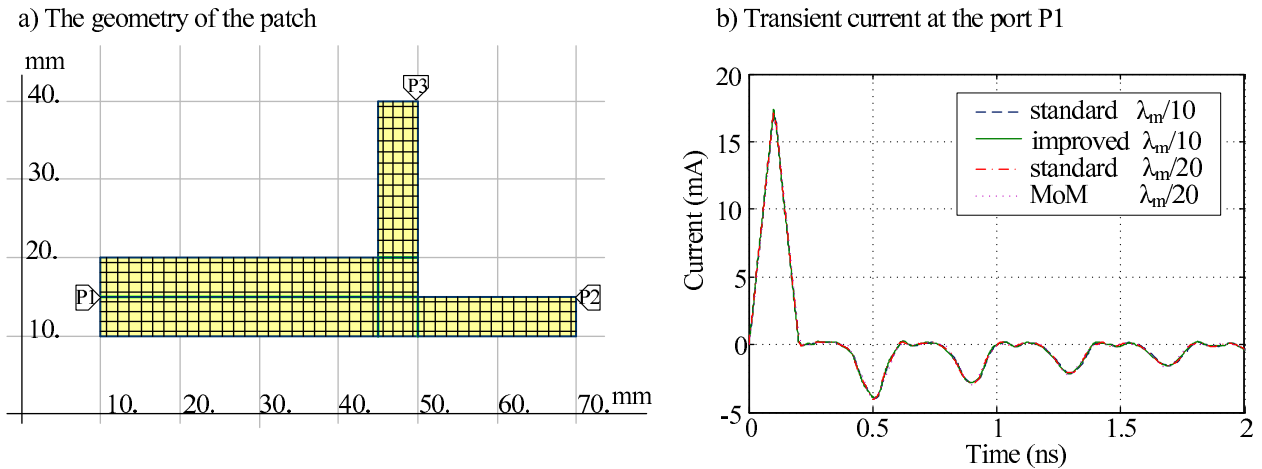


Figure 4.22: Flat interconnection structure (a) and the voltage-source current (b).

modified PEEC based on (4.89) with the discretization of $\lambda/10$. It may be resumed that the improved PEEC model shows results with higher accuracy as compared to the standard one for the same discretization.

Example: two-dimensional discretization

A flat interconnection structure requiring a two-dimensional discretization is considered (see Fig. 4.22a). A copper patch is located $100 \mu\text{m}$ above a perfectly conducting ground. The thickness of the patch is $35 \mu\text{m}$. The interconnection system has three ports. Port $P1$ is excited by a lumped voltage source. Ports $P2$ and $P3$ are open and used for measurement.

The PEEC model with three-point difference quotients for two-dimensional structures is derived analogous to the model for one-dimensional structures. Since the patch in Fig. 4.22a is defined as three quadrangles, all cells on edges of quadrangles are considered as irregular cells. In two-dimension case, the number of irregular cells is much larger than that in the one-dimension case. However, this number is insignificant as compared to the total number of cells. We interpolate potentials on edge points of the patch using formulas similar to (4.88). As result, a model with additional controlled voltage sources in all cells located on edges is set up.

First, the model is validated. The port $P1$ is excited by a triangle pulse. The rise and fall times are 100 ps , the maximum value is 1 V , the internal impedance of the source is 50Ω . The patch has been discretized for the maximum frequency of interest of 10 GHz . The voltage-source current has been calculated by the standard PEEC method with the cell size defined according to the criteria $\lambda/10$ and $\lambda/20$, and by the improved model with $\lambda/10$. The frequency-domain solution obtained by the MoM code (CONCEPT) with $\lambda/20$ is used as the reference after the consequent IFFT transformation. One observes no remarkable differences between all curves shown in Fig. 4.22b. Thus, the precision of the standard and modified PEEC models are similar if the discretization is done accurately.

The next numerical experiment is done for an incorrect discretization. The Heaviside step

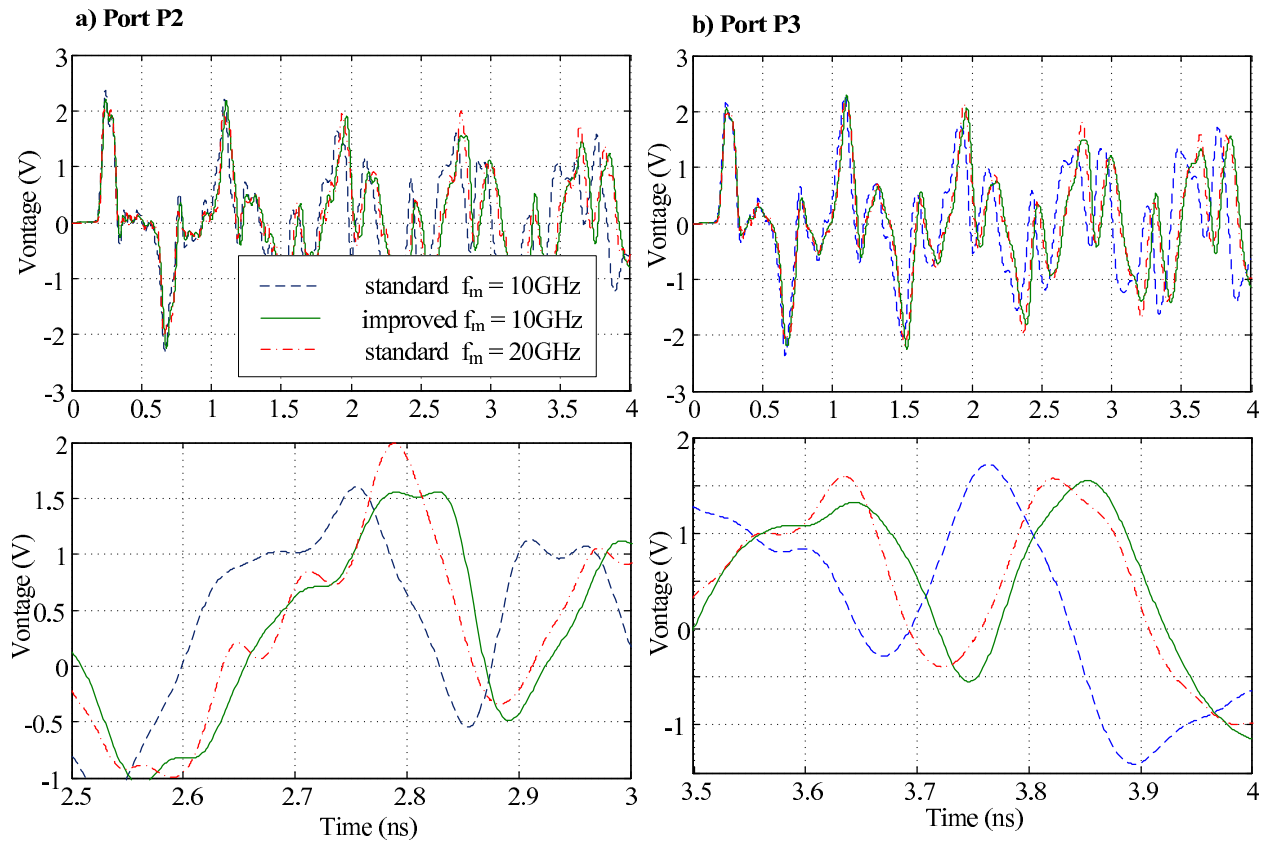


Figure 4.23: Simulation results for the step response.

function is applied as an excitation. The internal impedance of the voltage source is zero. The maximum frequency of interest for this excitation is the infinity. Since only a limited value f_m may be chosen, one can observe the response of the numerical model on excitation with frequencies higher than f_m used as the basis for discretization. The standard PEEC models excited by a Heaviside step function show solutions with strong high frequency oscillations. These oscillations are the methodical error caused by application of difference quotients. More accurate discretization can only reduce but never avoid the oscillations. The step response of voltages at ports $P2$ and $P3$ has been computed by the standard and improved PEEC models. The curves in Fig. 4.23a and Fig. 4.23b show the transient responses calculated by the standard PEEC model with $f_m=10$ GHz and $f_m=20$ GHz respectively, and by the improved PEEC model with $f_m=10$ GHz.

One observes the predictable result. The curves calculated by the PEEC model with three-point different quotients are just so exact as results calculated by the standard PEEC with more accurate discretization. We resume that the time response of the improved PEEC method on the excitation with frequencies higher than f_m is more precise than the response of the standard model.

4.5.3 Stability of the PEEC method

At the beginning of § 4.5, the static and dynamic accuracy of the PEEC method was defined. The previous subsection deals with the static inaccuracy, while the dynamic inaccuracy is studied here. Since the *dynamic inaccuracy* of the full-wave PEEC method appears as an *instability* of time-domain solutions, both topics are considered together. A transient solution obtained via a computational model is called unstable if it is correct until a finite time but after this time the correct solution is superimposed with divergent oscillations. For the PEEC method, the frequency of these oscillations is out of the maximum frequency of interest used for the grid generation. This kind of instability is also called late-time instability. Since the instability may have many causes, we first need to conduct a survey of the state-of-the-art in the stability of the PEEC method, and, then we can study separately the instability caused by the dynamic inaccuracy.

State-of-the-art in the stability of the PEEC method

Usually, one simulates the PEEC model using SPICE-like circuit simulators. Hence, a linear differential equation (LDE) or a linear delayed differential equation (LDDE) system is integrated by numerical methods used for ODEs. The necessary stability analysis consists of two basic aspects. First, the stability of the differential equation system has to be considered. If the differential equation system derived from the MPIE is unstable, its numerical solution is generally unstable as well. However, sometimes one can obtain a stable numerical solution by using a numerical rule, whose region of the *absolute stability* makes it possible to obtain a stable solution for unstable equations [95]. Unfortunately, one cannot be sure that this solution corresponds well with the physical processes in the interconnection structure. Secondly, an unstable solution may be caused by the numerical method itself. Different numerical methods have different regions of absolute stability. They can be described as A-stable, L-stable, etc. (see § 2.2). Of course, different classes of numerical methods are suitable for different classes of differential equations. Thus, one can try to define numerical methods, which are optimal for the use in PEEC solvers. Both possibilities have been studied by several groups of researchers.

Ruehli et al. [133] have focused their investigations on the influence of the numerical-method features on the stability of full-wave PEEC models. The authors have defined P-stability of a numerical method applied to a LDDE system. They have used this definition as a criterion for choosing an appropriate numerical method. It has been concluded that a stable solution can be obtained only for a stable model if an appropriate numerical rule is employed. The backward Euler (BE) and Lobatto III-C have also been proposed as suitable numerical methods for the PEEC method. More recently, Bellen et al. [20] found an analytical approach for the transformation of the LDDE system into an ODE system and a coupled algebraic recursive system, which is solved numerically. The criteria for the delay independent stability of a LDDE system has been developed and applied to a simple PEEC circuit. The stability and contractivity of numerical methods in application to PEEC have been investigated. The Lobatto III-C method has been considered suitable for computations

of the PEEC models.

The general opinion of the authors who tried to improve the stability of the full-wave PEEC method through the modification of the numerical rules can be summarized as follows: the stability of PEEC models can be improved only by the modification of the initial mathematical model, i.e., LDDE system. This seems fair, since the PEEC model usually has a quite uniform discretization, i.e., the sizes of cell can differ, but not too much. Thus, the time constants in all parts of the PEEC circuit are relatively similar, and the condition number of the system matrix is not large. Consequently, the differential equation system resulted by the PEEC method is not a stiff problem, and its solution may be achieved without special numerical methods.

In the following, we study the stability of the PEEC method without regard to the numerical integration technique applied. In contrast to FW-PEEC models, quasi-static ones are seldom affected by the late-time instability. This can be well explained by the fact that the QS-PEEC model is only a circuit composed of resistances, self and mutual inductances, and capacitances. Such a circuit produces stable solutions if the criterion (4.55) is satisfied. The QS-PEEC models, whose partial elements do not satisfy the criterion (4.55) have been investigated by Ekman, Antonini, et al. [43]. A large number of examples in [43] show that the unstable solutions can appear in cases of an "unsuitable" discretization. The unsuitable discretization means introduction of cells with very different geometrical size located close to each other or current cells with a length much shorter than the width. In these cases, the division of the interconnection structure into the current and potential cells is unphysical, which leads to instability.

It may be deduced that the stable solution is guaranteed if the interconnection system is discretized heuristically. The cell size should be varied slightly, the large interconnections in the proximity of small interconnections should be finely subdivided. Thus, in contrast to the FW-PEEC method, the stability for the QS-PEEC method may be achieved with minor efforts.

The present section deals with the stability of the standard FW-PEEC method that is an important issue. As a rule, the FW-PEEC method has an unstable solution if we do not apply special techniques for its improvement.

Ruehli et al. [134] have shown that the discretization of PEEC models can lead to differential equations with unstable solutions. The authors revealed that the stability of the PEEC solution depends on values of time delays. The stabilization scheme introduced in this work concerns so-called split cells considered comprehensively in [45]. The self inductances of the standard PEEC model are replaced by split cells, i.e., cells subdivided into two sub-cells. These split cells result in two self inductances and a mutual inductance with a time delay between the subcells. Such a structure improves the approximation of generalized partial inductance. Investigations show that the variation of delays in split-cells can improve the stability of differential equations. The further development of this approach has been made by Garret et al. [47]. Inductive cells have been subpartitioned into a number of subcells with time delays between these partitions. Analogous to the approach in [134] this method leads to an improvement of the stability. In [134, 47] and more specified in [45], the stability

of PEEC models has been investigated in the frequency domain by the introduction of frequency dependent eigenvalues. The resonances above the frequency range of interest have been observed and supposed as the cause for instabilities. Damping resistances introduced in parallel to self inductances have been suggested as an effective tool for the stabilization of the solution [47]. This modification increases the damping in the differential equation system and, consequently, improves the stability. Moreover, this approach does not increase the order of the LDDE system, which is a significant advantage of this approach.

More recently, a new step for understanding and improvement of instability was accomplished by Kochetov and Wollenberg [78], [77], and [79]. It has been explicitly shown that the instability of FW-PEEC models is caused by using ideal time-delay sources that are included via the approximation (4.31). I.e., the instability is caused by the dynamic inaccuracy of the method. The usual time-delay sources have frequency responses undamped towards the increase of the frequency, while the generalized partial elements (4.16) and (4.25) have damped frequency responses. Therefore, the standard FW-PEEC model does not represent properly the MPIE and, thus, the physical behavior of passive interconnection structures. A modification of the PEEC method has been proposed in [79], [77]. The frequency responses of generalized partial elements have been approximated by parametrical macromodels, i.e., equivalent circuits, whose transfer-function magnitude tends to zero at high frequencies as the generalized partial elements. Such improved PEEC models provide stable solutions, which are more precise and physical than those of the standard PEEC method. However, the main disadvantage of this approach is the introduction of additional circuit elements leading to additional variables, which increases the simulation time of the model drastically.

The macromodels for generalized partial elements based on the vector-fitting technique (see § 3.6) have been proposed by Antonini et al. [14]. The frequency dependence of partial elements is taken into account by two terms: a delay term like in the standard FW-PEEC model and a remaining frequency dependent term approximated by a rational function given in Foster's canonical form. The last term is the basis for synthesizing linear RLC-circuits using the approach given by Antonini [11]. The obtained broadband PEEC models with improved stability and accuracy can be incorporated in a time-domain MNA based solver.

Recently, Kochetov and Wollenberg continued the investigations started in [77] with an advanced approach presented in [81] and [81]. These papers are focused on the development of fast time-domain models of generalized partial elements being applicable for use in SPICE-like circuit simulators. This investigation has motivated the authors to develop a suitable approach for macromodeling called full-spectrum convolution macromodeling (see § 3.6). The stable full-wave PEEC (S-FW-PEEC) model using the FSCM is thoroughly studied in § 4.5.5.

Consistency of the FW-PEEC model

Before considering the stability of the standard FW-PEEC method, its consistency has to be proved. The simplified model of a lossless wire shown in Fig. 4.24a is used for the investigation of the consistency. The wire is divided into three current cells, the potential cells are not considered due to simplification. We set the partial inductances $L_{11} = L_{22} =$

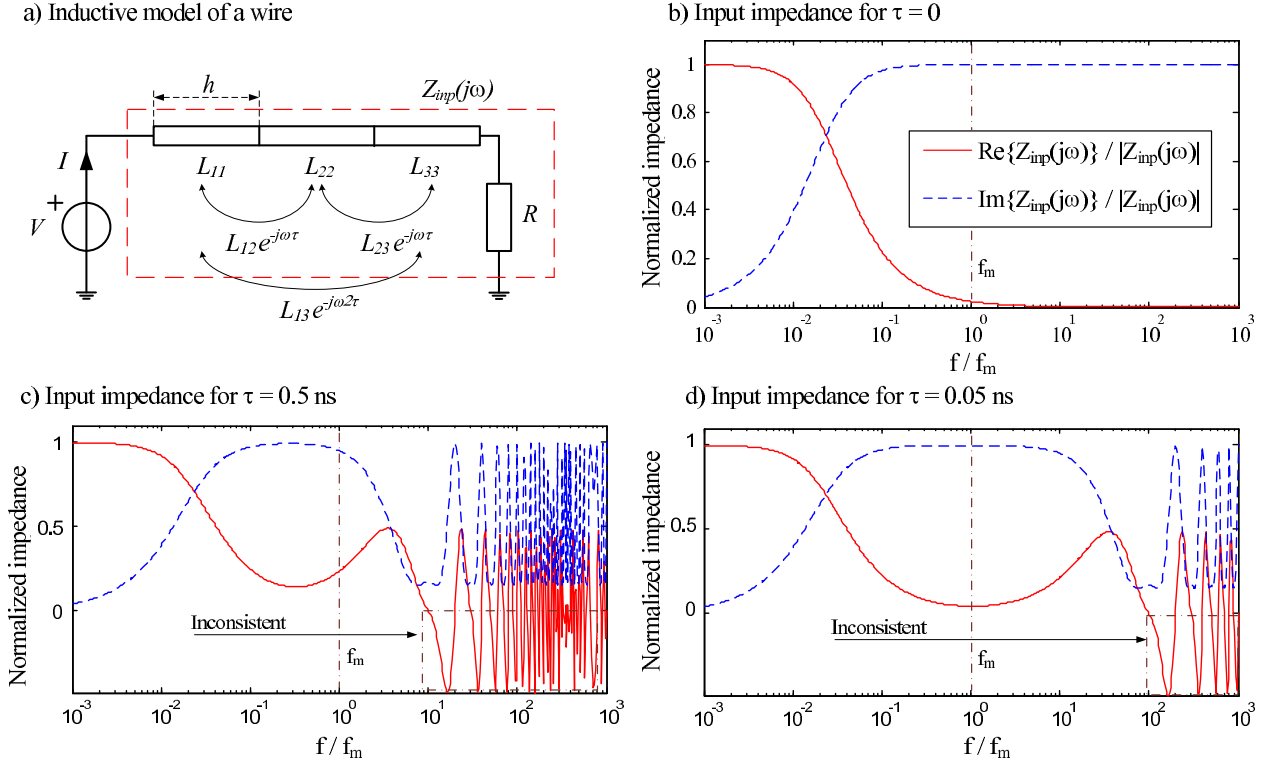


Figure 4.24: Inconsistency of the standard FW-PEEC model.

$L_{33} = 10$ nH, $L_{12} = L_{23} = 9$ nH, $L_{13} = 8$ nH, the cell length $h = 0.3$ m, the delay time between two adjacent cells $\tau = 0.5$ ns. The artificially chosen set of parameters satisfies the stability criterion for the QS-PEEC method (4.55) and may be considered as a possible case. Since the cell length is 0.3 m, one calculates the maximum frequency of interest coupled with the grid step as follows: $f_m = c/(20h) = 100$ MHz. The ends of the wire are connected to a voltage source V and a load resistance $R = 1 \Omega$.

The input impedance for three serially connected current cells yields

$$Z_{inp}(j\omega) = \frac{V}{I} = R + j\omega (3L_{11} + 4L_{12}e^{-j\omega\tau} + 2L_{13}e^{-j\omega2\tau}).$$

The frequency response of $\Re\{Z_{inp}(j\omega)\}/|Z_{inp}(j\omega)|$ and $\Im\{Z_{inp}(j\omega)\}/|Z_{inp}(j\omega)|$ in the case $\tau=0$, i.e., for the QS-PEEC model is shown in Fig. 4.24b. The impedance has a typical inductive behavior, namely, the smooth change from the ohmic resistance at low frequencies to the reactance at high frequencies. This function satisfies the passivity condition of an one-port network based on the maximum modulus theorem given in [69]:

$$\Re\{Z_{inp}(j\omega)\} \geq 0.$$

The quite different behavior is shown by $Z_{inp}(j\omega)$ calculated with $\tau=0.5$ ns (see Fig. 4.24c). One observes that $\Re\{Z_{inp}(j\omega)\}$ oscillates at high frequencies. It may be resumed that the FW-PEEC model is not passive at some frequencies higher than $10f_m$, since $\Re\{Z_{inp}(j\omega)\} <$

0. Thus, a passive interconnection is simulated by an active circuit. Obviously, this model has a contradiction with the modeled object. The principal behavioral contradictions between the object and its model are called the model *inconsistency*. The time-domain FW-PEEC models are represented by linear active circuits containing the controlled voltage and current sources with time delays. Mathematically, such circuits are described by the systems of linear delay differential equations (LDDE). The instability is a typical feature of the LDDE system. Hence, the principle error is in the modeling of passive interconnections in FW-PEEC models that are not completely consistent.

Since the wire in Fig. 4.24c becomes active at $f \geq 10f_m$ and the spectrum of the excitation is limited by f_m , it may be assumed that the inconsistency is not critical. This, however, is not always the case. Usually, f_m is chosen as a cut off frequency for the spectrum of a broad band-pulse. Consequently, out of f_m , the spectrum magnitude decreases quickly, but is not exactly zero. Additionally, the application of difference quotients in the PEEC model introduces the static inaccuracy, which appears in the solution as oscillations at frequencies higher than f_m (see § 4.5.1). A more precise discretization can improve this situation, e.g., Fig. 4.24d represents the FW-PEEC model with $\tau=0.05$ ns. It simulates the wire with cells that are 10 times shorter. Obviously, the inconsistency remains, but it is shifted by a decade. Thus, the correspondence between the FW-PEEC model and the interconnection may be improved through the redundant discretization, i.e., choice of the cell length $\lambda_m/100$ or finer. In practice, this approach is not applicable, as it dramatically increases the run time.

Alternatively, the stability may be improved via the introduction of a consistent modification of the FW-PEEC model. First, we return to the assumption of the standard PEEC method given by (4.31) for revealing the cause of the instability. The generalized partial elements $L_{\alpha,m}(j\omega)$ and $p_{\alpha,i}(j\omega)$ are approximated by the functions $\tilde{L}_{\alpha,m}(j\omega)$ and $\tilde{p}_{\alpha,i}(j\omega)$, respectively. Thus, only static space-convolution integrals are calculated, and the ideal time delays between centers of cells are introduced. The frequency dependencies $L_{\alpha,m}(j\omega)$ and $p_{\alpha,i}(j\omega)$ differ only by units and constant factors. Therefore, we denote the abstract generalized partial element $\xi(j\omega) = \{L_{\alpha,m}(j\omega), p_{\alpha,i}(j\omega)\}$ and its approximation $\tilde{\xi}(j\omega) = \{\tilde{L}_{\alpha,m}(j\omega), \tilde{p}_{\alpha,i}(j\omega)\}$. The functions $\xi(j\omega)$ and $\tilde{\xi}(j\omega)$ for an example cell geometry are shown in Fig. 4.25. Two rectangular flat current cells with the length of $\Delta l = 1.5$ cm, the width of 0.5 mm, and the thickness of $50 \mu\text{m}$ are investigated at two distances between their centers: $20\Delta l$ (see Fig. 4.25a) and Δl (see Fig. 4.25b). The maximum frequency of interest is $f_m = 1$ GHz that corresponds to $\Delta l = \lambda_m/20$ and $\lambda_m = c/f_m$. The cells lie on a straight line.

Obviously, $\tilde{\xi}(j\omega)$ is a good approximation for $\xi(j\omega)$ at $f < f_m$. However, the generalized partial elements have essential damping at $f \geq f_m$, while the approximation $\tilde{\xi}(j\omega)$ has no damping. Additionally, if cells are located near to each other, the time delay computed between the centers of cells deviates from the equivalent delay realized by $\xi(j\omega)$. Clearly, these minor deviations in the approximation (4.31), which are named the *dynamic inaccuracy*, are responsible for the inconsistency of the FW-PEEC model appearing in Fig. 4.24c as an unphysical frequency response at $f \geq f_m$.

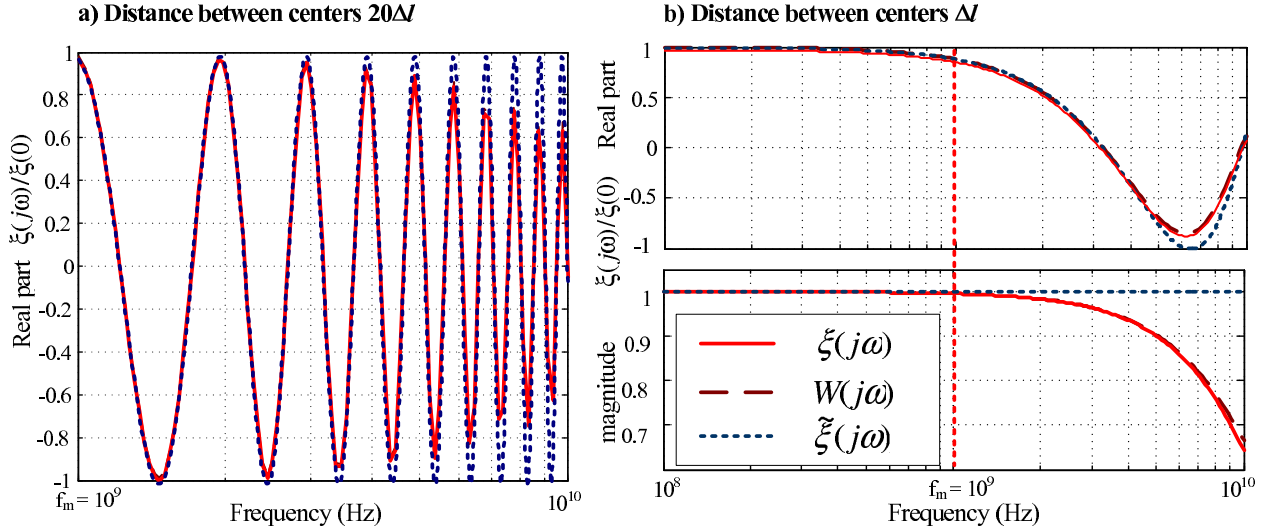


Figure 4.25: Comparison between $\xi(j\omega)$, $\tilde{\xi}(j\omega)$, and $W(j\omega)$ (see § 4.5.5).

Approach for the stability analysis for the FW-PEEC model

The inconsistency of the FW-PEEC model does not lead certainly to the instability of the solution. The stability of the LDDE system corresponding to a FW-PEEC model may be examined via different methods used in the control-system theory. The Lyapunov-Razumikhin functions approach and Lyapunov-Krasovskii functional method estimate the stability in time domain [40], whereas the matrix-pencil technique is a good Laplace-domain approach [40]. The disadvantage of these approaches is the difficult application for the problems with a huge number of time delayed functions as the PEEC models. Moreover, we need not only proving the stability but also observing the influence of damping in $\xi(j\omega)$ on the stability. The following approach has been developed by the author in order to solve this problem.

The idea of the approach consists of the transformation of the LDDE system into an equivalent LDE system, which is set up via parametric macromodeling the delayed sources. Then, the stability of the LDE system may be trivially proved using the eigenvalues of the system matrix.

First, the time-delay controlled source with the transfer function $\tilde{\xi}(j\omega)$ should be approximated. We denote

$$Y = \tilde{\xi}(j\omega)X, \quad \tilde{\xi}(j\omega) = \tilde{\xi}e^{-j\tau\omega}, \quad (4.90)$$

where X and Y are the input and output variables, respectively. τ is the time delay. Because of a large number of controlled sources in the PEEC model, it is very important to build a macromodel, whose parameters can be computed in a simple and fast way. Since the general approaches studied in § 3.6 need a relatively complex preprocessing, and the shape of $\tilde{\xi}(j\omega)$ is predefined, a special macromodel for the time-delay function on the basis of the following

rational function is proposed:

$$H_n(j\omega) = \left(\frac{n/\tau}{j\omega + n/\tau} \right)^n. \quad (4.91)$$

$H_n(j\omega)$ approximates the time-delay function (4.90) in a limited frequency range. The relative error of the approximation at the maximum frequency of interest $\omega_m = 2\pi f_m$ is defined as follows:

$$\epsilon_t = 1 - \left(\frac{n/\tau}{\sqrt{(n/\tau)^2 + \omega_m^2}} \right)^n. \quad (4.92)$$

Using (4.92), we estimate n as a function of ω_m , τ and the required relative error ϵ_t . Fig. 4.26a shows the comparison between $H_n(j\omega)$ and $\xi(j\omega)/\tilde{\xi}$. Fig. 4.26a applies a special normalized frequency $\tilde{\omega}$ on the abscissa axis:

$$\tilde{\omega} = \frac{\omega d}{\omega_m \Delta l}, \quad (4.93)$$

where d is the distance between cells, Δl is the length of cells. $\tilde{\omega}$ provides invariant scaling, which is independent of the grid step and the distance between their centers. At $f = f_m$, the macromodel has an error of about 0.6% for $d = \Delta l$, 2.5% for $d = 2\Delta l$. Further increase of the distance needs increasing n . Thus, the proposed macromodels are applicable for the analysis of only relatively simple interconnection systems. The important advantage of $H_n(j\omega)$ is the similarity of its frequency response with the generalized partial elements. On the one hand, these macromodels with sufficient numbers of stages may be applied to the stability analysis. On the other hand, the macromodels (4.91) with insufficient numbers of stages may be applied to the observation of the influence of the damping in the generalized partial elements on the stability.

The time response of $H_n(j\omega)$ denoted by $y(t)$ on a waveform $x(t)$ can be calculated in the time domain as a solution of the n -dimensional LDE system [77]. Fig. 4.26b shows the time response of $H_n(j\omega)$ on the ramp function with a rise time 2.5 ns. The time delay τ amounts to 0.25 ns that corresponds to the distance of 0.075 m. The stage number n is varied from 1 up to 38. Obviously, the results for $H_n(j\omega)$ converges to the ideal time-delay response by increasing n . Generally, the considered macromodels introduce additional damping but with $n \rightarrow \infty$ they converge to the ideal delay function.

Stability analysis for the FW-PEEC model

The above-proposed approach for the stability analysis is applied to an example structure: the short single transmission line (copper wire with a rectangular cross-section 1×1 mm) above a perfectly conducting ground. The left end of the transmission line is excited by a voltage source with the ramp waveform and 1 Ω internal impedance, while the right side is loaded by a 10 Ω resistance.

The wire is divided with different precisions $\Delta l = \lambda_m/10$, $\lambda_m/20$, and $\lambda_m/30$ that leads to 2, 4, and 6 current cells, respectively. First, the voltage-source current is calculated using the standard FW-PEEC model ($\lambda_m/10$, 2 cells) and applying the equivalent LDE system

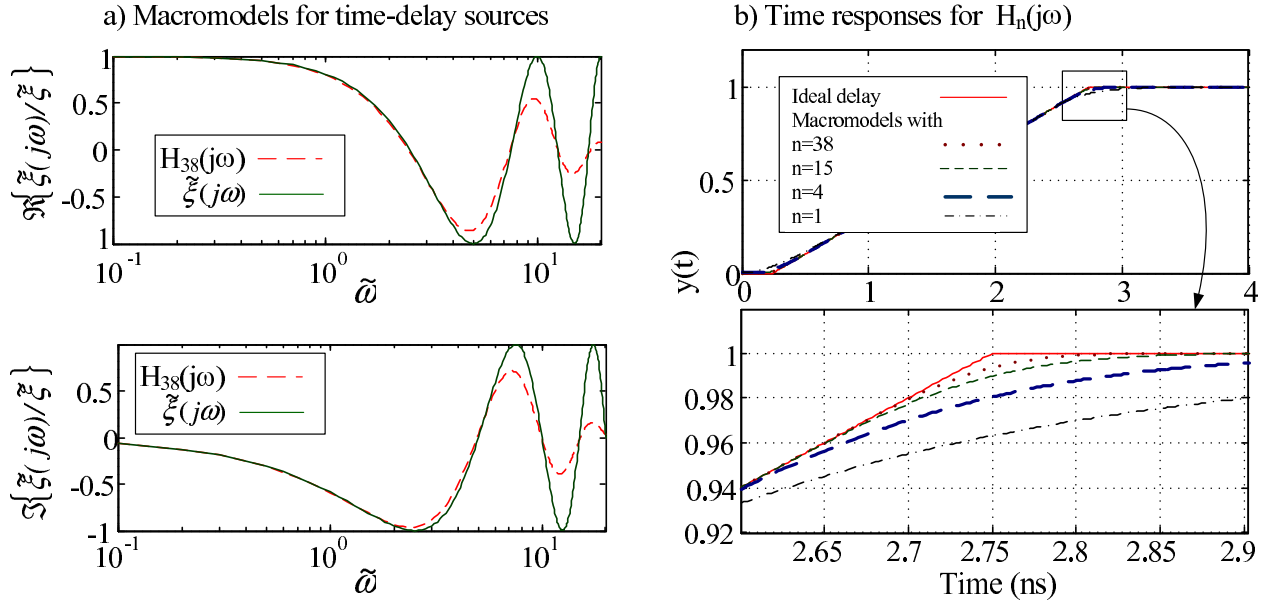


Figure 4.26: The frequency response of $H_n(j\omega)$ (a), and the time response of $H_n(j\omega)$ on the ramp function (b).

(see Fig. 4.27. The number of stages in the macromodels is chosen so as the cutoff frequency amounts to 20 GHz. The relative error ϵ_t at the frequency of the divergent oscillations $\omega = 5.6605 \cdot 10^9 \text{ s}^{-1}$ is 3.1%, while at the maximum frequency of interest, the error is 0.6%. Thus, this model represents well the behavior of the system at frequencies, where the instability occurs. Moreover, one may remark that the inaccuracy introduce additional damping and, consequently, make the solution more stable. Thus, the approach for the stability analysis may be considered as "optimistic", since the inaccurate macromodels lead to the wrong definition of the system as stable. The results shown in Fig. 4.27 are unstable. The both results show a very good agreement over the presented time range. Hence, we have applied a precise LDE model for the FW-PEEC model. Moreover, it may be resumed that the LDE model describes the instability of the FW-PEEC model using only linear differential equations.

Further, we estimate the stability of the LDDE system using the eigenvalues of the equivalent LDE system. There is only one eigenvalue with a positive real part $\lambda = (3.2287 \cdot 10^7 \pm 5.6826 \cdot 10^9 j) \text{ s}^{-1}$. The analysis of the transient current computed by the FW-PEEC model shows that the radian frequency of the divergent oscillation is $5.6605 \cdot 10^9 \text{ s}^{-1}$. It coincides well with the imaginary part of the eigenvalue considered. The time constant of the divergent oscillations is about $3.1 \mu\text{s}$ (see Fig. 4.27). It corresponds well to the real part of the eigenvalue. Thus, the instability of the FW-PEEC model is described by the eigenvalue with a positive real part of the equivalent LDE system.

Then, we calculate the eigenvalues of the PEEC circuit discretized with $\lambda_m/20$, i.e., composed of 4 current cells. Three conjugate-complex pairs with positive real parts are found:

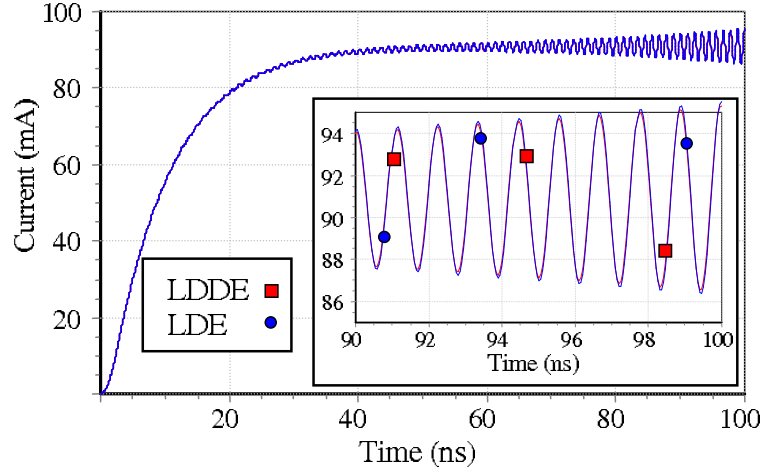


Figure 4.27: Load current computed by the FW-PEEC model and its LDE model.

$$\begin{aligned}\lambda_1 &= (1.5447 \cdot 10^7 \pm 6.2602 \cdot 10^9 j) \text{ s}^{-1}, \\ \lambda_2 &= (2.7418 \cdot 10^7 \pm 1.4784 \cdot 10^{10} j) \text{ s}^{-1}, \\ \lambda_3 &= (7.9153 \cdot 10^7 \pm 1.1373 \cdot 10^{10} j) \text{ s}^{-1}.\end{aligned}$$

Obviously, this solution diverges faster than that in the previous example. Then, we compute eigenvalues for a discretization with $\lambda_m/30$, i.e., for 6 current cells and obtain four conjugate-complex pairs with positive real parts. One of them is $\lambda = (8.4105 \cdot 10^7 \pm 1.2162 \cdot 10^{10} j) \text{ s}^{-1}$. It has a larger real part than the eigenvalues for the discretization with $\lambda_m/20$. It may be concluded that the increase of the discretization precision will not ever lead a stable solution.

Instability of the FW-PEEC method: conclusion

- Since the calculation of eigenvalues does not involve the numerical integration, the hypothesis that the numerical integration leads to the instability is disproved.
- Since the LDE system, whose eigenvalues have a positive real part, yields an unstable homogeneous solution, the stability of the FW-PEEC model does not depend on the excitation.
- The introduction of the attenuation in the time-delay sources approaches their frequency responses to the initial damped frequency responses of generalized partial elements. The eigenvalues with a positive real part disappear if the macromodels $H_n(j\omega)$ introduce the same damping as $\xi(j\omega)$ at $f > f_m$.
- The approximation (4.31) leads to an inconsistent numerical model and, as consequence, to instability.
- The exact approximation of $\xi(j\omega)$ in the FW-PEEC model avoids the dynamic inaccuracy and to improves the stability.

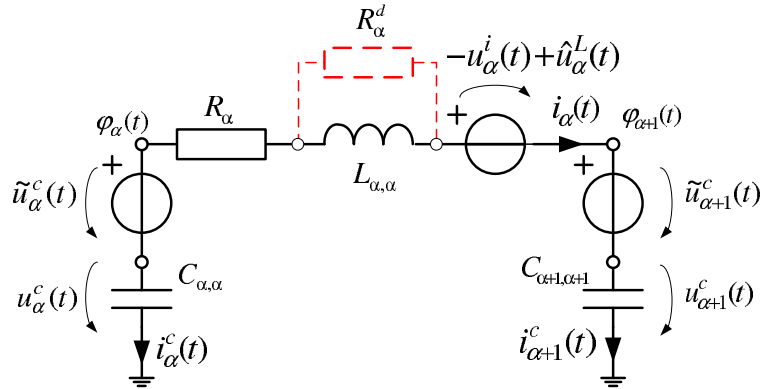


Figure 4.28: The FW-PEEC model with the damping resistances.

4.5.4 Stability improvement for the full-wave PEEC method

Heuristic approach

As early as the generalized partial elements was not introduced and the inconsistency of the approximation (4.31) was not explicitly shown, it was observed that the additional dissipation at high frequencies can improve the stability. Several more or less applicable approaches for it are mentioned at the beginning of § 4.5.3. The most useful heuristic approach consists in the addition of the so-called *damping resistances*, which are connected in parallel to the partial self inductance of each current cell [47], as shown in Fig. 4.28. The damping resistances produce some additional dissipation in the PEEC model leading to reducing the instability. The value of the damping resistance is estimated in [47] as follows:

$$R_{\alpha}^d = \kappa \omega_m L_{\alpha,\alpha}, \quad (4.94)$$

where κ is a constant between 10 and 100. The value of κ for a particular PEEC model cannot be determined uniquely, which is a disadvantage of this approach. Generally, a small κ improves the stability and, in the same time, diminishes the accuracy, while a large κ influences weak the stability as well as the accuracy.

The damping resistances do not improve the approximation of generalized potential coefficients at all and introduce a damping (often redundant) only to self generalized partial inductances. Consequently, this approach does not produce a fair broad band model at $f \leq f_m$, since the solution at frequencies near to f_m is inaccurate. However, the addition of damping resistances do not change the complexity of the problem, and it may be applied as an approximate solution.

Parametric macromodels for the generalized partial elements

The first method for the stability improvement via the exact time-domain approximation of the generalized partial elements has been proposed in [77], as a heuristic continue for the approach for the stability analysis given in the previous section.

The application of (4.31) introduces the standard partial inductances and potential coefficients that lead to the standard FW-PEEC model with the time-delay controlled sources (see Fig. 4.6). In contrast, the exact approximation of generalized partial elements returns the derivation to the generalized equivalent circuit of the DGF-PEEC model (see Fig. 4.2). The generalized partial inductances and the generalized potential coefficients for the free-space FW-PEEC model are calculated by (4.30) and (4.33), respectively. As it has been mentioned, the frequency responses of $L_{\alpha,m}(j\omega)$ and $p_{\alpha,i}(j\omega)$ have similar features. Thus, we consider an abstract generalized partial element $\xi(j\omega) = \{L_{\alpha,m}(j\omega), p_{\alpha,i}(j\omega)\}$. The rational functions (4.91) used for the investigation of the stability in § 4.5.3 may be used also for the approximation of the generalized partial elements:

$$\xi(j\omega) \approx \tilde{\xi}(j\omega) = \xi H_n(j\omega) e^{-j\omega\tau_r}. \quad (4.95)$$

$\tilde{\xi}(j\omega)$ consists of three parts: ξ is the static partial element computed by (4.32) or (4.35), $H_n(j\omega)$ represents the damping at high frequencies, $e^{-j\omega\tau_r}$ is a time delay function.

The estimation of unknown parameters for (4.95) requires calculation of $\xi(j\omega)$ at two frequency points. First, we compute the static partial element, which yields ξ . Then, we compute the generalized partial element at the frequency ω_g :

$$\omega_g = \min \left\{ \omega_m, \frac{0.1\pi}{\tau_{\alpha,m}} \right\}, \quad (4.96)$$

where $\tau_{\alpha,m}$ is the time delay between centers of cells. The equivalent time delay for a generalized partial element is estimated as follows:

$$\tau_{eq} = -\frac{\arg \{\xi(j\omega_g)\}}{\omega_g}. \quad (4.97)$$

Setting a suitable n , usually $n = \overline{1, 4}$, we estimate τ from the condition that the damping of the both functions $\xi(j\omega)$ and $\tilde{\xi}(j\omega)$ is equal at ω_g :

$$|\xi(j\omega_g)| = |\tilde{\xi}(j\omega_g)| \Rightarrow \tau = \frac{\sqrt{1 - \delta^{2/n}}}{\omega_g \delta^{1/n}}, \quad \text{with } \delta = \frac{|\xi(j\omega_g)|}{\xi}. \quad (4.98)$$

The time delay τ_r is computed from the condition that the total delay of $\tilde{\xi}(j\omega_g)$ is $\tau + \tau_r$:

$$\tau_r = \tau_{eq} - \tau \quad (4.99)$$

with τ_{eq} calculated by (4.97).

The time-domain model for $\tilde{\xi}(j\omega_g)$ can be realized with the standard elements of SPICE [77]. The stages of $H_n(j\omega)$ are modeled as cascaded RL-circuits, the time delay function for τ_r is realized in SPICE via a time table analogous to the standard FW-PEEC model (see § 4.3.1). The details of this model are not shown here because its efficiency is very low, and it cannot be applied to the solution of large problems. However, the simulation results obtained are stable and accurate in contrast to the standard FW-PEEC model, but the run

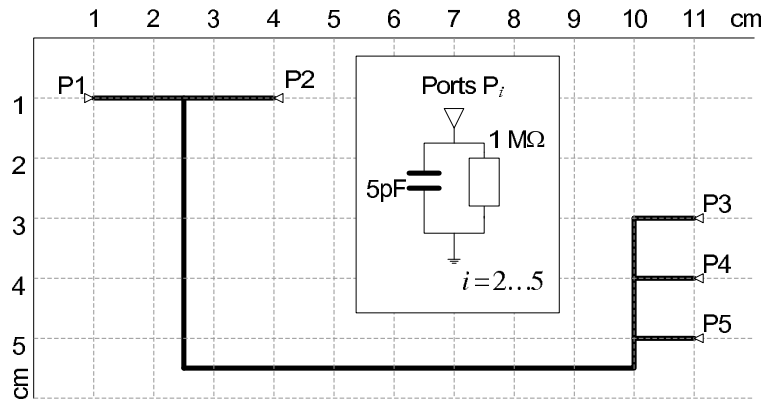


Figure 4.29: Routing of the printed circuit.

time is drastically increased. This can be explained by increasing the dimension of the MNA problem caused by the inclusion of a huge number of nodes. Since the PEEC model with N cells has the number of controlled sources proportional to N^2 , the number of additional nodes is also proportional to N^2 . Furthermore, small values of elements in the RL-circuits need decreasing the time step of the numerical integration. Although the FW-PEEC model with an improved stability is inefficient, we may apply it to an example, in order to observe its stability and accuracy.

Example of simulation: the FW-PEEC model with improved stability

The PCB traces shown in Fig. 4.29 are considered. The copper traces have a rectangular cross-section with a width of 0.5 mm and a thickness of 50 μm . The traces are located 1 mm above a perfectly conducting ground. The interconnection system has five ports denoted by P_i , $i = 1 \dots 5$. Ports P_i with $i = 2 \dots 5$ are connected to the ground through a lumped circuit modeling the input impedance of integral circuits. This circuit consists of a resistance of 1 M Ω connected in parallel to a capacitance of 5 pF. The lumped voltage source with an internal resistance of 0.1 Ω is connected to P_1 . The voltage source excites the system by a single trapezoidal pulse with a rise time of 400 ps, a roof time of 5 ns, and a fall time of 400 ps. The maximum value of the pulse is 10 V. The discretization of interconnections is done for $f_m = 2.5$ GHz.

The voltage at the port P_2 has been computed by the standard PEEC method using the damping resistances with different parameters κ (see (4.94)), by the improved PEEC method, and by the QS-PEEC model as the reference (see Fig. 4.30). Since losses are insufficient, the time response of the system has an oscillatory character. Hence, there are fast transients, on the one hand, and prolonged oscillations, on the other hand. The simulation of such systems is generally difficult, particularly, by the PEEC method. The voltage at the port P_2 calculated by the standard PEEC with different parameters κ is presented in Fig. 4.30(c-d). The time response in Fig. 4.30d shows divergent high frequency oscillations as a typical late-time instability. It may be concluded that $\kappa = 75$ is too large in this case. The results in Fig. 4.30c are stable at least until 50 ns. The value $\kappa = 70$ provides a stable solution and may

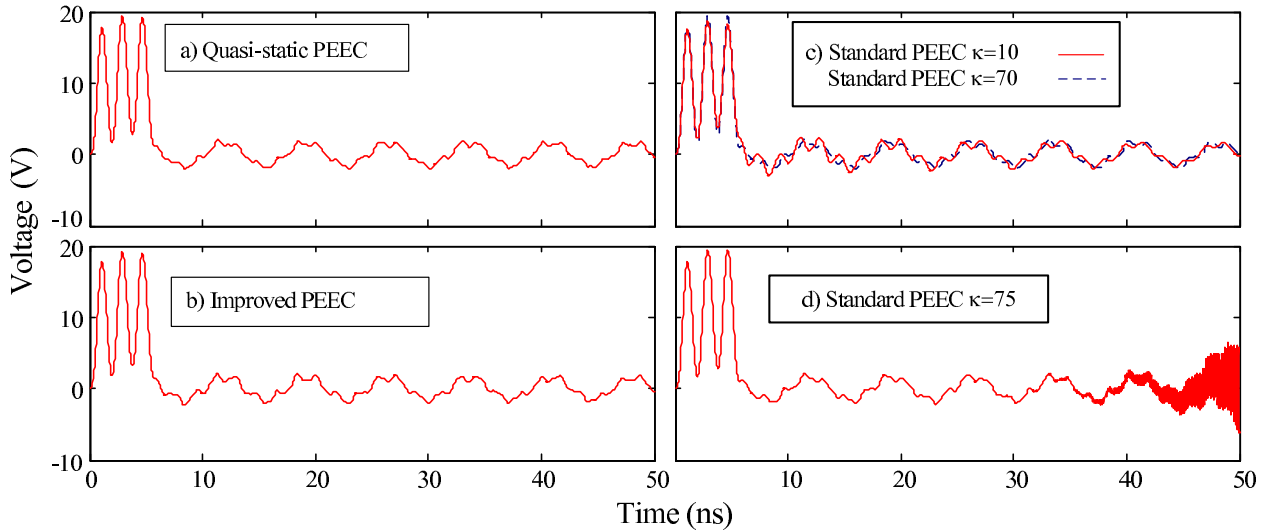


Figure 4.30: Load voltage at the port P_2 computed by different methods.

be supposed as correct. The curve computed with $\kappa = 10$ is stable but eliminates the high frequency components of the time response. In contrast, the improved PEEC method (see Fig. 4.30b) yields a correct and stable solution. It shows a very small dissipation as predicted. It may be resumed that this solution is congruent with the reference (see Fig. 4.30a).

Resume

The time-domain approximation of the generalized partial elements leads to stable and precise solutions. However, the macromodels of $L_{\alpha,m}(j\omega)$ and $p_{\alpha,i}(j\omega)$ are inefficient. Hence, a new efficient macromodel is required.

4.5.5 Stable and effective PEEC models based on the FSCM

In the following, our goal is the development of efficient time-domain models for generalized partial elements being applicable for using in SPICE-like circuit simulators. The novel approach based on the full-spectrum convolution macromodeling has been presented by the author in [81].

According to the strategy of the FSCM given in § 3.6, the first step of macromodeling is the approximation of the generalized partial elements in the frequency domain. As in the previous section, an abstract generalized partial element $\xi(j\omega) = \{L_{\alpha,m}(j\omega), p_{\alpha,i}(j\omega)\}$ is considered. The approximation of $\xi(j\omega)$ has to describe its frequency response and to be suitable for the development of effective time-domain macromodels. Due to the stability, this function must have the same asymptotic as $\xi(j\omega)$, whose magnitude tends to zero at $f \gg f_m$.

This section provides two types of FSCM models, the first one is suitable for the modeling of the generalized partial elements between remote located cells, the second one is applied

for modeling self partial elements and the mutual partial elements between closely located cells.

The FSCM for the generalized partial elements with large time delays

The first proposed frequency-domain model for the generalized partial elements is the following function:

$$\xi(j\omega) \approx W(j\omega) = \xi e^{-(\alpha\omega)^2} e^{-j\omega\tilde{\tau}}. \quad (4.100)$$

The parameters of (4.100) may be explicitly calculated using two frequency points of the original function. The first parameter ξ corresponds exactly to the static partial element: $\xi = \xi(0)$. The computation of α and $\tilde{\tau}$ needs an additional frequency point $\omega = \omega_g$, which is defined by (4.96). The parameter α is estimated from the condition that $|\xi(j\omega_g)| = |W(j\omega_g)|$ as follows:

$$\alpha = \frac{1}{\omega_g} \sqrt{\ln \frac{|\xi|}{|\xi(\omega_g)|}}. \quad (4.101)$$

The equivalent time delay is estimated as

$$\tilde{\tau} = -\frac{\arg \{\xi(\omega_g)\}}{\omega_g}. \quad (4.102)$$

The accuracy of the approximation by the function $W(j\omega)$ is illustrated in Fig. 4.25. The chosen frequency-domain model for $\xi(j\omega)$ correctly fits its frequency response at low frequency as well as at high frequencies.

The time response of the controlled source $Y = W(j\omega)X$ can be determined via the Duhamel integral (3.19), where $y(t) = \mathfrak{F}^{-1}\{Y\}$ is the output function, $x(t) = \mathfrak{F}^{-1}\{X\}$ is the input function, $g(t) = \mathfrak{F}^{-1}\{W(j\omega)\}$ is the impulse response, and $s(t)$ is the step response. The impulse and step responses for $W(j\omega)$ are derived in a closed form:

$$g(t) = \frac{\xi}{2\alpha\sqrt{\pi}} \exp \left[-\left(\frac{\tau - t}{2\alpha} \right)^2 \right], \quad (4.103)$$

$$s(t) = \frac{1}{2} \left[1 - \operatorname{erf} \left(\frac{\tau - t}{2\alpha} \right) \right]. \quad (4.104)$$

Obviously, the impulse response is a Gauss function with a maximum in the point $t = \tau$. The step response shows a smooth switching expressed by an error function.

The proposed approximation $W(j\omega)$ gives very strong damping at high frequencies, which is an advantage as compared to other functions. However, it has also one disadvantage related to its causality (see § 1.6). The application of the Paley-Wiener causality criterion (1.104) to the frequency response $W(j\omega)$ shows that this function is not causal. However, it may be considered as causal if the delay time τ is larger than the width of the Gauss function τ_α , and the Gauss function is assumed to be equal to zero out of the interval $\tau - \tau_\alpha < t < \tau + \tau_\alpha$. One may define τ_α as follows:

$$\tau_\alpha = 2\nu\alpha \quad (4.105)$$

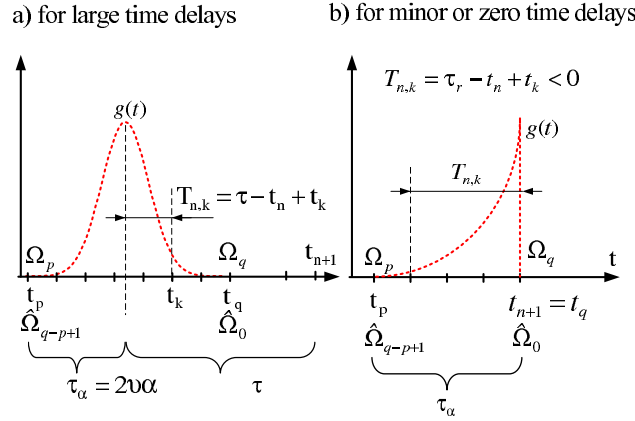


Figure 4.31: Coefficients in the moving average (4.107).

with ν chosen in the range between 2 and 3. The value $\nu = 2$ provides quite inaccurate results with $g(\tau - \tau_\alpha)/g(\tau) = 0.0183$, while $\nu = 3$ gives already fair precision with $g(\tau - \tau_\alpha)/g(\tau) = 0.00012$. We have used $\nu = 3$ for all computations. Thus, the models based on the approximation (4.100) are applied only for $\tau > \tau_\alpha$, while the second approximation will be applied to shorter delay times.

Further, the time response $y(t)$ on an arbitrary input signal $x(t)$ is considered at discrete time points. For simplicity, it is assumed that the time step is constant and equal to Δt . Thus, the notation $n\Delta t = t_n$, $x(t_n) = x_n$, and $y(t_n) = y_n$ may be introduced. The input function $x(t)$ is linearly interpolated between the discrete points according to (3.20). The convolution integral in (3.19) can be represented as a sum of integrals over the intervals between time steps:

$$y_{n+1} = \sum_{k=0}^n \int_0^{\Delta t} g(t_{n+1} - t_k - \vartheta)(a_{k+1}\vartheta + b_{k+1})d\vartheta. \quad (4.106)$$

The convolution integral (4.106) is solved in closed form. Since $\tau < \tau_\alpha$, $s(0)$ yields zero. After several transformations a moving-average formula for the output function is obtained as follows:

$$y_{n+1} = \sum_{k=p}^q \Omega_k x_k. \quad (4.107)$$

The coefficients of the formula (4.107) may be computed before the numerical integration of the PEEC model by following expressions:

$$\Omega_k = \begin{cases} \frac{\alpha}{\sqrt{\pi}} \frac{1}{\Delta t} [\Psi_{n+1,p+1} - \Psi_{n+1,p}] + \frac{T_{n+1,p+1}}{2\Delta t} [\Phi_{n+1,p+1} - \Phi_{n+1,p}], & k = p \\ \frac{\alpha}{\sqrt{\pi}} \frac{1}{\Delta t} [\Psi_{n+1,q-1} - \Psi_{n+1,q}] + \frac{T_{n+1,q-1}}{2\Delta t} [\Phi_{n+1,q-1} - \Phi_{n+1,q}], & k = q \\ \frac{\alpha}{\sqrt{\pi}} \frac{1}{\Delta t} [\Psi_{n+1,k+1} - 2\Psi_{n+1,k} + \Psi_{n+1,k-1}] + \\ + \frac{T_{n+1,k-1}}{2\Delta t} [\Phi_{n+1,k-1} - \Phi_{n+1,k}] + \frac{T_{n+1,k+1}}{2\Delta t} [\Phi_{n+1,k+1} - \Phi_{n+1,k}], & \text{else} \end{cases} \quad (4.108)$$

with

$$\Psi_{n,k} = \exp \left[- \left(\frac{T_{n,k}}{2\alpha} \right)^2 \right], \quad \Phi_{n,k} = \operatorname{erf} \left(\frac{T_{n,k}}{2\alpha} \right), \quad T_{n,k} = \tau - t_n + t_k, \quad (4.109)$$

where $\operatorname{erf}(x)$ is the error function that may be efficiently calculated using a polynomial approximation from [2]. Because of the selectivity of the impulse response $g(t)$ shown in Fig. 4.31, we have to calculate only a few summands in the moving average (4.107), namely, the time points between t_p and t_q . The boundaries for subscripts p and q are chosen in the range from 0 up to n as follows

$$p = \max \left\{ \left\lfloor \frac{t_{n+1} - \tau - \tau_\alpha}{\Delta t} \right\rfloor, 0 \right\}, \quad q = \left\lceil \frac{t_{n+1} - \tau + \tau_\alpha}{\Delta t} \right\rceil. \quad (4.110)$$

The FSCM for the generalized partial elements with minor or zero time delays

The second proposed frequency-domain model for the generalized partial elements with minor time delays is the first-order rational function already applied in (4.95):

$$\xi(j\omega) \approx H_1(j\omega) = \frac{\xi}{1 + j\omega\tau} e^{-j\omega\tau_r}, \quad (4.111)$$

whose parameters are explicitly calculated according to (4.96)-(4.99). The accuracy of this approximation has been already investigated in § 4.5.3 and will not be discussed one time more. The impulse and step responses of $H_1(j\omega)$ are derived in closed form as follows:

$$g(t) = \frac{\xi}{\tau} e^{-\frac{t-\tau_r}{\tau}} h(t - \tau_r), \quad (4.112)$$

$$s(t) = \xi(1 - e^{-\frac{t-\tau_r}{\tau}}) h(t - \tau_r), \quad (4.113)$$

where $h(t)$ is the Heaviside step function. The time response $y(t)$ on the excitation $x(t)$ is computed via the Duhamel integral. Applying (4.106), in view that $s(0) = 0$, we obtain the moving average formula (4.107), whose coefficients Ω_k are calculated as follows:

$$\Omega_k = \frac{1}{\eta} \begin{cases} e^{T_{n+1,k}} - (1 + \eta) e^{T_{n+1,k+1}} & k = p \\ e^{T_{n+1,k-1}} + (\eta - 1) e^{T_{n+1,k}} & k = q \\ e^{T_{n+1,k-1}} - 2e^{T_{n+1,k}} + e^{T_{n+1,k+1}} & \text{else} \end{cases} \quad (4.114)$$

with

$$T_{n,k} = \tau_r - t_n + t_k, \quad \eta = \frac{\Delta t}{\tau}. \quad (4.115)$$

Since $g(t)$ is a selective function shown in Fig. 4.31b, we have to calculate only a few summands in the moving average (4.107), namely, the time points between t_p and t_q . The

width of the moving average is denoted by τ_α . Since the coefficients Ω_k may be calculated consequently from q until p , the index p may be estimated from the heuristic condition:

$$\Omega_p < \delta_{err} \sum_{k=p+1}^q \Omega_k, \quad (4.116)$$

where δ_{err} is the relative error.

Discussion

The total number of terms in (4.107) denoted by n_α for the both FSCM models depends on the ratio between the period related to the maximum frequency of interest and the integration step. E.g., the suitable ratio 40 yields the number of summands between 3 and 8 depending on the cell geometry for the first type of model and 3-4 times more points for the second one. Thus, the second macromodel is less efficient, but it is applied to the minority of partial elements with small or zero delays, while the majority of partial elements are modeled by the first macromodel. Generally, the calculation of (4.107) does not result in large increase of the run time as compared to the standard FW-PEEC model. The FW-PEEC model computes the time delay sources using a table with delayed values of control variables (see § 4.3.1). The moving average (4.107) uses the same table, but it computes the instantaneous value of the controlled source using several points. Since the coefficients Ω_k are computed only one time as preprocessing, the run time of a step of the numerical integration is approximately equal to the one of the FW-PEEC method multiplied by the mean number of summands in controlled sources. Nevertheless, since other algorithms for the modeling of the frequency dependence of partial elements add variables in the MNA equation system, the proposed method is the best choice.

Inclusion of FSCM models into a SPICE-like circuit simulator

Since the FSCM of the generalized partial elements are described by the formula (4.107), they cannot be realized by standard lumped elements. Therefore, we include them in the SPICE-like circuit simulator only in the form of associated discrete circuits studied in § 2.2. Since the parameters of associated discrete circuits depend on the time step and on the numerical method, we should choose the integration rule explicitly. In the following, the backward differentiation formula of the second order (BD2) is applied (see § 4.3.2).

ADC for the generalized self partial inductance

In the following, the current and voltage of the generalized self partial inductance are denoted by $u^{\alpha,\alpha}(t) = \mathfrak{F}^{-1}\{U^{\alpha,\alpha}\}$ and $i^\alpha(t) = \mathfrak{F}^{-1}\{I_\alpha\}$, respectively. The voltage on the generalized self partial inductance is computed in the frequency domain as $U^{\alpha,\alpha} = j\omega L_{\alpha,\alpha}(j\omega) I_\alpha$ (see Fig. 4.2). Now, we develop a time-domain model for an one-port circuit, whose voltage and current are related to the same equation. Since (4.107) provides a time-domain model

for $L_{\alpha,\alpha}(j\omega)$, and assuming $x(t) = i'_\alpha = \partial i_\alpha / \partial t$ and $y(t) = u^{\alpha,\alpha}(t)$, we rewrite (4.107) in an equivalent form:

$$\begin{aligned} u_{n+1}^{\alpha,\alpha} &= \hat{u}_{n+1}^{\alpha,\alpha} + u_{n+1}^{L,\alpha}, \\ u_{n+1}^{L,\alpha} &= \hat{\Omega}_0^{\alpha,\alpha} i'_{n+1}, \quad \hat{u}_{n+1}^{\alpha,\alpha} = \sum_{k=p}^n \hat{\Omega}_{n-k+1}^{\alpha,\alpha} i'_k, \\ \hat{\Omega}_k^{\alpha,\alpha} &= \begin{cases} L_{\alpha,\alpha} [\Omega_{n+1}^{\alpha,\alpha}], & k = 0, \\ L_{\alpha,\alpha} \Omega_{n-k+1}^{\alpha,\alpha}, & \text{else,} \end{cases} \end{aligned} \quad (4.117)$$

where the coefficients $\hat{\Omega}_k^{\alpha,\alpha}$ are introduced for a more compact representation of (4.107). The subscript k of $\hat{\Omega}_k^{\alpha,\alpha}$ means the number of time steps delayed relatively to the actual time t_{n+1} . Thus, these coefficients are calculated once for all steps of the integration (see Fig. 4.31). They are real constants with inductance units. According to the used numerical method (BD2), the derivative of the current i'_{n+1} in (4.117) is computed by (2.15):

$$i'_{n+1} = \frac{4}{3}i_n - \frac{1}{3}i_{n-1} = \frac{2}{3}\Delta t \cdot i'_{n+1}. \quad (4.118)$$

Substituting (4.118) in (4.117), one derives

$$i'_{n+1} = g^{L,\alpha} u_{n+1}^{L,\alpha} + J_{n+1}^{L,\alpha} \quad (4.119)$$

with $g^{L,\alpha} = 2\Delta t / (3\hat{\Omega}_0^{\alpha,\alpha})$ and $J_{n+1}^{L,\alpha} = \frac{4}{3}i_n - \frac{1}{3}i_{n-1}$. (4.119) can be understood as an ADC of an inductance $L_{eq}^{\alpha,\alpha} = \hat{\Omega}_0^{\alpha,\alpha}$. According to (4.117), the controlled voltage source $\hat{u}_{n+1}^{\alpha,\alpha}$ connected in series to the equivalent inductance completes the ADC for the whole generalized self partial inductance. The current source $J_{n+1}^{L,\alpha}$ and the voltage source $\hat{u}_{n+1}^{\alpha,\alpha}$ have to be calculated at each time point using the retarded values of $i^\alpha(t)$. In the following, the MNA representation of a current cell introduces the unknowns: the nodal potential of the adjacent potential cells φ_{n+1}^α and $\varphi_{n+1}^{\alpha+1}$, the current in the cell i_{n+1}^α , and one additional nodal potential $\hat{\varphi}_{n+1}^\alpha$. These variables are shown on the full ADC of a conductor segment in Fig. 4.32. The contribution of the generalized self partial inductance to the MNA formulation is given below as a MNA-stamp studied in § 2.2.2:

	$\text{id}(\varphi_{n+1}^\alpha)$	$\text{id}(\varphi_{n+1}^{\alpha+1})$	$\text{id}(\hat{\varphi}_{n+1}^\alpha)$	$\text{id}(i_{n+1}^\alpha)$	RHS
$\text{id}(\varphi_{n+1}^\alpha)$	$\hat{g}^{L,\alpha}$		$-\hat{g}^{L,\alpha}$		$-J_{n+1}^{L,\alpha} / (1 + R_\alpha g^{L,\alpha})$
$\text{id}(\varphi_{n+1}^{\alpha+1})$				-1	
$\text{id}(\hat{\varphi}_{n+1}^\alpha)$	$-\hat{g}^{L,\alpha}$		$\hat{g}^{L,\alpha}$	1	$J_{n+1}^{L,\alpha} / (1 + R_\alpha g^{L,\alpha})$
$\text{id}(i_{n+1}^\alpha)$		-1	1		$\hat{u}_{n+1}^{\alpha,\alpha}$

where the notation $\text{id}(x)$ means the index of the variable x in the RHS vector.

Additionally, it should be noticed that the ADC model of the generalized self partial inductance allows one to calculate i'_n needed for the modeling of couplings to other cells:

$$i'_k = \frac{u_k^{L,\alpha}}{\hat{\Omega}_0^{\alpha,\alpha}} = \frac{i_k^\alpha - J_k^{L,\alpha}}{g^{L,\alpha} \hat{\Omega}_0^{\alpha,\alpha}}, \quad k \in [0, n+1]. \quad (4.120)$$

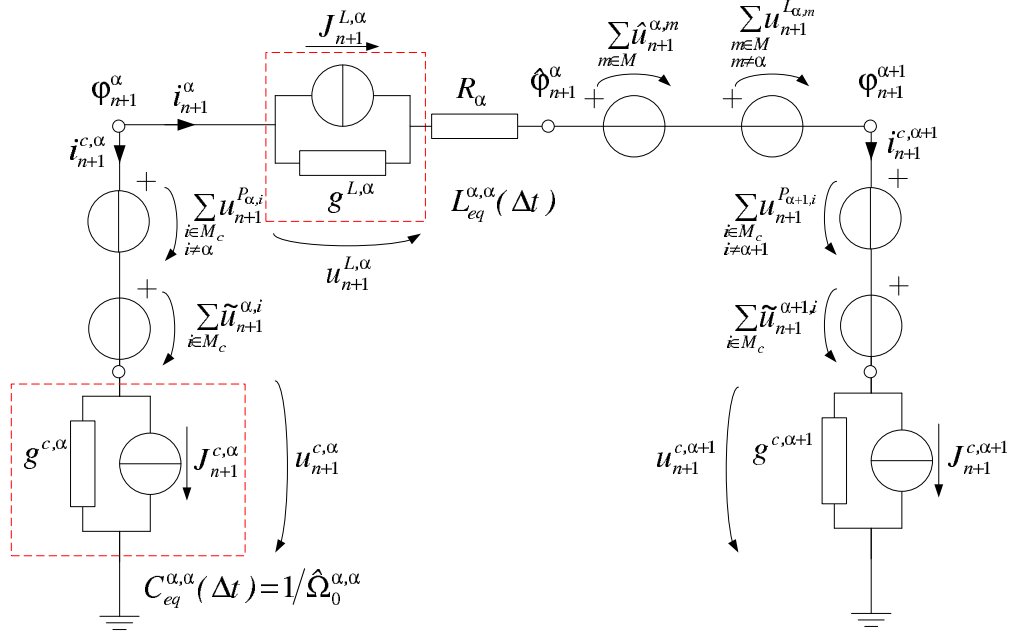


Figure 4.32: Associated discrete circuit for a conductor segment in S-FW-PEEC models.

ADC for the generalized mutual partial inductance

The mutual inductive coupling between cells α and m is described in the frequency-domain model (see Fig. 4.2) by the controlled voltage source $U^{\alpha,m} = j\omega L_{\alpha,m}(j\omega) I_m$. The time response of the voltage $u_{n+1}^{\alpha,m} = \mathfrak{F}^{-1}\{U^{\alpha,m}\}$ can be derived from (4.107):

$$u_{n+1}^{\alpha,m} = \begin{cases} u_{n+1}^{L_{\alpha,m}} + \hat{u}_{n+1}^{\alpha,m} & \text{with } u_{n+1}^{L_{\alpha,m}} = \hat{\Omega}_0^{\alpha,m} i_{n+1}^m, \quad \hat{u}_{n+1}^{\alpha,m} = \sum_{k=p}^n \hat{\Omega}_{q-k}^{\alpha,m} i_k^m, \quad \tau_{\alpha,m} \leq \tau_{\alpha}, \\ \hat{u}_{n+1}^{\alpha,m} & \text{with } \hat{u}_{n+1}^{\alpha,m} = \sum_{k=p}^q \hat{\Omega}_{q-k}^{\alpha,m} i_k^m, \quad \tau_{\alpha,m} > \tau_{\alpha}. \end{cases} \quad (4.121)$$

(4.121) has two cases with respect to the ratio between $\tau_{\alpha,m}$ and τ_{α} calculated by (4.105). The upper case of the formula ($\tau_{\alpha,m} \leq \tau_{\alpha}$) is valid only for close located cells α and m . In this case, the pulse response yields $g(t_{n+1}) \neq 0$ and, consequently, the subscript q is equal to $n+1$ as in Fig. 4.31b. Thus, the voltage $u_{n+1}^{L_{\alpha,m}}$ represents mutual inductive coupling without delay and may be modeled as a usual mutual inductance $L_{eq}^{\alpha,m} = \hat{\Omega}_0^{\alpha,m}$. It produces an entry in the MNA system matrix. The second term of the upper case represents an independent voltage source $\hat{u}_{n+1}^{\alpha,m}$ computed using the retarded values of i_k^m . The control variable i_k^m is calculated in the previous subsection via (4.120). The MNA stamp for the case $\tau \leq \tau_{\alpha}$ is shown below:

	$\text{id}(i_{n+1}^m)$	RHS
$\text{id}(i_{n+1}^{\alpha})$	$\frac{-\hat{\Omega}_0^{\alpha,m}}{g^{L,m} \hat{\Omega}_0^{\alpha,m}}$	$\frac{-\hat{\Omega}_0^{\alpha,m}}{g^{L,m} \hat{\Omega}_0^{\alpha,m}} J_{n+1}^{L,m} + \hat{u}_{n+1}^{\alpha,m}$

The weighting coefficients used in (4.121) are given by

$$\hat{\Omega}_k^{\alpha,m} = \begin{cases} L_{\alpha,m} \Omega_{n+1}^{\alpha,m}, & k = 0, \\ L_{\alpha,m} \Omega_{n-k+1}^{\alpha,m}, & \text{else.} \end{cases} \quad (4.122)$$

The lower case of (4.121) is valid for $\tau > \tau_\alpha$ and corresponds to Fig. 4.31a. Because the subscript q is less than $n + 1$ the term being equivalent to a mutual inductance $L_{eq}^{\alpha,m}$ is zero, and the whole mutual coupling is given by $\hat{u}_{n+1}^{\alpha,m}$ with the modified weighting coefficients:

$$\hat{\Omega}_k^{\alpha,m} = \xi_{\alpha,m}^v \Omega_{q-k}^{\alpha,m}. \quad (4.123)$$

The MNA contribution in this case is given by the following stamp:

	$\mathbf{id}(i_{n+1}^m)$	RHS
$\mathbf{id}(i_{n+1}^\alpha)$		$\hat{u}_{n+1}^{\alpha,m}$

ADC for the generalized self potential coefficient

The derivation of the associated discrete models of the generalized potential coefficients is completely analogous to the generalized partial inductances. This concerns both self and mutual potential coefficients. The ADC of the generalized self potential coefficient is shown in Fig. 4.32. The equations for its parameters are

$$\begin{aligned} \varphi_{n+1}^{\alpha,\alpha} &= \tilde{u}_{n+1}^{\alpha,\alpha} + u_{n+1}^{c,\alpha}, \\ u_{n+1}^{c,\alpha} &= \hat{\Omega}_0^{\alpha,\alpha} q_{n+1}^\alpha, \quad \tilde{u}_{n+1}^{\alpha,\alpha} = \sum_{k=p}^n \hat{\Omega}_{n-k+1}^{\alpha,\alpha} q_k^\alpha \end{aligned} \quad (4.124)$$

with

$$\begin{aligned} \hat{\Omega}_k^{\alpha,\alpha} &= \begin{cases} p_{\alpha,\alpha} [\Omega_{n+1}^{\alpha,\alpha}], & k = 0 \\ p_{\alpha,\alpha} \Omega_{n-k+1}^{\alpha,\alpha}, & \text{else} \end{cases} \\ q_k^\alpha &= \int_{t=0}^{t_k} i^{c,\alpha}(t) dt = u_k^{c,\alpha}(t) / \hat{\Omega}_0^{\alpha,\alpha}, \\ g^{c,\alpha} &= \frac{3}{2\Delta t \hat{\Omega}_0^{\alpha,\alpha}}, \quad J_{n+1}^{c,\alpha} = g^{c,\alpha} \left(-\frac{4}{3} u_n^{c,\alpha} + \frac{1}{3} u_{n-1}^{c,\alpha} \right). \end{aligned} \quad (4.125)$$

The MNA representation of a potential cell uses three variables: the potentials φ_{n+1}^α and $u_{n+1}^{c,\alpha}$, and the transversal current $i_{n+1}^{c,\alpha}$, which are shown in Fig. 4.32. The relation between $i^{c,\alpha}(t)$ and $u^{c,\alpha}$ can be understood as a capacitance $C_{eq}^{\alpha,\alpha} = 1/\hat{\Omega}_0^{\alpha,\alpha}$ as shown in Fig. 4.32. The MNA stamp for the contribution of a generalized self potential coefficient is given by

	$\mathbf{id}(\varphi_{n+1}^\alpha)$	$\mathbf{id}(u_{n+1}^{c,\alpha})$	$\mathbf{id}(i_{n+1}^{c,\alpha})$	RHS
$\mathbf{id}(\varphi_{n+1}^\alpha)$			1	
$\mathbf{id}(u_{n+1}^{c,\alpha})$		$g^{c,\alpha}$	-1	$-J_{n+1}^{c,\alpha}$
$\mathbf{id}(i_{n+1}^{c,\alpha})$	1	-1		$\tilde{u}_{n+1}^{\alpha,\alpha}$

ADC for the generalized mutual potential coefficient

The associated discrete model of the modified mutual potential coefficients is shown in Fig. 4.32. The equations for its parameters are

$$u_{n+1}^{\alpha,i} = \begin{cases} \tilde{u}_{n+1}^{\alpha,i} + u_{n+1}^{P_{\alpha,i}} & \text{with } u_{n+1}^{P_{\alpha,i}} = \hat{\Omega}_0^{\alpha,i} q_{n+1}^i, \quad \tilde{u}_{n+1}^{\alpha,i} = \sum_{k=p}^n \hat{\Omega}_{q-k}^{\alpha,i} q_k^i, \quad \tau_{\alpha,i}^c \leq \tau_{\alpha} \\ \tilde{u}_{n+1}^{\alpha,i} & \text{with } \tilde{u}_{n+1}^{\alpha,i} = \sum_{k=p}^q \hat{\Omega}_{q-k}^{\alpha,i} q_k^i, \quad \tau_{\alpha,i}^c > \tau_{\alpha} \end{cases} \quad (4.126)$$

with

$$\hat{\Omega}_k^{\alpha,m} = \begin{cases} \xi_{\alpha,m}^s [\Omega_{n+1}^{\alpha,\alpha}], & k = 0, \\ \xi_{\alpha,m}^s \Omega_{n-k+1}^{\alpha,\alpha}, & \text{else.} \end{cases} \quad (4.127)$$

The MNA stamps for both cases of the generalized mutual potential coefficients are derived analogous to the mutual partial inductances. The upper case of (4.126) ($\tau_{\alpha,i}^c \leq \tau_{\alpha}$) corresponds to close located cells (see Fig. 4.31b). The voltage $u_{n+1}^{P_{\alpha,i}}$ (see Fig. 4.32) represents a mutual capacitive coupling without delay and may be modeled as an static potential coefficient $p_{eq}^{\alpha,i} = \hat{\Omega}_0^{\alpha,i}$. It produces an entry in the nodal admittance matrix. The MNA-stamp in this case is

	$i\mathfrak{d}(u_{n+1}^{c,i})$	RHS
$i\mathfrak{d}(i_{n+1}^{c,\alpha})$	$-\hat{\Omega}_0^{\alpha,i} / \hat{\Omega}_0^{i,i}$	$\tilde{u}_{n+1}^{\alpha,i}$

The MNA-stamp in the lower case of (4.126) ($\tau_{\alpha,i}^c > \tau_{\alpha}$) is written for an independent time-delay source:

	$i\mathfrak{d}(u_{n+1}^{c,i})$	RHS
$i\mathfrak{d}(i_{n+1}^{c,\alpha})$		$\tilde{u}_{n+1}^{\alpha,i}$

The complete S-FW-PEEC model

The complete associated discrete circuit of a conductor segment using the above approach is shown in Fig. 4.32. This model is called stable full-wave PEEC model (S-FW-PEEC model). It has been programmed in the SPICE-like special-purpose circuit simulator NEAN (see § 4.3.2). This code has similar lumped elements as the usual SPICE and, additionally, different kinds of PEEC models for arbitrary interconnection systems. In the following, all calculations by the standard and S-FW-PEEC models have been made using the same grid and the MNA solver. Thus, the following comparison between the FW-PEEC and S-FW-PEEC methods is correct, since the computational models are consistent with respect to the discretization and solver.

Example of simulation: Transmission line with a microstrip geometry

A printed transmission line is shown in Fig. 4.33a. The copper trace has a rectangular cross-section with a width of 3 mm and a thickness of 35 μm . It is located 100 μm above a

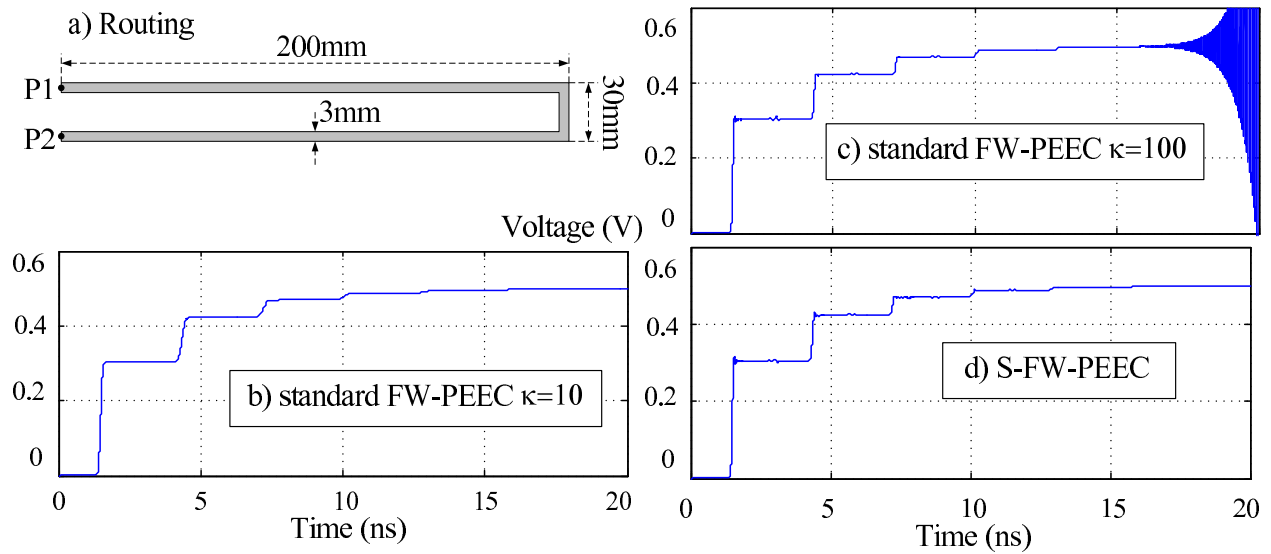


Figure 4.33: Routing of the microstrip transmission line, and the voltage at the port P_2 .

perfectly conducting ground. The dielectric has been assumed as air. The transmission line is terminated by two ports denoted by P_1 and P_2 (see Fig. 4.33a). The port P_1 is excited by a lumped voltage source with an internal impedance of 50Ω , the port P_2 is loaded by a lumped resistance of 50Ω . The voltage source has a ramp waveform with a rise from zero to 1 V in 100 ps. The maximum frequency of interest is assumed 10 GHz. The discretization of the interconnection system according to the criterion $\lambda_m/20$ results in a number of current and potential cells of 289 and 292, respectively. The number of unknowns in the MNA equation system is 889. The total number of controlled sources for current and potential cells is 79055. The voltage at the port P_2 has been computed by the standard FW-PEEC and the S-FW-PEEC model. The first one shows an unstable solution.

The stability of the standard FW-PEEC is improved by the addition of damping resistances defined in (4.94). As is above mentioned, the value of κ for a FW-PEEC model cannot be determined uniquely. Decreasing κ leads to the stability, but it may introduce too strong damping and decrease the accuracy (see Fig. 4.33b). The increase of κ makes the PEEC models more exact, but does not protect from instabilities (see Fig. 4.33c). In contrast, the S-FW-PEEC model results in a stable and precise solution (see Fig. 4.33d).

In the following, the computational efficiency of both models is compared. The calculation has been accomplished by a single Pentium Xeon 2.66 GHz and 1 GB of RAM. The time t_s needed for one step of numerical the integration amounts to $t_s = 12.7 \text{ ms}$ for the FW-PEEC model, while the S-FW-PEEC model needs $t_s = 29.6 \text{ ms}$. Thus, the calculation time of a time step of the S-FW-PEEC model is 2.33 times higher than that of the standard PEEC model. On the other hand, the numerical convergence of the standard PEEC model has needed 29980 time steps, while S-FW-PEEC has required only 8001 steps. Thus, the total run time of the S-FW-PEEC (236.8s) is even shorter than of the standard FW-PEEC (381.1s).

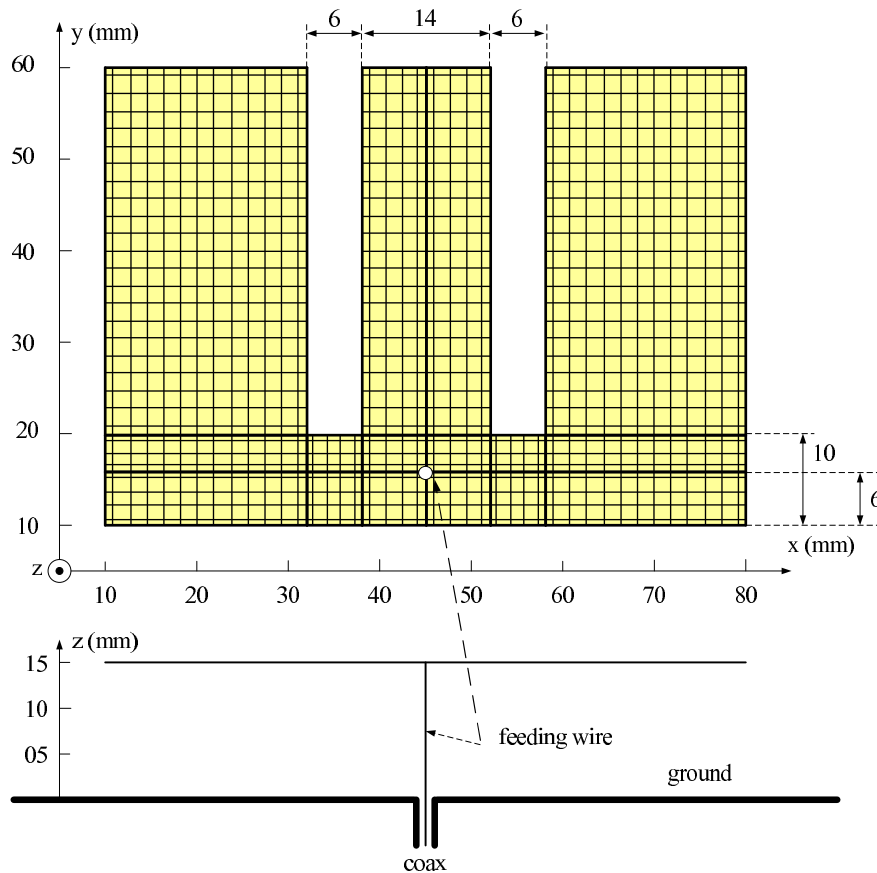


Figure 4.34: Geometry of the patch antenna.

Example of simulation: Wide-band E-shaped patch antenna

The wide-band E-shaped patch antenna (see Fig. 4.34) proposed for wireless communications in [162] is the second example of the application of the S-FW-PEEC method. The antenna has only one patch with two slots added in [162] in order to expand the bandwidth of the antenna. The copper patch is located 15 mm above a perfectly conducting ground. A straight copper feeding wire with a radius 0.1 mm connects the patch with the coaxial cable. The antenna is excited by a lumped voltage source located at the base of the feeding wire. The internal impedance of the source is 50Ω . The patch is assumed as a thin conductor and discretized in two dimensions as shown in Fig. 4.34.

The waveform of the excitation is a triangle pulse with a rise and fall times equal to 500 ps. The total time of simulation is 10 ns. The maximum frequency of interest is assumed 2 GHz. In the following, a set of calculations with the different precision of the discretization is provided. This has been made in order to compare the run time of the standard and S-FW-PEEC models. We have chosen following steps for discretization: $\lambda_m/15$, $\lambda_m/35$, $\lambda_m/50$, and $\lambda_m/60$. The standard FW-PEEC model with the damping resistances yields unstable solutions in all these cases. The S-FW-PEEC model shows stable and very similar solutions

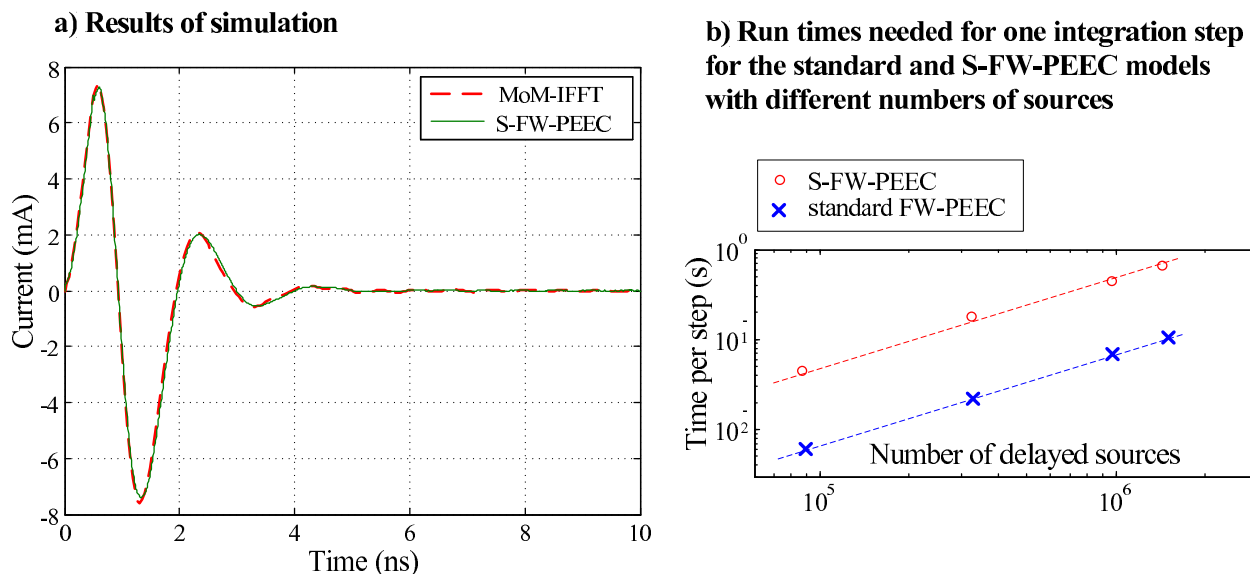


Figure 4.35: Current at the base of the feeding wire (a), and the efficiency comparison (b).

for all numerical experiments. The current at the base of the feeding wire computed by the S-FW-PEEC model ($\lambda_m/60$) is shown in Fig. 4.35a. This curve has been verified by the MoM code (CONCEPT, see [141]) in the frequency domain with the subsequent IFFT transformation. The comparison of the results is presented in Fig. 4.35a, the both curves show good agreement.

After the validation, we may compare characteristic parameters of computations by the standard and improved PEEC models with different number of unknowns (Table 4.1). The columns of the table correspond to different discretization steps. Columns "S-FW" mean computations by the S-FW-PEEC model, while columns "FW" mean computations by the standard FW-PEEC method.

Discretization:	$\lambda_m/15$		$\lambda_m/35$		$\lambda_m/50$		$\lambda_m/60$	
Num. of current cells:	296		604		1066		1305	
Num. of potential cells:	207		381		635		764	
Num. of delayed sources:	86,089		325,209		965,093		1,428,314	
Num. of MNA unknowns:	1149		1940		3063		3625	
Method:	S-FW	FW	S-FW	FW	S-FW	FW	S-FW	FW
Run time per step(s):	0.045	0.00595	0.189	0.0209	0.45	0.0653	0.656	0.0989
Total run time (s):	54.4	14.04	531.4	58.5	900.25	261.26	1574.9	316.53
Run time per step ratio:	7.5		9.08		6.89		6.63	

Table 4.1: Characteristics of numerical experiments

The numerical experiments with the both modifications of PEEC and the same grid step differ from each other only by models of delayed sources. Thus, numbers of currents cells, potential cells, unknowns in MNA formulation, and the number of partial elements are equal.

The difference between methods appears in the run time. The most interesting parameter in Table 4.1 is the ratio between the run times per integration step. It characterizes the difference in run times between the standard and S-FW-PEEC models. Obviously, this ratio does not increase with the augmentation of the cell number. This feature can be well illustrated by Fig. 4.35b. The run time of the standard and S-FW-PEEC models increases in a logarithmic scale as two parallel straight lines. This means that the both algorithms have the same order of the computational complexity.

Conclusion for the S-FW-PEEC model

The S-FW-PEEC method is a novel improved with respect to the stability modification of the FW-PEEC method. Its advantages are listed below.

- The number of variables is not changed with respect to the standard FW-PEEC model.
- The frequency dependence of the generalized partial elements is precisely approximated.
- Decrease of the step of the numerical integration is not needed.
- The S-FW-PEEC model is compatible with the SPICE-like circuit simulators.

The disadvantage is increasing the run time for preprocessing and for the time-domain computation. However, this is not a critical problem, since the ratio between run times for the standard and S-FW-PEEC models does not depend on the number of unknowns (see Fig. 4.35b), approximately.

Chapter 5

PEEC modeling of PCB boards

Printed circuit boards (PCB) represent a special class of interconnection structures, which consist of a number of layers with printed traces, via holes, and bonding pads located in a stratified dielectric. Since PCB boards are used to connect the pins of integrated circuits (IC) and other active devices, their direct frequency-domain analysis can be impossible due to the non-linear circuit environment. Moreover, in the case of a linear circuit environment, the simulation in the frequency domain may be applied, but in the event of a wide-band excitation it results in a too long run time. Therefore, the importance of the time-domain methods for the PCB-boards simulation is growing.

This chapter considers the possibilities for the modeling of PCB boards using the PEEC method. The first and simplest approach is studied in § 5.1. It applies the standard half-space PEEC model derived in § 4.2.2 with the effective parameters of the PCB substrate. Since this approach is quite inaccurate, a novel concept called the DGFLM-PEEC method is developed and investigated in this chapter. It is based on the general formulation of the DGF-PEEC method (see § 4.2.1) applying the MPIE with the dyadic Green's functions for layered media. This approach was recently derived by Kochetov, Wollenberg, and Leone [82], [75], [74], [72], and [73]. § 5.2 - § 5.5 are devoted to the derivation, explanation, discussion, and validation of the DGFLM-PEEC method.

5.1 Half-space full-wave PEEC models for PCB boards

This section discusses the simplest PEEC model, which may be applied to the modeling of PCB boards. The concept of the effective permittivity means the replacement of the inhomogeneous medium of the PCB board by an equivalent homogeneous one. Of course, this may be done correctly only for the transmission-line like interconnections and at relatively low frequencies.

One of the most wide-spread types of interconnections on the PCB boards are microstrip lines, whose half-space PEEC models may be developed analogous to the approach proposed for the method of moments by Leone [96], [98] and by Leone, Brüns, and Singer [100]. Moreover, the authors [102], [101] have expanded this MoM formulation on the analysis of

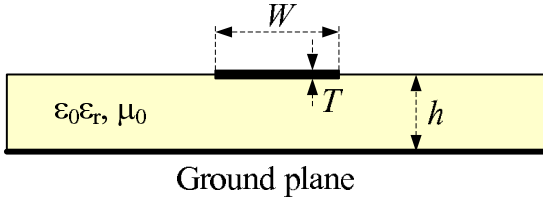
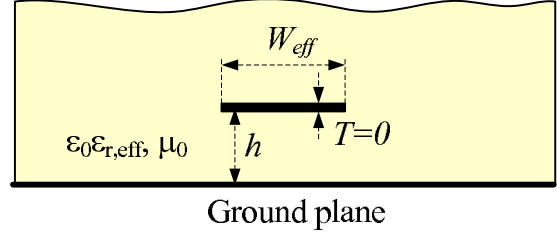
a) Microstrip line**b) Equivalent line in the half-space**

Figure 5.1: Microstrip line (a) and its equivalent model in the homogeneous medium (b).

the influence of an external electromagnetic field on the PCB traces. Thus, this technique may be applied to the PEEC method as well.

In the following, the concept of the effective permittivity will be studied by the example of the microstrip line shown in Fig. 5.1a, where W and T are the width and thickness of the line, h is the thickness of the substrate, whose relative permittivity is ϵ_r . The principle propagation mode for a microstrip line is a quasi-TEM wave, since the medium is inhomogeneous [64]. This means that, at relatively low frequencies, the longitudinal components of the electric and magnetic fields are much less than the transversal ones. Hence, these waves may be approximately considered as TEM waves. The increase of the frequency leads to appearing high-frequency modes, which make the wave hybrid, i.e., composed of the TM and TE waves explained in [34]. Thus, the quasi-TEM wave may be considered as a TEM wave at frequencies below a boundary frequency denoted by f_b . This boundary is estimated in [64] as follows:

$$f_b = \frac{21.3 \text{ mm}}{(W + 2h)\sqrt{\epsilon_r + 1}} \text{ GHz}. \quad (5.1)$$

Since the TEM mode dominates at $f < f_b$, the microstrip line may be considered as a uniform transmission line in a homogeneous medium with a constant propagation velocity. The propagation velocity in a homogeneous space is related to the permittivity. The permittivity corresponding to this propagation velocity is named the *effective permittivity*, which is estimated for a microstrip line according to the following formula given in [54]:

$$\epsilon_{r,eff} = \frac{\epsilon_r + 1}{2} + \frac{\epsilon_r - 1}{2} \left(1 + \frac{10h}{W}\right)^{-\frac{1}{2}} - \frac{\epsilon_r - 1}{4.6} \frac{T/h}{\sqrt{W/h}}. \quad (5.2)$$

Thus, the initial problem with a microstrip line may be replaced by the equivalent one shown in Fig. 5.1b. The equivalent problem is a half-space problem, where the upper half-space is homogeneous and has the relative permittivity $\epsilon_{r,eff}$. The geometry of the microstrip line in the equivalent problem is slightly changed. The thickness is assumed to be zero, while the width is modified to W_{eff} , which is estimated in [54] as follows:

$$W_{eff} = W + 1.25 \frac{T}{\pi} \begin{cases} 1 + \ln 4\pi \frac{W}{T}, & \frac{W}{h} \leq \frac{1}{2\pi} \\ 1 + \ln \frac{2}{T/h}, & \frac{W}{h} > \frac{1}{2\pi} \end{cases}. \quad (5.3)$$

Since the problem with inhomogeneous medium is replaced by an equivalent half-space problem, it may be simulated using the half-space MoM model (see [96]) or the HS-FW-PEEC model presented in § 4.2.2. In this case, the partial inductances are computed via (4.32), (4.44), and (4.45) considering that the width of the cells is modified to its effective values. The generalized potential coefficients are computed via (4.46), while the formulation for the static potential coefficients (4.35) and (4.47) is slightly changed due to the effective permittivity:

$$\begin{aligned} p_{\alpha,i} &= \frac{1}{4\pi\epsilon_0\epsilon_{r,eff}S_\alpha S'_i} \iint_{S_\alpha} \iint_{S'_i} \frac{dS'_i dS_\alpha}{|\mathbf{r} - \mathbf{r}'|}, \\ p_{\alpha,i}^{(i)} &= \frac{1}{4\pi\epsilon_0\epsilon_{r,eff}S_\alpha S'_i} \iint_{S_\alpha} \iint_{S'_i} \frac{dS'_i dS_\alpha}{|\mathbf{r} - \bar{\mathbf{I}}_i \cdot \mathbf{r}'|}. \end{aligned} \quad (5.4)$$

The influence of the external field on the microstrip traces may be added to the FW-PEEC model analogous to the MoM [102], [101]. For a thorough explanation of this issue, the reader is referenced to the paper of Vahrenholt, Bruns, Singer, and Rimolo-Donaldo [153].

Discussion

The approach presented above for the modeling of microstrip lines is very simple to realize, which is its main advantage. However, the precision of this approach is not perfect, since the effective permittivity is estimated for a single value of the trace width. Thus, microstrip lines with different width can require different values of $\epsilon_{r,eff}$, while the half-space PEEC model needs unified parameters for the homogeneous medium. Moreover, the effective permittivity introduced for the microstrip lines can be incorrect with regard to vertical interconnections that may not be considered as transmission lines. Thus, in the case $f < f_b$, the PEEC model using the effective permittivity is rigorously applicable only for groups of the microstrip lines with the same width and is approximately applicable for more complex interconnections. At higher frequencies, appearing higher propagation modes makes the half-space PEEC model unsuitable for any geometries of interconnections. This drawback has motivated the author of this monograph to develop more advanced DGF-PEEC models based on the dyadic Green's functions for layered media that are presented in the next sections.

5.2 MPIE for layered media

The derivation of the DGF-PEEC model for a multilayer PCB involves the dyadic Green's functions for plane-stratified media. Since they cannot be derived for an arbitrary PCB structure, we make several assumptions and introduce a simplified geometry of PCB boards applied for the derivation of the Green's functions (see Fig. 5.2a). A PCB with n dielectric

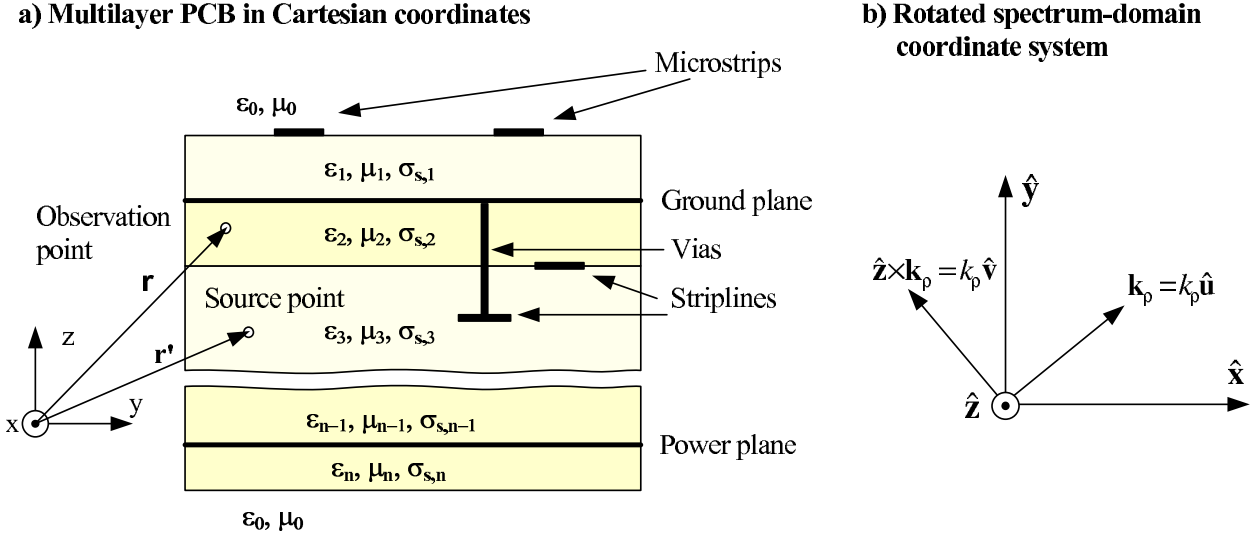


Figure 5.2: Multilayer PCB in Cartesian coordinates (a), and the rotated spectrum-domain coordinate system (b).

layers is considered, the dielectric layer $i \in \overline{1, n}$ is defined by its permittivity ϵ_i , permeability μ_i , and the conductivity of dielectric $\sigma_{s,i}$. In the following, the permeability of all layers is equal to μ_0 . The dielectric is assumed to be piecewise homogeneous with respect to layers and unbounded in the (x, y) plane. In general, the MPIE for such a layered medium may be derived for an anisotropic dielectric. However, due to simplification, we consider only the piece-wise isotropic one, i.e., the permittivity in a layer is a scalar constant. The space under and above the PCB is a vacuum with the permittivity ϵ_0 and the permeability μ_0 .

The printed circuit board is located in the (x, y) plane, which is defined also as the horizontal plane, while the z -axis is orthogonal to the PCB and is defined as the vertical direction (see Fig. 5.2a). The layered dielectric contains n_p conductor layers. Some of these layers are the completely metalized power and ground planes assumed solid and unbounded in the horizontal plane as the dielectric. Other conductor layers hold microstrips and striplines as shown in Fig. 5.2a. The vias connect interconnections from different conductor layers. It is assumed that the microstrips, striplines, and vias do not influence the homogeneity of the substrate and its parameters.

Using the generalized DGF-PEEC formulation derived in § 4.1, an effective time-domain PEEC model on the basis of the MPIE for layered media (MPIE-LM) is obtained in § 5.4. Since the MPIE-LM is derived using the dyadic Green's functions for the electric and magnetic fields in layered media, this section has the following structure:

- the derivation of DGFs for the electric and magnetic fields,
- then, the derivation of MPIE-LM using these Green's functions.

In general, the fundamental theory required for the derivation of the dyadic Green's functions for layered media was developed in a large number of classical books: Sommerfeld

[142], Felsen and Markuvitz [44], Lindell [104], Tai [145], Chew [30], Weit [159], et al. The MPIE for layered media has been originally derived by Michalski [108]. The further development of this integral-equation formulation has been provided by Mosig [116], Michalski and Zheng [111], [112], Bernardi and Cicchetti [22], Michalski and Mosig [110], Bungler and Arndt [26], Michalski [109], Tsang et al. [150]. This study applies the theory developed by the aforementioned authors and formulates the mixed-potential integral equation in a form suitable for further use with the DGF-PEEC method.

5.2.1 Dyadic Green's functions for the electric and magnetic fields in layered media

Conventions

In the following, we will introduce several conventions. Since the solution regions is unbounded in the horizontal plane, the Green's functions for the electric and magnetic fields can be expressed by the eigenfunctions (plain TM and TE modes) that form a continuous space. Since these modes propagate along the z-axis, the vertical direction is called **longitudinal**, while the horizontal plane is called **transversal**. In the following, we apply this notation due to the consistency with the classical literature listed above.

An arbitrary vector \mathbf{A} may be decomposed into two terms $\mathbf{A} = \mathbf{A}_z + \mathbf{A}_t$, where $\mathbf{A}_z = A_z \hat{\mathbf{z}} = \hat{\mathbf{z}} \hat{\mathbf{z}} \cdot \mathbf{A}$ is its longitudinal component, while

$$\mathbf{A}_t = -\hat{\mathbf{z}} \times \hat{\mathbf{z}} \times \mathbf{A} \quad (5.5)$$

is its transversal component calculated according to the identity (A.3).

This section involves the direct and inverse two-dimensional spatial Fourier transformations (see (A.22) and (A.23)), which are denoted by $\mathfrak{F}_s\{\}$ and $\mathfrak{F}_s^{-1}\{\}$, respectively. The direct transformation maps the three-dimensional space into a spectrum space. The functions of the spatial coordinate \mathbf{r} are mapped into the spectrum space as functions of (z, \mathbf{k}_ρ) , where the rotating vector \mathbf{k}_ρ is located in the transversal plane (see Fig. 5.2b). The mapped functions are called *spectrum-domain* functions in contrast to their originals called *spatial-domain* functions. In the following, the spatial-domain functions are written with a tilde in the spectrum domain, e.g., $\tilde{\mathbf{E}}(z, \mathbf{k}_\rho) = \mathfrak{F}_s\{\mathbf{E}(\mathbf{r})\}$ and $\mathbf{H}(\mathbf{r}) = \mathfrak{F}_s^{-1}\{\tilde{\mathbf{H}}(z, \mathbf{k}_\rho)\}$. The spatial-domain Green's functions receive a font change in the spectrum domain, e.g., $\mathbf{g}(z, z', \mathbf{k}_\rho) = \mathfrak{F}_s\{g(\mathbf{r}, \mathbf{r}')\}$. The spectrum space is described by the rotating right coordinate system (u, v, z) , where the vectors $\hat{\mathbf{u}}$ and \mathbf{k}_ρ are codirectional and $\hat{\mathbf{z}} = \hat{\mathbf{u}} \times \hat{\mathbf{v}}$ (see Fig. 5.2b).

Derivation

The electric and magnetic fields are considered at the point \mathbf{r} , which is located in the layer m . Due to simplicity, we denote $\epsilon_m = \epsilon$ and $\sigma_{s,m} = \sigma_s$. The derivation of the EFIE

starts from Maxwell equations (1.9) rewritten below for a lossy dielectric:

$$\begin{aligned}\nabla \times \mathbf{E} &= -j\omega\mu_0\mathbf{H} - \mathbf{M}, \\ \nabla \times \mathbf{H} &= j\omega\epsilon\mathbf{E} + \mathbf{J},\end{aligned}\tag{5.6}$$

where ϵ is the complex permittivity of the lossy dielectric:

$$\epsilon = \epsilon - \frac{j\sigma_s}{\omega}.\tag{5.7}$$

The curl equations (5.6) may be rewritten in the spectrum domain using the representation for the curl operator given in (A.24):

$$\hat{\mathbf{z}} \times \frac{\partial \tilde{\mathbf{E}}}{\partial z} - j\mathbf{k}_\rho \times \tilde{\mathbf{E}} = -j\omega\mu_0\tilde{\mathbf{H}} - \tilde{\mathbf{M}},\tag{5.8}$$

$$\hat{\mathbf{z}} \times \frac{\partial \tilde{\mathbf{H}}}{\partial z} - j\mathbf{k}_\rho \times \tilde{\mathbf{H}} = j\omega\epsilon\tilde{\mathbf{E}} + \tilde{\mathbf{J}},\tag{5.9}$$

where the parameters (z, \mathbf{k}_ρ) of all spectrum-domain functions are omitted due to compactness. The projection of (5.8) and (5.9) on the z -axis yields:

$$\hat{\mathbf{z}} \cdot (5.8) \Rightarrow j\mathbf{k}_\rho \cdot (\hat{\mathbf{z}} \times \tilde{\mathbf{E}}_t) = -j\omega\mu_0\tilde{H}_z - \tilde{M}_z,\tag{5.10}$$

$$\hat{\mathbf{z}} \cdot (5.9) \Rightarrow -j\mathbf{k}_\rho \cdot (\tilde{\mathbf{H}}_t \times \hat{\mathbf{z}}) = j\omega\epsilon\tilde{E}_z + \tilde{J}_z.\tag{5.11}$$

The projection of (5.8) on the transversal plane using the identities (A.3), (A.2), (A.9), and the substitution of (5.10) yields after several transformations:

$$\hat{\mathbf{z}} \times (5.8) \Rightarrow -\frac{\partial \tilde{\mathbf{E}}_t}{\partial z} = -\frac{\underline{k}^2 - \mathbf{k}_\rho\mathbf{k}_\rho}{j\omega\epsilon} \cdot (\tilde{\mathbf{H}}_t \times \hat{\mathbf{z}}) - \frac{\mathbf{k}_\rho\tilde{J}_z}{\omega\epsilon} - \hat{\mathbf{z}} \times \tilde{\mathbf{M}}_t,\tag{5.12}$$

where $\underline{k} = \omega\sqrt{\mu_0\epsilon}$ is the wave number, and $\mathbf{k}_\rho\mathbf{k}_\rho$ is a dyad used due to compactness, in view of (A.9). The projection of (5.9) on the transversal plane is derived analogously.

$$\hat{\mathbf{z}} \times (5.9) \Rightarrow -\frac{\partial \tilde{\mathbf{H}}_t}{\partial z} = -\frac{\underline{k}^2 - \mathbf{k}_\rho\mathbf{k}_\rho}{j\omega\mu_0} \cdot (\hat{\mathbf{z}} \times \tilde{\mathbf{E}}_t) - \frac{\mathbf{k}_\rho\tilde{M}_z}{\omega\mu_0} + \hat{\mathbf{z}} \times \tilde{\mathbf{J}}_t.\tag{5.13}$$

The partial differential equations (5.12) and (5.13) relate the transversal components of $\tilde{\mathbf{E}}$ and $\tilde{\mathbf{H}}$, which are hybrid waves, in general. The obtained equations (5.12) and (5.13) may be simplified by the decomposition of the vectors $\tilde{\mathbf{E}}_t$ and $\tilde{\mathbf{H}}_t \times \hat{\mathbf{z}}$ into their projections on coordinates $(\hat{\mathbf{u}}, \hat{\mathbf{v}})$:

$$\begin{aligned}\tilde{\mathbf{E}}_t &= V' \hat{\mathbf{u}} + V'' \hat{\mathbf{v}}, \\ \tilde{\mathbf{H}}_t \times \hat{\mathbf{z}} &= I' \hat{\mathbf{u}} + I'' \hat{\mathbf{v}}.\end{aligned}\tag{5.14}$$

The second equation in (5.14) is equivalent to $\tilde{\mathbf{H}}_t = I' \hat{\mathbf{v}} - I'' \hat{\mathbf{u}}$, consequently, the hybrid waves $(\tilde{\mathbf{E}}_t, \tilde{\mathbf{H}}_t)$ are decoupled into two waves $(V' \hat{\mathbf{u}}, I' \hat{\mathbf{v}})$ and $(V'' \hat{\mathbf{v}}, -I'' \hat{\mathbf{u}})$ propagating along z . In the case of a source-free space, one may substitute the electric field intensity $V' \hat{\mathbf{u}}$ in (5.10) and the magnetic field intensity $I'' \hat{\mathbf{u}}$ in (5.11) that leads to $\tilde{H}_z = 0$ and $\tilde{E}_z = 0$, respectively. Thus, $(V' \hat{\mathbf{u}}, I' \hat{\mathbf{v}})$ is a TM wave, while $(V'' \hat{\mathbf{v}}, -I'' \hat{\mathbf{u}})$ is a TE wave, whose definitions may be found in [34]. The transverse magnetic and electric current sources may also be decomposed into $\hat{\mathbf{u}}$ and $\hat{\mathbf{v}}$ components:

$$\tilde{\mathbf{J}}_t = \tilde{J}_u \hat{\mathbf{u}} + \tilde{J}_v \hat{\mathbf{v}}, \quad \tilde{\mathbf{M}}_t = \tilde{M}_u \hat{\mathbf{u}} + \tilde{M}_v \hat{\mathbf{v}}. \quad (5.15)$$

If (5.14) and (5.15) are substituted in (5.12), $(5.12) \cdot \hat{\mathbf{u}}$ results:

$$-\frac{\partial V'}{\partial z} = -\frac{k^2 - k_\rho^2}{j\omega\epsilon} I' - \frac{k_\rho}{\omega\epsilon} \tilde{J}_z + \tilde{M}_v, \quad (5.16)$$

while $(5.12) \cdot \hat{\mathbf{v}}$ gives:

$$-\frac{\partial V''}{\partial z} = -\frac{k^2}{j\omega\epsilon} I'' - \tilde{M}_u. \quad (5.17)$$

Using the substitution of (5.14) and (5.15) in (5.13), $(5.13) \cdot \hat{\mathbf{u}}$ yields:

$$-\frac{\partial I''}{\partial z} = -\frac{k^2 - k_\rho^2}{j\omega\epsilon} V'' + \frac{k_\rho}{\omega\mu_0} \tilde{M}_z + \tilde{J}_v, \quad (5.18)$$

while $(5.13) \cdot \hat{\mathbf{v}}$ leads to:

$$-\frac{\partial I'}{\partial z} = -\frac{k^2}{j\omega\mu_0} V' + \tilde{J}_u, \quad (5.19)$$

It may be observed that the unknowns (V', I') appear only in (5.16) and (5.19), while (V'', I'') only in (5.17) and (5.18). These equation pairs are well known transmission-line PDE systems. Hence, (5.12) and (5.13) are decoupled into two independent pairs of the transmission-line equations with respect to the TM and TE modes. The transmission-line equations for the TM and TE modes may be rewritten in the usual form as follows:

$$-\frac{\partial V'}{\partial z} = jk_z Z' I' + V'_s, \quad -\frac{\partial I'}{\partial z} = \frac{jk_z}{Z'} V' + J'_s, \quad (5.20)$$

and

$$-\frac{\partial V''}{\partial z} = jk_z Z'' I'' + V''_s, \quad -\frac{\partial I''}{\partial z} = \frac{jk_z}{Z''} V'' + J''_s, \quad (5.21)$$

where the following notations are used: V' and V'' are equivalent voltages, I' and I'' are equivalent currents, J'_s and J''_s are equivalent current sources, V'_s and V''_s are equivalent voltage sources, and Z' and Z'' are equivalent wave impedances for TM and TE modes. k_z is the longitudinal wave number. The equivalent parameters are calculated as follows:

$$k_z = \sqrt{k^2 - k_\rho^2}, \quad Z' = \frac{k_z}{\omega\epsilon}, \quad Z'' = \frac{\omega\mu_0}{k_z}, \quad (5.22)$$

$$V'_s = \tilde{M}_v - \frac{k_\rho}{\omega\epsilon} \tilde{J}_z, \quad V''_s = -\tilde{M}_u, \quad J'_s = \tilde{J}_u, \quad J''_s = \tilde{J}_v + \frac{k_\rho}{\omega\mu_0} \tilde{M}_z.$$

Since the Green's functions for the two-wire transmission-line equations (5.20) and (5.21) are derived in § 1.5.2, one may express the dyadic Green's functions for the electric and magnetic fields through these scalar transmission-line Green's functions. Since the transmission line may be excited by current and voltage sources and we calculate the current and voltage, eight scalar Green's functions (SGF) for the TM and TE modes have to be defined:

$I'_i(z, z')$ and $I''_i(z, z')$ are SGF for currents excited by currents sources (TM and TE modes), $I'_u(z, z')$ and $I''_u(z, z')$ are SGF for currents excited by voltage sources (TM and TE modes), $V'_i(z, z')$ and $V''_i(z, z')$ are SGF for voltages excited by currents sources (TM and TE modes), $V'_u(z, z')$ and $V''_u(z, z')$ are SGF for voltages excited by voltage sources (TM and TE modes). The currents and voltages of the equivalent transmission lines are calculated at the point z on the basis of the known Green's functions as follows:

$$\begin{aligned}
I'(z, \mathbf{k}_\rho) &= - \int_{\tilde{z}}^{\hat{z}} I'_i(z, z') J'_s(z', \mathbf{k}_\rho) dz' - \int_{\tilde{z}}^{\hat{z}} I'_u(z, z') V'_s(z', \mathbf{k}_\rho) dz', \\
V'(z, \mathbf{k}_\rho) &= - \int_{\tilde{z}}^{\hat{z}} V'_i(z, z') J'_s(z', \mathbf{k}_\rho) dz' - \int_{\tilde{z}}^{\hat{z}} V'_u(z, z') V'_s(z', \mathbf{k}_\rho) dz', \\
I''(z, \mathbf{k}_\rho) &= - \int_{\tilde{z}}^{\hat{z}} I''_i(z, z') J''_s(z', \mathbf{k}_\rho) dz' - \int_{\tilde{z}}^{\hat{z}} I''_u(z, z') V''_s(z', \mathbf{k}_\rho) dz', \\
V''(z, \mathbf{k}_\rho) &= - \int_{\tilde{z}}^{\hat{z}} V''_i(z, z') J''_s(z', \mathbf{k}_\rho) dz' - \int_{\tilde{z}}^{\hat{z}} V''_u(z, z') V''_s(z', \mathbf{k}_\rho) dz',
\end{aligned} \tag{5.23}$$

assuming that the sources exist in the area between \tilde{z} and \hat{z} . The electric field intensity is composed of its longitudinal and transversal components:

$$\tilde{\mathbf{E}}(z) = \tilde{E}_z(z) \hat{\mathbf{z}} + \tilde{\mathbf{E}}_t(z). \tag{5.24}$$

$\tilde{E}_z(z)$ can be calculated via $\tilde{\mathbf{H}}_t(z)$ using (5.11). $\tilde{\mathbf{E}}_t(z)$ and $\tilde{\mathbf{H}}_t(z)$ are expressed in terms of equivalent transmission-line voltages and currents according to (5.14). Finally, one may derive:

$$\tilde{\mathbf{E}}(z, \mathbf{k}_\rho) = - \frac{\tilde{J}_z(z', \mathbf{k}_\rho)}{j\omega\epsilon} \hat{\mathbf{z}} - \frac{k_\rho}{\omega\epsilon} I'(z) \hat{\mathbf{z}} + V'(z) \hat{\mathbf{u}} + V''(z) \hat{\mathbf{v}}. \tag{5.25}$$

The substitution of (5.23) in (5.25) leads to the final formulation:

$$\tilde{\mathbf{E}}(z, \mathbf{k}_\rho) = - \int_{\tilde{z}}^{\hat{z}} \overline{\overline{\mathfrak{G}}}_J^E(z, z') \cdot \tilde{\mathbf{J}}(z', \mathbf{k}_\rho) dz' - \int_{\tilde{z}}^{\hat{z}} \overline{\overline{\mathfrak{G}}}_M^E(z, z') \cdot \tilde{\mathbf{M}}(z', \mathbf{k}_\rho) dz', \tag{5.26}$$

where $\overline{\overline{\mathfrak{G}}}_J^E(z, z')$ and $\overline{\overline{\mathfrak{G}}}_M^E(z, z')$ are the spectrum-domain dyadic Green's functions for the

electric field excited by the electric and magnetic currents respectively:

$$\begin{aligned} \overline{\overline{\mathfrak{G}}}_J^E(z, z') &= \left(\frac{\delta(z - z')}{j\omega\epsilon} + \left(\frac{k_\rho}{\omega\epsilon} \right)^2 I'_u(z, z') \right) \hat{\mathbf{z}}\hat{\mathbf{z}} - \frac{k_\rho}{\omega\epsilon} I'_i(z, z') \hat{\mathbf{z}}\hat{\mathbf{u}} - \\ &\quad - \frac{k_\rho}{\omega\epsilon} V'_u(z, z') \hat{\mathbf{u}}\hat{\mathbf{z}} + V'_i(z, z') \hat{\mathbf{u}}\hat{\mathbf{u}} + V''_i(z, z') \hat{\mathbf{v}}\hat{\mathbf{v}}, \end{aligned} \quad (5.27)$$

$$\overline{\overline{\mathfrak{G}}}_M^E(z, z') = \frac{k_\rho}{\omega\epsilon} I'_u(z, z') \hat{\mathbf{z}}\hat{\mathbf{v}} + V'_u(z, z') \hat{\mathbf{u}}\hat{\mathbf{v}} - V''_u(z, z') \hat{\mathbf{v}}\hat{\mathbf{u}} + \frac{k_\rho}{\omega\mu_0} V''_i(z, z') \hat{\mathbf{v}}\hat{\mathbf{z}}. \quad (5.28)$$

Then, we derive the Green's functions for the magnetic field intensity, which is composed of its longitudinal and transversal components:

$$\tilde{\mathbf{H}}(z) = \tilde{H}_z(z) \hat{\mathbf{z}} + \tilde{\mathbf{H}}_t(z). \quad (5.29)$$

$\tilde{H}_z(z)$ is calculated by (5.10). $\tilde{\mathbf{E}}_t(z)$ and $\tilde{\mathbf{H}}_t(z)$ are expressed in terms of the equivalent transmission-line voltages and currents according to (5.14). Finally, the magnetic field intensity yields:

$$\tilde{\mathbf{H}}(z, \mathbf{k}_\rho) = \frac{1}{j\omega\mu_0} \left(jk_\rho V''(z) - \tilde{M}_z \right) \hat{\mathbf{z}} - I''(z) \hat{\mathbf{u}} + I'(z) \hat{\mathbf{v}}. \quad (5.30)$$

The substitution of (5.23) in (5.30) leads to the final formulation:

$$\tilde{\mathbf{H}}(z, \mathbf{k}_\rho) = - \int_{\hat{\mathbf{z}}}^{\hat{\mathbf{z}}} \overline{\overline{\mathfrak{G}}}_J^H(z, z') \cdot \tilde{\mathbf{J}}(z', \mathbf{k}_\rho) dz' - \int_{\hat{\mathbf{z}}}^{\hat{\mathbf{z}}} \overline{\overline{\mathfrak{G}}}_M^H(z, z') \cdot \tilde{\mathbf{M}}(z', \mathbf{k}_\rho) dz', \quad (5.31)$$

where $\overline{\overline{\mathfrak{G}}}_J^H(z, z')$ and $\overline{\overline{\mathfrak{G}}}_M^H(z, z')$ are the spectrum-domain dyadic Green's functions for the magnetic field excited by the electric and magnetic currents respectively:

$$\overline{\overline{\mathfrak{G}}}_J^H(z, z') = I'_i(z, z') \hat{\mathbf{v}}\hat{\mathbf{u}} - I''_i(z, z') \hat{\mathbf{u}}\hat{\mathbf{v}} - \frac{k_\rho}{\omega\epsilon} I'_u(z, z') \hat{\mathbf{v}}\hat{\mathbf{z}} + \frac{k_\rho}{\omega\mu_0} V''_i(z, z') \hat{\mathbf{z}}\hat{\mathbf{v}} \quad (5.32)$$

$$\begin{aligned} \overline{\overline{\mathfrak{G}}}_M^H(z, z') &= \left(\frac{\delta(z - z')}{j\omega\mu_0} + \left(\frac{k_\rho}{\omega\mu_0} \right)^2 V''_i(z, z') \right) \hat{\mathbf{z}}\hat{\mathbf{z}} + I''_u(z, z') \hat{\mathbf{u}}\hat{\mathbf{u}} + \\ &\quad + I'_u(z, z') \hat{\mathbf{v}}\hat{\mathbf{v}} - \frac{k_\rho}{\omega\mu_0} I''_i(z, z') \hat{\mathbf{u}}\hat{\mathbf{z}} - \frac{k_\rho}{\omega\mu_0} V''_u(z, z') \hat{\mathbf{z}}\hat{\mathbf{u}}. \end{aligned} \quad (5.33)$$

The electric-field integral equation (1.56) may be applied to stratified media using the dyadic Green's function for the electric field calculated via the inverse Fourier transformation of the spectrum-domain Green's function as follows: $\overline{\overline{\mathbf{G}}}_J^E(\mathbf{r}, \mathbf{r}') = \mathfrak{F}_s^{-1} \left\{ \overline{\overline{\mathfrak{G}}}_J^E(z, z') \right\}$, while the remained spectrum-domain dyadic Green's functions are used in § 5.2.2 for the derivation of the MPIE for layered media.

5.2.2 Derivation of the MPIE for layered media

The free-space MPIE (1.63) is derived in § 1.4.2 using the scalar electric and vector magnetic potentials. In the following, we will attempt to introduce the scalar electric and vector magnetic potentials for layered media and derive the MPIE-LM on the basis of these potentials as in § 1.4.2. We suppose that the electric field intensity may be computed using two auxiliary functions as follows:

$$\tilde{\mathbf{E}}(z, \mathbf{k}_\rho) = -j\omega \tilde{\mathbf{A}}'(z, \mathbf{k}_\rho) - \tilde{\nabla} \tilde{\phi}(z, \mathbf{k}_\rho), \quad (5.34)$$

where $\tilde{\nabla}$ is the spectrum-domain nabla operator defined in (A.24), $\tilde{\phi}(z, \mathbf{k}_\rho)$ is the spectrum-domain scalar electric potential, and $\tilde{\mathbf{A}}'(z, \mathbf{k}_\rho)$ is the spectrum-domain vector magnetic potential defined analogous to the free-space vector magnetic potential (1.14):

$$\mu_0 \tilde{\mathbf{H}}(z, \mathbf{k}_\rho) = \tilde{\mathbf{B}}(z, \mathbf{k}_\rho) = \tilde{\nabla} \times \tilde{\mathbf{A}}'(\tilde{\mathbf{r}}). \quad (5.35)$$

According to the Helmholtz decomposition theorem [86], a vector function may be uniquely defined by its curl and divergence. Thus, we may make the definition of the vector potential unique applying the Lorenz gauge:

$$\tilde{\nabla} \cdot \tilde{\mathbf{A}}'(z, \mathbf{k}_\rho) = -j\omega \mu_0 \underline{\epsilon} \tilde{\phi}(z, \mathbf{k}_\rho). \quad (5.36)$$

It may be assumed that the electromagnetic field is excited by the electric current distribution. In this case, the magnetic field and the vector potential are computed by (1.49) and (1.69) respectively, which yields in the spectrum domain:

$$\begin{aligned} \tilde{\mathbf{A}}'(z, \mathbf{k}_\rho) &= \mu_0 \int_{\tilde{z}}^{\hat{z}} \overline{\overline{\mathfrak{G}}}^{A'}(z, z') \cdot \tilde{\mathbf{J}}(z', \mathbf{k}_\rho) dz', \\ \tilde{\mathbf{H}}(z, \mathbf{k}_\rho) &= - \int_{\tilde{z}}^{\hat{z}} \overline{\overline{\mathfrak{G}}}^H_J(z, z') \cdot \tilde{\mathbf{J}}(z', \mathbf{k}_\rho) dz', \end{aligned} \quad (5.37)$$

where $\overline{\overline{\mathfrak{G}}}^{A'}(z, z')$ is the spectrum-domain dyadic Green's function for the vector potential $\tilde{\mathbf{A}}'(z, \mathbf{k}_\rho)$, while $\overline{\overline{\mathfrak{G}}}^H_J(z, z')$ is computed by (5.32). The substitution of (5.37) in (5.35) results in

$$\overline{\overline{\mathfrak{G}}}^H_J(z, z') = -\tilde{\nabla} \times \overline{\overline{\mathfrak{G}}}^{A'}(z, z'). \quad (5.38)$$

One can propose several structures of $\overline{\overline{\mathfrak{G}}}^{A'}(z, z')$, which lead to the correspondence between components of $\overline{\overline{\mathfrak{G}}}^H_J(z, z')$ in (5.32) and $-\tilde{\nabla} \times \overline{\overline{\mathfrak{G}}}^{A'}(z, z')$. The three possibilities have been proposed by Michalski [108], [110]. The most appropriate one is used in this monograph:

$$\overline{\overline{\mathfrak{G}}}^{A'}(z, z') = \mathfrak{G}_t^{A'}(z, z') \overline{\overline{\mathbf{I}}}_t + \mathfrak{G}_{zu}^{A'}(z, z') \hat{z} \hat{u} + \mathfrak{G}_{zz}^{A'}(z, z') \hat{z} \hat{z}, \quad (5.39)$$

where $\mathfrak{G}_t^{A'}(z, z')$, $\mathfrak{G}_{zu}^{A'}(z, z')$, and $\mathfrak{G}_{zz}^{A'}(z, z')$ are the scalar components of the dyadic Green's function, which may be derived through the substitution of (5.39) in (5.38). $\bar{\mathbf{I}}_t = \hat{\mathbf{u}}\hat{\mathbf{u}} + \hat{\mathbf{v}}\hat{\mathbf{v}}$ is the transverse identity dyadic. The comparison of $-\tilde{\nabla} \times \overline{\overline{\mathfrak{G}}}^{A'}(z, z')$ with (5.32) results in four equations:

$$\begin{aligned} \frac{\partial}{\partial z} \mathfrak{G}_t^{A'}(z, z') + jk_\rho \mathfrak{G}_{zu}^{A'}(z, z') &= -I'_i(z, z'), \\ \frac{\partial}{\partial z} \mathfrak{G}_t^{A'}(z, z') &= -I''_i(z, z'), \\ jk_\rho \mathfrak{G}_{zz}^{A'}(z, z') &= \frac{k_\rho}{\omega \underline{\epsilon}} I'_u(z, z'), \\ -jk_\rho \mathfrak{G}_t^{A'}(z, z') &= -\frac{k_\rho}{\omega \mu_0} V''_i(z, z'). \end{aligned} \quad (5.40)$$

The formulation for the scalar components is derived from (5.40) as follows:

$$\begin{aligned} \mathfrak{G}_{zu}^{A'}(z, z') &= \frac{1}{jk_\rho} (I''_i(z, z') - I'_i(z, z')), \\ \mathfrak{G}_{zz}^{A'}(z, z') &= \frac{1}{j\omega \underline{\epsilon}} I'_u(z, z'), \\ \mathfrak{G}_t^{A'}(z, z') &= \frac{1}{j\omega \mu_0} V''_i(z, z'). \end{aligned} \quad (5.41)$$

The scalar potential $\tilde{\phi}(z, \mathbf{k}_\rho)$ may be obtained via the Lorenz gauge (5.36) and using (5.37):

$$\tilde{\phi}(z, \mathbf{k}_\rho) = -\frac{1}{j\omega \underline{\epsilon}} \int_{\tilde{z}}^{\hat{z}} \tilde{\nabla} \cdot \overline{\overline{\mathfrak{G}}}^{A'}(z, z') \cdot \tilde{\mathbf{J}}(z', \mathbf{k}_\rho) dz'. \quad (5.42)$$

The conventional form of the MPIE (1.65) requires the computation of the scalar electric potential as a response on the charge density distribution that may be written as follows:

$$\tilde{\varphi}(z, \mathbf{k}_\rho) = \frac{1}{\underline{\epsilon}} \int_{\tilde{z}}^{\hat{z}} \mathfrak{K}^\varphi(z, z') \tilde{\rho}_v(z', \mathbf{k}_\rho) dz', \quad (5.43)$$

where $\mathfrak{K}^\varphi(z, z')$ is the spectrum-domain Green's function for the scalar electric potential $\tilde{\varphi}$ ($K^\varphi(\mathbf{r}, \mathbf{r}') = \mathfrak{F}_s^{-1}\{\mathfrak{K}^\varphi(z, z')\}$). Of course, the scalar potentials $\tilde{\varphi}$ and $\tilde{\phi}$ may be different. The charge density $\tilde{\rho}_v(z', \mathbf{k}_\rho)$ is introduced through the charge conservation law:

$$\tilde{\rho}_v(z', \mathbf{k}_\rho) = -\frac{1}{j\omega} \tilde{\nabla}' \cdot \tilde{\mathbf{J}}(z', \mathbf{k}_\rho), \quad (5.44)$$

where $\tilde{\nabla}'$ is the spectrum-domain nabla operator with respect to \mathbf{r}' explained in (A.25). In the following, we denote the difference between the scalar potentials $\tilde{\varphi}$ and $\tilde{\phi}$ by $\tilde{\phi}_\Delta$. Thus, one may write

$$\tilde{\phi}(z, \mathbf{k}_\rho) = \tilde{\varphi}(z, \mathbf{k}_\rho) + \tilde{\phi}_\Delta(z, \mathbf{k}_\rho). \quad (5.45)$$

Based on the fact that the conduction currents are tangent to the surface of the conductor and applying the volume Gauss theorem (A.15), we may write:

$$\int_{V'} \nabla' \cdot (K^\varphi(\mathbf{r}, \mathbf{r}') \mathbf{J}(\mathbf{r}')) dV' = \int_{S=\partial V'} K^\varphi(\mathbf{r}, \mathbf{r}') \mathbf{J}(\mathbf{r}') \cdot d\mathbf{S}' = 0, \quad (5.46)$$

In view of (5.46) and (5.44), and applying the identity (A.4), we rewrite (5.43) in the following form:

$$\tilde{\varphi}(z, \mathbf{k}_\rho) = \frac{1}{j\omega \underline{\epsilon}} \int_{\tilde{z}}^{\hat{z}} \left(\tilde{\nabla}' \mathfrak{K}^\varphi(z, z') \right) \cdot \tilde{\mathbf{J}}(z', \mathbf{k}_\rho) dz'. \quad (5.47)$$

Then, (5.47) is substituted in (5.45), which gives

$$\begin{aligned} \tilde{\phi}_\Delta(z, \mathbf{k}_\rho) &= \frac{1}{j\omega \underline{\epsilon}} \int_{\tilde{z}}^{\hat{z}} \mathfrak{K}^{\phi_\Delta}(z, z') \cdot \tilde{\mathbf{J}}(z', \mathbf{k}_\rho) dz', \\ \mathfrak{K}^{\phi_\Delta}(z, z') &= -\tilde{\nabla} \cdot \overline{\mathfrak{G}}^{A'}(z, z') - \tilde{\nabla}' \mathfrak{K}^\varphi(z, z'), \end{aligned} \quad (5.48)$$

where $\mathfrak{K}^{\phi_\Delta}(z, z')$ is the vector Green's function for $\tilde{\phi}_\Delta(z, \mathbf{k}_\rho)$. The vectors $\tilde{\nabla} \cdot \overline{\mathfrak{G}}^{A'}(z, z')$ and $\tilde{\nabla}' \mathfrak{K}^\varphi(z, z')$ consist of the following components:

$$\begin{aligned} \tilde{\nabla} \cdot \overline{\mathfrak{G}}^{A'}(z, z') &= \left(\frac{\partial}{\partial z} \mathfrak{G}_{zu}^{A'}(z, z') - jk_\rho \mathfrak{G}_t^{A'}(z, z') \right) \hat{\mathbf{u}} + \frac{\partial}{\partial z} \mathfrak{G}_{zz}^{A'}(z, z') \hat{\mathbf{z}}, \\ \tilde{\nabla}' \mathfrak{K}^\varphi(z, z') &= jk_\rho \mathfrak{K}^\varphi(z, z') \hat{\mathbf{u}} + \frac{\partial}{\partial z'} \mathfrak{K}^\varphi(z, z') \hat{\mathbf{z}}. \end{aligned} \quad (5.49)$$

Generally, one may choose several formulations for $\mathfrak{K}^\varphi(z, z')$, which satisfy to (5.49). A suitable one is proposed in [110]:

$$\mathfrak{K}^\varphi(z, z') = \mathfrak{G}_t^{A'}(z, z') - \frac{1}{jk_\rho} \frac{\partial}{\partial z} \mathfrak{G}_{zu}^{A'}(z, z'). \quad (5.50)$$

The substitution of (5.50) in (5.48) leads to a compact formulation for $\mathfrak{K}^{\phi_\Delta}(z, z')$:

$$\mathfrak{K}^{\phi_\Delta}(z, z') = \left(\frac{\partial}{\partial z'} \mathfrak{K}^\varphi(z, z') + \frac{\partial}{\partial z} \mathfrak{G}_{zz}^{A'}(z, z') \right) \hat{\mathbf{z}}. \quad (5.51)$$

Finally, we substitute (5.45) in (5.34) and derive the alternative formulation for the electric field intensity through the modified vector magnetic and scalar electric potentials:

$$\tilde{\mathbf{E}}(z, \mathbf{k}_\rho) = -j\omega \tilde{\mathbf{A}}(z, \mathbf{k}_\rho) - \tilde{\nabla} \tilde{\varphi}(z, \mathbf{k}_\rho). \quad (5.52)$$

The modified scalar potential $\tilde{\varphi}(z, \mathbf{k}_\rho)$ is already defined by (5.43), while the formulation for the vector potential is derived analogous to (1.69):

$$\tilde{\mathbf{A}}(z, \mathbf{k}_\rho) = \mu_0 \int_{\tilde{z}}^{\hat{z}} \overline{\mathfrak{G}}^A(z, z') \cdot \tilde{\mathbf{J}}(z', \mathbf{k}_\rho) dz', \quad (5.53)$$

where $\overline{\overline{\mathfrak{G}}}^A(z, z')$ is the spectrum-domain dyadic Green's function for the modified vector potential:

$$\overline{\overline{\mathfrak{G}}}^A(z, z') = \overline{\overline{\mathfrak{G}}}^{A'}(z, z') + \frac{\tilde{\nabla} \mathfrak{R}^{\phi\Delta}(z, z')}{k^2}. \quad (5.54)$$

The introduction of the potentials $\tilde{\mathbf{A}}(z, \mathbf{k}_\rho)$ and $\tilde{\varphi}(z, \mathbf{k}_\rho)$ produces decoupling the electric field into two parts induced by the current and charge density distribution, respectively. The substitution of (5.53) and (5.43) in (5.52) leads to the mixed-potential integral equation in the conventional form (1.65).

We should add an important explanation concerning the potentials $\tilde{\mathbf{A}}(z, \mathbf{k}_\rho)$ and $\tilde{\varphi}(z, \mathbf{k}_\rho)$. As we know, the initially introduced potentials $\tilde{\mathbf{A}}'(z, \mathbf{k}_\rho)$ and $\tilde{\varphi}'(z, \mathbf{k}_\rho)$ are coupled through the Lorenz gauge, while the modified ones differ and do not satisfy (5.36). Therefore, a special gauge is derived in this section. It differs from the Lorentz gauge and allows decoupling the equations for the electric and magnetic potentials in layered media.

Derivation of the Green's function $\mathfrak{R}^\varphi(z, z')$

The Green's function for the scalar electric potential $\tilde{\varphi}(z, \mathbf{k}_\rho)$ is defined by (5.50) through the scalar components of $\overline{\overline{\mathfrak{G}}}^{A'}(z, z')$ that are given by (5.41). The substitution of (5.41) in (5.50) leads to

$$\mathfrak{R}^\varphi(z, z') = \frac{1}{j\omega\mu_0} V_i''(z, z') + \frac{1}{k_\rho^2} \frac{\partial}{\partial z} (I_i''(z, z') - I_i'(z, z')). \quad (5.55)$$

The derivatives of $I_i''(z, z')$ and $I_i'(z, z')$ in (5.55) is expressed using the transmission-line equations (5.21) and (5.20) respectively:

$$\frac{\partial}{\partial z} I_i''(z, z') = -j \frac{k_z}{Z''} V_i''(z, z') + \delta(z - z'), \quad \frac{\partial}{\partial z} I_i'(z, z') = -j \frac{k_z}{Z'} V_i'(z, z') + \delta(z - z'). \quad (5.56)$$

The substitution of (5.56) in (5.55) and several simplifications result in the compact final formulation for the Green's function:

$$\mathfrak{R}^\varphi(z, z') = \frac{j\omega\epsilon}{k_\rho^2} (V_i'(z, z') - V_i''(z, z')). \quad (5.57)$$

Derivation of the dyadic Green's function $\overline{\overline{\mathfrak{G}}}^A(z, z')$

The Green's function for the magnetic vector potential is defined by (5.54) as a sum of two terms. The first term is the known dyadic Green's function $\overline{\overline{\mathfrak{G}}}^{A'}(z, z')$, the second one involves $\mathfrak{R}^{\phi\Delta}(z, z')$, which has to be derived via (5.51).

Using the reciprocity theorem for the transmission-line Green's functions (1.99), we write

$$\begin{aligned} V_i'(z, z') &= V_i'(z', z), & V_i''(z, z') &= V_i''(z', z), \\ I_i'(z', z) &= -V_u'(z, z'), & I_i''(z', z) &= -V_u''(z, z'). \end{aligned} \quad (5.58)$$

Using the transmission-line equations (5.20) and (5.21), and applying (5.58), we obtain:

$$\begin{aligned}\frac{\partial}{\partial z'} \mathfrak{K}^\varphi(z, z') &= \frac{k^2}{k_\rho^2} V_u''(z, z') - \frac{k_z^2}{k_\rho^2} V_u'(z, z'), \\ \frac{\partial}{\partial z} \mathfrak{G}_{zz}^{A'}(z, z') &= -V_u'(z, z').\end{aligned}\quad (5.59)$$

The final formulation for $\mathfrak{K}^{\phi\Delta}(z, z')$ is derived through the substitution of (5.59) in (5.51):

$$\mathfrak{K}^{\phi\Delta}(z, z') = \frac{k^2}{k_\rho^2} [V_u''(z, z') - V_u'(z, z')] \hat{\mathbf{z}}. \quad (5.60)$$

In view of (5.60), the dyadic $\tilde{\nabla} \mathfrak{K}^{\phi\Delta}(z, z')/k^2$ in (5.54) is rewritten in the following form:

$$\frac{\tilde{\nabla} \mathfrak{K}^{\phi\Delta}(z, z')}{k^2} = \frac{1}{j\omega\epsilon} \left[\frac{k^2}{k_\rho^2} I_u''(z, z') - \frac{k_z^2}{k_\rho^2} I_u'(z, z') \right] \hat{\mathbf{z}}\hat{\mathbf{z}} + \frac{1}{jk_\rho} [V_u''(z, z') - V_u'(z, z')] \hat{\mathbf{u}}\hat{\mathbf{z}}. \quad (5.61)$$

Finally, we substitute (5.61) in (5.54) and derive the scalar components for the dyadic Green's function:

$$\begin{aligned}\overline{\overline{\mathfrak{G}}}^A(z, z') &= \mathfrak{G}_t^A(z, z') \overline{\overline{\mathbf{I}}}_t + \mathfrak{G}_{zu}^A(z, z') \hat{\mathbf{z}}\hat{\mathbf{u}} + \mathfrak{G}_{uz}^A(z, z') \hat{\mathbf{u}}\hat{\mathbf{z}} + \mathfrak{G}_{zz}^A(z, z') \hat{\mathbf{z}}\hat{\mathbf{z}}, \\ \mathfrak{G}_t^A(z, z') &= \frac{1}{j\omega\mu_0} V_i''(z, z'), \\ \mathfrak{G}_{zu}^A(z, z') &= \frac{1}{jk_\rho} [I_i''(z, z') - I_i'(z, z')], \\ \mathfrak{G}_{uz}^A(z, z') &= \frac{1}{jk_\rho} [V_u''(z, z') - V_u'(z, z')], \\ \mathfrak{G}_{zz}^A(z, z') &= \frac{1}{j\omega\epsilon} \left[\frac{k^2}{k_\rho^2} I_u''(z, z') + \frac{k_\rho^2 - k_z^2}{k_\rho^2} I_u'(z, z') \right].\end{aligned}\quad (5.62)$$

The Green's functions in the spatial domain

The spectrum-domain Green's functions have to be transformed into the spatial domain with the help of inverse Fourier transformation given in (A.23). The computation of the double integrals in (A.23) may be simplified in view of the circular symmetry of the Green's functions in the transversal plane. The double integrals (A.23) may be replaced by single *Sommerfeld integrals*, as shown in (A.26). The definition of Sommerfeld integrals is presented in (A.27).

Finally, we derive the MPIE formulation for layered media in the spatial domain according to (1.65). The Green's functions for this MPIE are expressed in terms of Sommerfeld integrals of their spectrum-domain counterparts and summarized below. The spatial-domain scalar Green's function for the electric scalar potential is

$$K^\varphi(\mathbf{r}, \mathbf{r}') = S_0 \{ \mathfrak{K}^\varphi(z, z') \}, \quad \mathfrak{K}^\varphi(z, z') = \frac{j\omega\epsilon}{k_\rho^2} (V_i'(z, z') - V_i''(z, z')). \quad (5.63)$$

The spatial-domain dyadic Green's function for the magnetic vector potential has the following structure:

$$\overline{\overline{\mathbf{G}}}^A(\mathbf{r}, \mathbf{r}') = G_{zz}^A(\mathbf{r}, \mathbf{r}') \hat{\mathbf{z}}\hat{\mathbf{z}} + G_t^A(\mathbf{r}, \mathbf{r}') \overline{\overline{\mathbf{I}}}_t + G_{\rho z}^A(\mathbf{r}, \mathbf{r}') \hat{\boldsymbol{\rho}}\hat{\mathbf{z}} + G_{z\rho}^A(\mathbf{r}, \mathbf{r}') \hat{\mathbf{z}}\hat{\boldsymbol{\rho}}, \quad (5.64)$$

with

$$\begin{aligned} G_{zz}^A(\mathbf{r}, \mathbf{r}') &= S_0 \{ \mathfrak{G}_{zz}^A(z, z') \}, \quad \mathfrak{G}_{zz}^A(z, z') = \frac{1}{j\omega\epsilon} \left[\frac{k^2}{k_\rho^2} I_u''(z, z') + \frac{k_\rho^2 - k_z^2}{k_\rho^2} I_u'(z, z') \right], \\ G_t^A(\mathbf{r}, \mathbf{r}') &= S_0 \{ \mathfrak{G}_t^A(z, z') \}, \quad \mathfrak{G}_t^A(z, z') = \frac{1}{j\omega\mu_0} V_i''(z, z'), \\ G_{\rho z}^A(\mathbf{r}, \mathbf{r}') &= S_1 \left\{ \frac{\mathfrak{G}_{uz}^A(z, z')}{jk_\rho} \right\}, \quad \mathfrak{G}_{uz}^A(z, z') = \frac{1}{jk_\rho} [V_u''(z, z') - V_u'(z, z')], \\ G_{z\rho}^A(\mathbf{r}, \mathbf{r}') &= S_1 \left\{ \frac{\mathfrak{G}_{zu}^A(z, z')}{jk_\rho} \right\}, \quad \mathfrak{G}_{zu}^A(z, z') = \frac{1}{jk_\rho} [I_i''(z, z') - I_i'(z, z')], \end{aligned} \quad (5.65)$$

where the unit vector $\hat{\boldsymbol{\rho}}$ is defined as follows: $\hat{\boldsymbol{\rho}} = \boldsymbol{\rho} / \|\boldsymbol{\rho}\|$, $\boldsymbol{\rho} = (x - x')\hat{\mathbf{x}} + (y - y')\hat{\mathbf{y}}$.

The derivation of $K^\varphi(\mathbf{r}, \mathbf{r}')$, $G_{zz}^A(\mathbf{r}, \mathbf{r}')$, and $G_t^A(\mathbf{r}, \mathbf{r}')$ is elementary, it is produced only by the IFT using Sommerfeld integral of the zero order, while the derivation of $G_{\rho z}^A(\mathbf{r}, \mathbf{r}')$ and $G_{z\rho}^A(\mathbf{r}, \mathbf{r}')$ have to be explained. The dyads $\hat{\mathbf{z}}\hat{\mathbf{u}}$ and $\hat{\mathbf{u}}\hat{\mathbf{z}}$ in (5.62) contain the rotating unit vector $\hat{\mathbf{u}}$, which is expressed in the unit vectors $\hat{\mathbf{x}}$ and $\hat{\mathbf{y}}$: $\hat{\mathbf{u}} = \hat{\mathbf{x}}k_x/k_\rho + \hat{\mathbf{y}}k_y/k_\rho$. This has to be considered by the integration. E.g., we write for the $\hat{\mathbf{z}}\hat{\mathbf{u}}$ component:

$$\mathfrak{F}_s^{-1} \{ \mathfrak{G}_{zu}^A(z, z') \hat{\mathbf{z}}\hat{\mathbf{u}} \} = \mathfrak{F}_s^{-1} \{ \mathfrak{G}_{zu}^A(z, z') k_x/k_\rho \} \hat{\mathbf{z}}\hat{\mathbf{x}} + \mathfrak{F}_s^{-1} \{ \mathfrak{G}_{zu}^A(z, z') k_y/k_\rho \} \hat{\mathbf{z}}\hat{\mathbf{y}} \quad (5.66)$$

The substitution of (A.26) in (5.66) leads to

$$(\cos \zeta \hat{\mathbf{z}}\hat{\mathbf{x}} + \sin \zeta \hat{\mathbf{z}}\hat{\mathbf{y}}) S_1 \left\{ \frac{\mathfrak{G}_{uz}^A(z, z')}{jk_\rho} \right\} = \hat{\mathbf{z}}\hat{\boldsymbol{\rho}} S_1 \left\{ \frac{\mathfrak{G}_{uz}^A(z, z')}{jk_\rho} \right\}, \quad (5.67)$$

since $\hat{\boldsymbol{\rho}} = \cos \zeta \hat{\mathbf{x}} + \sin \zeta \hat{\mathbf{y}}$. The expression for $\mathfrak{F}_s^{-1} \{ \mathfrak{G}_{uz}^A(z, z') \hat{\mathbf{u}}\hat{\mathbf{z}} \}$ is obtained analogous to $\mathfrak{F}_s^{-1} \{ \mathfrak{G}_{zu}^A(z, z') \hat{\mathbf{z}}\hat{\mathbf{u}} \}$.

Since the general formulation for the spatial-domain Green's functions is expressed in terms of Sommerfeld integrals, the calculation of such integrals has to be specified. The integrand in (A.27) is an oscillating slowly decreasing function with a branch-point singularity at the point of origin caused by the Hankel function. The direct numerical integration of Sommerfeld integrals using a quadrature is generally inefficient. However, a numerical solution integrals may be calculated using the fast Hankel transformation (FHT) [138], [6], [65], [150]. On the one hand, this approach is robust as the usual FFT algorithm, on the other hand, it results in a pure numerical solution, which has to be applied to the space-convolution integration of the Green's function in order to obtain a MoM or a PEEC model. The closed-form solution for Sommerfeld integrals may be obtained via the asymptotic evaluation of integrals [44], [106], [120]. The complex-image approach developed by Chow et al. [31], [32] uses the expansion of the spectrum-domain Green's functions in a sum of complex

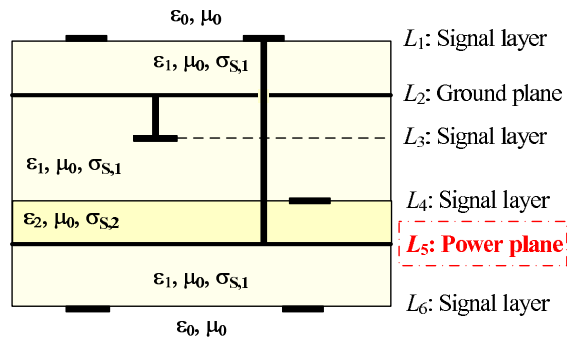


Figure 5.3: 6-layer PCB with power and ground planes.

exponentials (after a regularization), whose Sommerfeld integrals may be computed in closed form via the Sommerfeld identity. The investigations and developments in this area have been also provided in a large number of papers [29], [41], [117], [42], [119], [104], [3], [5], [149], [4]. Some other approaches for calculation of Sommerfeld integrals apply the Chebyshev decomposition [7], the eigenfunction approach [59], the extrapolation [109], [116], the expansion of the spectrum-domain Green's function in the functions (3.9) [49], [48], and this list is not complete.

5.2.3 MPIE formulation for PCB boards with power planes

The Green's functions derived in the previous section allow for the calculation of the electric field intensity scattered by the current and charge sources located in layered media (see Fig. 5.2). In general, the scatterers are all conducting structures including the ground and power planes. The numerical solution of the MPIE-LM using the method of moments (§ 3.3) or the DGF-PEEC method (§ 4.1) requires the discretization of all scatterers. Hence, the direct consideration of the field scattered by the currents in the power and ground planes needs their two-dimensional discretization. This leads to an essential increase in the number of unknowns. Additionally, the computational model applying the discretization of the power and ground planes is based on the dyadic Green's functions for several dielectric layers constrained by air. These Green's functions have a more sophisticated structure and are less selective than the ones for the typical microstrip or stripline regions constrained from one or two sides (see § 5.3). The interconnections located in layers separated by the ground planes may be assumed to be uncoupled. E.g., see Fig. 5.3, where the three regions above the ground plane, under the power plane, and between the ground and power planes are decoupled. Thus, the dyadic Green's functions for such interconnection subsystems may be developed separately (e.g., see the Green's functions for the stripline region § 5.3). This leads to an essential simplification of their derivation and to the dominance of the diagonal elements of the system matrix in the MoM and PEEC models.

The efficient approach for the consideration of the ground planes requires their inclusion in the Green's functions. In this case, the computational methods discretize only traces and vias. The inclusion of the ground planes in the Green's function is explained in § 5.3, but this

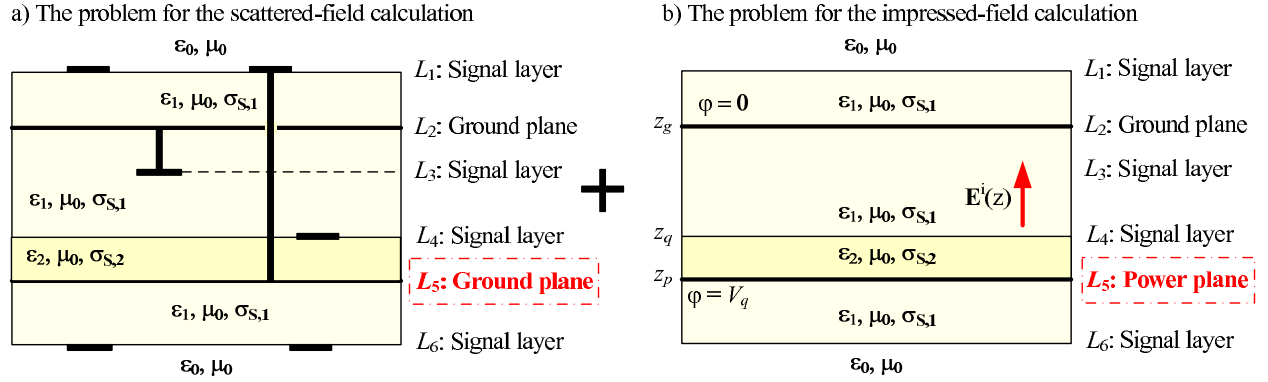


Figure 5.4: Decomposition of the electric field into the scattered and impressed parts.

technique deals with passive ground planes. They are modeled as thin layers with infinite conductivity. Unfortunately, this may not be directly applied to the power planes.

An efficient approach for the modeling of the power planes is explained in the example of the 6-layer PCB shown in Fig. 5.3. This PCB has four signal layers, one power plane (layer L_5), and one ground plane (layer L_2). We assume that the ground and power planes have potentials 0 and V_s , respectively. Thus, we consider a boundary-value problem (5.6) with an inhomogeneous boundary condition $\varphi(\mathbf{r}) = V_s$ on the power plane and an excitation by the current and charge sources.

The superposition principle states that the solution for a linear inhomogeneous PDE with inhomogeneous boundary conditions is computed as a superposition of the solutions of two auxiliary problems [86]. The first problem is the same inhomogeneous PDE with homogeneous boundary conditions, and the second is the homogeneous PDE with inhomogeneous boundary conditions. Guided by this principle, we may develop an effective solution for the PCB with a power plane Fig. 5.3.

First, we set the potentials on the power planes equal to zero, i.e., we replace all power planes with ground planes, e.g., see Fig. 5.4a. In this case, the electric field intensity denoted by $\mathbf{E}^s(\mathbf{r})$ is scattered by the current and charge sources located in the traces and vias. It may be computed through the vector magnetic and scalar electric potentials using the Green's functions for layered media with the ground planes formulated in (5.63), (5.64):

$$\mathbf{E}^s(\mathbf{r}) = -j\omega\mathbf{A}(\mathbf{r}) - \nabla\varphi(\mathbf{r}). \quad (5.68)$$

This solution for the electric field intensity corresponds to the inhomogeneous BVP with homogeneous boundary conditions.

The second auxiliary problem may be constructed assuming all currents and charges equal to zero, while the potential on ground planes is V_s . At the beginning of § 5.2, we assumed that traces and vias do not influence the homogeneity of the substrate and its parameters. Since the currents and charges do not induce the field and do not change the parameters of the substrate, the electric field intensity $\mathbf{E}^i(\mathbf{r})$ impressed by the non-zero boundary conditions is calculated using the auxiliary geometry shown in Fig. 5.4b. The electric field in the region

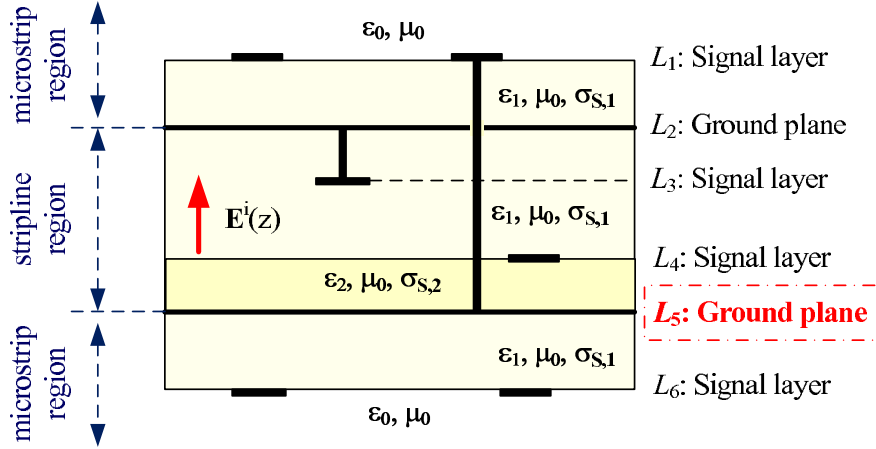


Figure 5.5: Accounting for the power plane by the impressed electric field.

between a ground and a power plane (as, e.g., between layers L_2 and L_5 in Fig. 5.4b) is static homogeneous and independent of the transverse coordinates. Hence, it is calculated from the trivial equation:

$$V_s = \int_{z_p}^{z_g} E^i(z) dz, \quad (5.69)$$

where z_g and z_p are the coordinates of the ground and power planes. Since $E^i(z)$ does not change in a region with a constant permittivity, it is computed trivially. E.g., the PCB in Fig. 5.4b has the following static solution:

$$\mathbf{E}^i(z) = \hat{\mathbf{z}} \begin{cases} \frac{V_s \epsilon_2}{\epsilon_2(z_g - z_q) + \epsilon_1(z_q - z_p)}, & z \in [z_q, z_g] \\ \frac{V_s \epsilon_1}{\epsilon_2(z_g - z_q) + \epsilon_1(z_q - z_p)}, & z \in [z_p, z_q] \end{cases} \quad (5.70)$$

It may be simply proved that the static electric field in microstrip regions (e.g., above the layer L_2 in Fig. 5.4b) is equal to zero. Thus, the impressed field is computed only in areas between power and ground planes.

The superposition of the solutions for the auxiliary problems (5.68) and (5.70) results in the electric field intensity for the initial problem:

$$\mathbf{E}(\mathbf{r}) = \mathbf{E}^i(\mathbf{r}) + \mathbf{E}^s(\mathbf{r}). \quad (5.71)$$

Obviously, (5.71) is identical to the boundary condition (1.55) used for the derivation of the MPIE (1.65). Hence, the MPIE-LM for a PCB with power planes may be written in the standard form (1.65), where the influence of power planes is considered by the impressed field $\mathbf{E}^i(\mathbf{r})$, which is calculated in areas between ground and power planes (see Fig. 5.5). The MPIE-LM uses the dyadic Green's functions for layered media, where all power planes are replaced by ground planes.

5.3 Green's functions for the stripline region

Motivation

The general theory presented in the previous section leads to different formulations of the Green's functions for the particular geometries of the printed circuit board. An arbitrary multilayer PCB may be considered as a set of subsystems separated by ground and power planes (see, e.g., in Fig. 5.5). The fields in the layers separated by ground planes may be assumed to be uncoupled. Thus, the dyadic Green's functions for such interconnection subsystems may be developed separately that leads to an essential simplification of the derivation. In the following, we define two basic PCB substructures.

The upper and lower parts of the PCB consisting of a dielectric substrate on the ground (or power) plane and a set of traces (see Fig. 5.5) are denoted by the *microstrip regions*. Since the microstrip region is constrained from the exterior side by air, it corresponds to a half-open problem. A large number of publications has been devoted to the derivation and application of the dyadic Green's functions for the microstrip region, e.g., see [3], [5], [31], [32], [117], [41], [42], [119], [104], [149], [4], [109], [116], [49], [48], [97], [99] et al.

The structure composed of one or more dielectric layers limited from both sides by ground or power planes is denoted by the *stripline region* (see Fig. 5.5). The stripline region corresponds to a closed problem with respect to the z -axis and to an open problem with respect to the horizontal plane. The Green's functions for the stripline region may be derived in closed form.

Obviously, an arbitrary multilayer printed circuit board may be approximately considered as a set of the microstrip and stripline regions, whose interconnections are coupled only through vias. Thus, only two kinds of Green's functions are required for the modeling of the PCB using the MPIE-LM. In the following, we develop the Green's functions for the stripline region and apply them in order to set up a particular realization of the DGFLM-PEEC model.

The stripline region considered in this section is unambiguously defined in Fig. 5.6a. Due to simplification, we consider the homogeneous lossy dielectric between two ground planes. The Green's functions for this structure are also applicable to the dielectric between the ground and power planes (see § 5.2.3). The losses in dielectric are included in the complex permittivity $\underline{\epsilon}$ defined by (5.7), where σ_s is the conductivity of the substrate, and ϵ is the permittivity. The thickness of the dielectric is denoted by h , the ground planes are assumed to be perfectly conducting.

5.3.1 Green's functions in the spectrum domain

Green's functions for the equivalent transmission-line equations

Since the spectrum-domain Green's functions for scalar electric (5.57) and vector magnetic (5.62) potentials are expressed in terms of the transmission-line Green's functions for TM and TE modes, they have to be derived at first. As the derivation of the Green's func-

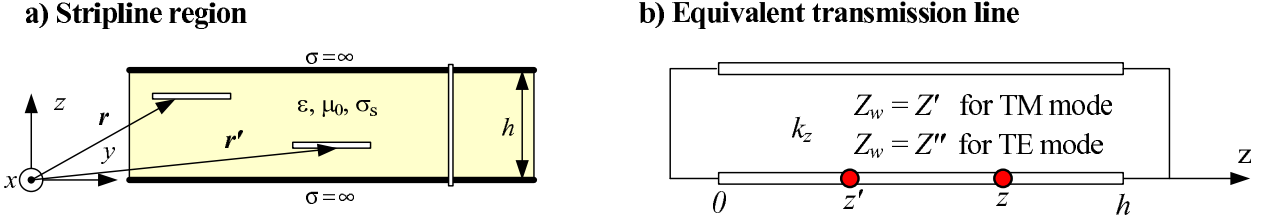


Figure 5.6: The stripline region (a), and its equivalent transmission-line model (b).

tions for transmission-line equations is explained in § 1.5.2, in the following, we apply this approach to the TM- and TE-mode transmission-line equations derived for the stripline region according to the theory presented in § 5.2. The equations for the TM-mode are given by (5.20), while and for the TE-mode in (5.21). The wave number for both equation systems is k_z , the wave impedances for TM- and TE-modes are defined by (5.22). As only one dielectric layer exists, the equivalent transmission line model for the layered medium consists of only one loaded section. The perfectly conducting grounds are modeled as the lumped terminations for this line. The load impedances for TM- and TE-modes may be derived using the definition for their wave impedances (5.22) and the perfect conductivity of ground planes:

$$\lim_{\sigma_s \rightarrow \infty} \underline{\epsilon} = -j\sigma_s/\omega, \quad \lim_{\sigma_s \rightarrow \infty} k_z = \lim_{\sigma_s \rightarrow \infty} \underline{k} = \sqrt{-j\sigma_s\mu_0\omega},$$

$$\lim_{\sigma_s \rightarrow \infty} Z' = \lim_{\sigma_s \rightarrow \infty} \frac{k_z}{\omega \underline{\epsilon}} = 0, \quad \lim_{\sigma_s \rightarrow \infty} Z'' = \lim_{\sigma_s \rightarrow \infty} \frac{\omega\mu_0}{k_z} = 0.$$

Thus, the equivalent transmission lines for TM- and TE-modes have closed termination impedances (see Fig. 1.4b):

$$\overleftarrow{Z}(0) = 0, \quad \overrightarrow{Z}(h) = 0, \quad (5.72)$$

the corresponding circuit model is shown in Fig. 5.6b. The reflection coefficients at the ends of the equivalent line are calculated using (1.75):

$$\overleftarrow{\Gamma}(0) = -1, \quad \overrightarrow{\Gamma}(h) = -1. \quad (5.73)$$

Since the equivalent TL-equations for TM- and TE-modes (Fig. 5.6b) differ only in wave impedances, in the following, we develop the general formulations for the Green's functions with the wave impedance Z_w , which may be replaced by Z' or Z'' .

Using (1.85) and (1.85) we obtain:

$$\begin{aligned} \overleftarrow{Z}(z') &= 1/\overleftarrow{Y}(z') = Z_w \frac{1 - e^{-jk_z 2z'}}{1 + e^{-jk_z 2z'}}, \\ \overrightarrow{Z}(z') &= 1/\overrightarrow{Y}(z') = Z_w \frac{1 - e^{-jk_z 2(h-z')}}{1 + e^{-jk_z 2(h-z')}}, \\ \overleftrightarrow{Z}(z') &= Z_w \frac{2(1 - e^{-jk_z 2h})}{(1 + e^{-jk_z 2z'})(1 + e^{-jk_z 2(h-z')})}, \\ \overleftrightarrow{Y}(z') &= \frac{2}{Z_w} \frac{(1 - e^{-jk_z 2h})}{(1 - e^{-jk_z 2z'})(1 - e^{-jk_z 2(h-z')})}. \end{aligned} \quad (5.74)$$

The substitution of (5.74) in the equations for the Green's functions (1.89), (1.90), (1.92), and (1.91) leads after some elementary simplifications to the final formulation written in view of reciprocity of the Green's functions (1.99) as follows:

$$V_u(z, z') = \begin{cases} \zeta_{0,1}(z, z'), & z > z', \\ -\zeta_{1,0}(z', z), & z < z', \end{cases} \quad (5.75)$$

$$V_i(z, z') = Z_w \begin{cases} \zeta_{1,1}(z, z'), & z > z', \\ \zeta_{1,1}(z', z), & z < z', \end{cases} \quad (5.76)$$

$$I_u(z, z') = \frac{1}{Z_w} \begin{cases} \zeta_{0,0}(z, z'), & z > z', \\ \zeta_{0,0}(z', z), & z < z', \end{cases} \quad (5.77)$$

$$I_i(z, z') = \begin{cases} \zeta_{1,0}(z, z'), & z > z', \\ -\zeta_{0,1}(z', z), & z < z', \end{cases} \quad (5.78)$$

with

$$\zeta_{s,t}(z, z') = \frac{(e^{jk_z z'} + (-1)^s e^{-jk_z z'}) (e^{-jk_z z} + (-1)^t e^{-jk_z (2h-z)})}{2(1 - e^{-jk_z 2h})}. \quad (5.79)$$

As the transmission-line Green's functions are derived, the spectrum-domain Green's functions for vector and scalar potentials may be obtained by substitution of (5.75), (5.76), (5.77), and (5.78) in (5.57) and (5.62) in view that according to (5.22), $Z_w = Z' = \frac{k_z}{\omega \epsilon}$ for TM-mode, and $Z_w = Z'' = \frac{\omega \mu_0}{k_z}$ for TE-mode. The derived formulations for the spectrum-domain scalar components of the dyadic Green's function for the vector magnetic potential and the spectrum-domain scalar Green's function for the scalar electric potential are given below:

$$\begin{aligned} \mathfrak{G}_{zu}^A(z, z') &= \mathfrak{G}_{uz}^A(z, z') = 0, \\ \mathfrak{G}_{zz}^A(z, z') &= \frac{1}{jk_z} \begin{cases} \zeta_{0,0}(z, z'), & z > z', \\ \zeta_{0,0}(z', z), & z < z', \end{cases} \\ \mathfrak{G}_t^A(z, z') = \mathfrak{K}^\varphi(z, z') &= \frac{1}{jk_z} \begin{cases} \zeta_{1,1}(z, z'), & z > z', \\ \zeta_{1,1}(z', z), & z < z'. \end{cases} \end{aligned} \quad (5.80)$$

The equation $\mathfrak{G}_{zu}^A(z, z') = \mathfrak{G}_{uz}^A(z, z') = 0$ means that the currents in the horizontal plane do not produce the scattered electric field in the vertical direction, and the vertical currents do not produce the scattered electric field in the horizontal plane. Thus, the spatial-domain counterparts for these components are also zero $G_{\rho z}^A(\mathbf{r}, \mathbf{r}') = G_{z\rho}^A(\mathbf{r}, \mathbf{r}') = 0$.

5.3.2 Green's functions in the spatial domain

Derivation of $G_t^A(\mathbf{r}, \mathbf{r}')$ and $K^\varphi(\mathbf{r}, \mathbf{r}')$

The spatial-domain Green's functions $G_t^A(\mathbf{r}, \mathbf{r}')$ and $K^\varphi(\mathbf{r}, \mathbf{r}')$ are derived through the calculation of Sommerfeld integrals of the zero order according to (5.63) and (5.65). In the

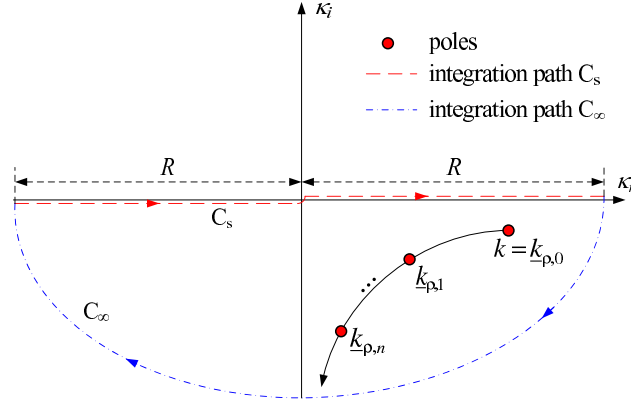


Figure 5.7: Integration path for the computation of the Sommerfeld integral.

following, we derive only $K^\varphi(\mathbf{r}, \mathbf{r}')$ in view that $G_t^A(\mathbf{r}, \mathbf{r}') = K^\varphi(\mathbf{r}, \mathbf{r}')$. We rewrite (5.63) and obtain:

$$K^\varphi(\mathbf{r}, \mathbf{r}') = \frac{1}{4\pi} \int_{-\infty}^{+\infty} \mathfrak{R}^\varphi(z, z', k_\rho) k_\rho H_n^{(2)}(k_\rho \rho) dk_\rho. \quad (5.81)$$

This integral may be calculated in terms of the contour integration for the function of a complex variable. Thus, we introduce the complex variable $\underline{k}_\rho = \kappa_r + j\kappa_i$ instead of k_ρ . In this case, the integral (5.81) is computed as the integral over the Sommerfeld path C_s shown in Fig. 5.7 and defined as follows:

$$C_s = \{ \underline{k}_\rho \mid \kappa_i = 0, -R < \kappa_r < R, R \rightarrow \infty \}. \quad (5.82)$$

The semicircle path with the center at the point of origin and radius $R \rightarrow \infty$ is denoted by C_∞ . These two integration paths constitute a closed loop denoted $C = C_s \cup C_\infty$. The contour integral over C is calculated using the residue theorem [86] if the integrand is a meromorphic function, i.e., it has only simple poles, in the region constrained by the contour S , $C = \partial S$. For the clockwise direction of the integration, we may write:

$$\int_C \vartheta(\underline{k}_\rho) d\underline{k}_\rho = -2\pi j \sum_{n=1}^p \text{res}\{\vartheta(\underline{k}_{\rho,n})\}, \quad (5.83)$$

with $\vartheta(\underline{k}_\rho) = \mathfrak{R}^\varphi(z, z', \underline{k}_\rho) \underline{k}_\rho H_n^{(2)}(\underline{k}_\rho \rho)$,

where $\text{res}\{\vartheta(\underline{k}_{\rho,n})\}$ is the residue of the function $\vartheta(\underline{k}_\rho)$ at the pole $\underline{k}_\rho = \underline{k}_{\rho,n}$, and p is the number of poles in S . The residue is defined for the pole of the m -th order as follows [86]:

$$\text{res}\{\vartheta(\underline{k}_{\rho,n})\} = \frac{1}{(m-1)!} \lim_{\underline{k}_\rho \rightarrow \underline{k}_{\rho,n}} \left[\frac{d^{m-1}}{d\underline{k}_\rho^{m-1}} (\underline{k}_\rho - \underline{k}_{\rho,n})^m \vartheta(\underline{k}_{\rho,n}) \right]. \quad (5.84)$$

First, we have to prove if the integrand is meromorphic in the region S . The Green's function $\mathfrak{R}^\varphi(z, z', k_\rho)$ does not have branch-point singularities, as the layered medium is

constrained from both sides with impenetrable boundaries [44] in contrast to the Green's functions for microstrip lines. This statement may be explained: \mathfrak{K}^φ is a function of k_z , which is a function of k_ρ , according to (5.22), k_z has two branches as a square function $k_z = \pm\sqrt{\underline{k}^2 - k_\rho^2}$. However, it may be proved that \mathfrak{K}^φ is an even function of k_z , i.e., $\mathfrak{K}^\varphi(z, z', -k_z) = \mathfrak{K}^\varphi(z, z', k_z)$, and, consequently, this function is one-valued. Thus, $\mathfrak{K}^\varphi(z, z', k_z)$ is a meromorphic function. It may be shown that $\mathfrak{G}_t^{A'}(z, z', k_z)$ and $\mathfrak{G}_{zz}^{A'}(z, z', k_z)$ are meromorphic functions as well. The Hankel function in (5.81) has a logarithmic branch-point singularity at $k_\rho = 0$. The negative part of the real axis is the branch cut for this branching point. Since the Sommerfeld integration path (C_s) is located on the lower side of the branch cut (see Fig. 5.7), the contour C does not intersect branch cuts, and the function $\vartheta(\underline{k}_\rho)$ is meromorphic in S , and (5.83) is valid.

Since $C = C_s \cup C_\infty$, the integral over the Sommerfeld integration path may be expressed as the difference between the contour integral and the integral over C_∞ :

$$\int_{C_s} \vartheta(\underline{k}_\rho) d\underline{k}_\rho = \int_C \vartheta(\underline{k}_\rho) d\underline{k}_\rho - \int_{C_\infty} \vartheta(\underline{k}_\rho) d\underline{k}_\rho. \quad (5.85)$$

The last integral in (5.85) becomes zero because of the Sommerfeld radiation condition (see § 1.2.2) for the spectrum-domain Green's functions. Thus, after substitution of (5.83) in (5.85) we obtain

$$\int_{-\infty}^{+\infty} \vartheta(k_\rho) dk_\rho = \int_{C_s} \vartheta(\underline{k}_\rho) d\underline{k}_\rho = -2\pi j \sum_{n=1}^p \text{res}\{\vartheta(\underline{k}_{\rho,n})\}, \quad (5.86)$$

and, using (5.81), for the Green's function

$$K^\varphi(\mathbf{r}, \mathbf{r}') = \frac{1}{2j} \sum_{n=1}^p \text{res}\{\vartheta(\underline{k}_{\rho,n})\}. \quad (5.87)$$

Now, the number and location of poles of the spectrum-domain Green's function have to be calculated, in order to compute the residues for (5.87). The poles may be calculated as the roots of the denominator of the Green's function (see (5.80)):

$$1 - e^{-jk_z 2h} = 0. \quad (5.88)$$

The roots $k_{z,n}$ of this simple equation are computed as follows:

$$k_{z,n} = \frac{\pi n}{h}, \quad \text{with} \quad k_{z,n}^2 = \underline{k}^2 + \underline{k}_{\rho,n}^2 = (k_r + jk_i)^2 + (\kappa_{r,n} + j\kappa_{i,n})^2, \quad (5.89)$$

where $\underline{k}_{\rho,n}$ are poles of the spectrum-domain Green's function on the \underline{k}_ρ -plane, $\underline{k} = k_r + jk_i$, and $k_{\rho,n} = \kappa_{r,n} + \kappa_{i,n}$. The relation between the real and imaginary parts of \underline{k}_ρ is produced from (5.89):

$$\kappa_{r,n} = \frac{k_r k_i}{\kappa_{i,n}}. \quad (5.90)$$

Thus, the poles are located on the parabolas given by (5.90) in the second and fourth quotes of the complex plane, the parabola in the fourth quote located in the region S is shown in Fig. 5.7. The location of poles on the parabola is calculated from the biquadratic equation developed through substitution of (5.90) in (5.89):

$$\kappa_{i,n}^4 + (k_r^2 - k_i^2 - k_z^2) \kappa_{i,n}^2 - k_r^2 k_i^2 = 0. \quad (5.91)$$

Obviously, the 0-th pole $\underline{k}_{\rho,0}$ is equal to \underline{k} . The poles $\underline{k}_{\rho,n}$ for $n > 0$ are located on the parabola under the point \underline{k} as shown in Fig. 5.7. Finally, we define the poles as follows:

$$\kappa_{i,n} = -\sqrt{\frac{-b_n + \sqrt{b_n^2 - 4c_n}}{2}}, \quad \text{with } b_n = k_r^2 - k_i^2 - k_z^2, \quad c_n = -k_r^2 k_i^2. \quad (5.92)$$

Now, the poles in the region S are found, and we compute the residues at poles.

Derivation of the residue at the point $\underline{k}_\rho = \underline{k}$

The residue calculation according to (5.84) requires to find the order of the pole. This may be accomplished using the generalized Taylor series expansion of $\vartheta(\underline{k}_\rho)$ in the proximity of \underline{k} . Since

$$\lim_{\underline{k}_\rho \rightarrow \underline{k}} (1 - e^{-jk_z 2h}) = 2j \sqrt{-2\underline{k}h} \sqrt{\underline{k}_\rho - \underline{k}} + O(\underline{k}_\rho - \underline{k}), \quad (5.93)$$

we may calculate the residue at the 0-th pole substituting (5.93) in (5.84) as follows:

$$\text{res}\{\vartheta(\underline{k}_{\rho,0})\} = \lim_{\underline{k}_\rho \rightarrow \underline{k}} (\underline{k}_\rho - \underline{k}) \vartheta(\underline{k}) = 0, \quad (5.94)$$

i.e., in reality, the total integrand $\vartheta(\underline{k}_\rho)$ is regular at the point $\underline{k}_\rho = \underline{k}$.

Derivation of residues at points $\underline{k}_\rho = \underline{k}_{\rho,n}$ for $n \in \overline{1, \infty}$

The Taylor series for the denominator of $\vartheta(\underline{k}_\rho)$ at points $\underline{k}_\rho = \underline{k}_{\rho,n}$ yields:

$$\lim_{\underline{k}_\rho \rightarrow \underline{k}_{\rho,n}} (1 - e^{-jk_z 2h}) = -\frac{2jh\underline{k}_\rho}{k_{z,n}} (\underline{k}_\rho - \underline{k}) + O(\underline{k}_\rho - \underline{k})^2, \quad (5.95)$$

thus, the integrand has poles of the first order at these points. The calculation of the residues according to (5.84) in view of (5.95) leads after several simplifications to the following result:

$$\text{res}\{\vartheta(\underline{k}_{\rho,n})\} = \lim_{\underline{k}_\rho \rightarrow \underline{k}_{\rho,n}} (\underline{k}_\rho - \underline{k}_{\rho,n}) \vartheta(\underline{k}_{\rho,n}) = \frac{1}{h} (\sin k_{z,n} z' \sin k_{z,n} z) H_0^{(2)}(\rho \underline{k}_{\rho,n}). \quad (5.96)$$

The final formulation for the Green's functions $G_t^A(\mathbf{r}, \mathbf{r}')$ and $K^\varphi(\mathbf{r}, \mathbf{r}')$

Finally, we substitute the expressions for the residues at poles (5.96) and (5.94) in (5.87) and derive the spatial-domain Green's functions:

$$G_t^A(\mathbf{r}, \mathbf{r}') = K^\varphi(\mathbf{r}, \mathbf{r}') = \frac{1}{j2h} \sum_{n=1}^{\infty} \sin k_{z,n} z' \sin k_{z,n} z H_0^{(2)}(\rho \underline{k}_{\rho,n}). \quad (5.97)$$

Derivation of $G_{zz}^A(\mathbf{r}, \mathbf{r}')$

The spatial-domain Green's functions $G_{zz}^A(\mathbf{r}, \mathbf{r}')$ are derived through the calculation of Sommerfeld integrals of the zero order according to (5.65). We rewrite (5.65) and obtain:

$$G_{zz}^A(\mathbf{r}, \mathbf{r}') = \frac{1}{4\pi} \int_{-\infty}^{+\infty} \mathfrak{G}_{zz}^A(z, z', k_\rho) k_\rho H_n^{(2)}(k_\rho \rho) dk_\rho. \quad (5.98)$$

This integral may be calculated in terms of the contour integration analogous to the integral (5.81) :

$$\int_{-\infty}^{+\infty} \theta(k_\rho) dk_\rho = \int_{C_s} \theta(\underline{k}_\rho) d\underline{k}_\rho = -2\pi j \sum_{n=1}^p \text{res}\{\theta(\underline{k}_{\rho,n})\}, \quad (5.99)$$

where $\theta(\underline{k}_\rho)$ is the integrand in (5.98) :

$$\theta(\underline{k}_\rho) = \mathfrak{G}_{zz}^A(z, z', \underline{k}_\rho) \underline{k}_\rho H_n^{(2)}(\underline{k}_\rho \rho). \quad (5.100)$$

Since the integrands in (5.81) and (5.98) differ only by signs in their numerators and have poles at same points of the plane, we may choose the same integration contour $C = C_s \cup C_\infty$ as for the previous Green's function (see Fig. 5.7). The poles of $\theta(\underline{k}_\rho)$ are located at points $\underline{k}_{\rho,n}$ defined in (5.90) and (5.92) as shown in Fig. 5.7.

Derivation of the residue at the point $\underline{k}_\rho = \underline{k}$

The residue at the point $\underline{k}_\rho = \underline{k}$ is calculated by substitution of the already derived in (5.93) generalized Taylor series expansion for the denominator in (5.84):

$$\text{res}\{\theta(\underline{k}_{\rho,0})\} = \lim_{\underline{k}_\rho \rightarrow \underline{k}} (\underline{k}_\rho - \underline{k}) \theta(\underline{k}) = \frac{1}{2h} H_n^{(2)}(\underline{k}\rho). \quad (5.101)$$

Obviously, $\theta(\underline{k}_\rho)$ has a pole of the first order at $\underline{k}_\rho = \underline{k}$, and, in contrast to (5.94), the residue differs from zero.

Derivation of residues at points $\underline{k}_\rho = \underline{k}_{\rho,n}$ for $n \in \overline{1, \infty}$

The Taylor series for the denominator of $\theta(\underline{k}_\rho)$ at points $\underline{k}_\rho = \underline{k}_{\rho,n}$ is given by (5.95). The calculation of the residues according to (5.84) in view of (5.95) leads after several simplifications to the following result:

$$\text{res}\{\theta(\underline{k}_{\rho,n})\} = \lim_{\underline{k}_\rho \rightarrow \underline{k}_{\rho,n}} (\underline{k}_\rho - \underline{k}_{\rho,n}) \theta(\underline{k}_{\rho,n}) = \frac{1}{h} (\cos k_{z,n} z' \cos k_{z,n} z) H_0^{(2)}(\rho \underline{k}_{\rho,n}). \quad (5.102)$$

The final formulation for the Green's functions $G_{zz}^A(\mathbf{r}, \mathbf{r}')$

Finally, we substitute the expressions for the residues at poles (5.96) and (5.94) in (5.87) and derive the spatial-domain Green's functions:

$$G_{zz}^A(\mathbf{r}, \mathbf{r}') = \frac{1}{j4h} H_0^{(2)}(\rho \underline{k}) + \frac{1}{j2h} \sum_{n=1}^{\infty} \cos k_{z,n} z' \cos k_{z,n} z H_0^{(2)}(\rho \underline{k}_{\rho,n}). \quad (5.103)$$

5.3.3 Behavior and physical interpretation

The solution obtained in (5.97) and (5.103) expands the Green's functions in terms of cylindrical-wave modes with the wave numbers $\underline{k}_{\rho,n}$ propagating in the horizontal plane. These propagating modes are standing waves with respect to the z -axis, as the longitudinal wave numbers $k_{z,n}$ are real. Usually, such modes appear in the Green's functions for microstrips (see, e.g., [30], [31], and [44]), they are called *lateral waves* as in [30] or *surface waves* as in [44], since these modes propagate in the lateral direction.

Since the transversal wave numbers $\underline{k}_{\rho,n}$ are located on the hyperbola shown in Fig. 5.7, $\kappa_i = \Im \{ \underline{k}_{\rho,n} \} \rightarrow -\infty$ for $n \rightarrow \infty$. The asymptotic expansion of the Hankel-function for large arguments yields [2]:

$$H_0^{(2)}(\rho \underline{k}_{\rho,n}) \approx H_0^{(2)}(\rho \kappa_i) \sim \sqrt{\frac{2}{\pi \rho \kappa_i}} e^{\rho \kappa_i + \pi/4}. \quad (5.104)$$

Hence, the lateral wave modes with large numbers are exponentially damped. They propagate on the distances less or comparable with the infinitesimal distance $|1/\kappa_i|$. Thus, the sum in (5.97) and (5.103) is an exponentially convergent series with a final number of terms N_s required to reach a reasonable accuracy for any finite transverse distance ρ . An approximated heuristic criterion for the number of summands is

$$N_s \geq \frac{h}{\pi} \sqrt{\omega^2 \mu_0 \epsilon + \left(\frac{Q}{\rho} \right)^2}. \quad (5.105)$$

The constant Q can be evaluated from the following equation: $\left| H_0^{(2)}(-jQ) \right| = \delta_{err} \left| H_0^{(2)}(\rho k_{\rho,1}) \right|$, where δ_{err} is a required relative error. The number of summands increases if the frequency grows and if we approach the singularity at the source point $\rho = 0$. As we operate in a limited frequency range up to the maximum frequency of interest (f_m) and we do not need to compute the Green's function at the singular point (we compute only spatial convolution integrals of these functions), N_s is a finite value. Practically, N_s seldom exceeds several tenfold except for the proximity of $\rho = 0$. In the following, all Green's functions for the

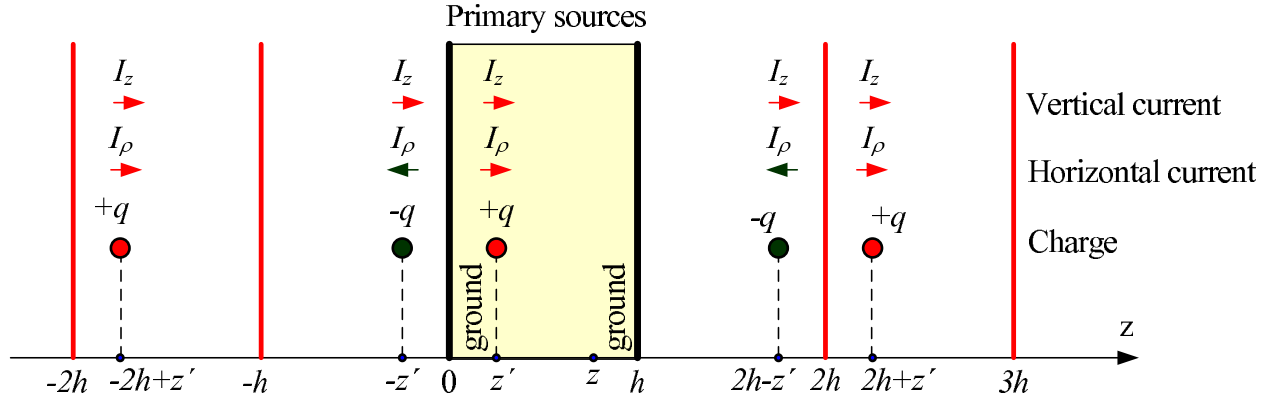


Figure 5.8: Imaged current and charge excitation in the stripline region.

stripline region are given in the final form with a finite number of terms:

$$\begin{aligned}
 G_{tz}^A(\mathbf{r}, \mathbf{r}') &= G_{zt}^A(\mathbf{r}, \mathbf{r}') = 0, \\
 G_t^A(\mathbf{r}, \mathbf{r}') &= K^\varphi(\mathbf{r}, \mathbf{r}') = \frac{1}{j2h} \sum_{n=1}^{N_s} \sin k_{z,n} z' \sin k_{z,n} z H_0^{(2)}(\rho \underline{k}_{\rho,n}), \\
 G_{zz}^A(\mathbf{r}, \mathbf{r}') &= \frac{1}{j4h} H_0^{(2)}(\rho \underline{k}) + \frac{1}{j2h} \sum_{n=1}^{N_s} \cos k_{z,n} z' \cos k_{z,n} z H_0^{(2)}(\rho \underline{k}_{\rho,n}).
 \end{aligned} \tag{5.106}$$

Before the consideration of the frequency response of the Green's functions we should study their alternative formulations developed independent on the theory presented in § 5.2 but using the image theory (or the volume equivalence principle).

Alternative formulation for the Green's functions

The Green's functions for the stripline region defined in Fig. 5.6 may be derived using a quite simple approach based on the image theory [147]. The stripline region may be replaced by an equivalent homogeneous dielectric free-space region with the same complex wave number \underline{k} . The primary current or charge sources are imaged in the upper and lower grounds, the imaged sources are imaged consequently, as shown in Fig. 5.8.

According to the volume equivalence principle, the charges (q in Fig. 5.8) and horizontal currents (I_ρ in Fig. 5.8) are images with the opposite sign. The location for positive and negative images may be deduced from Fig. 5.8 as follows:

$$\begin{aligned}
 -q &: 2hn - z', \\
 +q &: 2hn + z',
 \end{aligned} \quad \text{for } n \in \overline{-\infty, \infty}. \tag{5.107}$$

The vertical currents (I_z in Fig. 5.8) are imaged with the same sign at points given in (5.107) for positive and negative images.

The alternative formulation for the Green's functions is derived as a sum of free-space Green's functions for all image sources:

$$\begin{aligned}
G_t^A(\mathbf{r}, \mathbf{r}') &= K^\varphi(\mathbf{r}, \mathbf{r}') = \\
&= \frac{1}{4\pi} \sum_{n=-\infty}^{\infty} \left(\frac{e^{-\underline{k}\sqrt{\rho^2+(z-z'-2hn)^2}}}{\sqrt{\rho^2+(z-z'-2hn)^2}} - \frac{e^{-\underline{k}\sqrt{\rho^2+(z+z'-2hn)^2}}}{\sqrt{\rho^2+(z+z'-2hn)^2}} \right), \\
G_{zz}^A(\mathbf{r}, \mathbf{r}') &= \frac{1}{4\pi} \sum_{n=-\infty}^{\infty} \left(\frac{e^{-\underline{k}\sqrt{\rho^2+(z-z'-2hn)^2}}}{\sqrt{\rho^2+(z-z'-2hn)^2}} + \frac{e^{-\underline{k}\sqrt{\rho^2+(z+z'-2hn)^2}}}{\sqrt{\rho^2+(z+z'-2hn)^2}} \right).
\end{aligned} \tag{5.108}$$

The obtained formulation uses a slowly converging series, whose precise calculation requires usually a huge number of summands. Its convergence can be better only for a dielectric with large losses that is not typical for printed circuit boards. However, this numerically inefficient formulation may be used for better explanation and validation of (5.106), and for derivation of an asymptotic solution for $\rho = 0$.

The Green's functions given by (5.106) have a singularity at $\rho = 0$, whose order cannot be trivially estimated. The Green's functions are computed as infinite (according to (5.105)) sum of terms with logarithmic singularities. In order to develop the DGF-PEEC model on the basis of the MPIE (see § 5.4), we calculate the spatial-convolution integral of the Green's function. The precise integration at the proximity of $\rho = 0$ needs development of an asymptotic expression for this region, and estimation of the singularity order to assure that the spatial-convolution integral is a regular function.

The first equation in (5.108) is under consideration. We set ρ at the proximity of zero and assume the frequency low, i.e., $\rho \ll h$ and $\underline{k} = 0$. The first equation in (5.108) yields:

$$\frac{1}{4\pi} \sum_{n=-\infty}^{\infty} \left(\frac{1}{\sqrt{\rho^2+(z-z'-2hn)^2}} - \frac{1}{\sqrt{\rho^2+(z+z'-2hn)^2}} \right). \tag{5.109}$$

(5.107) may be combined in the following form:

$$\frac{1}{4\pi} \left(\sum_{n=1}^{\infty} \frac{-2z'}{(2hn-z)^2 - z'^2} + \frac{1}{\rho} - \frac{1}{|z+z'|} + \sum_{n=-\infty}^{-1} \frac{2z'}{(2hn-z)^2 - z'^2} \right). \tag{5.110}$$

Since both infinite sums in (5.110) are convergent series, we develop an asymptotic low-frequency expansion for $G_t^A(\mathbf{r}, \mathbf{r}') = K^\varphi(\mathbf{r}, \mathbf{r}')$ for $\rho \rightarrow 0$ and denote them $G_{t,st}^A(\rho, z, z')$ and $K_{st}^\varphi(\rho, z, z')$.

$$\begin{aligned}
G_t^A(\mathbf{r}, \mathbf{r}') &= K^\varphi(\mathbf{r}, \mathbf{r}') \sim \\
G_{t,st}^A(\rho, z, z') &= K_{st}^\varphi(\rho, z, z') = \frac{1}{4\pi\rho} + C(z, z', h), \\
C(z, z', h) &= \frac{1}{4\pi|z+z'|} + \frac{1}{8\pi h} \left[\Psi \left(1 + \frac{z+z'}{2h} \right) + \Psi \left(1 - \frac{z+z'}{2h} \right) \right. \\
&\quad \left. - \Psi \left(1 + \frac{z'-z}{2h} \right) - \Psi \left(1 - \frac{z'-z}{2h} \right) \right],
\end{aligned} \tag{5.111}$$

where $C(z, z', h)$ is a finite constant defined via geometry and $\Psi()$ is the digamma function [2]. Through (5.111) we see that the singularity is a pole of the first order defined by $1/\rho$.

Frequency responses of Green's functions

As we see in (5.106), the Green's functions for the MPIE have two kinds of frequency dependence. The first one $G_t^A(j\omega)$ represents the coupling between charges or transversally directed currents (i.e., between currents in traces). The second one $G_{zz}^A(j\omega)$ represents the coupling between vertical currents (i.e., between currents in vias). The behavior of both functions at relatively high frequencies is quite similar. They have a set of resonances at the frequency points corresponding to the condition $\hat{k}_{\rho,n} = 0$, $n \in \overline{1..∞}$ for lossless dielectric. The resonance frequencies can be calculated in the case of negligible losses as follows:

$$\omega_r^{(n)} = n\omega_r, \quad \omega_r = \frac{\pi}{h\sqrt{\mu_0\epsilon}}. \quad (5.112)$$

ω_r is the frequency of the first resonance and $\omega_r^{(n)}$ is the frequency of the n -th resonance. It can be noticed that the low frequency behaviors of $G_t^A(j\omega)$ and $G_{zz}^A(j\omega)$ differ. The function $G_t^A(j\omega)$ converges for frequencies $\omega \ll \omega_r$ to a static value while $G_{zz}^A(j\omega)$ becomes infinite. It is caused by the pole of $H_0^{(2)}(\rho k)$ in (5.106). The pole of $H_0^{(2)}(\rho k)$ at the point $k = 0$ is a logarithmic singularity that can be physically explained. As the grounds are assumed to be infinite, according to the image principle (see Fig. 5.8), the vertical currents are reflected from ground planes infinitely many times with equal sign [147]. DC currents do not obtain a phase shift via the time delay and, thus, the infinite sum of such currents diverges for a finite ρ . The relatively weak logarithmic singularity of G_{zz}^A is regularized in the MPIE (1.65) by multiplication on $j\omega$. Because $\lim_{k \rightarrow 0} j\omega H_0^{(2)}(\rho k) = 0$, the electric field intensity resulted by the magnetic vector potential $-j\omega \mathbf{A}$ converges to zero at low frequencies and does not lead to an unphysical infinite solution.

Fig. 5.9 shows an example of the frequency responses $G_{zz}^A(j\omega)$ and $G_t^A(j\omega)$ calculated with the following parameters: $h = 1$ mm, $\sigma_s = 1$ mS/m, $\epsilon_r = 4.0$, and $z = z' = h/2$. The frequency of the first resonance is 75 GHz. One can notice that operational frequencies in modern digital electronic systems are essentially below this frequency. Strong crosstalk caused by the lateral-wave resonances will appear if this condition is not satisfied. Therefore, the PCB-designer should keep the thickness of layers small, in order to avoid this crosstalk. Thus, we consider this condition for all practical problems concerning the design of PCBs, while considering the full dynamic behavior of the Green's functions is of interest only for microwave applications. The time-domain DGF-PEEC model developed in this paper takes into account only the *quasi-dynamic* (defined for microstripes in [31]) behavior of Green's functions including the time delays that differ it from a *static* model. However, this quasi-dynamic model does not consider longitudinal resonances caused by lateral waves. The frequency-domain DGF-PEEC model may be trivially realized using the full-dynamic Green's functions.

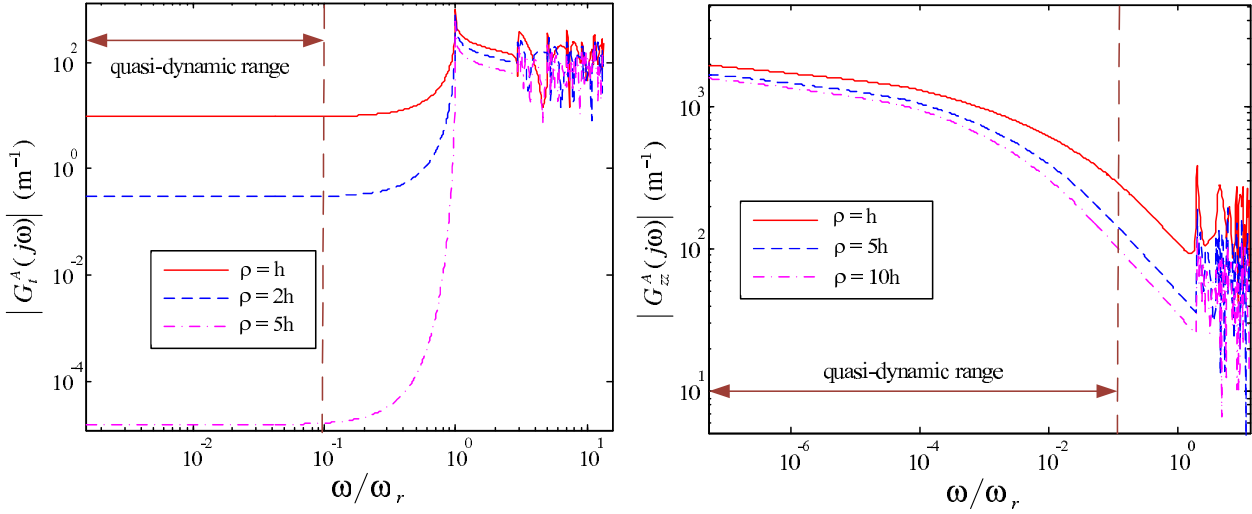


Figure 5.9: Scalar components of the dyadic Green's functions for the stripline region.

Frequency responses of Green's functions with different dielectric losses

The next question to be discussed is the influence of the dielectric losses on the Green's function frequency responses. First we should remember that the resonances at frequencies (5.112) associated with the lateral waves are caused by the singularity of the Hankel function at $\underline{k}_{\rho,n}(\omega_r^{(n)}) = 0$ for the lossless dielectric. It was observed that the magnitude of $H_0^{(2)}(\underline{k}_{\rho,n})$ can show a finite maximum at $\omega_r^{(n)}$ in the case of a lossy dielectric with relatively small σ_s . This means a damped propagated lateral waves mode, while a large σ_s shows no resonance, and consequently, no lateral wave propagation.

The explanation of this fact requires an additional consideration of the frequency response for $\underline{k}_{\rho,n}$ based on its definition in (5.22). We can write

$$\underline{k}_{\rho,n} = \sqrt{\underline{k}^2 - k_{z,n}^2}. \quad (5.113)$$

Using (5.112) and (5.7) we rewrite it as

$$\underline{k}_{\rho,n} = \sqrt{(\omega^2 - n^2\omega_r^2)\mu_0\epsilon - j\omega\mu_0\sigma_s}. \quad (5.114)$$

The frequency dependence of the transversal wave number for the first pole (5.114) is shown in Fig. 5.10, where the left-hand side presents the imaginary and real parts, while the right-hand side shows the magnitude of $\underline{k}_{\rho,n}$. The function is calculated for three different values of the substrate conductivity defined in Fig. 5.10 through the special ratio:

$$\chi = \frac{1}{\omega_r} \frac{\sigma_s}{\epsilon\sqrt{2}}, \quad (5.115)$$

which will be explained below. The first result is calculated for $\chi \ll 1$, i.e., for $\sigma_s \ll \sqrt{2}\epsilon\omega_r$. $|\underline{k}_{\rho,n}|$ shows a sharp minimum at ω_r . Since the real part is near zero at $\omega < \omega_r$ and increases

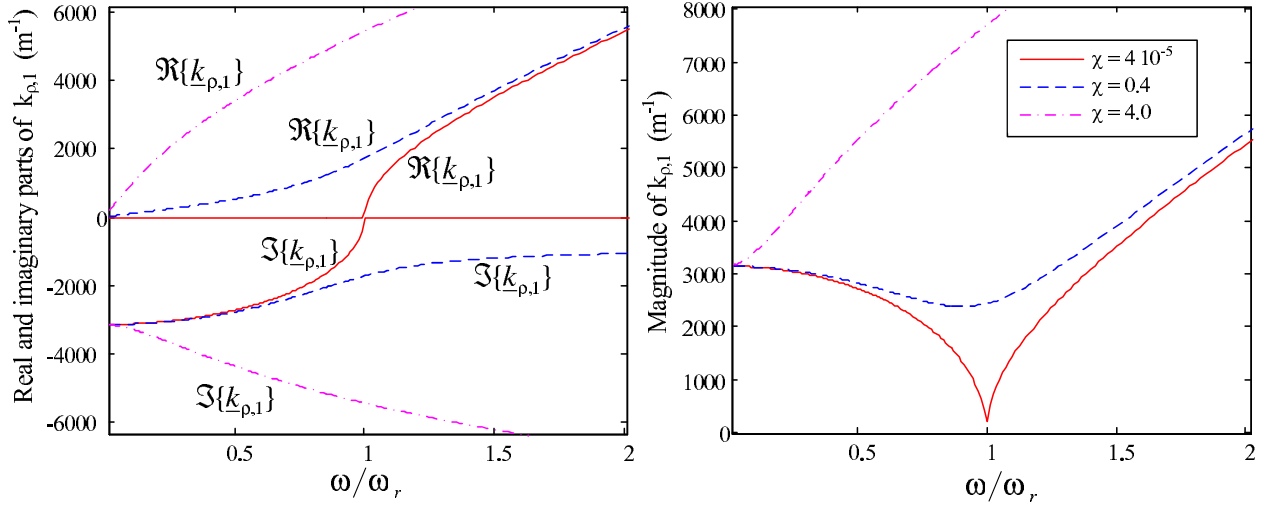


Figure 5.10: Frequency dependence of transversal wave numbers by different dielectric losses.

at $\omega > \omega_r$, the lateral waves $e^{-j\Re\{k_{\rho,n}\}\rho}$ are radiated only at $\omega \geq \omega_r$. These radiated waves have weak damping given by $e^{\Im\{k_{\rho,n}\}\rho}$ because the imaginary part is tiny at high frequencies. The second result is calculated for $\chi = 0.4$, i.e., σ_s is slightly less than $\sqrt{2}\epsilon\omega_r$. $|k_{\rho,n}|$ shows a very damped minimum at ω_r . Since the real part increases at all frequencies, and the absolute value of the imaginary part decreases, strong fast-damped radiated waves appear only at high frequencies. The last result uses $\chi > 1$, i.e., for $\sigma_s > \sqrt{2}\epsilon\omega_r$. $|k_{\rho,n}|$ is a monotone increasing function. The imaginary part is a monotone decreasing function, consequently, damping increases with the frequency. Thus, the lateral waves are not radiated and the resonance at ω_r is disappeared.

Qualitatively we may tell that the lateral wave modes have with respect to losses two principally different kinds behavior: the radiation of lateral waves (resonant frequency response) for "low losses" and the damped wave (wide-band pulse frequency response) for "high losses". A quantitative measure for the losses defined by σ_s may be derived. Consideration of Fig. 5.10 allows one to deduce that $|k_{\rho,n}|$ is a decreasing function for "low losses" and an increasing function for "high losses" at $\omega \rightarrow 0$. In the following, we calculate σ_s corresponding to the constant $|k_{\rho,n}|$ at $\omega \rightarrow 0$, it will be the boundary value for σ_s between two types behavior.

The functions $|k_{\rho,n}|$ and $|k_{\rho,n}|^2$ have the same extrema, further, we consider $|k_{\rho,n}|^2$ in order to simplify the derivation. Using (5.114) we obtain:

$$|k_{\rho,n}|^2 = [(\omega^2 - n^2\omega_r^2)\mu_0\epsilon]^2 + [\omega\mu_0\sigma_s]^2. \quad (5.116)$$

Decreasing of the function $|k_{\rho,n}|^2$ at low frequencies is guaranteed with the following condition:

$$\frac{\partial}{\partial\omega}|k_{\rho,n}|^2 < 0, \text{ for } \omega \rightarrow 0 \Rightarrow -2n^2\omega_r^2\epsilon^2 + \sigma_s^2 < 0. \quad (5.117)$$

Introducing the variable χ according to (5.115) and using (5.117), we develop a quantitative

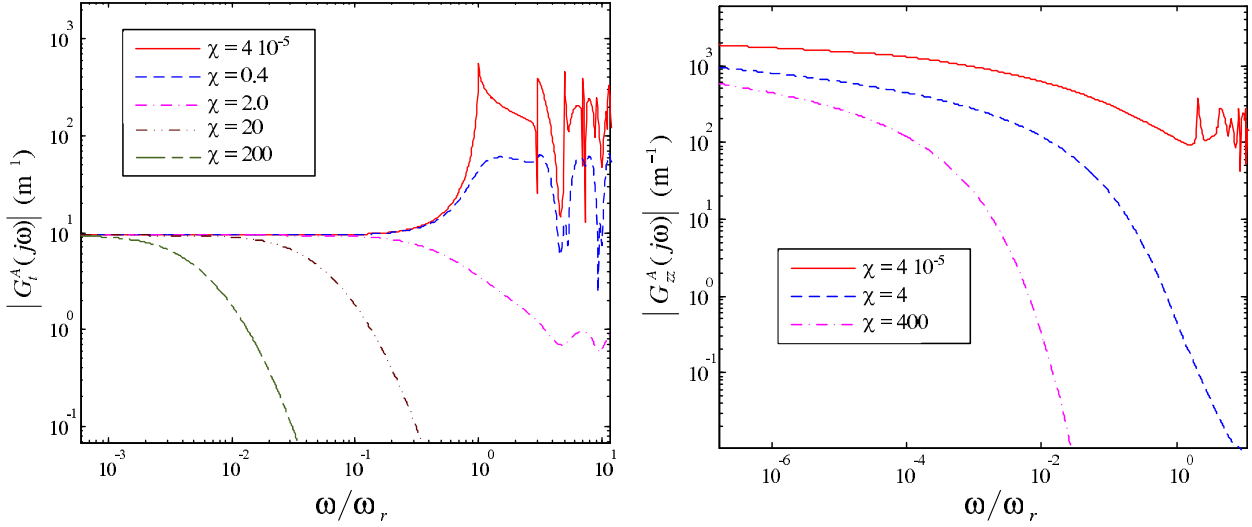


Figure 5.11: Magnitude of the Green's functions by different dielectric losses.

condition for appearing of the n -th resonance:

$$\chi < n, \quad \Leftrightarrow \quad \frac{\sigma_s}{\epsilon\sqrt{2}} < n\omega_r, \quad n = \overline{1, \infty}. \quad (5.118)$$

Fig. 5.11 presents an example of the frequency responses $G_{zz}^A(j\omega)$ and $G_t^A(j\omega)$ calculated with $h = 1$ mm, $\epsilon_r = 4.0$, and $z = z' = h/2$ and different values of σ_s . The left side of Fig. 5.11 consists five frequency responses of $G_t^A(j\omega)$. The first curve calculated with $\chi = 4 \cdot 10^{-5}$ has sharp resonances at all poles, the second one with $\chi = 0.4$ has resonances at all poles, but the resonance at $\omega = \omega_r$ is damped. The third curve with $\chi = 2$ has resonances at $\omega = n\omega_r$ for $n > 2$, but the damping at these frequencies is so strong that $|G_{zz}^A(j\omega)|$ at poles is about ten times less than at low frequencies. The fourth and fifth curves calculated with $\chi = 20$ and $\chi = 200$ respectively show a principally same behavior as the third curve. Namely, the propagating lateral-wave modes appear only for $n \gg 1$ with a huge damping and may be neglected. The influence of the dielectric conductivity on the frequency response $G_{zz}^A(j\omega)$ is shown on the right side of Fig. 5.11. Generally, σ_s influences the damping in the frequency response analogous to $G_t^A(j\omega)$. The only difference is the pole of $G_{zz}^A(j\omega)$ at $\omega = 0$. The character of this term in (5.106) does not depend on σ_s , but the magnitude of the Green's functions at low frequencies decreases if σ_s grows.

The influence of losses on the Green's functions cannot be completely studied without its consideration in the time domain. As an example, we observe here the impulse response for $G_t^A(j\omega)$ calculated using the IFFT algorithm $g_t^A(t) = \mathfrak{F}^{-1}\{G_t^A(j\omega)\}$. Fig. 5.12a shows the impulse response calculated with $\chi = 0.4$. Here we do not consider some imperfections (high frequency oscillations) of this time response caused by a numerical calculation of a Dirac delta function, but we consider only the principle behavior. The first short pulse which width depends on σ_s appear with a delay about 0.66 ps, this time corresponds to the wave propagation in the dielectric with $\epsilon_r = 4.0$ on the distance between the source and observation points equal to h . The second negative pulse appears with a delay about 9.42 ps

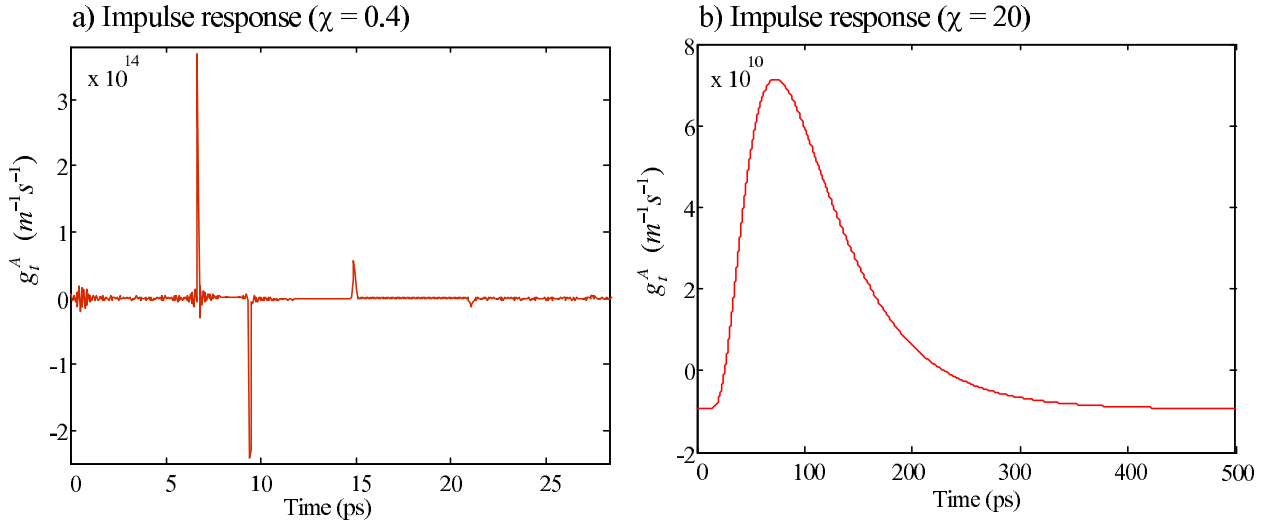


Figure 5.12: Impulse responses for $G_t^A(j\omega)$ with relatively weak (a) and strong (b) losses.

that corresponds to the wave propagation from the first imaged point (see Fig. 5.8) on the distance $h\sqrt{2}$, the third pulse delaying on 14.9 ps is caused by the second imaged point (see Fig. 5.8) on the distance $h\sqrt{5}$, etc. Thus, the high frequency oscillations corresponding to the lateral-wave modes compose in sum a damped series of pulses, which are physically explained in terms of the image theory (5.108).

Another matter is the impulse response calculated with $\chi = 20$ (see Fig. 5.12b). The frequency response of $G_t^A(j\omega)$ (see Fig. 5.11) corresponds to a wide-band pulse in this case. The time constant of this pulse may be approximately calculated as $1/\omega_c$, where ω_c is the cut-off frequency of $G_t^A(j\omega)$.

Since the conditions $\chi < 1$ guarantees the propagation of all lateral-wave modes, we accept $\chi = 1$ as the qualitative boundary between the oscillatory and aperiodic behavior of the Green's function in the time domain.

5.4 PEEC method based on the MPIE for layered media

5.4.1 Motivation

The MPIE derived in § 5.2 for layered media is an integrodifferential equation with respect to the unknown distribution of the current and charge density on the surface of interconnections in the PCB board. In the typical practice, the method of moments (see § 3.3) is the standard computational technique applied to the numerical solution of the MPIE equations. The thorough description of the MoM formulation for the MPIE-LM is given in [36]. The elements of the MoM system matrix are computed via the space-convolution integrals of the spatial-domain Green's functions expanded in terms of Sommerfeld integrals multiplied by the weighing and basis functions. As already mentioned in § 5.2, the calculation of Sommerfeld integrals is a hard problem, which is seldom solved in closed form. Thus, the

computation of a large number (generally, the number of segments to the power of two) of the MoM matrix elements is a very responsible task that may be the "bottle-neck" of the algorithm. A large number of authors have concentrated their efforts on the development of robust and effective approaches for the approximative calculation of the MoM matrix elements (see, e.g., [3], [4], [5], [42], and [119]).

This monograph provides a novel possibility for the numerical solution of the MPIE with the dyadic Green's functions for layered media with the DGF-PEEC method, the general formulation of which is presented in § 4.1. The DGF-PEEC method based on the MPIE for layered media is called the DGFLM-PEEC method. It has been developed by Kochetov, Wollenberg, and Leone [72], [73], [75], [74], and [82]. The frequency-domain formulation of the DGFLM-PEEC (FD-DGFLM-PEEC) method does not differ significantly from the equivalent MoM formulation. The circuit interpretation of the DGFLM-PEEC model does not bring many benefits in the frequency domain as compared to the MoM. On the contrary, the MoM may apply more complicated basis and weighting functions and, thus, yields more precise results. In addition, the MoM formulation is simpler to program. Thus, the FD-DGFLM-PEEC method is interesting as the second universal computational method based on the MPIE with DGFLM, but the method of moments seems to be preferable.

However, the time-domain DGFLM-PEEC method may be considered as preferable as compared to the method of moments. The PEEC method represents an arbitrary interconnection structure in terms of the generalized partial inductances and potential coefficients. The features of the multilayer substrate are modeled via the frequency response of the generalized partial elements. The time-domain macromodeling of the generalized partial elements results in an equivalent-circuit representation, which may be simulated simultaneously with the active devices using a circuit-simulator code.

In general, the DGFLM-PEEC method is a novel research area in the computational electromagnetics that is at least as large as the MoM modeling of the interconnection structures in layered media. This monograph formulates the basic principles of the approach in § 5.4.2 and provides the classification of the perspective DGFLM-PEEC models. Of course, only a few of these models are realized and tested in this work, since the Green's functions for the different geometries of layered media have different derivations, structures and frequency dependencies. Thus, they need the different formulations for the generalized partial elements and the different time-domain macromodels. This monograph develops and verifies the DGFLM-PEEC model for only one particular type of PCB geometry. This model applies the simplest particular realization of the DGFLM derived in § 5.3 for the stripline region. § 5.4.3 derives the full-wave frequency-domain DGFLM-PEEC model and the formulation for the generalized partial elements. Then, the time-domain DGFLM-PEEC model with the *quasi-dynamic* macromodels for the generalized partial elements is developed in § 5.4.4.

An additional benefit of the DGFLM-PEEC method concerns the closed-form formulation for the inductive and capacitive couplings between interconnections. These expressions are developed as a corollary from the general DGFLM-PEEC formulation in terms of mutual inductances and partial capacitances. These simple closed-form estimations for crosstalk between the parts of the interconnection structure is an interesting novel issue for the EMC

analysis. The mutual inductances and partial capacitances for the stripline region are derived and investigated in § 5.4.5 using the particular DGFLM-PEEC model given in § 5.4.3.

5.4.2 General formulation of the DGFLM-PEEC method

The currents and charges in an arbitrary interconnection system located in the layered medium are governed by the MPIE (1.65) with the dyadic Green's function for the vector magnetic potential (5.64) and the scalar Green's function for the scalar electric potential (5.63). Since the general DGF-PEEC model is developed for every geometry, which may be modeled via the MPIE (1.65), the DGFLM-PEEC model is only a particular case of the DGF-PEEC model. According to the strategy shown in § 4.1, (1.65) may be transformed into the KVL equation for a conductor segment (4.28) written in terms of the generalized partials elements, which are defined in (4.16) and (4.25).

Since the dyadic Green's function for the vector magnetic potential obtains a particular structure, the expression for the generalized partial inductances (4.16) may be simplified. The integrand in the space-convolution integral (4.16) is

$$\hat{\mathbf{e}}_\alpha \cdot \overline{\overline{\mathbf{G}}}^A(\mathbf{r}, \mathbf{r}') \cdot \hat{\mathbf{e}}_m, \quad (5.119)$$

where $\hat{\mathbf{e}}_\alpha$ and $\hat{\mathbf{e}}_m$ are the unit vectors specifying the direction of currents in the cells α and m . The vector-dyadic dot product in (5.119) is a scalar function, which may be derived using the dyadic identity (A.9) and the structure of $\overline{\overline{\mathbf{G}}}^A(\mathbf{r}, \mathbf{r}')$ given by (5.64):

$$\begin{aligned} \hat{\mathbf{e}}_\alpha \cdot \overline{\overline{\mathbf{G}}}^A(\mathbf{r}, \mathbf{r}') \cdot \hat{\mathbf{e}}_m = & G_{zz}^A(\mathbf{r}, \mathbf{r}') \beta_{zz}^{\alpha,m} + G_t^A(\mathbf{r}, \mathbf{r}') \beta_t^{\alpha,m} + \\ & G_{\rho z}^A(\mathbf{r}, \mathbf{r}') \beta_{\rho z}^{\alpha,m} + G_{z\rho}^A(\mathbf{r}, \mathbf{r}') \beta_{z\rho}^{\alpha,m} \end{aligned} \quad (5.120)$$

with

$$\begin{aligned} \beta_{zz}^{\alpha,m} &= (\hat{\mathbf{e}}_\alpha \cdot \hat{\mathbf{z}})(\hat{\mathbf{e}}_m \cdot \hat{\mathbf{z}}), & \beta_t^{\alpha,m} &= \hat{\mathbf{e}}_\alpha \cdot \overline{\overline{\mathbf{I}}}_t \cdot \hat{\mathbf{e}}_m, \\ \beta_{\rho z}^{\alpha,m} &= (\hat{\mathbf{e}}_\alpha \cdot \hat{\boldsymbol{\rho}})(\hat{\mathbf{e}}_m \cdot \hat{\mathbf{z}}), & \beta_{z\rho}^{\alpha,m} &= (\hat{\mathbf{e}}_\alpha \cdot \hat{\mathbf{z}})(\hat{\mathbf{e}}_m \cdot \hat{\boldsymbol{\rho}}). \end{aligned}$$

The substitution of (5.120) in (4.16) leads to the scalar formulation for the frequency dependent generalized partial inductances:

$$L_{\alpha,m}(j\omega) = \frac{\mu_0}{d_m d_\alpha} \iint_{A_\alpha} \iint_{A'_m} \left[G_{zz}^A(\mathbf{r}, \mathbf{r}') \beta_{zz}^{\alpha,m} + G_t^A(\mathbf{r}, \mathbf{r}') \beta_t^{\alpha,m} + \right. \\ \left. + G_{\rho z}^A(\mathbf{r}, \mathbf{r}') \beta_{\rho z}^{\alpha,m} + G_{z\rho}^A(\mathbf{r}, \mathbf{r}') \beta_{z\rho}^{\alpha,m} \right] dA'_m dA_\alpha, \quad (5.121)$$

which may be applied to an arbitrary structure of layered media. The scalar coefficients $\beta^{\alpha,m}$ in (5.121) may be alternatively represented as the products of trigonometric functions of the angles explained in Fig. 5.13.

$$\begin{aligned} \beta_{zz}^{\alpha,m} &= \cos \theta_1 \cos \theta_2, \\ \beta_t^{\alpha,m} &= \sin \theta_1 \sin \theta_2 \cos \theta_5, \\ \beta_{\rho z}^{\alpha,m} &= \sin \theta_1 \cos \theta_2 \cos \theta_3, \\ \beta_{z\rho}^{\alpha,m} &= \cos \theta_1 \sin \theta_2 \cos \theta_4, \end{aligned}$$

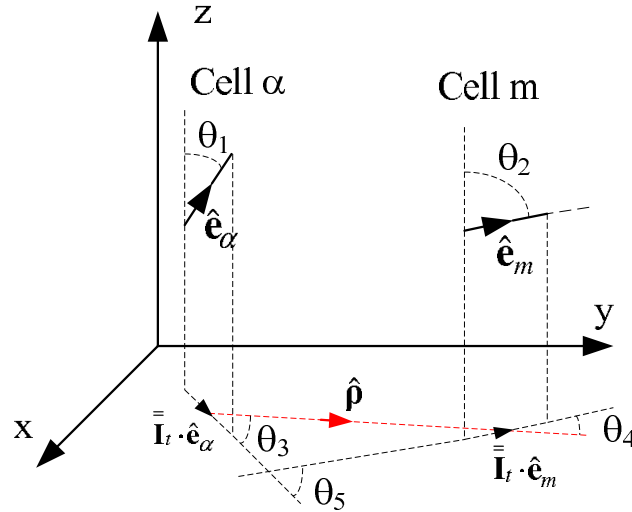


Figure 5.13: Explanation for the structure of the generalized partial inductance.

where θ_1 and θ_2 are vertical angles of the currents in the cells, θ_5 is the azimuthal angle between the currents in the cells, θ_3 is the azimuthal angle between \hat{e}_α and $\hat{\rho}$, and θ_4 is the azimuthal angle between \hat{e}_m and $\hat{\rho}$. Since θ_3 and θ_4 change during the space-convolution integration, these angles are shown in Fig. 5.13 between the middle points of cells. This geometrical formulation of the coefficients $\beta^{\alpha,m}$ leads to the physical interpretation of the terms in (5.121). The first term is related to the inductive coupling between the vertical components of currents. The second term gives the inductive coupling between two parallel components of the currents located in the horizontal plane. The last two terms in (5.121) account for the inductive coupling between the vertical and horizontal current components.

The frequency response of the generalized partial inductances (5.121) and the generalized potential coefficients given by the usual DGF-PEEC formulation (4.25) is completely dependent on the Green's functions derived for the particular kind of geometry. The classification of the models, which may be derived according to the DGFLM-PEEC concept, are summarized in Table 5.1. The DGFLM-PEEC models are subdivided with respect to the Green's function into the models for the stripline and microstrip regions, and the general multilayer structure (see three columns with the double edges in Table 5.1). Since the Green's functions for the single dielectric layer (denoted by "single diel."), the source region of the multilayer dielectric (denoted by "s.r."), and the non-source region of the multilayer dielectric (denoted by "n.s.r.") differ from each other (see [44]), the large columns are subdivided into these three subclasses. The second classification criterion is the qualitative frequency range of the model. Since the frequency response of the generalized partial elements becomes either constant or very simple at low frequencies, one may develop the *quasi-static* DGFLM-PEEC (QS-DGFLM-PEEC) models (see the first row in Table 5.1). In this case, the generalized partial elements are the usual partial inductances and capacitances, which are calculated through the more sophisticated equations. The QS-DGFLM-PEEC model does not differ significantly from the PEEC model for the free-space studied in § 4.2.

	Stripline region			Microstrip region			General PCB
	single diel.	multilayer diel.		single diel.	multilayer diel.		
		s.r.	n.s.r.		s.r.	n.s.r.	
Quasi-static	TD/FD	-	-	-	-	-	-
Quasi-dynamic	TD/FD	-	-	-	-	-	-
Full-wave	-	-	-	-	-	-	-

Table 5.1: Classification of the DGFLM-PEEC models

A more advanced kind of the model, which may be proposed, is called the *quasi-dynamic* DGFLM-PEEC (QD-DGFLM-PEEC) model (see the second row in Table 5.1). It is set up by the exact modeling of the generalized partial elements in the quasi-dynamic frequency range, i.e., only the quasi-dynamic features of the lateral waves are considered (see Fig. 5.9), while the model is full-wave with respect to the time delays. These simple and efficient models are the most important for the EMC analysis, since the usual PCB boards are designed in order to avoid the lateral-wave modes, which are an unacceptable signal integrity problem.

The *full-wave* DGFLM-PEEC (FW-DGFLM-PEEC) model completes the classification of the method in Table 5.1. It may be simply developed in the frequency domain analogous to the MoM model based on the same Green's functions. The time-domain FW-DGFLM-PEEC model may be principally set up using the time-domain macromodeling of the generalized partial elements with a universal approach, e.g., the vector fitting technique. Unfortunately, this approach cannot be recommended because of its instability, which is caused by the tiny imperfections in the macromodels, since no macromodels can guarantee perfect accuracy at the full-spectrum range. Several attempts to develop such a model have resulted in unstable solutions. Thus, further investigations in this direction have been discontinued.

Table 5.1 denotes the realized DGFLM-PEEC models in the time and frequency domain by "TD" and "FD" respectively, while the modifications, which have not yet been programmed and verified, are denoted by dashes. Obviously, most of the DGFLM-PEEC models classified in Table 5.1 may be considered as perspective models that will be set up in the future. Only the time- and frequency-domain QS- and QD-DGFLM-PEEC models have been programmed, investigated, and validated in this work.

5.4.3 Frequency-domain DGFLM-PEEC model for the stripline region

The particular DGF-PEEC models differ only in formulations for the generalized partial elements, which depend on the Green's functions and on the geometry of the current and potential cells. Hence, this section develops the frequency-domain formulations for the generalized partial elements for the most important geometries of cells using the Green's functions for the stripline region derived in § 5.3. In § 4.2, the derivation of the closed-form expressions for the partial elements for the standard free-space PEEC model has been omitted as a trivial problem. The reader has been referenced to the literature on this topic. In

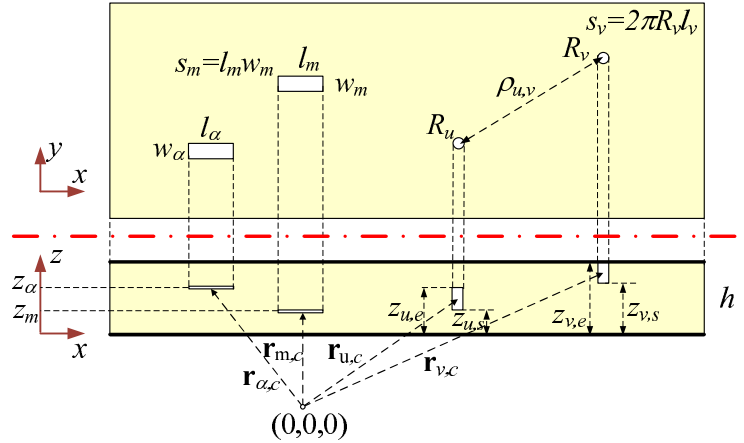


Figure 5.14: Geometrical location of current and potential cells and the necessary notations.

contrast, the completely novel DGFLM-PEEC method requires this derivation. This section derives the computationally efficient closed-form formulations for the generalized partial elements introducing some assumptions and approximations. Alternatively, one may calculate the space-convolution integrals of the generalized partial elements numerically, which leads to significant increase of the computational efforts. Hence, the approximated closed-form expressions are preferable.

In the following, we use a general notation for the derivation of the generalized partial elements. All types of cells with the necessary geometrical notations are shown in two projections in Fig. 5.14. Each cell (e.g., denoted by m) has the length l_m , surface s_m , perimeter d_m , and geometrical center $\mathbf{r}_{m,c}$. The model presented in this monograph divides the flat interconnections located in the horizontal plane into a number of *rectangular* cells. Of course, the real traces are not ever rectangular. Therefore, the formulations for usual partial elements for non-rectangular cells are developed in [130]. Applying the technique given in [130], the formulations for rectangular cells may be expanded on non-rectangular cells. Since the frequency responses of the generalized partial elements for the rectangular and non-rectangular cells may have only quantitative deviations, we consider only rectangular cells in order to simplify the derivation. The width and z -coordinate of the rectangular cell m are denoted by w_m and z_m respectively (see Fig. 5.14).

The second most important type of the interconnections in PCB boards is the vias, which are assumed to have a cylindrical cross-section. They are discretized into a number of so-called *cylindrical* cells. A cylindrical cell (e.g., u in Fig. 5.14) has a radius R_u . It starts at $z = z_{u,s}$ and ends at $z = z_{u,e}$. The transversal distance between the centers of two cells u and v is denoted by $\rho_{u,v}$. The vias with other cross-sections and via pads are not considered due to simplification.

Since all traces and vias are divided into the rectangular and cylindrical cells respectively, we derive the self and mutual generalized partial elements for both these types of cells on the basis of the general formulations (5.121) and (4.25) using the example cells of both types α , m , v , and u in Fig. 5.14.

Generalized partial self inductance for a current cell in a via

The current cell u (see Fig. 5.14) located in a via with a round cross-section is considered. The self partial inductance is computed by the general formulation (5.121), where the dyadic Green's function for the vector magnetic potential (5.106) has two non-zero scalar components $G_t^A(\mathbf{r}, \mathbf{r}')$ and $G_{zz}^A(\mathbf{r}, \mathbf{r}')$. Since the current in the via flows in the vertical direction, we obtain $\beta_{zz}^{u,u} = 1$ and $\beta_t^{u,u} = 0$ in (5.121). Thus, we may rewrite (5.121) as follows:

$$L_{u,u}(j\omega) = \frac{\mu_0}{d_u d_u} \iint_{A_u} \iint_{A'_u} G_{zz}^A(\mathbf{r}, \mathbf{r}') dA'_u dA_u. \quad (5.122)$$

A closed-form solution for $L_{u,u}(j\omega)$ may be derived using the standard *thin wire assumption* (see, e.g., [136]). We assume that the source current flows over the axis of the via and the via radius is much less than $\lambda_m/20$. Since the source current flows over the axis of the via, the surface integral over sources in (5.122) may be replaced by the following line integral:

$$L_{u,u}(j\omega) = \frac{\mu_0}{d_u} \iint_{A_u} \int_{l'_u} G_{zz}^A(\mathbf{r}, \mathbf{r}') dl'_u dA_u. \quad (5.123)$$

The transverse distance between the excitation and observation points in (5.123) is R_u because the source current is located on the axis of the via, while the observation point is located on the cylindrical surface A'_u . Therefore, the integrand depends only on z and z' . We rewrite (5.123) in the following line-integral form

$$L_{u,u}(j\omega) = \mu_0 \int_{l_u} \int_{l'_u} G_{zz}^A(z, z', \rho = R_u) dl'_u dl_u. \quad (5.124)$$

Finally, the double integral in (5.124) is derived in closed form as follows:

$$L_{u,u}(j\omega) = \frac{\mu_0}{2jh} \left(\frac{l_u^2}{2} H_0^{(2)}(R_u k) + \sum_{n=1}^{N_s} \frac{\xi_n}{k_{z,n}^2} H_0^{(2)}(R_u k_{\rho,n}) \right) \quad (5.125)$$

with $\xi_n = (\sin k_{z,n} z_{u,e} - \sin k_{z,n} z_{u,s})^2$.

In the following, the frequency response of the partial self inductance is explained in an example. A via with a radius $R_u = 0.1$ mm is located in the PCB with parameters: $h = 1$ mm, $\sigma_s = 1$ mS/m, and $\epsilon_r = 4.0$. The partial self inductance has been calculated for the three current cells with the length h , $h/2$, and $h/4$ respectively, whose location is shown in Fig. 5.15b. The real and imaginary parts of the generalized partial inductance account for the inductive coupling and ohmic losses, respectively. Since the losses in this example are low, we consider only the real part of the partial inductance shown in Fig. 5.15a. Obviously, all variants of the frequency response increase logarithmically towards low frequencies and show the resonances at high frequencies due to the poles in (5.125). For $l_u = h$ and $|R_u k| \ll 1$, the general formula (5.125) may be essentially simplified.

$$L_{u,u}(j\omega) = \frac{h\mu_0}{2\pi} \left(\ln \frac{2}{R_u k} - \gamma \right), \quad (5.126)$$

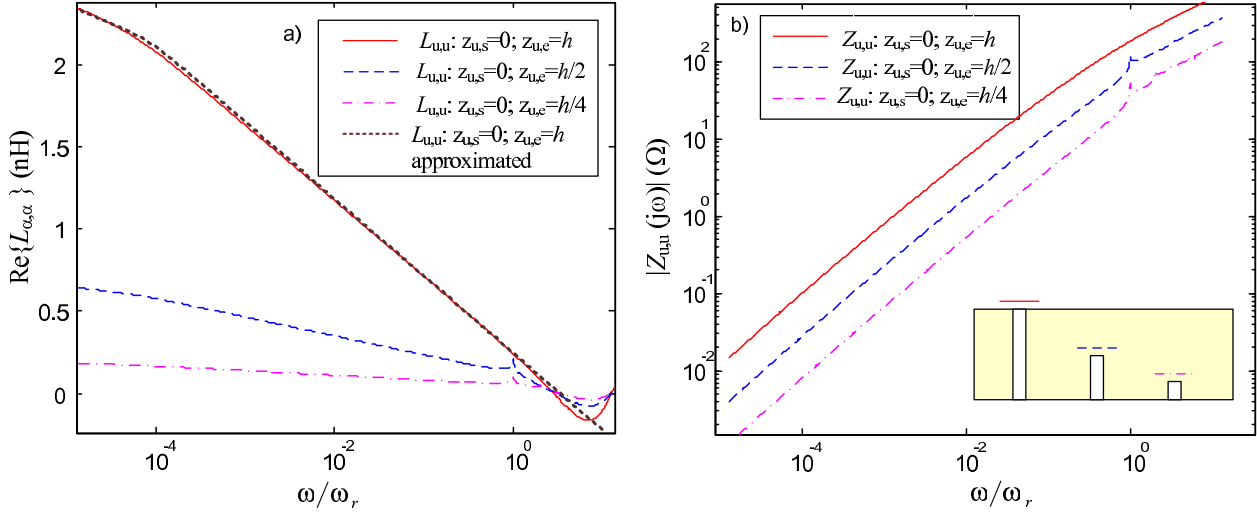


Figure 5.15: Generalized partial self inductance (a), and the impedance $Z_{u,u}(j\omega)$ (b).

where $\gamma \approx 0.57722$ is Euler's constant. The frequency response calculated by the simplified expression (5.126) is shown in Fig. 5.15a by the dotted line, which corresponds to the exact curve at low frequencies. These results can be compared with a rough approximation of the static via inductance given in [58] under the free-space assumption:

$$L_{via} = 5.08 \cdot 10^{-9} h (\ln 2h/R_u + 1). \quad (5.127)$$

(5.127) yields a value of 0.02 nH, which is much lower than our result shown in Fig. 5.15a. Moreover, this approximation does not take into account the frequency dependence.

In PEEC circuits (see Fig. 4.2), the inductive couplings are modeled by the voltage sources controlled by a current derivative. In particular, the voltage drop on the current cell due to the partial self inductance is $U_u^L = j\omega L_{u,u}(j\omega)I_u$. The factor $j\omega L_{u,u}(j\omega)$ may be considered as the impedance of an one-port element $Z_{u,u}(j\omega)$, whose current and voltage are I_u and U_u^L , respectively. The frequency response of $|Z_{u,u}(j\omega)|$ is shown in Fig. 5.15b. This function decreases towards zero at low frequencies and increases proportionally to the frequency. Thus, the given by $L_{u,u}(j\omega)$ inductive coupling does not cause a singularity at low frequencies.

Generalized partial mutual inductance between two cells in vias

Two current cells u and v belong to vias with a round cross-section (see Fig. 5.14). The similar derivation as in the previous subsection has been applied. Using the thin-wire assumption, a closed-form expression for the partial inductance yields:

$$L_{u,v}(j\omega) = \frac{\mu_0}{2jh} \left(\frac{l_v l_u}{2} H_0^{(2)}(\rho_{u,v} k) + \sum_{n=1}^{N_s} \frac{\xi_n}{k_{z,n}^2} H_0^{(2)}(\rho_{u,v} k_{\rho,n}) \right), \quad (5.128)$$

$$\xi_n = (\sin k_{z,n} z_{u,e} - \sin k_{z,n} z_{u,s})(\sin k_{z,n} z_{v,e} - \sin k_{z,n} z_{v,s}).$$

An important explanation should be added to this equation. Due to the thin wire assumption, $\rho_{u,v}$ is replaced by the radius of the via, in the case of two coaxial cells. The comparison

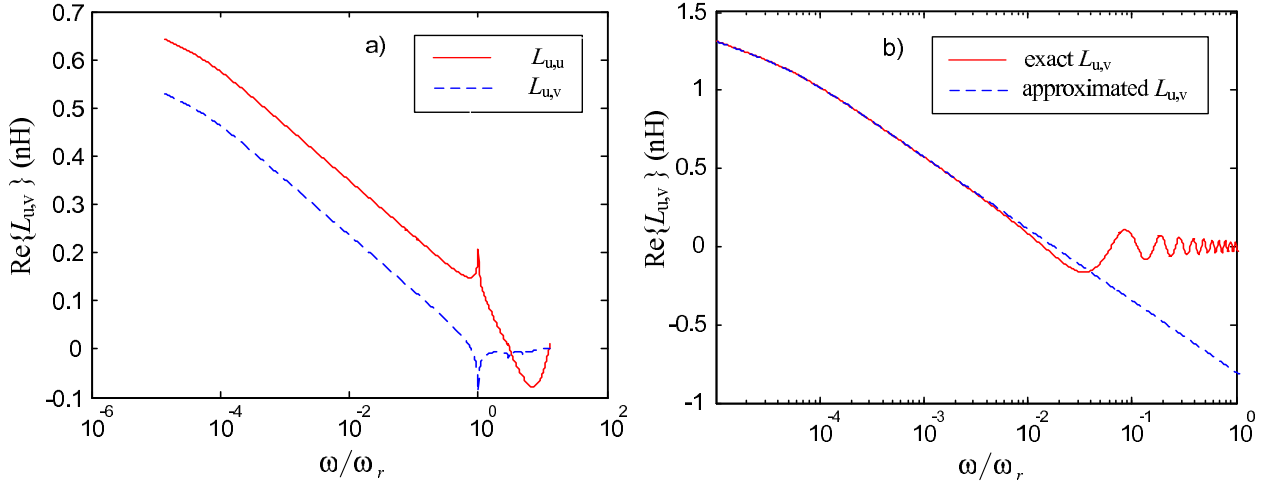


Figure 5.16: Comparison between self and mutual inductances (a) and between exact and approximated formulas for the via inductance (b).

of the frequency responses of the self and mutual partial inductances for two coaxial cells is shown in Fig. 5.16a. The geometrical parameters are $h = 1$ mm, $\sigma_s = 1$ mS/m, $\epsilon_r = 4.0$, $z_{u,s} = 0$, $z_{v,s} = h/2$, $z_{u,e} = h/2$, $z_{v,e} = h$, $\rho_{u,v} = 0$ mm, and $R_u = R_v = 0.1$ mm. The both frequency responses are similar. The mutual inductance is less than the self inductance in the quasi-dynamic frequency range. This looks similar to the ratio between self and mutual inductances in the free-space PEEC model.

If $l_v = l_u = h$, the general expression (5.128) may be simplified using its low-frequency asymptotic expansion:

$$L_{u,v}(j\omega) = \frac{h\mu_0}{2\pi} \left(\ln \frac{2}{\rho_{u,v}k} - \gamma \right). \quad (5.129)$$

The comparison of this approximate formula with the exact expression (5.128) is shown in Fig. 5.16b for the parameters: $h = l_v = l_u = 1$ mm, $\sigma_s = 1$ mS/m, $\epsilon_r = 4.0$, $\rho_{u,v} = 20$ mm, and $R_u = R_v = 0.1$ mm. The results show good correspondence at low frequencies. One may resume that (5.129) is a poor static approximation of (5.128), which does not take into account the time delays.

Generalized self and mutual potential coefficients for the cells in vias

The generalized self and mutual potential coefficients are computed by the general formulation (4.25), where the Green's function for the scalar electric potential in the stripline region is given by (5.106). The derivation of its closed-form expressions has been accomplished analogous to the generalized partial inductances (see above). The final result for the self potential coefficient of the cell u according to Fig. 5.14 is

$$p_{u,u}(j\omega) = \frac{1}{2jh_l^2\epsilon} \sum_{n=1}^{N_s} \frac{\xi_n}{k_{z,n}^2} H_0^{(2)}(R_u k_{\rho,n}), \quad \xi_n = (\cos k_{z,n} z_{u,e} - \cos k_{z,n} z_{u,s})^2. \quad (5.130)$$

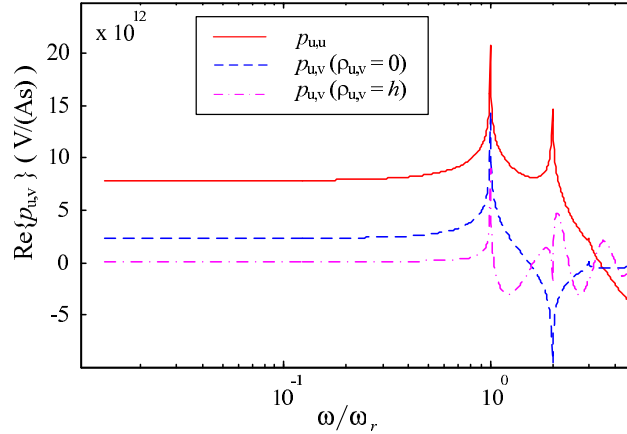


Figure 5.17: Comparison between the self and mutual potential coefficients for cells in vias.

The mutual potential coefficient between the cells u and v (see Fig. 5.14) has been derived as follows:

$$p_{u,v}(j\omega) = \frac{1}{2jhl_v l_u \epsilon} \sum_{n=1}^{N_s} \frac{\xi_n}{k_{z,n}^2} H_0^{(2)}(\rho_{u,v} k_{\rho,n}), \quad (5.131)$$

$$\xi_n = (\cos k_{z,n} z_{u,e} - \cos k_{z,n} z_{u,s})(\cos k_{z,n} z_{v,e} - \cos k_{z,n} z_{v,s}),$$

where $\rho_{u,v}$ has to be replaced by the radius of the via if the cells u and v are coaxial.

The typical example of the frequency response of the self and mutual potential coefficients is shown in Fig. 5.17. The geometrical parameters of the stripline region are $h = 1$ mm, $\sigma_s = 1$ mS/m, $\epsilon_r = 4.0$. The self potential coefficient is computed for the cylindrical cell u with $z_{u,s} = 0$, $z_{v,s} = h/2$, and $R_u = 0.1$ mm. The mutual potential coefficients are calculated between the cells u and v with $z_{u,s} = h/2$, $z_{v,e} = h$, and $R_v = 0.1$ mm. The first mutual potential coefficient (the dash line in Fig. 5.17) is calculated for $\rho_{u,v} = 0$, i.e., the cells are coaxial. The second mutual potential coefficient (the dash-dot line in Fig. 5.17) is calculated for $\rho_{u,v} = h$, i.e., the cells are shifted transversally by h .

One may observe that all generalized potential coefficients have resonances at $\omega \geq \omega_r$ and are constant at $\omega \ll \omega_r$. The real part of the generalized potentials coefficients is positive and may be considered as a usual static potential coefficient. The static potentials coefficients decrease exponentially with respect to the transversal distance between cells. The exponential dependence is caused by the asymptotic behavior of Hankel functions in (5.131). Since at low frequencies $k_\rho \approx -jk_z$, Hankel functions in (5.131) get an argument $-j\rho_{u,v} k_{z,n}$. In view of the asymptotic expansion of Hankel function (5.104), this leads to an exponential decrease of the potential coefficients. The self potential coefficient is larger than mutual potential coefficients at low frequencies. This ratio between the self and mutual partial elements is typical for the standard PEEC method and corresponds to the stability condition of the QS-PEEC model (4.55).

Generalized partial inductances for the horizontal current cells

The flat rectangular current cells α and m located in the horizontal plane are considered (see Fig. 5.14). Such cells are applied to modeling PCB traces. The mutual partial inductance between cells α and m is computed by the general formulation (5.121), where the dyadic Green's function for the vector magnetic potential in the stripline region (5.106) has two non-zero scalar components $G_t^A(\mathbf{r}, \mathbf{r}')$ and $G_{zz}^A(\mathbf{r}, \mathbf{r}')$. Since the current in the trace flows in the horizontal plane, we obtain $\beta_t^{\alpha, \alpha} = \hat{\mathbf{e}}_\alpha \cdot \hat{\mathbf{e}}_m$ and $\beta_{zz}^{\alpha, \alpha} = 0$. Thus, (5.121) yields

$$L_{\alpha, m}(j\omega) = \frac{\mu_0}{w_\alpha w_m} \iint_{A_\alpha} \iint_{A'_m} G_t^A(\mathbf{r}, \mathbf{r}') dA'_m dA_\alpha. \quad (5.132)$$

The direct closed-form integration of $G_t^A(\mathbf{r}, \mathbf{r}')$ in the horizontal plane is impossible because the Green's function contains $H_0^{(2)}(\rho k_{\rho, n})$. The direct numerical integration is computationally expensive, since $G_t^A(\mathbf{r}, \mathbf{r}')$ is singular at $\rho = 0$, which is possible for adjacent cells. In order to find a solution, we consider the frequency response $G_t^A(\mathbf{r}, \mathbf{r}')$ (see Fig. 5.9). In contrast to $G_{zz}^A(\mathbf{r}, \mathbf{r}')$, this function tends to a constant value at $\omega = 0$. Thus, we may simplify the integration analogous to the free-space FW-PEEC method that approximates the dynamic free-space Green's function via (4.31). This standard approximation requires the integration only of the static part of the Green's function, while its frequency dependence is taken into account with respect to the geometrical centers of cells denoted by $\mathbf{r}_{m, c}$ and $\mathbf{r}_{\alpha, c}$. Thus, we compute exactly the static partial inductance $L_{\alpha, m}$ and approximately $L_{\alpha, m}(j\omega)$ at high frequencies. The Green's function $G_t^A(\mathbf{r}, \mathbf{r}')$ may be approximated in the same form:

$$G_t^A(\mathbf{r}, \mathbf{r}') \approx G_{t, st}^A(\mathbf{r}, \mathbf{r}') G_{t, dyn}^A(\mathbf{r}_{\alpha, c}, \mathbf{r}_{m, c}) \quad (5.133)$$

with

$$G_{t, st}^A(\mathbf{r}, \mathbf{r}') = G_t^A(\mathbf{r}, \mathbf{r}', j\omega = 0) \text{ and } G_{t, dyn}^A(\mathbf{r}_{\alpha, c}, \mathbf{r}_{m, c}, j\omega) = \frac{G_t^A(\mathbf{r}_{\alpha, c}, \mathbf{r}_{m, c}, j\omega)}{G_{t, st}^A(\mathbf{r}, \mathbf{r}')}. \quad (5.134)$$

The Green's function is divided into two terms. The static part $G_{t, st}^A(\mathbf{r}, \mathbf{r}')$ depends on the space coordinates, while the dynamic part $G_{t, dyn}^A(\mathbf{r}_{\alpha, c}, \mathbf{r}_{m, c}, j\omega)$ depends only on frequency. At low frequencies the dynamic part is equal to one. We substitute (5.133) into (5.132) and obtain

$$L_{\alpha, m}(j\omega) = \frac{\mu_0}{w_\alpha w_m} G_{t, dyn}^A(\mathbf{r}_{\alpha, c}, \mathbf{r}_{m, c}, j\omega) \iint_{A_\alpha} \iint_{A'_m} G_{t, st}^A(\mathbf{r}, \mathbf{r}') dA'_m dA_\alpha. \quad (5.135)$$

The inner integral over the surface A'_m in (5.135) is a function proportional to the vector magnetic potential, which cannot change significantly inside the cell α , since the cell size is electrically small. Hence, the outer integral over the surface A_α may be accurately calculated using the middle-point rule of the numerical integration:

$$L_{\alpha, m}(j\omega) \approx \frac{\mu_0}{w_\alpha w_m} G_{t, dyn}^A(\mathbf{r}_{\alpha, c}, \mathbf{r}_{m, c}, j\omega) A_\alpha \iint_{A'_m} G_{t, st}^A(\mathbf{r}_{\alpha, c}, \mathbf{r}') dA'_m. \quad (5.136)$$

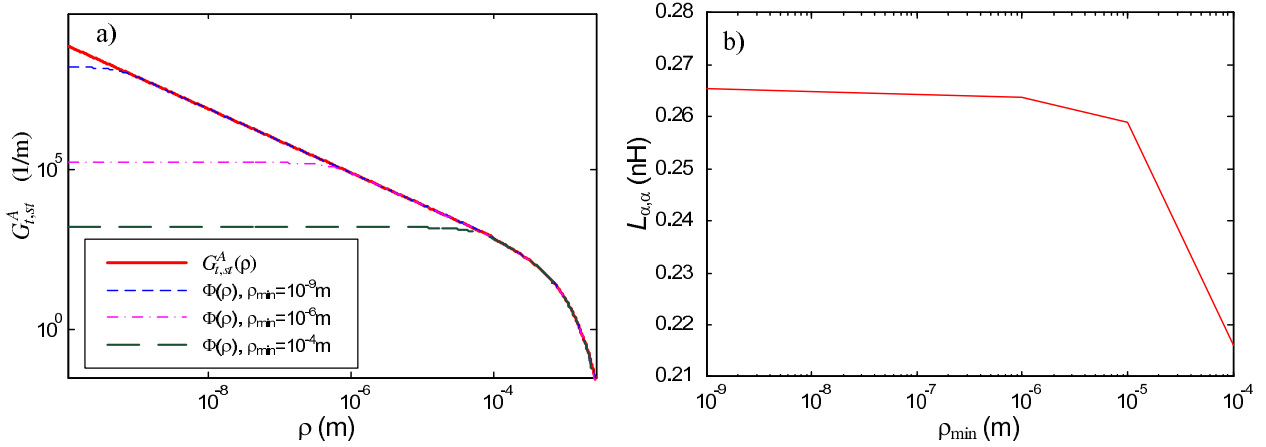


Figure 5.18: Approximation of the Green's function (a), and the sensitivity of the approximated solution $L_{\alpha,\alpha}$ to the variation of ρ_{min} (b).

Unfortunately, the integral of the static part in (5.136) plane may not be derived in closed form. Due to simplification, we have expanded the dependence of $G_{t,st}^A(\mathbf{r}, \mathbf{r}') = G_{t,st}^A(\rho, z = z_{\alpha,c}, z' = z_{m,c})$ on the transversal distance ρ in the special basis functions (3.9):

$$G_{t,st}^A(\rho, z, z') \approx \Phi(\rho, z, z') = \sum_{i=1}^n \frac{a_i}{(b_i^2 + \rho^2)^{3/2}}. \quad (5.137)$$

The surface integrals of the terms in (5.137) may be computed in closed form. The expansion coefficients a_i and b_i may be calculated by the numerically efficient least square procedure [62]. The sampling points for the least square procedure are chosen in the range, whose boundaries are denoted by ρ_{min} and ρ_{max} .

ρ_{max} should be determined as the largest transversal distance on the PCB board. The choice of ρ_{min} raises a question related to the singularity at $\rho = 0$. The correctness of the approximation of the singular function $G_{t,st}^A(\rho)$ by a non-singular function $\Phi(\rho)$ has to be proved.

The asymptotic formulation (5.111) derived in § 5.3 may be used for the proof. According to (5.111), the singular part of $G_{t,st}^A(\rho)$ is $\frac{1}{4\pi\rho}$, whose double undefined integral is a regular function. The corollary from this fact is

$$\lim_{s \rightarrow 0} \iint_s G_{t,st}^A(\rho) ds = 0 \Rightarrow \iint_{s'_m} G_{t,st}^A(\rho) ds'_m = \iint_{s'_m} \Phi(\rho) ds'_m,$$

if $\Phi(\rho) = G_{t,st}^A(\rho)$ for $\rho > \rho_{min}$, which is much less than the size of the cell, although $\Phi(0) \neq G_{t,st}^A(0) = \infty$. This may be reformulated as the following criterion that will be refined in (5.139):

$$\rho_{min} \ll \lambda_m/20. \quad (5.138)$$

In the following, we investigate the sensitivity of the solution for the static partial inductances calculated via the approximation of the static Green's function by (5.137). Since the computation of the self partial inductance requires the integration at $\rho = 0$, we consider the self partial inductance with the parameters: $l_\alpha = 0.746$ mm ($f_m = 10$ GHz), $w_\alpha = 0.3$ mm, $h = 1$ mm, $\sigma_s = 1$ mS/m, $\epsilon_r = 4.0$, and $z_\alpha = h/2$. The approximation $\Phi(\rho)$ has been computed for several values of ρ_{min} between 1 nm (27 terms in the sum (5.137)) and 0.1 mm (6 terms in the sum (5.137)). The results are shown in Fig. 5.18a as compared to the reference curve $G_{t,st}^A(\rho)$. Obviously, all approximations fit the reference well at all points between ρ_{min} and ρ_{max} . An error appears only for $\rho < \rho_{min}$. Fig. 5.18b shows the dependence of the computed static value $L_{\alpha,\alpha}$ on ρ_{min} used for the approximation. We observe that the values calculated with ρ_{min} equal to 1 nm and 10 nm do not differ. $\rho_{min} = 1$ μ m produces an error of 0.6%, 10 μ m - 2.4%, and 0.1 mm - 19%. The error increases strongly if ρ_{min} approaches $\lambda_m/20 = 0.75$ mm. Fair accuracy of the approximation is obtained with

$$\rho_{min} < \lambda_m/10000. \quad (5.139)$$

According to (5.111), the singular part of $G_{t,st}^A(\rho)$ does not depend on h , σ_s , and ϵ . Hence, the criterion for the choice of ρ_{min} (5.139) may be applied to every stripline region.

The approximation (5.137) allows the derivation of the generalized partial mutual inductance in the compact form:

$$L_{\alpha,m}(j\omega) = L_{\alpha,m} G_{t,dyn}^A(\mathbf{r}_{\alpha,c}, \mathbf{r}_{m,c}, j\omega), \quad L_{\alpha,m} = \frac{\mu_0}{w_\alpha w_m} I_{\alpha,m}, \quad (5.140)$$

where $I_{\alpha,m}$ is the space-convolution integral of the static Green's function computed using the approximation (5.137):

$$I_{\alpha,m} = A_\alpha \iint_{A'_m} \Phi(\rho, z_{\alpha,c}, z_{m,c}) dA'_m. \quad (5.141)$$

The approximation (5.135) may also be applied to the computation of the generalized self partial inductances but in an approximated form because $G_{t,dyn}^A(\mathbf{r}_{\alpha,c}, \mathbf{r}_{\alpha,c}, j\omega)$ is singular:

$$L_{\alpha,\alpha}(j\omega) = \frac{\mu_0}{w_\alpha^2} G_{t,dyn}^A(z_\alpha, z_\alpha, \rho_{\alpha,\alpha}, j\omega) \iint_{A_\alpha} \iint_{A'_\alpha} G_{t,st}^A(\mathbf{r}, \mathbf{r}') dA'_\alpha dA_\alpha, \quad (5.142)$$

where $\rho_{\alpha,\alpha}$ is the geometrically mean size of the cell α (analogous to the geometrically mean size defined in [147]). It is calculated numerically from the equation

$$G_{t,st}^A(z_\alpha, z_\alpha, \rho_{\alpha,\alpha}) = \frac{I_{\alpha,\alpha}}{A_\alpha^2} \quad (5.143)$$

using the Newton iterations for solving algebraic equations [62]. Thus, we may rewrite (5.142) in the compact form:

$$L_{\alpha,\alpha}(j\omega) = L_{\alpha,\alpha} G_{t,dyn}^A(z_\alpha, z_\alpha, \rho_{\alpha,\alpha}, j\omega), \quad L_{\alpha,\alpha} = \frac{\mu_0}{w_\alpha^2} I_{\alpha,\alpha}. \quad (5.144)$$

Remaining generalized potential coefficients

Since $G_t^A(\mathbf{r}, \mathbf{r}') = K^\varphi(\mathbf{r}, \mathbf{r}')$, the remaining variants of the potential coefficients are derived using the above given concepts. In the following, we present the final formulations expressed in terms of the space-convolution integrals of the static Green's function for the scalar electric potential defined analogous to (5.141):

$$I_{\alpha,m}^s = S_\alpha \iint_{S'_m} \Phi(\rho, z_{\alpha,c}, z_{m,c}) dS'_m, \quad (5.145)$$

where $\Phi(\rho, z_{\alpha,c}, z_{m,c})$ is the approximation for $K^\varphi(\mathbf{r}, \mathbf{r}', \omega = 0)$ according to (5.137). S_α and S'_m are surfaces of the potential cells. Finally, we obtain the self potential coefficient for the flat rectangular cell α (see Fig. 5.14)

$$p_{\alpha,\alpha}(j\omega) = p_{\alpha,\alpha} K_{dyn}^\varphi(z_\alpha, z_\alpha, \rho_{\alpha,\alpha}, j\omega), \quad p_{\alpha,\alpha} = \frac{I_{\alpha,\alpha}}{\epsilon S_\alpha^2}, \quad (5.146)$$

where $\rho_{\alpha,\alpha}$ is the geometrically mean size of the potential cell. The mutual potential coefficient for the flat cells α and m (see Fig. 5.14) is given by:

$$p_{\alpha,m}(j\omega) = p_{\alpha,m} K_{dyn}^\varphi(\mathbf{r}_{\alpha,c}, \mathbf{r}_{m,c}, j\omega), \quad p_{\alpha,m} = \frac{I_{\alpha,m}}{\epsilon S_\alpha S'_m}. \quad (5.147)$$

The mutual potential coefficient between the flat cell α and the vertical cell u belonging to a via (see Fig. 5.14) is computed as

$$p_{\alpha,u}(j\omega) = p_{\alpha,u} K_{dyn}^\varphi(\mathbf{r}_{\alpha,c}, \mathbf{r}_{u,c}, j\omega), \quad p_{\alpha,u} = \frac{I_{u,\alpha}}{\epsilon S_\alpha S'_u}. \quad (5.148)$$

5.4.4 Quasi-static time-domain DGFLM-PEEC model

The FD-DGFLM-PEEC model with the generalized partial elements derived in § 5.4.3 may be included in a circuit-simulator code as a usual FD-DGF-PEEC model. The frequency dependent generalized partial elements are modeled in terms of linear controlled sources with the frequency depended factors as it is explained in § 4.3. In contrast, the time-domain DGFLM-PEEC model is not trivial for the implementation. The frequency dependence of the partial elements has to be approximated using some time-domain macromodels. As it is introduced in § 5.4.2, one may consider the three levels of modeling with respect to the dynamic of the generalized partial elements: the quasi-static, quasi-dynamic, and full-wave modeling. This section studies the quasi-static one and presents the QS-DGFLM-PEEC models in the time domain.

The QS-DGFLM-PEEC method is derived from the frequency-domain DGFLM-PEEC model analogous to the QS-PEEC model in the free space (see § 4.2.4). The QS-PEEC model in the free space is developed assuming all time delays equal to zero, which means neglecting the dynamic part of the generalized partial elements. The generalized partial

elements involving the integration in the horizontal plane are computed using the extraction of their static part. Hence, the quasi-static representations are obtained via neglecting their dynamic parts. We derive $L_{\alpha,m}^{qs} = \Re \{L_{\alpha,m}\}$ in (5.140), $L_{\alpha,\alpha}^{qs} = \Re \{L_{\alpha,\alpha}\}$ in (5.144), $p_{\alpha,\alpha}^{qs} = \Re \{p_{\alpha,\alpha}\}$ in (5.146), $p_{\alpha,m}^{qs} = \Re \{p_{\alpha,m}\}$ in (5.147), and $p_{\alpha,u}^{qs} = \Re \{p_{\alpha,u}\}$ in (5.148), where the superscript qs denotes the static partial elements for the QS-DGFLM-PEEC model. Another situation may be observed for the generalized partial inductances between vertical current cells, which do not have static values but tend to infinity logarithmically. Since the main advantage of the QS-PEEC model is its realization only by standard circuit elements, we have to calculate the static partial inductances in order to keep this advantage. The static partial inductance may be approximately calculated as the real part of the generalized one given by (5.125) or (5.128) at the maximum frequency of interest:

$$L_{u,u}^{qs} = \Re \{L_{u,u}(j\omega_m)\}, \quad L_{u,v}^{qs} = \Re \{L_{u,v}(j\omega_m)\}. \quad (5.149)$$

This choice of the tasting frequency is motivated by the fact that the inductive coupling is proportional to the frequency. Thus, the partial inductance makes the maximal influence on the solution at ω_m , and this choice guarantees the best precision if the frequency response of the generalized partial inductance is not considered.

Since the static partial elements for the QS-DGFLM-PEEC model are real constants, the time-domain implementation of this model is completely the same with free-space QS-PEEC model described in § 4.2.4. This model has the following disadvantages.

- Dielectric losses are not considered.
- Time delays are not considered.
- Lateral-wave resonances are not considered.

This model has the following advantages.

- It is realized using the standard circuit elements and may be simulated by SPICE without additional efforts.
- In contrast to transmission-line models, the non-uniform structure of traces and vias is considered.
- The influence of the substrate is approximated by the partial elements, it is correct at relatively low frequencies.

In general, we resume that the QS-DGFLM-PEEC model has a practical significance. It may be applied instead of the transmission-line models, whose parameters are computed using the features of the substrate and grounds. In this case, the QS-DGFLM-PEEC model will provide the same level of precision with respect to the substrate but more flexibility with respect the geometry of interconnections.

5.4.5 Quasi-dynamic time-domain DGFLM-PEEC model

The quasi-dynamic model approximates the frequency dependence of the generalized partial elements at frequencies, where the lateral-wave resonances of the PCB are negligible, as it is introduced in § 5.3.3. This level of modeling takes into account the losses in dielectric and the time delays of the inductive and capacitive couplings.

General concept

At the beginning, we consider the concept of the quasi-dynamic modeling by the example of the system described by the transfer function $G(j\omega)$ and impulse response $g(t)$:

$$\begin{aligned} G(j\omega) &= \frac{\beta^2 + \omega_r^2}{(j\omega + \beta)^2 + \omega_r^2}, \quad \omega_r = 2\pi f_r, \\ g(t) &= \mathfrak{F}^{-1}\{G(j\omega)\} = \frac{\beta^2 + \omega_r^2}{\omega_r} e^{-\beta t} \sin \omega_r t. \end{aligned} \quad (5.150)$$

We use the following parameters of the functions: $\omega_r = 471.2 \cdot 10^9 \text{ s}^{-1}$ and $\beta = 10^{-6} \omega_r$. Thus, the transfer function has a sharp resonance at $f_r = 75 \text{ GHz}$, which frequency corresponds to the first lateral-wave resonance of the Green's function shown in Fig. 5.9. Since the resonance is sharp, the impulse response has the slowly damped oscillatory character (see Fig. 5.19a). It may be assumed that the principle part of the spectrum of the input waveform is limited by the frequency f_m that is much lower than ω_r , e.g., we set $f_m = 3 \text{ GHz}$ ($\omega_m = 2\pi f_m$). An bi-exponential waveform shown in Fig. 5.19b satisfies this condition. The time response on this waveform calculated using the Duhamel integral (3.19) is shown in Fig. 5.19c. One may observe that the output function $y(t)$ consists of the input waveform $x(t)$ and oscillations at the frequency 75 GHz introduced by the impulse function. The magnitude of this oscillations is minor with respect to the input waveform. Thus, the input waveform seems to be distorted by a noise.

It may be resumed that the resonances of the transfer function located much higher than f_m do not influence the principle waveform but introduce oscillations with small magnitudes, whose frequencies are not supported by the discretization grid related to f_m according to (3.12). § 4.5.3 devoted to the stability of the standard FW-PEEC-method has asserted that the application of the dynamic partial elements producing high frequency oscillations leads to the instability of the time-domain solution. Thus, the influence of resonances on the useful waveform is insignificant, but the application of full-dynamic macromodels for the generalized partial elements is potentially dangerous with respect to stability. The several attempts to set up a full-dynamic DGFLM-PEEC model have resulted in instable solutions also for the excitations with $f_m \ll f_r$. The stability is the main motivation for the development of the QD-DGFLM-PEEC model.

In the following, we will try to replace the oscillatory impulse response $g(t)$ by an equivalent aperiodic function $g^{ad}(t)$ so that the principal waveform $y(t)$ remains the same. One may compute the time response of the considered system on the input waveform $z(t)$ shown

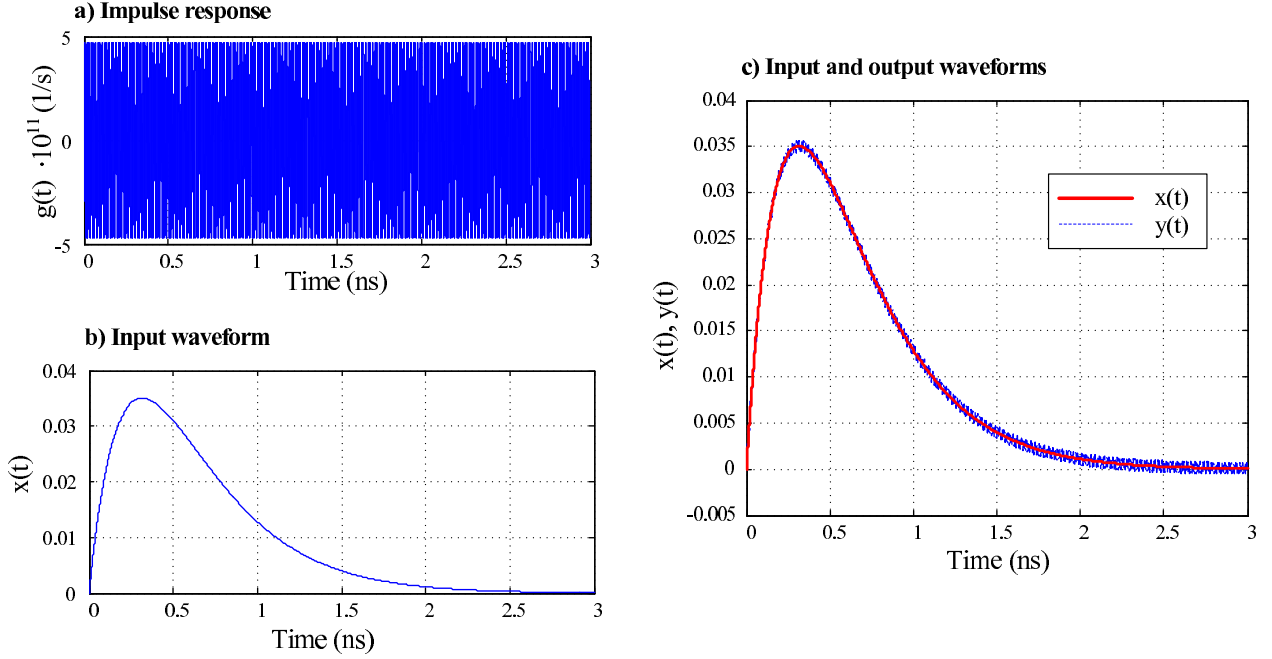


Figure 5.19: Example of the signal propagation $Y(j\omega) = G(j\omega)X(j\omega)$.

in Fig. 5.20. Obviously, $z(t)$ is almost equal to $x(t)$, but this function is defined sophisticatedly. It is the time response of the system with the transfer function $W(j\omega)$ (4.100) and the impulse response $w(t)$ (4.103) on the waveform $x(t)$. The parameters of $W(j\omega)$ are $\xi = 1$, $\tilde{\tau} = 0.01$ ps, and

$$\alpha = \frac{\sqrt{-\ln \eta}}{\omega_m}, \quad (5.151)$$

where $\eta = 0.99$, i.e., $|W(j\omega_m)| = 0.99$. Since we set a tiny time delay and only 1 % damping at ω_m , the time response on the excitation $x(t)$ computed using the Duhamel integral (3.19) has only minor deviations from $x(t)$. Of course, the time response of the system with the impulse response $g(t)$ on the $z(t)$ does not differ from $y(t)$ shown in Fig. 5.19c. Thus, we may write

$$y(t) \approx \mathfrak{D}\{g(t), z(t)\} = \mathfrak{D}\{g(t), \mathfrak{D}\{w(t), x(t)\}\}, \quad (5.152)$$

where $\mathfrak{D}\{g(t), z(t)\}$ denotes the Duhamel integral for the impulse response $g(t)$ and excitation $z(t)$. (5.152) may be alternatively written in the frequency domain as

$$Y(j\omega) \approx G(j\omega)Z(j\omega) = G(j\omega)[W(j\omega)X(j\omega)] = [G(j\omega)W(j\omega)]X(j\omega). \quad (5.153)$$

One may rewrite (5.153) as

$$Y(j\omega) \approx G^{dq}(j\omega)X(j\omega), \quad G^{dq}(j\omega) = G(j\omega)W(j\omega), \quad (5.154)$$

where the notation $G^{dq}(j\omega)$ means the quasi-dynamic equivalent transfer function (QDETf) for $G(j\omega)$ (see Fig. 5.20b). It is identical to the initial function $G(j\omega)$ at $f < f_m$, but the resonances of $G(j\omega)$ at higher frequencies are completely eliminated. We should remark that

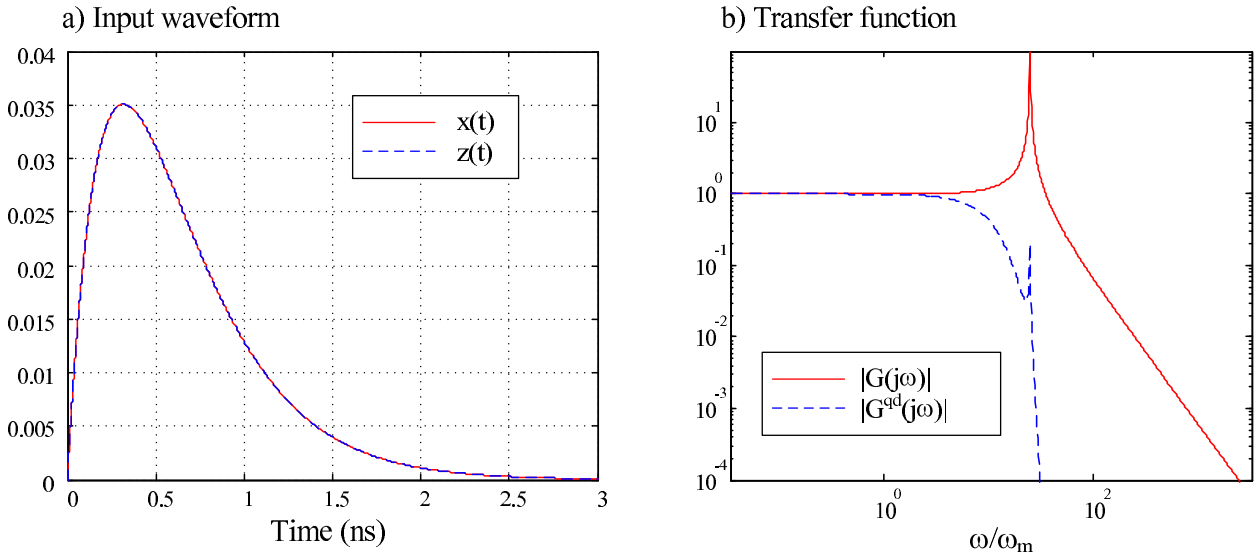


Figure 5.20: Explanation for the quasi-dynamic transfer function.

the time delay of the initial function is retained in its QDETf. Thus, the QDETf takes into account the dynamic except for the resonances, whose frequencies are much higher than f_m . The impulse response $g^{qd}(t) = \mathfrak{F}^{-1}\{G^{qd}(j\omega)\}$ does not consist of high frequency oscillations as $g(t)$. Hence, the calculation of the Duhamel integral for an excitation waveform does not lead to high-frequency oscillations in the time response. This allows one to set up a stable and dynamic solution in the frequency range limited by f_m .

The QDETf for a full-dynamic transfer function may be obtained by two approaches. The first one is shown above, we multiply the initial transfer function by a function, which is real and equal to 1.0 at $f < f_m$ and is damped at $f > f_m$. The second approach is the approximation of the initial transfer function by a suitable one that is equal to the full-dynamic transfer function at $f < f_m$ and is damped at $f > f_m$.

The quasi-dynamic modeling of the generalized partial elements

The generalized partial elements developed in § 5.4.3 have two types of the frequency response. The first type is associated with the partial elements (5.130), (5.131), (5.146), (5.147), and (5.148) derived on the basis of $G_t^A(\mathbf{r}, \mathbf{r}')$ and $K^\varphi(\mathbf{r}, \mathbf{r}')$. These frequency responses tend to a constant at low frequencies. The second type of the frequency response is associated with the partial inductances between two vias (5.125) and (5.128). At low frequencies, it tends to infinity logarithmically. In the following, the time-domain macro-models for the both types of frequency responses are developed. Moreover, the both types of the generalized partial elements have different forms of the frequency response due to the dielectric losses (see Fig. 5.11). Hence, two different quasi-dynamic time-domain models are required:

- without DC ohmic resistance, for minor losses;

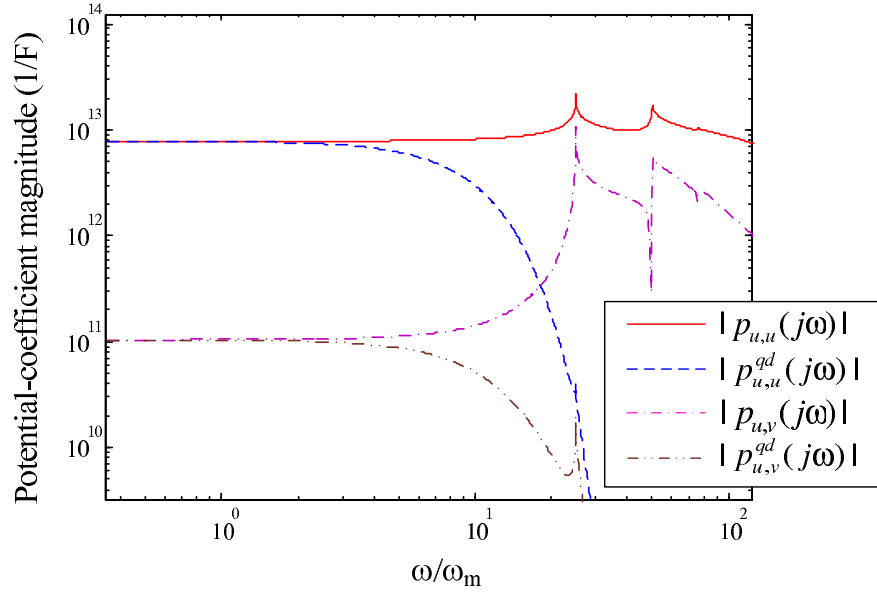


Figure 5.21: Quasi-dynamic model for the generalized partial elements of the first type.

- with DC ohmic resistance, for significant losses.

The time-domain model for weak losses may be developed using the FSCM models presented in § 4.5.5 for the free-space PEEC model, while the time-domain model for strong losses needs a completely different FSCM model. Such a model has been developed but is not yet programmed and verified. Therefore, this monograph presents only the QD-DGFLM-PEEC model for minor losses.

FSCM model for the first type of the partial elements

The quasi-dynamic model for the generalized partial elements of the first type is explained by the example of the self and mutual potential coefficients for vertical cells given by (5.130) and (5.131), respectively. The frequency response of the partial elements is calculated with the same PCB parameters as in the example in Fig. 5.17. The mutual potential coefficient $p_{u,v}(j\omega)$ is computed with $\rho_{u,v} = h$. Thus, it corresponds to the dash-dot curve in Fig. 5.17.

The QDETf approximations for the partial elements are calculated according to (5.154):

$$p_{u,u}^{qd}(j\omega) = p_{u,u}(j\omega)e^{-(\alpha\omega)^2}, \quad p_{u,v}^{qd}(j\omega) = p_{u,v}(j\omega)e^{-(\alpha\omega)^2}, \quad (5.155)$$

where α is estimated using (5.151). Fig. 5.21 shows the comparison between the full-wave and quasi-dynamic frequency responses. The quasi-dynamic functions precisely fit the full-dynamic ones at $f < f_m$ and show strong damping at higher frequencies. Obviously, the quasi-dynamic models do not differ significantly from the generalized partial elements in the free-space. They are featured by the static value, equivalent time delay, and damping at high frequencies. Therefore, the first type of the generalized partial elements may be successfully modeled by the FSCM macromodels developed in § 4.5.5 for the S-FW-PEEC model.

FSCM model for the second type of the partial elements

As it has been mentioned, the generalized partial inductances between the vertical cells tend to infinity at low frequencies. Since their behavior in the quasi-dynamic frequency range may not be described only by the time delay and the static value, we need to develop a new FSCM description. This FSCM model should be equal to the initial frequency response at $f < f_m$ and should be damped at $f > f_m$. According to the strategy of FSCM given in § 3.6, the first step of modeling is the approximation of the generalized partial elements in the frequency domain. We approximate an abstract self or mutual generalized partial inductance $\xi(j\omega) = \{L_{u,u}(j\omega), L_{u,v}(j\omega)\}$. The following function is a suitable approximation of $\xi(j\omega)$ in the quasi-dynamic frequency range:

$$\xi(j\omega) \approx \xi^{qd}(j\omega) = \xi_s^{qd}(j\omega) e^{-j\omega\tilde{\tau}}, \quad \xi_s^{qd}(j\omega) = \xi \ln \frac{j\omega + \beta}{j\omega + \alpha}. \quad (5.156)$$

The exponential term represents the time delay and may be calculated explicitly as the time delay between the centers of cells for the mutual partial inductances:

$$\tilde{\tau} = \rho_{u,v} \sqrt{\epsilon\mu_0}, \quad (5.157)$$

or as the time delay for the radius of the via for the self partial inductances:

$$\tilde{\tau} = R_u \sqrt{\epsilon\mu_0}. \quad (5.158)$$

The remaining term $\xi_s^{qd}(j\omega)$ accounts for the initial frequency response after the delay extraction $\xi_s(j\omega) = \xi(j\omega)/e^{-j\omega\tilde{\tau}}$. The parameter α has to be chosen much less than ω_m . Usually, we apply $\alpha = \omega_m 10^{-6}$. This assumption allows one to write at frequencies comparable to ω_m the following equation:

$$\Re \{ \xi_s^{qd}(j\omega) \} = \frac{\xi}{2} \ln \frac{\omega^2 + \beta^2}{\omega^2}. \quad (5.159)$$

Using (5.159) and values of $\xi(j\omega)$ calculated at two points, one may estimate the parameters β and ξ . We calculate $\xi_m = \Re \{ \xi_s(j\omega_m) \}$ and $\xi_g = \Re \{ \xi_s(j\omega_g) \}$ with $\omega_g = \omega_m/100$. The parameter β may be estimated via the numerical solution (e.g., by the Newton iterations [62]) of the algebraic equation of one variable:

$$\xi_g \ln \frac{\omega_m^2 + \beta^2}{\omega_m^2} = \xi_m \ln \frac{\omega_g^2 + \beta^2}{\omega_g^2}. \quad (5.160)$$

The use the initial point $100 \omega_m$ for the Newton iterations leads to the convergence of the numerical solution in a few iterations. The last parameter ξ is calculated as

$$\xi = 2 \xi_g \left(\ln \frac{\omega_g^2 + \beta^2}{\omega_g^2} \right)^{-1}. \quad (5.161)$$

The quality of the proposed approximation may be observed in Fig. 5.22a. The self partial inductance for the via cell u is compared with its approximation by (5.156). The parameters

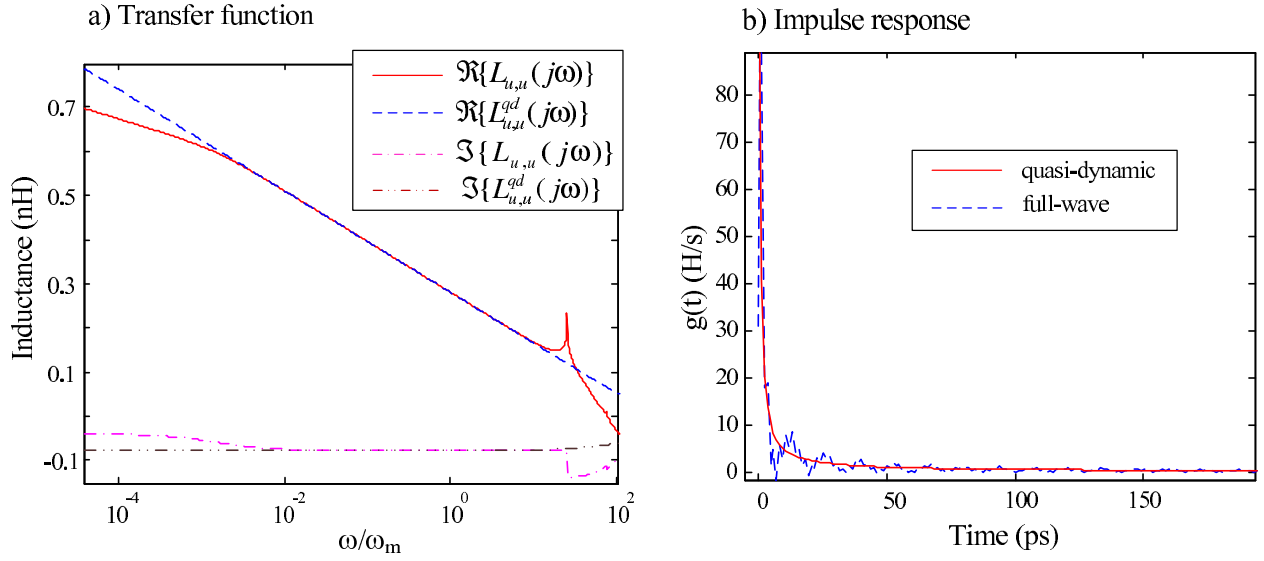


Figure 5.22: Quasi-dynamic FSCM model for the generalized partial inductance between the vertical cells.

of the stripline region and via used for the computation are $h = 1$ mm, $\sigma_s = 1$ mS/m, $\epsilon_r = 4.0$, $z_{u,s} = 0$, $z_{u,e} = h/2$, and $R_u = 0.1$ mm. One may observe that the function $\xi^{qd}(j\omega)$ with parameters estimated according to (5.157), (5.160), and (5.161) is a perfect approximation for $L_{u,u}(j\omega)$ for $0.001 \omega_m < \omega < 10 \omega_m$. However, this function does not have the resonances of $L_{u,u}(j\omega)$ at high frequencies.

The next matter should be considered is the deviation between $L_{u,u}(j\omega)$ and $\xi^{qd}(j\omega)$ at low frequencies. Since the inductive coupling is proportional to the frequency, the importance of the approximation accuracy increases towards the frequency, while the minor deviations at low frequencies do not influence the transients. This may be well observed in Fig. 5.22b, where the impulse response related to the initial and quasi-dynamic frequency responses is calculated. The impulse response for $L_{u,u}(j\omega)$ is calculated numerically using the IFFT transformation, while the impulse and step responses for $\xi^{qd}(j\omega)$ are derived in closed form (without the time delay, which may be added later, see (5.163)):

$$\begin{aligned}
 g(t) &= \xi \frac{e^{-\alpha t} - e^{-\beta t}}{t} h(t), \\
 s(t) &= \xi \left(\ln \frac{\beta}{\alpha} + \text{Ei}_1(\beta t) - \text{Ei}_1(\alpha t) \right) h(t),
 \end{aligned} \tag{5.162}$$

where $\text{Ei}_1(x)$ are the exponential integrals (see [2]). Obviously, the only difference between the both impulse responses is the absence of the high frequency oscillations on the quasi-dynamic one. Thus, (5.156) may be accepted as a fair quasi-dynamic approximation.

In view that $s(0) = 0$, the time response of the generalized partial inductance $y(t)$ on an

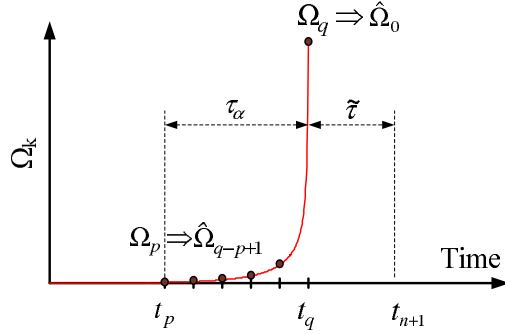


Figure 5.23: Moving average for the FSCM of the quasi-dynamic model (5.156).

arbitrary excitation $x(t)$ may be calculated using the Duhamel integral (3.19):

$$y(t) = \int_0^t g(t - \vartheta) x(\vartheta - \tilde{\tau}) d\vartheta. \quad (5.163)$$

Using the approach already explained in § 4.4.3 and § 4.5.5, we derive the moving-average discrete formulation for the integral (5.163) at the time point $t = t_{n+1}$:

$$y_{n+1} = \sum_{k=p}^q \Omega_k x_k. \quad (5.164)$$

The coefficients of the formula (5.164) may be computed before the numerical integration of the PEEC model:

$$\Omega_k = \frac{\xi}{2} \begin{cases} \begin{aligned} & \text{Ei}_1(\beta T_{n+1,k}) - \text{Ei}_1(\alpha T_{n+1,k}) \\ & - \text{Ei}_1(\beta T_{n,k}) + \text{Ei}_1(\alpha T_{n,k}) \end{aligned}, & k = p, \\ \begin{aligned} & \text{Ei}_1(\beta T_{n,k}) - \text{Ei}_1(\alpha T_{n,k}) \\ & - \text{Ei}_1(\beta T_{n-1,k}) + \text{Ei}_1(\alpha T_{n-1,k}) \end{aligned}, & k = q, \\ \begin{aligned} & \text{Ei}_1(\beta T_{n+1,k}) - \text{Ei}_1(\alpha T_{n+1,k}) \\ & - \text{Ei}_1(\beta T_{n-1,k}) + \text{Ei}_1(\alpha T_{n-1,k}) \end{aligned}, & \text{else,} \end{cases} \quad (5.165)$$

where

$$T_{n,k} = \tilde{\tau} - t_n + t_k.$$

The impulse response is a selective function $g(t)$, whose qualitative shape is shown in Fig. 5.23. Thus, we have to calculate only a few summands in the moving average (5.164), namely, the time points from t_p until t_q . The index of the time point q is defined on the basis of the time delay $\tilde{\tau}$ as

$$q = n - \left\lfloor \frac{\tilde{\tau}}{\Delta t} \right\rfloor. \quad (5.166)$$

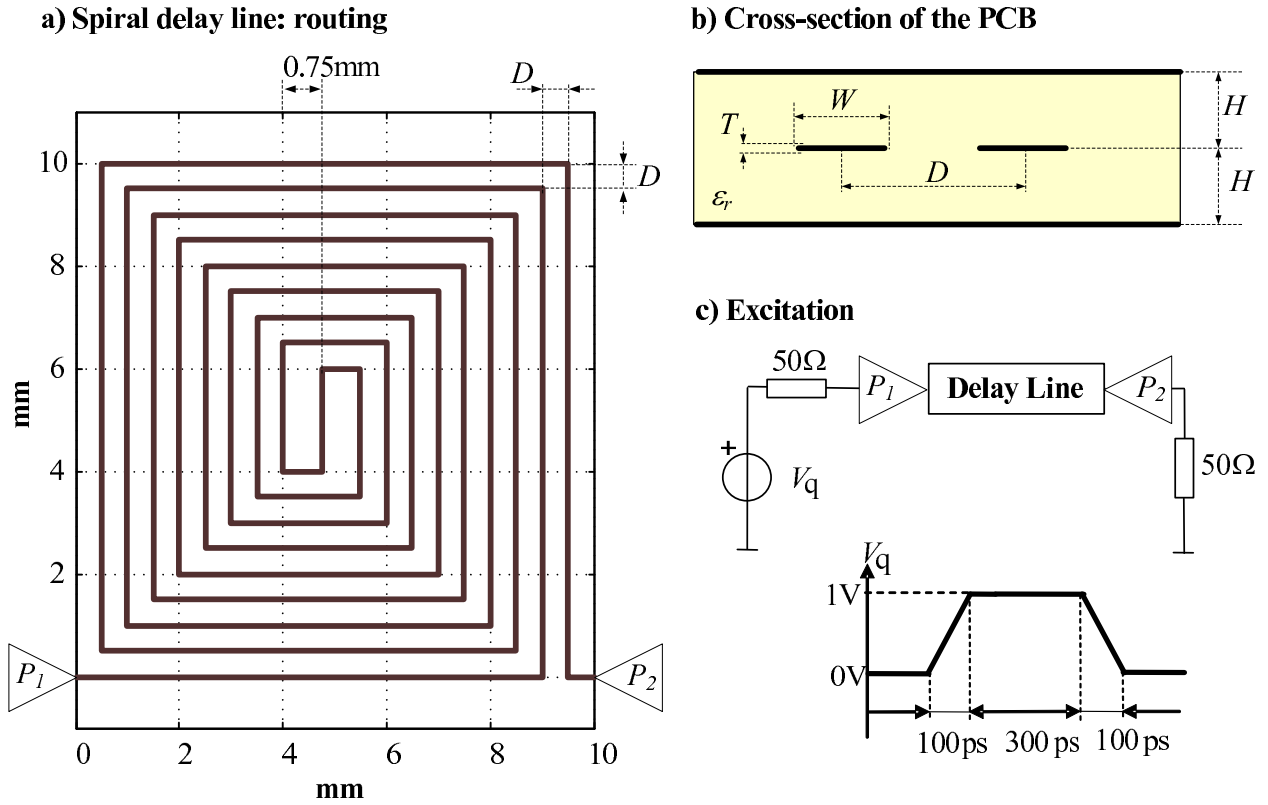


Figure 5.24: Spiral delay line and the excitation.

The index p depends on the width of the moving average denoted by τ_α (see Fig. 5.23). Since the coefficients Ω_k may be calculated consequently from q until p , the index p may be computed from the heuristic condition:

$$\Omega_p < \delta_{err} \sum_{k=p+1}^q \Omega_k, \quad (5.167)$$

where δ_{err} is the relative error.

Because the moving average formulation (5.164) has only quantitative differences with (4.107), we may apply to (5.164) all ADC models for the self and mutual partial inductances based on (4.107) that are developed in § 4.5.5.

Simulation example: Spiral Delay Line

In the following, we consider the spiral stripline configuration, which is originated from the benchmark catalog for the EMC analysis [1], [137]. The routing of this structure serving as a delay line is shown in Fig. 5.24a. This example has been computed by a commercial MoM code using the dyadic Green's functions for layered media. This code operates in the frequency domain, while the time-domain results have been calculated via the consequent IFFT transformation. Thus, the proposed example is an ideal possibility for the validation

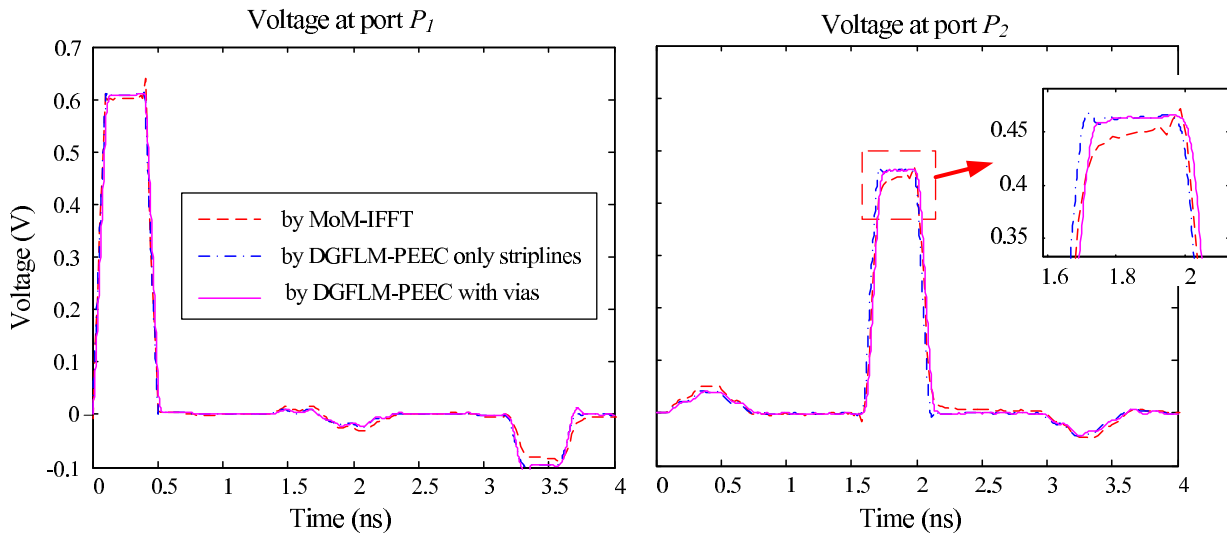


Figure 5.25: Voltage at ports P_1 and P_2 calculated by PEEC and MoM.

of the novel QD-DGFLM-PEEC model, since it uses exactly the same mathematical model (i.e., MPIE with DGFLM). The both solutions differ in the specific realization and in the solution domain, since the QD-DGFLM-PEEC model acts directly in the time domain, while MoM operates in the frequency domain.

The spiral delay line is routed in the dielectric substrate with the thickness of $2H = 0.8$ mm and relative permittivity of $\epsilon_r = 6$. The substrate is located between two parallel metallic planes assumed infinitely extended and perfectly conducting. The width of the copper traces is $W = 0.1$ mm, the thickness is $T = 10$ μm , and the conductivity is $\sigma = 5.8 \cdot 10^7$ S/m. The distance between the parallel traces is $D = 0.5$ mm. The cross-section of the PCB is shown in Fig. 5.24b.

The ends of the delay line are considered as ports P_1 and P_2 . The port P_1 is excited by a lumped voltage source V_q with the internal impedance 50 Ω and the trapezoidal waveform shown in Fig. 5.24c. The rise and fall times are 100 ps, the roof time is 300 ps. The roof voltage is 1 V. The port P_2 is loaded by a 50 Ω resistance (see Fig. 5.24c).

The discretization of the stripline for the computation by the PEEC and MoM models is related to the maximum frequency of interest supposed 10 GHz. The MoM code uses 400 unknowns, while the DGFLM-PEEC model is comprised by 343 current and 380 potential cells (excluding vias). Thus, both numerical models are consistent to each other. The delay line has been modeled by two variants of the PEEC model. The first one represents only the stripline without vias. The second one is the complete model of the structure: traces and two vias. The comparison of the computed voltages at the ports in Fig. 5.25 shows only minor deviations between the PEEC models. The complete PEEC model with vias shows less deviations from the reference than the model with only traces. The most important features of the delay line (the delay time and the wave impedance) are quite similar. Minor deviations in the dynamical behavior of the results may be explained by using different numerical algorithms for the computation of the generalized partial elements in the PEEC

model and for the computation of the matrix elements in the MoM code. The choice of the different basis and weighting functions in the PEEC and MoM codes may also produce some minor deviations in the results.

5.5 Description of crosstalk using the DGFLM-PEEC method

This section puts forward a novel circuit-based description of the crosstalk mechanism, which issues from the general formulation of the DGFLM-PEEC method developed in § 5.4.2. In general, crosstalk, which is the unintended coupling of energy between the parts of the product, is an important aspect in the design of the electromagnetically compatible devices. In particular for PCB boards, this interaction appears between traces, vias, connectors, packages, cables, and connecting wires. Crosstalk causes the signal-integrity as well as the EMC problems. The typical crosstalk influence on the signal integrity is the change of the effective parameters of printed transmission lines, namely, the wave impedances may be changed for striplines, while the wave impedances and propagation velocity may be changed for microstrips. Hence, the intended waveforms may be noticeably distorted [58]. The EMC problems issued from crosstalk are even more important. The crosstalk between interconnections in PCB boards causes the intrasystem interferences that may produce the functionality problems for logical devices and lead to failing the radiated emission regulatory requirements. Permanent increasing the pulse rates of the digital devices makes the mentioned problems more actual in future.

In the typical practice, crosstalk in PCB boards is described using the transmission-line theory [121]. This description represents all traces as the coupled multiconductor transmission lines featured by the per-unit-length inductances, capacitances, and resistances of traces. Thus, crosstalk is expressed quantitatively and qualitatively in terms of the per-unit-length mutual inductances and partial capacitances. The transmission-line models of crosstalk may be included in a circuit simulator using one of the well developed methods for the simulation of the multiconductor transmission lines. Of course, this description of crosstalk has disadvantages concerning the limitations of the TL models. The conventional transmission-line theory does not account for the two-dimensional current distribution, vertical interconnections, radiation. Usually, the full-wave methods are applied if these phenomena are decisive. However, they provide only the simulations, i.e., the quantitative results in contrast to the TL models that are a qualitative description of crosstalk.

The DGFLM-PEEC is a general propose full-wave method, which may simulate crosstalk in an arbitrary interconnection structure and give the quantitative results as other full-wave methods. However, the PEEC expresses the electromagnetic couplings in terms of the partial inductances and potential coefficients. This allows one to expand the traditional circuit description of crosstalk on some particular interconnections that may not be considered using the transmission-line theory. This monograph presents a lumped circuit model for crosstalk between two vias between in the stripline region.

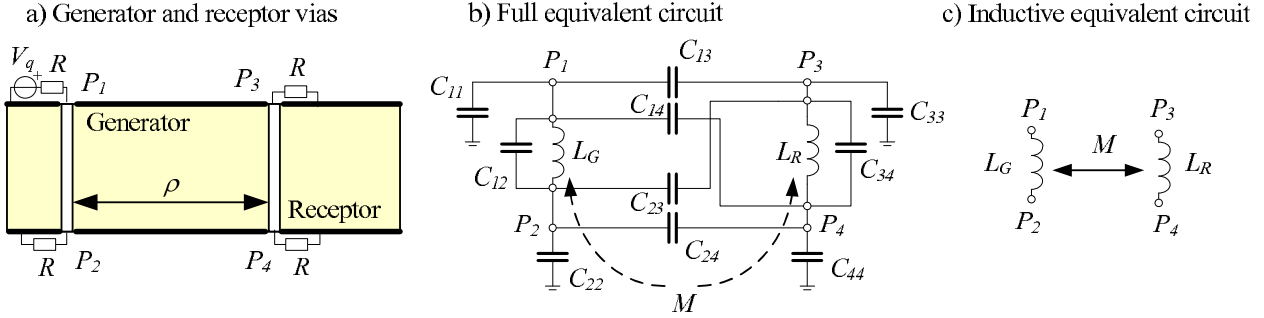


Figure 5.26: Crosstalk between two vias: geometry (a), and equivalent circuits (b,c).

5.5.1 Crosstalk between vias

We consider two vias analogous to the coupled transmission lines in the conventional crosstalk theory as shown in Fig. 5.26a. Two vias are located at the distance ρ between their axes. The first via is excited by the voltage source and is denoted by "generator" as for crosstalk between the transmission lines (see [121]), the second via is passive and is denoted by "receptor". Since the substrate thickness is electrically small, the DGFLM-PEEC model for these two vias may be set up only by one current cell for each of the vias. The DGFLM-PEEC model with two current cells and four potential cells results in the four-port equivalent circuit for the coupled vias expressed in terms of the generalized partial inductances and potential coefficients. The (2×2) -matrix with the generalized partial inductances denoted by \mathbb{L} is computed using (5.125) and (5.128), while the (4×4) -matrix with the generalized potential coefficients denoted by \mathbb{P} is computed using (5.130) and (5.131). The frequency dependent partial capacitances $C_{\alpha,i}(j\omega)$ may be calculated on the basis of \mathbb{P} as follows:

$$C_{\alpha,i}(j\omega) = \begin{cases} \sum_{j=1}^4 c_{\alpha,j}(j\omega), & \alpha = i \\ -c_{\alpha,i}(j\omega), & \alpha \neq i \end{cases} \quad \text{with } \mathbb{P}^{-1} = \{c_{\alpha,j}\}, \quad \alpha, j = \overline{1,4}. \quad (5.168)$$

A low-frequency circuit model for crosstalk may be derived using the constant partial elements calculated from the generalized ones at $\omega \ll \omega_r$:

$$\begin{aligned} L_G &= \Re \{L_{1,1}(j\omega)\}, & L_R &= \Re \{L_{2,2}(j\omega)\}, & M &= \Re \{L_{1,2}(j\omega)\}, \\ C_{\alpha,i} &= \Re \{C_{\alpha,i}(j\omega)\}, & \alpha, j &= \overline{1,4}. \end{aligned} \quad (5.169)$$

This equivalent circuit is set up using the concept of the QS-DGFLM-PEEC method (see § 5.4.4) and is shown in Fig. 5.26b. The presented equivalent circuit is completely analogous to the equivalent circuit developed for crosstalk in terms of multiconductor transmission lines, the only difference is that the per-unit-length inductances and capacitances are replaced by partial ones. The dependence of the equivalent-circuit parameters on the distance between the vias calculated at $f=100$ MHz is shown in Fig. 5.27. Since the parameters are derived in closed form, this dependence is expressed qualitatively. The partial capacitances decrease exponentially towards the increase of ρ . Hence, the crosstalk caused by the capacitive coupling becomes insignificant if the distance between the vias grows. Another dependence is

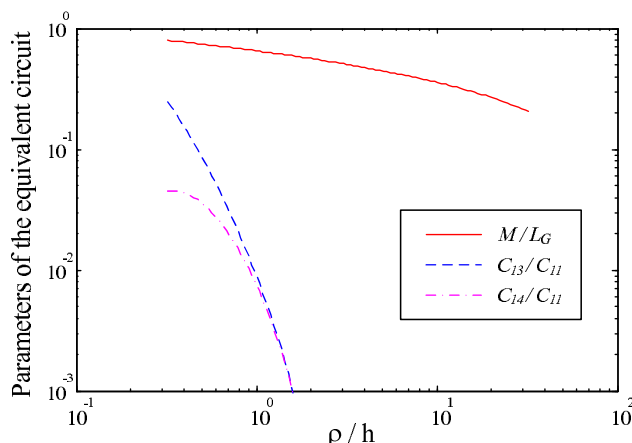


Figure 5.27: The dependence of the equivalent-circuit parameters on ρ at $f=100$ MHz.

shown by the mutual inductance M , which decreases logarithmically. Thus, the crosstalk caused by the inductive coupling between vias may be not negligible at relatively large distances between the vias. Since the inductive coupling dominates at large distances between vias (see Fig. 5.27), one may propose a simplified inductive model for the crosstalk between vias. It is shown in Fig. 5.26c, where all partial capacitances are neglected, while vias are represented only by the partial inductances.

It is known from literature, e.g., it is mentioned in [58] that crosstalk for traces in PCB boards decreases exponentially. Now, it may be stated that the crosstalk between the vias located between two ground or power planes caused by the inductive coupling decreases much slower, namely, logarithmically. Although the inductive coupling between vias decreases slower than the couplings between traces, their contribution in the total crosstalk can be insignificant, since vias are much shorter than traces, and the inductive coupling is proportional to the length of the interconnections.

In general, the proposed model of the crosstalk between vias expands the conventional one developed only for traces. The rough models for vias presented in literature, e.g., (5.127) (see [58]), provide much less accurate description than the generalized partial elements developed in this monograph.

5.5.2 Calculation of the wave impedance for striplines using the QS-DGFLM-PEEC method

This section shows another interesting consequence from the QS-DGFLM-PEEC method. The static values of the generalized partial elements developed in § 5.4.3 may be used for the approximated calculation of the per-unit-length parameters of striplines. Since the static mutual partial inductances and potential coefficients for traces decrease exponentially, the self partial elements dominate over the mutual ones. Hence, the per-unit-length inductance and capacitance of a stripline may be approximately computed through the corresponding

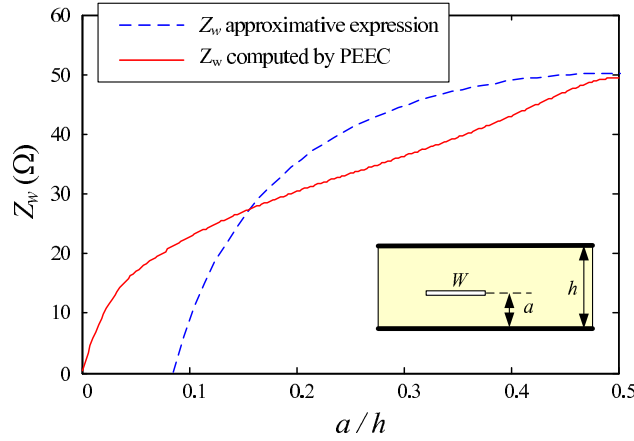


Figure 5.28: Wave impedance for an asymmetric stripline.

partial elements. A set of N coupled parallel striplines is considered. One may choose electrically small cells denoted by the numbers m in all striplines, these cells have to be located in the same cross-section of this multiconductor transmission line. The self and partial inductances and potential coefficients are calculated and saved in $(N \times N)$ -matrices $\mathbb{L} = \{L_{\alpha,m}\}$ and $\mathbb{P} = \{p_{\alpha,m}\}$, respectively. The matrix with the partial capacitances $\mathbb{C} = \{C_{\alpha,m}\}$ is calculated from the potential coefficients using (4.53). The self and mutual per-unit-length inductances and partial capacitances are calculated on the basis of the partial elements as follows:

$$L'_{\alpha,m} = L_{\alpha,m}/l_{\alpha}, \quad C'_{\alpha,m} = C_{\alpha,m}/l_{\alpha}, \quad (5.170)$$

where l_{α} is the length of the cell. Since the partial elements are calculated for an arbitrary arrangement of striplines, this approach allows one to calculate the per-unit-length parameters for an arbitrary structure of the MTL.

The validation example for the TL parameters calculated through the partial elements is shown in Fig. 5.28. It presents the dependence of the single-stripline wave impedance Z_w on the distance between the stripline and the ground plane denoted by a , which changes between 0 and $h/2$, where h is the distance between the ground planes. The thickness of the stripline is assumed to be zero. The wave impedance of the symmetric stripline (triplate) is computed by the known expression [58]:

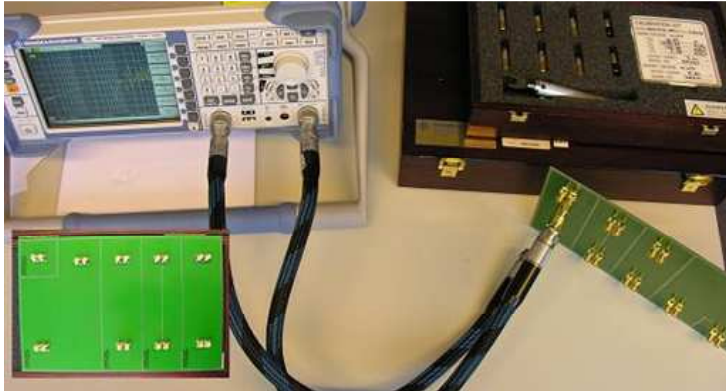
$$Z_w^{sym}(h) = \frac{60}{\sqrt{\epsilon_r}} \ln \frac{4h}{0.536\pi W} \quad (\Omega), \quad (5.171)$$

where W is the width of the stripline, and ϵ_r is the relative permittivity. If $a < h/2$, the wave impedance may not be calculated precisely in closed form, but [58] provides a rough approximation based on (5.171):

$$Z_w = 2 \frac{Z_w^{sym}(2a) Z_w^{sym}(h-a)}{Z_w^{sym}(2a) + Z_w^{sym}(h-a)}. \quad (5.172)$$

The values of the wave impedance Z_w calculated by (5.172) and through the partial elements

a) Measurements of the crosstalk



b) Cross-section of the PCB board

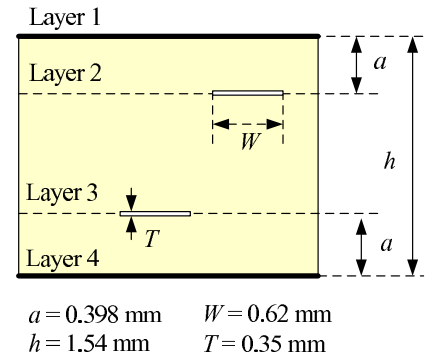


Figure 5.29: Measurements of crosstalk using the network analyzer.

by

$$Z_w \approx \sqrt{\frac{L_{\alpha,m}}{C_{\alpha,m}}} \quad (5.173)$$

are compared in Fig. 5.28. One may observe that the both results are very similar at $a = h/2$, where (5.171) produces an exact solution. Thus, one may resume that the wave impedance is calculated correctly through partial elements in the symmetric case. In contrast, the results differ significantly for $a < h/2$. The approximated expression (5.172) is very rough, e.g., it yields the negative wave impedance for $a < h/10$, which is unphysical, while the wave impedance calculated through the partial elements looks physically. Since the decrease of a leads to the increase of the capacitance and diminishing the inductance, Z_w falls from the maximum at $a = h/2$ to zero at $a = 0$. This last case with $Z_w = 0$ may exist only mathematically because the trace will be connected to the ground. Generally, one may resume that the calculation of the per-unit-length parameters for striplines through the partial elements shows precise results for arbitrary geometries.

5.5.3 Simulation example: crosstalk in a four-layer PCB board

In the following, a validation example for the DGFLM-PEEC model is presented. It shows the ability of the DGFLM-PEEC method for the simulation of the crosstalk in PCB boards. The complete frequency-domain DGFLM-PEEC is applied to the simulation of a four-layer PCB board. The computation results are verified by measurements.

The shown in Fig. 5.29a simplified PCB has been developed in order to validate the DGFLM-PEEC model by measurements. This PCB consists of five pairs of the coupled striplines with the different geometry, whose ends are terminated by SMA-connectors. Thus, the S-parameters for the generator and acceptor ports may be measured using a Network analyzer. The PCB, whose cross-section is shown in Fig. 5.29b, has four layers. The outside layers are used as ground planes, the two inside layers are used for the signal traces. The traces have a thickness $T = 35 \mu\text{m}$ and the width $W = 0.62 \text{ mm}$. The transversal distance

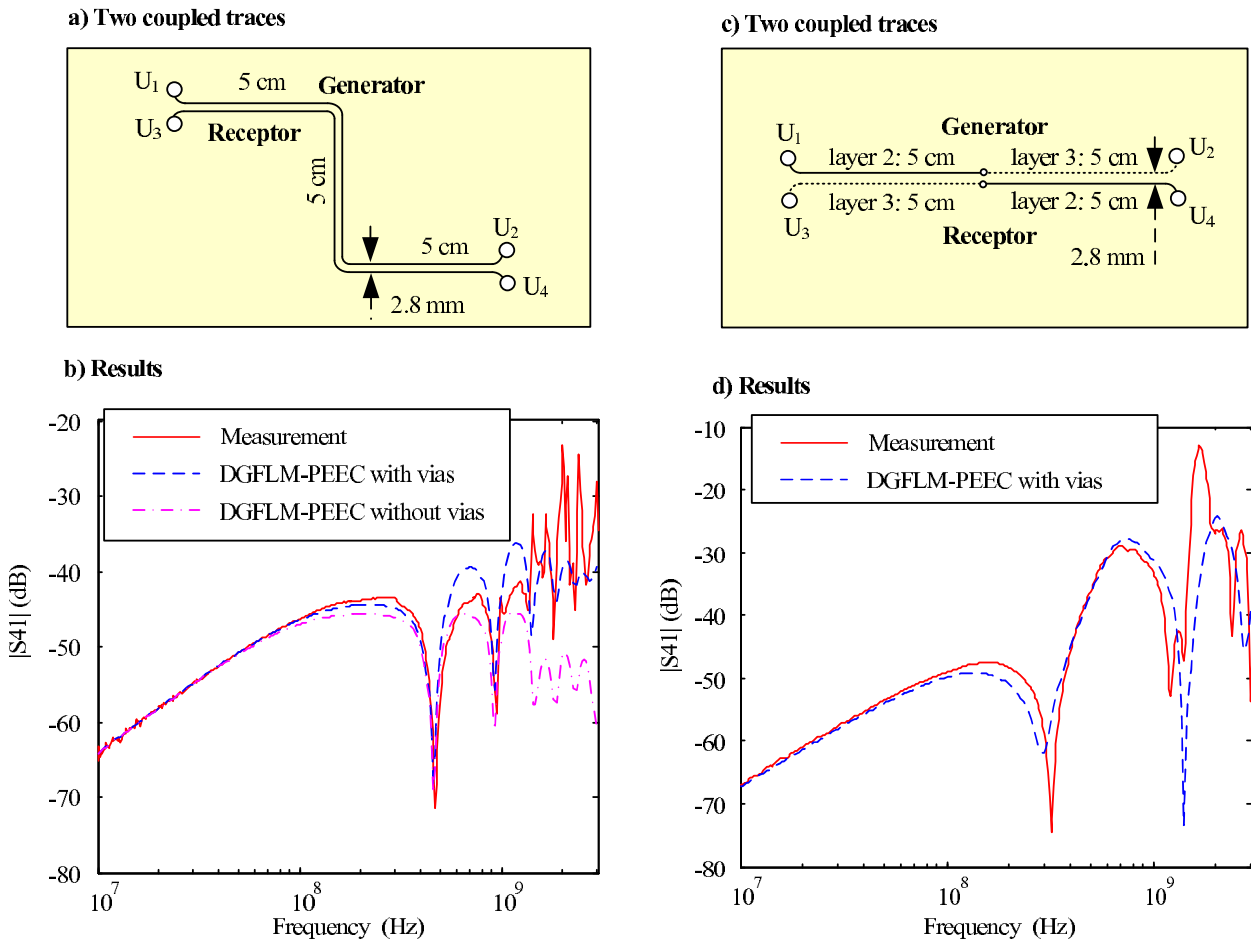


Figure 5.30: Comparison between the measurement and simulation results.

between the axes of two traces in a pair is about 2.8 mm. The copper traces have the conductivity of 58 MS/m. According to the data sheet, the relative permittivity of the substrate can be between 4 and 5.4. The typical values 4.5 has been used for the simulations.

Two coupled pairs of striplines are used in this monograph. The first one is shown in Fig. 5.30a, its total length is 15 cm, the direction of traces turns on 90° after each 5 cm of the length. The second one is shown in Fig. 5.30c. It is a straight line with a total length 10 cm, however, the generator and acceptor striplines belong to different layers. For the first 5 cm of the length, the generator line is located on the layer 2, while the receptor line on the layer 3. Both traces change the layer with the help of a via at the middle point and belong to the opposite layers for the remained length from 5 cm until 10 cm.

Fig. 5.30b shows the simulation and measurement results for $|S_{41}|$, i.e., the transfer function between the generator and far-end receptor ports. Obviously, good agreement between the measurement and the simulation is shown at $f < 450$ MHz. The influence of vias on the results has been investigated through an additional numerical experiment. The PCB is modeled by the two DGFLM-PEEC models, the first one simulates the vias, the second one connects the generator and the load directly to the striplines. The comparison of the results

in Fig. 5.30b shows that the deviation of $|S_{41}|$ calculated by the PEEC model without vias from the result of the measurement increases with the frequency, while $|S_{41}|$ computed by the complete PEEC model reproduces the measured curve more exact. At $f > 1$ GHz, the crosstalk calculated without vias is about 20 dB less than the result computed with vias. Thus, we can resume that the vias make a remarkable contribution in the crosstalk at high frequencies.

Fig. 5.30d shows the measured and simulated frequency responses of $|S_{41}|$ for two coupled striplines on different layers. As in the previous example, the DGFLM-PEEC model gives good results up to about 1 GHz. The cause for the deviation between the measurement and the simulation is the not exact information about the substrate parameters (especially $\epsilon_r(\omega)$) and the parasitic influences of connectors, which is not considered in the DGFLM-PEEC model.

Appendix A

Mathematical fundamentals

A.1 Vector identities

$$\mathbf{a} \cdot (\mathbf{b} \times \mathbf{c}) = \mathbf{b} \cdot (\mathbf{c} \times \mathbf{a}) = \mathbf{c} \cdot (\mathbf{a} \times \mathbf{b}) \quad (\text{A.1})$$

$$\mathbf{a} \times (\mathbf{b} \times \mathbf{c}) = (\mathbf{a} \cdot \mathbf{c})\mathbf{b} - (\mathbf{a} \cdot \mathbf{b})\mathbf{c} \quad (\text{A.2})$$

$$-\hat{\mathbf{z}} \times \hat{\mathbf{z}} \times \mathbf{a} = -\mathbf{a} \times \hat{\mathbf{z}} \times \hat{\mathbf{z}} = \mathbf{a} - (\mathbf{a} \cdot \hat{\mathbf{z}})\hat{\mathbf{z}} \quad (\text{A.3})$$

$$\nabla \cdot (\varphi \mathbf{a}) = (\nabla \varphi) \cdot \mathbf{a} + \varphi (\nabla \cdot \mathbf{a}) \quad (\text{A.4})$$

$$\nabla \cdot (\nabla \times \mathbf{a}) = 0 \quad (\text{A.5})$$

$$\nabla \times (\nabla \varphi) = 0 \quad (\text{A.6})$$

$$\nabla \times (\nabla \times \mathbf{a}) = \nabla(\nabla \cdot \mathbf{a}) - \nabla^2 \mathbf{a} \quad (\text{A.7})$$

$$\nabla \cdot (\mathbf{a} \times \mathbf{b}) = \mathbf{b} \cdot (\nabla \times \mathbf{a}) - \mathbf{a} \cdot (\nabla \times \mathbf{b}) \quad (\text{A.8})$$

A.2 Dyadic identities

$$\mathbf{a} \cdot \mathbf{bc} = (\mathbf{a} \cdot \mathbf{b}) \mathbf{c}, \quad \mathbf{ab} \cdot \mathbf{c} = \mathbf{a} (\mathbf{b} \cdot \mathbf{c}) \quad (\text{A.9})$$

$$\mathbf{a} \times \mathbf{bc} = (\mathbf{a} \times \mathbf{b}) \mathbf{c}, \quad \mathbf{ab} \times \mathbf{c} = \mathbf{a} (\mathbf{b} \times \mathbf{c}) \quad (\text{A.10})$$

$$\mathbf{a} \cdot \overline{\overline{\mathbf{B}}} \cdot \mathbf{c} = \mathbf{a} \cdot (\overline{\overline{\mathbf{B}}} \cdot \mathbf{c}) = (\mathbf{a} \cdot \overline{\overline{\mathbf{B}}}) \cdot \mathbf{c} \quad (\text{A.11})$$

$$\mathbf{a} \times \overline{\overline{\mathbf{B}}} \times \mathbf{c} = \mathbf{a} \times (\overline{\overline{\mathbf{B}}} \times \mathbf{c}) = (\mathbf{a} \times \overline{\overline{\mathbf{B}}}) \times \mathbf{c} \quad (\text{A.12})$$

The identity dyadic in Cartesian coordinates:

$$\overline{\overline{\mathbf{I}}} = \hat{x}\hat{x} + \hat{y}\hat{y} + \hat{z}\hat{z} \quad (\text{A.13})$$

$$\mathbf{a} = \overline{\overline{\mathbf{I}}} \cdot \mathbf{a} = \mathbf{a} \cdot \overline{\overline{\mathbf{I}}} \quad (\text{A.14})$$

A.3 Integral theorems

Gauss or volume divergence theorem

The integral over the volume V of the divergence of a vector function is equal to the surface integral of the outward normal component of this function over the closed surface $S = \partial V$ surrounding V .

$$\iiint_V \nabla \cdot \mathbf{A} \, dV = \oint_{S=\partial V} \mathbf{A} \cdot d\mathbf{S} \quad (\text{A.15})$$

Volume gradient theorem

The integral over the volume V of the gradient of a scalar function is equal to the surface integral of the outward normal vector multiplied by this function over the closed surface $S = \partial V$ surrounding V .

$$\iiint_V \nabla \phi \, dV = \oint_{S=\partial V} \phi \, d\mathbf{S} \quad (\text{A.16})$$

Stokes theorem

The integral of the curl of a vector function over the surface S is equal to the line integral around the close contour $C = \partial S$, which bounds the surface S .

$$\iint_S (\nabla \times \mathbf{A}) \cdot d\mathbf{S} = \oint_{C=\partial S} \mathbf{A} \cdot d\mathbf{S} \quad (\text{A.17})$$

The first Green's theorem

$$\iiint_V (\nabla \phi \cdot \nabla \varphi + \varphi \nabla^2 \phi) \, dV = \oint_{S=\partial V} \varphi \nabla \phi \cdot d\mathbf{S} \quad (\text{A.18})$$

The second Green's theorem

$$\iiint_V (\phi \nabla^2 \varphi - \varphi \nabla^2 \phi) \, dV = \oint_{S=\partial V} (\phi \nabla \varphi - \varphi \nabla \phi) \cdot d\mathbf{S} \quad (\text{A.19})$$

A.4 Integral transformations

One-dimensional Fourier transformation

Direct Fourier transformation (FT):

$$F(j\omega) = \mathfrak{F}\{f(t)\} = \int_{-\infty}^{+\infty} f(t)e^{-j\omega t} dt. \quad (\text{A.20})$$

Inverse Fourier transformation (IFT):

$$f(t) = \mathfrak{F}^{-1}\{F(j\omega)\} = \frac{1}{2\pi} \int_{-\infty}^{+\infty} F(j\omega)e^{j\omega t} d\omega. \quad (\text{A.21})$$

Two-dimensional spatial Fourier transformation

Direct two-dimensional spatial Fourier transformation:

$$\tilde{g}(z, z', \mathbf{k}_\rho) = \mathfrak{F}_s\{g(\mathbf{r}, \mathbf{r}')\} = \int_{-\infty}^{+\infty} \int_{-\infty}^{+\infty} g(\mathbf{r}, \mathbf{r}') e^{j\mathbf{k}_\rho \cdot \boldsymbol{\rho}} dx dy, \quad (\text{A.22})$$

Inverse two-dimensional spatial Fourier transformation:

$$g(\mathbf{r}, \mathbf{r}') = \mathfrak{F}_s^{-1}\{\tilde{g}(z, z', \mathbf{k}_\rho)\} = \frac{1}{4\pi^2} \int_{-\infty}^{+\infty} \int_{-\infty}^{+\infty} \tilde{g}(z, z', \mathbf{k}_\rho) e^{-j\mathbf{k}_\rho \cdot \boldsymbol{\rho}} dk_x dk_y, \quad (\text{A.23})$$

with

$$\begin{aligned} \mathbf{r} - \mathbf{r}' &= (z - z')\hat{\mathbf{z}} + \boldsymbol{\rho}, & \boldsymbol{\rho} &= (x - x')\hat{\mathbf{x}} + (y - y')\hat{\mathbf{y}}, \\ \mathbf{k}_\rho &= k_x\hat{\mathbf{x}} + k_y\hat{\mathbf{y}}, & \zeta &= \arctan \frac{y - y'}{x - x'}. \end{aligned}$$

The differential operators with respect to \mathbf{r} are mapped into the spectrum domain as products with the spectrum-domain operator $\tilde{\nabla}$:

$$\begin{aligned} \mathfrak{F}_s\{\nabla \cdot \mathbf{A}(\mathbf{r})\} &= \tilde{\nabla} \cdot \tilde{\mathbf{A}}(z, \mathbf{k}_\rho), \\ \mathfrak{F}_s\{\nabla \times \mathbf{A}(\mathbf{r})\} &= \tilde{\nabla} \times \tilde{\mathbf{A}}(z, \mathbf{k}_\rho), \\ \mathfrak{F}_s\{\nabla \phi(\mathbf{r})\} &= \tilde{\nabla} \tilde{\phi}(z, \mathbf{k}_\rho), \end{aligned} \quad (\text{A.24})$$

$$\text{where } \tilde{\nabla} = \left(\frac{\partial}{\partial z} \hat{\mathbf{z}} - j\mathbf{k}_\rho \right), \quad \nabla = \frac{\partial}{\partial x} \hat{\mathbf{x}} + \frac{\partial}{\partial y} \hat{\mathbf{y}} + \frac{\partial}{\partial z} \hat{\mathbf{z}}.$$

The differential operators with respect to \mathbf{r}' are mapped into the spectrum domain as products with the spectrum-domain operator $\tilde{\nabla}'$:

$$\begin{aligned}\mathfrak{F}_s\{\nabla' \cdot \mathbf{A}(\mathbf{r}, \mathbf{r}')\} &= \tilde{\nabla}' \cdot \tilde{\mathbf{A}}(z, z', \mathbf{k}_\rho), \\ \mathfrak{F}_s\{\nabla' \times \mathbf{A}(\mathbf{r}, \mathbf{r}')\} &= \tilde{\nabla}' \times \tilde{\mathbf{A}}(z, z', \mathbf{k}_\rho), \\ \mathfrak{F}_s\{\nabla' \phi(\mathbf{r}, \mathbf{r}')\} &= \tilde{\nabla}' \tilde{\phi}(z, z', \mathbf{k}_\rho),\end{aligned}\tag{A.25}$$

where $\tilde{\nabla}' = \left(\frac{\partial}{\partial z'} \hat{\mathbf{z}} + j\mathbf{k}_\rho \right)$, $\nabla' = \frac{\partial}{\partial x'} \hat{\mathbf{x}} + \frac{\partial}{\partial y'} \hat{\mathbf{y}} + \frac{\partial}{\partial z'} \hat{\mathbf{z}}$.

Because of the symmetry, the inverse Fourier transformations (A.23) may be alternatively expressed in terms of the Sommerfeld integrals, which are introduced in [142] as follows:

$$\begin{aligned}\mathfrak{F}_s^{-1}\{\tilde{g}(z, z', \mathbf{k}_\rho)\} &= S_0 \{ \tilde{g}(z, z', \mathbf{k}_\rho) \}, \\ \mathfrak{F}_s^{-1}\{jk_x \tilde{g}(z, z', \mathbf{k}_\rho)\} &= \cos \zeta S_1 \{ \tilde{g}(z, z', \mathbf{k}_\rho) \}, \\ \mathfrak{F}_s^{-1}\{jk_y \tilde{g}(z, z', \mathbf{k}_\rho)\} &= \sin \zeta S_1 \{ \tilde{g}(z, z', \mathbf{k}_\rho) \},\end{aligned}\tag{A.26}$$

where the Sommerfeld integral of the n-th order is defined as:

$$S_n \{ \tilde{g}(z, z', \mathbf{k}_\rho) \} = \frac{1}{4\pi} \int_{-\infty}^{+\infty} \tilde{g}(z, z', \mathbf{k}_\rho) k_\rho^{n+1} H_n^{(2)}(k_\rho \rho) dk_\rho.\tag{A.27}$$

Appendix B

Calculation of the internal longitudinal impedance of wires

Wire with a round cross-section according to [147]:

$$Z'(j\omega) = \frac{\sqrt{-j\omega\mu\sigma}}{2\pi R\sigma} \cdot \frac{J_0(R\sqrt{-j\omega\mu\sigma})}{J_1(R\sqrt{-j\omega\mu\sigma})} \Omega/\text{m}, \quad (\text{B.1})$$

where σ is the conductivity, R is the radius, $J_0()$, and $J_1()$ are the Bessel functions of the first kind.

Wire with a rectangular cross-section according to [50]:

$$Z'(j\omega) = \frac{R'_0}{2} \left\{ \sum_{k=1}^{\infty} \frac{\tanh \sqrt{\zeta_k(a/b)}}{\sqrt{\zeta_k(a/b)} \cdot \eta_k} + \sum_{k=1}^{\infty} \frac{\tanh \sqrt{\zeta_k(b/a)}}{\sqrt{\zeta_k(b/a)} \cdot \eta_k} \right\}^{-1},$$

with $\zeta_k(x) = \left(\frac{(2k-1)\pi x}{2} \right)^2 + \frac{jx\omega}{\omega_c}$, (B.2)

$$\eta_k = \left(\frac{(2k-1)\pi}{2} \right)^2, \quad \omega_c = \frac{4}{\mu\sigma ab}, \quad R'_0 = \frac{1}{ab\sigma},$$

where a , and b are the sides of the cross-section, and σ is the conductivity.

Bibliography

- [1] “Benchmark catalog for numerical field calculations in the area of EMC,” http://www.ewh.ieee.org/r8/germany/emc/ag_num/, online Benchmark Catalog of German IEEE EMC-Chapter.
- [2] M. Abramowitz and I. A. Stegun, *Handbook of Mathematical Functions*. New York, USA: Dover, 1965.
- [3] M. I. Aksun, “A robust approach for the derivation of closed-form Green’s functions,” *IEEE Trans. Microw. Theory Tech.*, vol. 44, no. 5, pp. 651–658, 1996.
- [4] L. Alatan, M. I. Aksun, K. Leblebicioglul, and M. Tuncay Birand, “Use of computationally efficient method of moments in the optimization of printed antennas,” *IEEE Trans. Antennas Propag.*, vol. 47, no. 4, pp. 725–732, 1999.
- [5] L. Alatan, M. I. Aksun, M. Mahadevan, and M. Tuncay Birand, “Analytical evaluation of the MoM matrix elements,” *IEEE Trans. Microw. Theory Tech.*, vol. 44, no. 4, pp. 519–525, 1996.
- [6] W. L. Anderson, “Fast Hankel transforms using related and lagged convolutions,” *ACM Transactions on Mathematical Software*, vol. 8, no. 4, pp. 344–368, 1982.
- [7] G. Annaert, “Evaluation of Sommerfeld integrals using chebyshev decomposition,” *IEEE Trans. Antennas Propag.*, vol. 41, no. 2, pp. 159–164, 1993.
- [8] G. Antonini, “Fast multipole method based extraction of PEEC parameters,” in *Proc. of Intern. Symp. on Electronics, Circuits and Systems*, Malta, Spain, 2001, pp. 509–512.
- [9] —, “Fast multipole formulation for PEEC frequency domain modeling,” in *ACES Newsletter*, vol. 17, no. 3, 2002.
- [10] —, “The fast multipole method for PEEC circuits analysis,” in *Proc. of Intern. Symp. on Electromagn. Compat.*, Minneapolis, USA, Aug. 2002, pp. 446–451.
- [11] —, “Spice compatible equivalent circuits of rational approximation of frequency domain responses,” *IEEE Trans. Electromagn. Compat.*, vol. 45, no. 3, pp. 502 – 512, 2003.

- [12] ———, “Rational models for tree structured interconnects,” in *IEE Proceedings on Science*, vol. 1, no. 3, pp. 170 – 178, 2007.
- [13] G. Antonini, S. Cristina, and A. Orlandi, “PEEC modeling of lightning protection systems and coupling to coaxial cables,” *IEEE Trans. Electromagn. Compat.*, vol. 40, no. 4, pp. 481 – 491, 1998.
- [14] G. Antonini, D. Deschrijver, and T. Dhaene, “Broadband macromodels for retarded partial element equivalent circuit (rPEEC) method,” *IEEE Trans. Electromagn. Compat.*, vol. 49, no. 1, pp. 35 – 48, 2007.
- [15] G. Antonini and A. Orlandi, “A wavelet-based time-domain solution for PEEC circuits,” *IEEE Trans. Electromagn. Compat.*, vol. 47, no. 11, pp. 1634–1639, 2000.
- [16] G. Antonini, A. Orlandi, and C. Paul, “Internal impedance of conductors of rectangular cross section,” *IEEE Trans. Electromagn. Compat.*, vol. 47, no. 7, pp. 979–985, 1999.
- [17] G. Antonini, A. Orlandi, and A. E. Ruehli, “Analytical integration of quasi-static potential integrals on nonorthogonal coplanar quadrilaterals for the PEEC method,” *IEEE Trans. Electromagn. Compat.*, vol. 44, no. 2, pp. 399–403, 2002.
- [18] C. A. Balanis, *Advanced Engineering Electromagnetics*. Hoboken, USA: Wiley, 1989.
- [19] R. Bancroft, *Understanding Electromagnetic Scattering Using the Moment Method - A Practical Approach*. Norwood, USA: Artech House, 1996.
- [20] A. Bellen, N. Guglielmi, and A. E. Ruehli, “Methods for linear systems of circuit delay differential equations of neutral type,” *IEEE Trans. Circuits Syst. I*, vol. 46, no. 1, pp. 212–215, 1999.
- [21] L. Bergeron, “Propagation d’ondes le long de lignes électrique,” *Bull. Soc. Fr. Electr.*, pp. 579–1004, Oct. 1937.
- [22] P. Bernardi and R. Cicchetti, “Dyadic Green’s functions for conductor-backed layered structures excited by arbitrary tridimensional sources,” *IEEE Trans. Microw. Theory Tech.*, vol. 42, no. 8, pp. 1474–1483, Aug. 1994.
- [23] W. T. Beyene, “Improving time-domain measurements with a network analyzer using a robust rational interpolation technique,” *IEEE Trans. Microw. Theory Tech.*, vol. 49, no. 3, pp. 500–508, Mar. 2001.
- [24] R. C. Booton, *Computational Methods for Electromagnetics and Microwaves*. Hoboken, USA: Wiley, 1992.
- [25] C. A. Brebbia, *The Boundary Element Method for Engineers*. London, UK: Pentech Press, 1978.

- [26] R. Bunger and F. Arndt, "Efficient MPIE approach for the analysis of three-dimensional microstrip structures in layered media," *IEEE Trans. Microw. Theory Tech.*, vol. 45, no. 8, pp. 1141–1153, Aug. 1997.
- [27] J. C. Chao, Y. J. Liu, F. J. Rizzo, P. O. Martin, and L. Udupa, "Regularized integral equation for curvilinear boundary elements for electromagnetic wave scattering in three dimensions," *IEEE Trans. Antennas Propag.*, vol. 43, pp. 1416–1422, Dec. 1995.
- [28] V. L. Chechurin, N. V. Korovkin, and M. Hayakawa, *Inverse Problems in Electric Circuits and Electromagnetics*. New York, USA: Springer, 2007.
- [29] W. C. Chew, "A quick way to approximate a Sommerfeld-Weyl-type integral," *IEEE Trans. Antennas Propag.*, vol. 36, no. 11, pp. 1654–1657, Nov. 1988.
- [30] —, *Waves and Fields in Inhomogeneous Media*. Piscataway, USA: IEEE Press, 1995.
- [31] Y. L. Chow, J. J. Yang, D. G. Fang, and G. E. Howard, "A close-form spatial green's function for the thick microstrip substrate," *IEEE Trans. Microw. Theory Tech.*, vol. 39, no. 3, pp. 588–592, 1991.
- [32] Y. L. Chow, J. J. Yang, and G. E. Howard, "Complex images for electrostatic field computation in multilayered media," *IEEE Trans. Microw. Theory Tech.*, vol. 39, no. 7, pp. 1120–1125, 1991.
- [33] L. O. Chua, *Computed-aided analysis of electronic circuits*. Englewood Cliffs, USA: Prentice-Hall, 1975.
- [34] R. E. Collin, *Field Theory of Guided Waves*, 2nd ed. Piscataway, USA: IEEE Press, 1991.
- [35] K. M. Coperich, A. E. Ruehli, and A. Cangellaris, "Enhanced skin effect for partial-element equivalent-circuit (PEEC) models," *IEEE Trans. Microw. Theory Tech.*, vol. 48, pp. 1435–1442, 2000.
- [36] D. B. Davidson, *Computational Electromagnetics for RF and Microwave Engineering*. Cambridge, UK: Cambridge University Press, 2005.
- [37] D. Deschrijver, B. Haegeman, and T. Dhaene, "Orthonormal vector fitting: a robust macromodeling tool for rational approximation of frequency domain responses," *IEEE Trans. Adv. Packag.*, vol. 30, no. 2, pp. 216–225, 2007.
- [38] A. Devgan, H. Ji, and W. Dai, "How to efficiently capture on-chip inductance effect: introducing a new circuit element K," in *Proc. IEEE International Conference on Computer Aided Design*, Nov. 2000, pp. 150–155.

- [39] A. R. Djordjevic and T. K. Sarkar, "Closed-form formulas for frequency-dependent resistance and inductance per unit length of microstrip and strip transmission lines," *IEEE Trans. Microw. Theory Tech.*, vol. 42, no. 2, pp. 241 – 248, Feb. 1994.
- [40] A. Dugard and E. I. Verriest, *Stability and Control of Time-Delay Systems: Lecture notes in control and information sciences*. New-York, USA: Springer.
- [41] J. M. Dunn, "A uniform asymptotic expansion for the green's functions used in microstrip calculations," *IEEE Trans. Microw. Theory Tech.*, vol. 39, no. 7, pp. 1223–1226, 1999.
- [42] G. Dural and M. I. Aksun, "Closed-form Green's functions for general sources and stratified media," *IEEE Trans. Microw. Theory Tech.*, vol. 43, no. 7, pp. 1545–1552, 1995.
- [43] J. Ekman, G. Antonini, A. Orlandi, and A. E. Ruehli, "Impact of partial element accuracy on peec model stability," *IEEE Trans. Electromagn. Compat.*, vol. 48, pp. 19–32, 2006.
- [44] L. B. Felsen and N. Marcuvitz, *Radiation and Scattering of Waves*, 2nd ed. Piscataway, USA: IEEE Press, 1994.
- [45] J. E. Garrett, "Advancement of the partial element equivalent circuit formulation," Ph.D. dissertation, University of Kentucky, USA, 1997.
- [46] J. E. Garrett and A. E. Ruehli, "PEEC-EFIE for modeling 3D geometries with lossy inhomogeneous dielectrics and incident fields," *IBM T. J. Watson Research Center, Yorktown Heights*, Oct 1993.
- [47] J. E. Garrett, A. E. Ruehli, and C. R. Paul, "Accuracy and stability improvements of integral equation models using the partial element equivalent circuit (PEEC) approach," *IEEE Trans. Antennas Propag.*, vol. 46, no. 12, pp. 1824–1832, 1998.
- [48] Y. Ge and K. P. Essele, "A fast and general complex image method for evaluating Sommerfeld integrals," *Micro. Opt. Tech. Let.*, vol. 30, no. 1, pp. 24–26, 2001.
- [49] —, "New closed-form Green's functions for microstrip structures - theory and results," *IEEE Trans. Microw. Theory Tech.*, vol. 50, no. 6, pp. 1556–1560, 2002.
- [50] L. J. Giacoletto, "Frequency- and time-domain analysis of skin effect," *IEEE Trans. Magn.*, vol. 32, no. 1, pp. 220–229, Jan 1996.
- [51] A. W. Glisson, "On the development of numerical techniques for treating arbitrary-shaped surfaces," Ph.D. dissertation, University of Mississippi, USA, 1978.
- [52] A. Goerisch, "Netzwerkorientierte modellierung und simulation elektrischer verbindungsstrukturen mit der methode per partiellen elemente," Ph.D. dissertation, Cuvillier Verlag, Goettigen, Germany, 2002.

- [53] A. Goerisch and G. Wollenberg, "Ermittlung linearer passiver zweipole durch approximation von impedanzverloefen," *Tagungsband zur Fachtagung Informations- und Mikrosystemstechnik in Magdeburg*, pp. 441–448, Maerz 1998.
- [54] K. C. Gupta, R. Gard, and R. Chada, *Computer-Aided Design of Microwave circuits*. Norwood, USA: Artech House Inc., 1981.
- [55] B. Gustavsen and A. Semlyen, "Rational approximation of frequency responses by vector fitting," *IEEE Trans. Power Del.*, vol. 14, pp. 1052–1061, 1999.
- [56] H. Haase, S. V. Kochetov, G. Wollenberg, and J. Nitsch, "Einkopplung externer Störfelder in ungleichförmige Leitungen - Analyse im Frequenz- und Zeitbereich," in *Internationale Fachmesse und Kongress für Elektromagnetische Verträglichkeit*, Düsseldorf, Germany, Feb. 2004, pp. 283–290.
- [57] H. Haase and J. Nitsch, "Full-wave transmission line theory for the analysis of three-dimensional wire-like structures," in *Proc. of 14th Intern. Symp. on Electromagn. Compat.*, Zürich, Switzerland, Feb. 2001, pp. 235–240.
- [58] S. H. Hall, G. W. Hall, and J. A. McCall, *High-Speed Digital System Design: A Handbook of Interconnect Theory and Design Practices*. New York, USA: Wiley-IEEE Press, 2000.
- [59] G. W. Hanson, "Dyadic Green's function for a multilayered planar medium - a dyadic eigenfunction approach," *IEEE Trans. Antennas Propag.*, vol. 52, no. 12, pp. 3350–3356, Dec. 2004.
- [60] R. F. Harrington, *Time-Harmonic Electromagnetic Fields*. New York, USA: McGraw-Hill, 1961.
- [61] ———, *Field Computation by Moment Methods*, 2nd ed. Piscataway, USA: IEEE Press, 1993.
- [62] F. B. Hildebrand, *Introduction to Numerical Analysis*, 2nd ed. New York, USA: Dover, 1987.
- [63] C. Hoer and C. Love, "Exact inductance equations for rectangular conductors with applications to more complicated geometries," *Journal of Research of the National Bureau of Standards*, vol. 69, 1966.
- [64] R. K. Hoffmann, *Handbook of microwave integrated circuits*. Norwood, USA: Artech House Inc., 1987.
- [65] R. C. Hsieh and E. T. Kuo, "Fast full-wave analysis of planar microstrip circuit elements in stratified media," *IEEE Trans. Microw. Theory Tech.*, vol. 46, pp. 1291–1297, Sep. 1998.

- [66] Y. Hua and T. K. Sarkar, "Generalized pencil-of-function method for extracting poles of an EM system from its transient response," *IEEE Trans. Antennas Propag.*, vol. 37, no. 2, pp. 229 – 234, Feb. 1989.
- [67] V. Jandhyala, Y. Wang, D. Gope, and R. Shi, "Coupled electromagnetic-circuit simulation of arbitrarily-shaped conducting structures using triangular meshes," in *Proc. of Intern. Symp. on Quality Electronic Design*, 2002, pp. 38–42.
- [68] D. S. Jones, *Methods in Electromagnetic Wave Propagation*, 2nd ed. Piscataway, USA: IEEE Press, 1995.
- [69] S. Kamri, *Network Theory: Analysis and Synthesis*. Boston, USA: Allyn and Bacon, 1966.
- [70] S. Kim and D. P. Neikirk, "Compact equivalent circuit model for the skin effect," *IEEE-MTT-S International Microwave Symposium*, pp. 1815–1818, 1996.
- [71] S. V. Kochetov, "A model for finite-length transmission lines considering skin and radiation effects," Ph.D. dissertation, Saint-Petersburg State Polytechnic University, Russia, 2000.
- [72] S. V. Kochetov and M. Leone, "Effiziente Zeitbereichsimulation von Crosstalk auf Leiterplatten mit der PEEC-Methode," in *Internationale Fachmesse und Kongress für Elektromagnetische Verträglichkeit*, Düsseldorf, Germany, Feb. 2008, pp. 555–562.
- [73] —, "Generalized PEEC method based on dyadic Green's functions in time and frequency domain," in *Proc. of Intern. Symp. EMC Europe*, Hamburg, Germany, in review.
- [74] S. V. Kochetov, M. Leone, and G. Wollenberg, "Neue Formulierung der PEEC-Methode mit dyadischen Greenschen Funktionen für die Simulation von Verbindungsstrukturen in geschichteten Medien," in *Internationale Fachmesse und Kongress für Elektromagnetische Verträglichkeit*, Düsseldorf, Germany, Feb. 2008, pp. 547–554.
- [75] —, "PEEC formulations based on dyadic Green's functions for layered media in the time and frequency domain," *IEEE Trans. Electromagn. Compat.*, in review.
- [76] S. V. Kochetov and G. Wollenberg, "PEEC models with multipoint approximations of derivatives," *28th General Assembly of URSI*, Sep. 2005.
- [77] —, "Stability of full-wave PEEC models: reason for instabilities and approach for correction," *IEEE Trans. Electromagn. Compat.*, vol. 47, pp. 738–748, Nov. 2005.
- [78] —, "Stability of full-wave PEEC models: reason for instabilities and way for correction," in *Proc. of 16th Int. Symp. on Electromagn. Compat.*, Zürich, Switzerland, Feb. 2005, pp. 543–546.

- [79] ———, “Stable time domain PEEC solution for pulse excited interconnection structures,” in *Proc. of Intern. Symp. on Electromagn. Compat.*, vol. 3, Chicago, USA, 2005, pp. 911–916.
- [80] ———, “Improvement of PEEC models via multipoint approximations of potentials,” in *Proc. of Intern. Symp. EMC Europe*, Barcelona, Spain, Sep. 2006, pp. 57–62.
- [81] ———, “Stable and effective full-wave PEEC models by full-spectrum convolution macro-modeling,” *IEEE Trans. Electromagn. Compat.*, vol. 49, pp. 25–34, 2007.
- [82] S. V. Kochetov, G. Wollenberg, and M. Leone, “PEEC-models based on dyadic Green’s functions for structures in layered media,” in *Proc. of Int. Symp. on Electromagn. Compat.*, Saint-Petersburg, Russia, Jun. 2007, pp. 179–182.
- [83] S. V. Kochetov, G. Wollenberg, and S. Thamm, “Modelling of common mode interferences produced by a switched mode power supply,” in *Proc. of Int. Symp. on Electromagn. Compat.*, Saint-Petersburg, Russia, Jun. 2005, pp. 29–33.
- [84] S. V. Kochetov, G. Wollenberg, T. Winkler, R. Döbelin, and H. Mecke, “Anwendung der Methode der partiellen Elemente zur Berücksichtigung von Verbindungsstrukturen und Koppelpfaden bei der Simulation leistungselektronischer Schaltungen,” in *Internationale Fachmesse und Kongress für Elektromagnetische Verträglichkeit*, Düsseldorf, Germany, Feb. 2004, pp. 807–812.
- [85] S. V. Kochetov, G. Wollenberg, T. Winkler, R. Döbelin, and S. Thamm, “Analysis of the influence of interconnections on switched mode power electronics systems by a circuit simulator expanded with PEEC models,” in *Proc. of 17th Int. Symp. on Electromagn. Compat.*, Wroclaw, Poland, Jun. 2004, pp. 188–191.
- [86] G. Korn and T. Korn, *Mathematical Handbook for Scientists and Engineers: Definitions, Theorems and Formulas*. New York, USA: McGraw-Hill, 1961.
- [87] N. V. Korovkin, *Macromodeling of electromagnetic processes described by stiff equations*. Saint-Petersburg, Russia: Dr.Sc. Dissertation, Saint-Petersburg State Polytechnic University.
- [88] N. V. Korovkin, V. L. Chechurin, and M. Hayakawa, *Inverse Problems in Electric Circuits and Electromagnetics*. New York, USA: Springer, 2007.
- [89] N. V. Korovkin, S. V. Kotchetov, E. E. Selina, and M. Ianoz, “Simulation of frequency characteristics of transmission lines for transient calculations,” in *Proc. of 13th Int. Symp. on Electromagn. Compat.*, Zürich, Switzerland, Feb. 1999, pp. 445–450.
- [90] N. V. Korovkin and E. E. Selina, *Modeling of Wave Processes in distributed electromagnetic systems*. Saint-Petersburg, Russia: SPUSStP, 1992.
- [91] A. Kost, *Numerische Methoden in der Berechnung elektromagnetischer Felder*. Berlin, Germany: Springer.

- [92] B. Krauter and L. Pileggi, "Generating sparse partial inductance matrices with guaranteed stability," *ICCAD*, pp. 45–52, Nov. 1995.
- [93] K. S. Kunz and R. J. Luebbers, *Finite Difference Time Domain Method for Electromagnetics*. Boca Raton, USA: CRC Press, 1993.
- [94] F. F. Kuo, *Network Analysis and Synthesis*. Hoboken, USA: Wiley, 1966.
- [95] J. D. Lambert, *Numerical Methods for Ordinary Differential Systems: The Initial Value Problem*. Hoboken, USA: Wiley, 1997.
- [96] M. Leone, "Berechnung der ein- und abstrahlungsverhaltens von leiterplatten mit der momentenmethode," Ph.D. dissertation, VDI Verlag, Düsseldorf, Germany, 2000.
- [97] —, "Design expressions for the trace-to-edge common-mode inductance of a printed circuit board," *IEEE Trans. Electromagn. Compat.*, vol. 43, no. 4, pp. 667–671, Nov. 2001.
- [98] —, "Radiated susceptibility on the printed-circuit-board level: simulation and measurement," *IEEE Trans. Electromagn. Compat.*, vol. 47, pp. 471–478, 2005.
- [99] —, "Closed-form expressions for the electromagnetic radiation of microstrip signal traces," *IEEE Trans. Electromagn. Compat.*, vol. 49, no. 2, pp. 322–328, May 2007.
- [100] M. Leone, H.-D. Brüns, and H. L. Singer, "Fast EMC analysis for printed circuit boards using an equivalent-wire Method of Moments," in *Proc. of Int. Symp. EMC Europe*, Roma, Italy, Sep. 1998, pp. 7–12.
- [101] —, "Fast susceptibility analysis for printed circuit boards using an equivalent-wire Method of Moments," in *Proc. of 13th Intern. Symp. on Electromagn. Compat.*, Zürich, Switzerland, Feb 1999, pp. 251 – 256.
- [102] M. Leone and H. L. Singer, "On the coupling of an external electromagnetic field to a printed circuit board trace," *IEEE Trans. Electromagn. Compat.*, vol. 41, no. 4, pp. 418 – 424, Nov. 1999.
- [103] M. A. Leontovich, *Investigations of Propagation of Radio Wave, Part II*. Moscow, Russia: Sc. Academy of USSR, 1948.
- [104] I. V. Lindell, *Methods for Electromagnetic Field Analysis*. Piscataway, USA: IEEE Press, 1995.
- [105] M. Magdowski, S. V. Kochetov, and M. Leone, "Modeling the skin effect in the time domain for the simulation of circuit interconnects," in *Proc. of Intern. Symp. EMC Europe*, Hamburg, Germany, in review.

- [106] M. Marin, S. Barkeshli, and P. H. Pathak, "Efficient analysis of planar microstrip geometries using a closed-form asymptotic representation of the grounded dielectric slab Green's function," *IEEE Trans. Microw. Theory Tech.*, vol. 37, no. 4, pp. 669–679, Apr. 1989.
- [107] R. Marklein, "Numerische verfahren zur modellierung von akustischen, elektromagnetischen, elastischen und piezoelektrischen wellenausbreitungsproblemen im zeitbereich basierend auf der finiten integrationstechnik," Ph.D. dissertation, Shaker Verlag, Herzogenrath, Germany.
- [108] K. A. Michalski, "Mixed-potential integral equation for objects in layered media," *Arch. Elek. Uebertragung*, vol. 39, pp. 317–322, 1985.
- [109] —, "Multilayered media Green's functions in integral equation formulations," *IEEE Trans. Antennas Propag.*, vol. 46, no. 10, pp. 1405–1418, 1998.
- [110] K. A. Michalski and J. R. Mosig, "Multilayered media Green's functions in integral equation formulations," *IEEE Trans. Antennas Propag.*, vol. 45, no. 3, pp. 508–519, 1997.
- [111] K. A. Michalski and D. Zheng, "Electromagnetic scattering and radiation by surfaces of arbitrary shape in layered media, part I: Theory," *IEEE Trans. Antennas Propag.*, vol. 38, no. 3, pp. 335–344, Mar. 1990.
- [112] —, "Electromagnetic scattering and radiation by surfaces of arbitrary shape in layered media, part II: Implementation and results for contiguous half-spaces," *IEEE Trans. Antennas Propag.*, vol. 38, no. 3, pp. 345–352, Mar. 1990.
- [113] E. K. Miller and T. K. Sarkar, *Frontiers in Electromagnetics*, D.H. Werner and R. Mittra ed. Piscataway, NJ: IEEE Press, 2000, ch. Model-order reduction in electromagnetics using model-based parameter estimation, pp. 371–436.
- [114] S.-H. Min and M. Swaminathan, "Construction of broadband passive macromodels from frequency data for simulation of distributed interconnect networks," *IEEE Trans. Electromagn. Compat.*, vol. 46, no. 4, pp. 544–558, 2004.
- [115] R. M. Mäkinen, H. D. Gerssem, T. Weiland, and M. A. Kivikoski, "Modeling of lossy curved surfaces in 3-D FIT/FDTD techniques," vol. 54, no. 11, pp. 3490–3498, 2006.
- [116] J. R. Mosig, *Numerical techniques for microwave and millimeter-wave passive structures*, T. Itoh ed. Hoboken, NJ: Wiley, 1989, ch. Integral equation technique, pp. 133–213.
- [117] A. A. Omar and Y. L. Chow, "A solution of coplanar waveguide with air-bridges using complex images," *IEEE Trans. Microw. Theory Tech.*, vol. 40, no. 11, pp. 2070–2077, 1992.

- [118] R. E. A. C. Paley and N. Wiener, "Fourier transforms in the complex domain," *Am. Math. Soc. Coloq. Pub.*, pp. 16–17, 1934.
- [119] I. Park, R. Mittra, and M. I. Aksun, "Numerically efficient analysis of planar microstrip configurations using closed-form Green's functions," *IEEE Trans. Microw. Theory Tech.*, vol. 43, no. 2, pp. 394–400, 1995.
- [120] S. O. Park and C. A. Balanis, "Analytical technique to evaluate the asymptotic part of the impedance matrix of Sommerfeld-type integrals," *IEEE Trans. Antennas Propag.*, vol. 45, no. 5, pp. 798–805, 1997.
- [121] C. R. Paul, *Introduction to Electromagnetic Compatibility*. Hoboken, USA: Wiley, 2006.
- [122] A. F. Peterson, S. L. Ray, and R. Mittra, *Computational Methods for Electromagnetics*. Piscataway, USA: IEEE Press, 1998.
- [123] E. Philippow, *Grundlagen der Elektrotechnik*, 10th ed. Berlin, Germany: Verlag Technik Berlin, 2000.
- [124] L. T. Pillage and R. A. Rohrer, "Asymptotic waveform evaluation for timing analysis," *IEEE Trans. Comput.-Aided Design Integr. Circuits Syst.*, vol. 9, no. 4, pp. 352–366, Apr. 1990.
- [125] S. M. Rao, D. R. Wilton, and A. W. Glisson, "Electromagnetic scattering by surfaces of arbitrary shapes," *IEEE Trans. Antennas Propag.*, vol. 30, no. 3, pp. 409–418, May 1982.
- [126] Y. S. Rickard and N. K. Nikolova, "Off-grid perfect boundary conditions for the FDTD method," *IEEE Trans. Microw. Theory Tech.*, vol. 53, no. 7, pp. 2274–2283, 2005.
- [127] V. Rokhlin, "Rapid solution of integral equations of scattering theory in two dimensions," *J. Comput. Phys.*, vol. 86, no. 2, pp. 414–439, Feb. 1990.
- [128] A. Rong and A. C. Cangellaris, "Generalized PEEC models for three-dimensional interconnect structures and integrated passives of arbitrary shapes," in *Proc. of Conf. on Dig. Electr. Perf. Electronic Packaging*, vol. 10, Oct. 2001, pp. 225–228.
- [129] A. E. Ruehli, "Equivalent circuit models for three-dimensional multiconductor systems," *IEEE Trans. Microw. Theory Tech.*, vol. 22, no. 3, pp. 216–221, 1974.
- [130] A. E. Ruehli, G. Antonini, J. Esch, J. Ekman, A. Mayo, and A. Orlandi, "Non-orthogonal PEEC formulation for time and frequency domain EM and circuit modeling," *IEEE Trans. Electromagn. Compat.*, vol. 45, no. 2, pp. 167 – 176, 2003.
- [131] A. E. Ruehli, J. E. Garrett, and C. R. Paul, "Circuit models for 3D structures with incident fields," in *Proc. of Intern. Symp. on Electromagn. Compat.*, Dallas, USA, Aug. 1993, pp. 28–32.

- [132] A. E. Ruehli and H. Heeb, "Circuit models for three-dimensional geometries including dielectrics," *IEEE Trans. Microw. Theory Tech.*, vol. 40, no. 7, pp. 1507–1516, 1992.
- [133] A. E. Ruehli, U. Miekala, A. Bellen, and H. Heeb, "Stable time domain solutions for EMC problems using PEEC circuit models," in *Proc. of Intern. Symp. on Electromagn. Compat.*, Chicago, USA, Aug 1994, pp. 371–376.
- [134] A. E. Ruehli, U. Miekala, and H. Heeb, "Stability of discretized partial element equivalent EFIE circuit models," *IEEE Trans. Antennas Propag.*, vol. 43, no. 6, pp. 553–559, 1995.
- [135] A. Sadigh and E. Arvas, "Treating the instabilities in marching-on in time method from a different perspective," *IEEE Trans. Antennas Propag.*, vol. 41, no. 1, pp. 1695–1702, 1993.
- [136] M. N. O. Sadiku, *Numerical Techniques in Electromagnetics*, 2nd ed. Boca Raton, USA: CRC Press, 2000.
- [137] V. Schulz and G. Mroczynski, "A benchmark catalog for numerical field calculations in the area of EMC," in *Proc. of 13th Int. Symp. on Electromagn. Compat.*, Zürich, Switzerland, Feb. 1999, pp. 115–121.
- [138] A. E. Siegman, "Quasi fast Hankel transform," *Optic Letters*, vol. 1, pp. 13–15, 1977.
- [139] P. P. Silvester, *Finite Elements for Wave Electromagnetics*. Piscataway, USA: IEEE Press, 1994.
- [140] H. L. Singer, H.-D. Brüns, and G. Bürger, "State of the art in the Method of Moments," in *Proc. of Intern. Symp. on Electromagn. Compat.*, Santa Clara, USA, Aug. 1996, pp. 122–127.
- [141] H. L. Singer, H.-D. Brüns, T. Mader, and A. Freiberg, *CONCEPT II - Manual of the program system*. Hamburg, Germany: Techn. Univ. Hamburg-Harburg, 1999.
- [142] A. Sommerfeld, *Partial Differential Equations*. New York, USA: Academic, 1949.
- [143] J. M. Song and W. C. Chew, "Multilevel fast-multipole algorithm for solving combined field integral equations of electromagnetic scattering," *Microwave Opt. Technol. Lett.*, vol. 10, no. 1, pp. 14–19, Sep. 1995.
- [144] A. Taflove, *Computational Electrodynamics - The Finite-Difference Time-Domain Method*. Norwood, USA: Artech House, 1995.
- [145] C.-T. Tai, *Dyadic Green's functions in Electromagnetic Theory*, 2nd ed. Piscataway, USA: IEEE Press, 1997.
- [146] —, *Generalized Vector and Dyadic Analysis: Applied Mathematics in Field Theory*, 2nd ed. Piscataway, USA: IEEE Press, 1997.

- [147] F. M. Tesche, M. Ianoz, and T. Karlsson, *EMC Analysis Methods and Computational Models*. Hoboken, USA: Wiley, 1997.
- [148] S. Thamm, S. V. Kochetov, G. Wollenberg, and M. Leone, "Alternative PEEC modeling with partial reluctances and capacitances for power electronics applications," in *Proc. of Int. Symp. on Electromagn. Compat.*, Saint-Petersburg, Russia, Jun. 2007, pp. 56–59.
- [149] A. Torabian and Y. L. Chow, "Simulated image method for Green's function of layered media," *IEEE Trans. Microw. Theory Tech.*, vol. 47, no. 9, pp. 1777–1781, 1999.
- [150] L. Tsang, C.-J. Ong, C.-C. Huang, and V. Jandhyala, "Evaluation of the Green's function for the mixed potential integral equation (MPIE) method in the time domain for layered media," *IEEE Trans. Antennas Propag.*, vol. 51, no. 7, pp. 1559 – 1570, Jul. 2003.
- [151] P. W. Tuinenga, *SPICE, A Guide to Circuit Simulation and Analysis using PSpice*. Englewood Cliffs, USA: Prentice-Hall, 1988.
- [152] V. Vahrenholt, H.-D. Bruns, and H. L. Singer, "Reduction of unknowns in peec structures by exploiting connectivity of PEEC cells," *IEEE Trans. Electromagn. Compat.*, vol. 49, no. 2, pp. 412–418, May 2007.
- [153] V. Vahrenholt, H.-D. Bruns, H. L. Singer, and R. Rimolo-Donaldo, "Verkopplung einer schnellen PEEC-Methode mit der Momentenmethode bei gedruckten Schaltungen mittels der elektrischen Feldstärke," in *Internationale Fachmesse und Kongress für Elektromagnetische Verträglichkeit*, Düsseldorf, Germany, Feb. 2008, pp. 563–570.
- [154] M. Van Blaricum and R. Mittra, "A technique for extracting the poles and residues of a system directly from its transient response," *IEEE Trans. Microw. Theory Tech.*, vol. 23, no. 6, pp. 777–781, Nov. 2001.
- [155] U. van Rienen, *Numerical Methods in Computational Electrodynamics*. New York, USA: Springer, 2001.
- [156] J. Vlach and K. Singhal, *Computer Methods for Circuit Analysis and Design*. Boston, USA: Kluwer, 1994.
- [157] A. Vladimirescu, *The SPICE book*. Hoboken, USA: Wiley, 1994.
- [158] T. Weiland, "Eine Methode zur Lösung der Maxwell'schen Gleichungen für sechskomponentige Felder auf diskreter Basis," *Arch. Elek. Uebertragung*, vol. 31, pp. 116–120, 1977.
- [159] J. R. Wait, *Electromagnetic Waves in Stratified Media*. Piscataway, USA: IEEE Press, 1996.

-
- [160] G. Wollenberg and A. Goerisch, "Analysis of 3D interconnect structures with PEEC using SPICE," *IEEE Trans. Electromagn. Compat.*, vol. 41, no. 4, pp. 412–417, 1999.
- [161] G. Wollenberg and S. V. Kochetov, "Modeling the skin effect in wire-like 3D interconnection structures with arbitrary cross section by a new modification of the PEEC method," in *Proc. of 15th Int. Symp. on Electromagn. Compat.*, Zürich, Switzerland, Feb. 2003, pp. 609–614.
- [162] F. Yang, X.-X. Zhang, X. Ye, and Y. Rahmat-Samii, "Wide-band E-shaped patch antennas for wireless communications," *IEEE Trans. Antennas Propag.*, vol. 49, no. 7, pp. 1094–1100, 2001.
- [163] K. S. Yee, "Numerical solution of initial boundary value problems involving Maxwell's equations in isotropic media," vol. 14, pp. 302–207, 1966.

Acknowledgment

At first, I would like to thank my professors at the Institute for Fundamental Electrical Engineering and Electromagnetic Compatibility, O.v.G.-University Magdeburg:

- Prof. Dr. Günter Wollenberg for trust me, for providing a pleasant research environment, for his steady friendly support in the professional and private areas, for making possible this work;
- Prof. Dr. Marco Leone for his constant friendly support in last two years, which has made possible this work, for valuable scientific discussions, for the pleasant team work.
- Prof. Dr. habil. Jürgen Nitsch for the pleasant joint work at the DGF research group FOR417 and his kind interest to my research activity.

As well, it is a great pleasure to thank the following people:

- Prof. Dr. Sc. Nikolay V. Korovkin for bringing me to my course of life and the supervision of my scientific activity at the State Polytechnic University St.-Petersburg, for the long-lived friendship and cooperation;
- Prof. Dr. Michel Ianoz for the support and many valuable discussions during my stay at the Swiss Federal Institute of Technology;
- Prof. Dr. Hermann Singer for his kind interest to this work and for interesting discussions;
- Prof. Dr. Sc. Elena Soloveva for interesting discussions and friendship;
- Sven Thamm, Margaritha Kuzmina, Kirill Brezhnyev, Mathias Magdowski for the nice joint work at the PEEC - research group;
- my present and former colleagues at the Institute for Fundamental Electrical Engineering and Electromagnetic Compatibility, namely, Helge Fredrich, Dr. habil. Frank Gronwald, Petra Knauff, Prof. Dr. habil. Hans Georg Krauthäuser, Oliver Krönig, Sven Plate, Dr. Wolfgang Schätzing, Dr. Hans-Jürgen Scheibe, Dr. Heinz-Peter Scheibe, Dr. Hans-Peter Schulze, Steffen Schulze, Dr. Torsten Steinmetz, Dr. Sergey Tkachenko;

Especially, I would like to thank my wife Alisa for her love and care during all these years, for the inspiration to the creative work, for her patience at some weekends and evenings.

Curriculum Vitae

Sergey V. Kochetov

born on April 17th, 1973, in Saint-Petersburg, Russia

Professional Experience

- 1996-2001 State Polytechnic University St.-Petersburg, Faculty of Electrical Engineering
Research assistant, Theoretical Electrical Engineering
- since 2001 Otto-von-Guericke University Mageburg,
Institute for Fundamental Electrical Engineering and
Electromagnetic Compatibility
Research assistant
- since 2003 Research assistant pursuing Habilitation degree
- since 2007 Lecturer "Numerical Methods in Classical Electrodynamics"

Education

- 1996-2000 State Polytechnic University St.-Petersburg, Faculty of Electrical Engineering
PhD degree, in Electrical Engineering, 2000
- 1990-1996 State Polytechnic University St.-Petersburg, Faculty of Technical Cybernetics
Master Degree, in Automation and Computer Engineering, 1996
- 1988-1990 Mathematical Gymnasium *N^o 470* St.-Petersburg,
Graduated "Abitur", 1990

Stay Abroad

- 1997-1998 Swiss Federal Institute of Technology (EPFL), Lausanne, Switzerland
Power Systems Laboratory (LRE)
Visiting Researcher, in Electrical Engineering

Awards

- 2007 The paper [81] has been selected by the IEEE Transactions
on Electromagnetic Compatibility as one of the three finalists for
the 2007 Richard B. Schulz Best Transactions Paper Award.
- 2008 The Best Paper Award from 13th Internationale Fachmesse und Kongress
für Elektromagnetische Verträglichkeit, Messe Düsseldorf, Germany

Res Electricae Magdeburgenses

MAGdeburger FORum zur Elektrotechnik



-
- Band 1** A. ORTHS: *Multikriterielle, optimale Planung von Verteilungsnetzen im liberalisierten Energiemarkt unter Verwendung von spieltheoretischen Verfahren*, 2003, ISBN 3-929757-57-5
- Band 2** M. PURMANN: *Optimierung des Betriebsverhaltens von PEM-Brennstoffzellen unter Berücksichtigung von elektrischem und Gesamtwirkungsgrad bei unterschiedlichen Lastanforderungen und Betriebsparametern*, 2004, ISBN 3-929757-63-X
- Band 3** M. AL-HAMID: *Extraktion von höheren Moden TEM-Wellenleitern*, 2004, ISBN 3-929757-64-8
- Band 4** H. HAASE, J. NITSCH, T. STEINMETZ: *Transmission-Line Super Theory – A new Approach to an Effective Calculation of Electromagnetic Interference*, 2004, ISBN 3-929757-67-2
- Band 5** A. BACHRY: *Power Quality Studies in Distribution Systems Involving Spectral Decomposition*, 2004, ISBN 3-929757-68-0
- Band 6** Z. STYCZYNSKI: *Power Network and Renewables – A Scientific Report*, 2004, ISBN 3-929757-69-9
- Band 7** E. BLUME: *Numerische Analyse der Kopplung linearer Antennen innerhalb eines Resonators*, 2004, ISBN 3-929757-71-0
- Band 8** E. HANDSCHIN, Z. STYCZYNSKI: *Power System Application of the Modern Battery Storage*, 2004, ISBN 3-929757-75-3
- Band 9** H. HAASE: *Full-Wave Field Interactions of Nonuniform Transmission Lines*, 2005, ISBN 3-929757-78-8
- Band 10** D. NITSCH: *Die Wirkung eingekoppelter ultrabreitbandiger elektromagnetischer Impulse auf komplexe elektronische Systeme*, 2005, ISBN 3-929757-79-6
- Band 11** B. HADZI-KOSTOVA: *Protection Concepts in Distribution Networks with Decentralised Energy Resources*, 2005, ISBN 3-929757-84-2
- Band 12** T. STEINMETZ: *Ungleichförmige und zufällig geführte Mehrfachleitungen in komplexen, technischen Systemen*, 2006, ISBN 3-929757-98-2
- Band 13** Z. STYCZYNSKI, J. HAUBROCK(Editors): *Influence of Distributed and Renewable Generation on Power System Security*, 2006, ISBN 3-929757-99-0

-
- Band 14** G. HEIDECK: *Ein autonomes Brennstoffzellensystem: Optimierungsansätze*, 2007, ISBN: 3-929757-94-X
- Band 15** Z. STYCZYNSKI, H. D. MUSIKOWSKI(Editors): *Dresdener Kreis Elektroenergieversorgung 7.*, 2006, ISBN: 3-929757-85-0
- Band 16** F. GRONWALD: *Antenna Theory in Resonating Systems derived from Fundamental Electromagnetism*, 2006, ISBN: 3-929757-93-1
- Band 17** H.-G. KRAUTHÄUSER: *Grundlagen und Anwendungen von Modenverwirbelungskammern*, 2007, ISBN: 978-3-929757-43-9
- Band 18** C. DZIENIS: *Ersatzmodelle nichtlinearer Lasten in elektrischen Verteilungsnetzen*, 2007, ISBN: 978-3-929757-07-1
- Band 19** Z. STYCZYNSKI, J. HAUBROCK(Editors): *Renewable and Dispersed Power Generation in Power Systems*, 2007, ISBN: 978-3-929757-44-6
- Band 20** J. HAUBROCK: *Parametrierung elektrischer Äquivalentschaltbilder von PEM Brennstoffzellen*, 2008, ISBN: 978-3-940961-02-0
- Band 21** A. N. ANGELOV: *Rechnergestütztes Lernen im Bereich der Regenerativen Energien (Ausgewählte Aspekte)*, 2008, ISBN: 978-3-940961-03-7
- Band 22** P. KOMARNICKI: *Anwendung hochgenauer, synchroner Messungen zur Verbesserung des Betriebs von Verteilungsnetzen*, 2008, ISBN: 978-3-940961-04-4
- Band 23** C. ROGGATZ: *Trainingssimulator für die Führung von elektrischen Systemen mit dezentralen Energieeinspeisungen - Trainingsszenarien und Umsetzung*, 2008, ISBN: 978-3-940961-05-1
- Band 24** K. RUDION: *Aggregated Modelling of Wind Farms*, 2008, ISBN: 978-3-940961-14-3
- Band 25** M. R. GANJAVI: *Protection System Coordination Using Expert System*, 2008, ISBN: 978-3-940961-15-0
- Band 26** S. BOFINGER: *Energieversorgungsnetze mit einem hohen Anteil an photovoltaischer Solarenergie: Standortbestimmung, Solarstromprognose, Netzintegration*, 2008, ISBN: 978-3-940961-25-9
- Band 27** Z. STYCZYNSKI, P. KOMARNICKI (Editorial Board): *Distributed and Renewable Power Generation*, 2008, ISBN: 978-3-940961-26-6
-